Development and Characterisation of

Nano-multilayer CrAlSiN Coating Systems for

Cutting Tools

Ran Ji

School of Metallurgy and Materials

The University of Birmingham

Supervisors:

Prof. H. Dong & Dr. X. Li

Synopsis

Cutting technique evolution, such as high speed cutting and lubrication-free machining, leads to an ever-increasing demand for new generation of tribological hard coating on cutting tool materials. During the last decade, TiN-based nanocomposite and nano-multilayer coatings have been employed as protective coatings for cutting tools due to the significantly enhanced properties, such as strength, toughness and oxidation resistance, by the introduction of alloying elements (e.g. Al, Si, etc.) and the advanced nanocomposite and/or nano-multilayer structure. However, no systematic work has been conducted on the more oxidation resistant CrN-based nano-structured coatings. This study has been directed at developing and characterising a new generation of CrAlSiN nano-multilayer coating system for high performance cutting tools.

In the present study, two types of CrAlSiN nano-multilayer coating with different microstructures were designed and synthesised on AISI M2 high speed steel, while CrN and TiAlSiN coatings were adapted as benchmarks. Selected coatings were also deposited on pre-nitrided M2 substrate to investigate the effect of duplex treatment.

A series of CrAlSiN coatings, which have sharp interfaces between individual nano-layers due to the target arrangement during the deposition process, were designed with varying bilayer thickness and named as Type I coatings. An fcc and an hcp phase were identified for all type I coatings, and it has been found that the bilayer thickness has a significant influence on the orientation of both phases, which in turn affects their mechanical properties.

A different target arrangement was employed to deposit the so-called type II CrAlSiN coating, which have blurred interfaces, and a medium bilayer thickness was adoped. Due to the insignificant difference in composition between neighbouring nano-layers, only one fcc phase was found in type II CrAlSiN coating.

Both types of CrAlSiN coatings have showed significantly improved mechanical properties, such as hardness and toughness, over the CrN coating, and better oxidation resistance than both CrN and TiAlSiN coatings.

Reciprocating sliding wear tests were carried out at both room temperature and elevated temperatures. It has been found that the wear resistance of the new nano-multilayer CrAlSiN coating is more than 10 times higher than CrN when tested at room and elevated temperatures. This could be attributed to high H/E ratio, high toughness and good oxidation resistance conferred by the nano-multilayer structure and multi-component composition of the CrAlSiN coatings. It has also found that duplex treatment can improve the wear resistance of nano-multilayer coating by two orders of magnitude due to the improved load bearing capacity of the coating system.

Compared with the benchmark monolayer binary CrN coating, the new multi-component, nano-multilayer CrAlSiN coating possesses a much better resistance to rolling-sliding wear mainly due to the improved toughness and oxidation resistance.

Acknowledgements

Abbreviations and Acronyms

ASPN   Active Screen Plasma Nitriding

BFI   Bright Field Image

BSE   Back Scattered Electron

C   CrAlSiN (for Sample Code)

CAE   Cathodic Arc Evaporation

CVD   Chemical Vapour Deposition

DCPN   Direct Current Plasma Carburising

FCC   Face Centred Cubic

FFT   Fast Fourier Transform

FIB   Focused Ion Beam

GAXRD   Glancing Angle X-Ray Diffraction

GDOES   Glow Discharge Optical Emission Spectroscopy

HCP   Hexagonal Close Packed

HSS   High Speed Steel

LCB   Load Bearing Capacity

MeN   Metal Nitride (where Me could be Cr,Al,Si orTi)

PVD   Physical Vapour Deposition

SAD   Selected Area Diffraction

SE   Secondary Electron (or Surface Engineering)

SEM   Scanning Electron Microscope

T   TiAlSiN (for Sample Code)

TEM   Transmission Electron Microscope

VSI   Vertical Scanning Interferometry

Contents

Chapter 1   Introduction and Objectives

1.1 Introduction

Continuous evolution of the manufacturing industry has imposed harsher conditions, which has led to an ever increasing demand for cutting tools with superior wear- and corrosion-resistance. Physical vapour deposition (PVD) techniques have been successfully used to produce a variety of hard coatings on cutting tools to increase their performance and lifetime for decades [1, 2].

TiN and CrN, widely used since the 1980s, are the first and the most well-established coatings for cutting tools [2-4]. However, they cannot withstand harsh environments because of their poor chemical stability and low hardness at high temperatures [2, 5, 6]. Improvement of their chemical stability and high temperature hardness can be achieved by introducing alloying elements and/or altering coating structure.

Ternary systems based on TiN and CrN (such as TiSiN, TiCrN, CrAlN) and quaternary systems (such as TiAlSiN and CrAlSiN) have been developed during the last two decades. Some of these multi-component coatings have good oxidation resistance of up to 1000°C [2, 5, 7-10]. Designed in the late 1980s, monolayer TiAlSiN and CrAlSiN coatings have a high hardness (about 40GPa) and excellent thermal stability (≥900°C) after years of subsequent development.

New nano-composite coatings, based on TiAlSiN coatings, have been developed recently to further increase their hardness to 45GPa [8]. More recently, novel nano-scaled multilayer TiAlSiN coatings are being researched to enhance their toughness,

oxidation resistance and damage resistance because of their nano-scaled multilayer structure and the associated numerous interfaces.

However, no systematic work on the microstructure and properties of nano-multilayer CrAlSiN coatings has been reported, despite the better performance of CrN-based coatings than TiN-based coatings at high temperature. Furthermore, it is expected that the performance of the nano-multilayer CrAlSiN coatings can be further improved by forming a relatively thick hardened subsurface (i.e. duplex surface treatment) but research into this has not been conducted yet.

1.2 Aims of the Project

The aims of this PhD project are (1) to develop and characterise a series of CrAlSiN coatings with different structures in order to advance scientific understanding and identify the optimal multilayer CrAlSiN coatings, and (2) to develop a novel duplex system by combining a multilayer CrAlSiN coating with plasma nitriding for high performance cutting tools.

To achieve the above-stated aims, the following specific objectives are identified：

- Characterisation of the microstructure of nano-multilayer CrAlSiN coating using XRD, SEM and TEM

- Evaluation of the mechanical and tribological properties of CrAlSiN nano-multilayer coatings using nano-indentation and tribological tests

- Establishment of the relationship between the nano-multilayer structure, properties and cathodic arc PVD conditions.

- Development of optimal plasma nitriding conditions for duplex coating systems

- Investigation of the effect of duplex treatment on the performance of tool materials

Chapter 2   Literature Review

2.1   Wear of Cutting Tools

2.1.1   Cutting Tools

2.1.1.1   Property Requirements

Machining operations often involve the removal of material (in most cases, metals) by cutting, which can create a very aggressive working environment, hence, the raise in critical property requirements for machining tools. This can be better understood by considering, by way of example, the stress distribution at tool rakes.

The stress at a cutting tool rake is dependent on the shear strength of the work material (k_{work}), which for the majority of materials lies in the range of 200 MPa and 800 MPa [11]. As can be seen in Figure 2.1.1- 1 [11], during the steady stage of the cutting process, the normal stress (σ) can be 1-3 k_{work}, while the shear stress (τ), generated from friction, at the tool rake face is suggested to be in the range of 0.5 and 1 k_{work}. The entry stage of the cutting process is more severe with the normal stress as high as 5 k_{work}, although the shear stress can be assumed to be zero. At this stage, the sliding of the tool against the work material has not been established. The exit stage may be even more severe, taking into account the shear stress.

The minimum requirements to avoid yielding and fracture of the tool are related to the geometry of the tool (i.e. the included angle, β, as defined in Figure 2.1.1- 1) and the k_{work} of corresponding work material. The smaller β is, the larger the maximum tensile and shear stress formed in the tool will be, generated by the bending of the tool edge region and by the contact stress, respectively. Hence, the smaller β is, the harder

and tougher the tool must be to avoid yielding and fracture. The minimum requirements of hardness (HV) and tensile rupture strength (TRS) of tool materials with respect to β and k_{work} is summarised in Figure 2.1.1- 2.

Ideal cutting tool materials are expected to exhibit combined high hardness and high toughness. Furthermore, moderate high-temperature strength to overcome the heat generated during the cutting process and high wear resistance is also crucial [12].

2.1.1.2 Tool materials

Materials used for cutting tools can be generally divided into the following types: high speed steel (HSS), cemented carbide (also called hard metals), cermet, ceramic and polycrystalline diamond (PCD) [12, 13]. The characteristics of these types of materials at room temperature can be seen in Figure 2.1.1- 3[11]. As shown in the figure, PCD and ceramic materials, most commonly Si_3N_4-based, Al_2O_3-based or cubic boron nitride (CBN), have high hardness whereas their toughness is low. Cermet and cemented carbides both exhibit intermediate hardness and toughness values, while HSS materials have the lowest hardness and highest toughness. It is worth noting that HSS is the only group of materials that is predominantly above the HV=3TRS line (in the left upper corner of the figure), which is a border for "yield before fracture" behaviour.

High temperature, which is normal characteristic in a machining process, promotes instability of the composition and structure, which often leads to the degradation of mechanical properties. In unlubricated conditions, the dominant composition change is oxidation, which is more critical to wear than to failure. Structural change is more critical to the failure of cutting tools. As summarised in Table 2.1- 1 [11], HSS materials undergo structural changes because of over-tempering from 550°C upwards,

depending on specific composition. At temperatures over 900℃ , a brittle phase is commenced via the dissolving of WC into the cobalt binder [14]. Ceramic cutting tools undergo a sudden decrease of strength at temperatures above a critical value (typically in the range of 1350 to 1500℃) associated with the liquidation of sintering binders. PCD reverts to graphite at temperatures above 700℃ . The structural change usually leads to the degradation of mechanical properties, which is proved by the decrease of hardness at high temperatures, as depicted in Figure 2.1.1- 4 [11].

Based on the properties and availability, different applications are assigned to each group of materials. The application of ceramic materials is limited to semi-finishing and finishing machining operations due to low toughness [12]. PCD has higher toughness and hardness in comparison to ceramic materials; however, the toughness is still relatively low considering all the available materials, and its application is confined to machining soft non-ferrous materials. Cermet with high hardness can be used in high speed cutting; however, it is not suitable for machining hard materials due to its relatively low toughness. Cemented carbides exhibit relatively high hardness and wear resistance at both room temperature and high temperatures, however, at high temperature, the occurrence of a cratering effect can lead to the rapid breakdown of the cutting edge [12]. Despite the aforementioned potential problem, cemented carbides have a wide range of applications, and are especially favoured in turning operations. HSS, compared to cemented carbides, have better toughness and bending strength, as well as better chipping and thermal shock resistance, whereas the hardness is lower, especially at high temperature. The major applications of HSS are drilling and milling; however, the cutting speed is limited due to their poor high-temperature performance.

According to recently published research[15], up to 90% of cutting tools produced worldwide are made from cemented carbides and HSS.

The price of HSS is approximately 10 times lower than cemented carbides. It is of interest for the industry to improve the properties of HSS to improve the performance of HSS tools and to broaden the range of their applications.

2.1.2 Tribology of Cutting Tools

2.1.2.1 Introduction to Tribology

Tribology, defined to be "the science and technology of interacting surfaces in relative motion and of related subjects and practices" [16], is covered by three disciplines: friction, wear and lubrication [17, 18]. The interactions between tribological surfaces are complex. They involve transmitting of forces, converting of mechanical energies, altering of the physical and chemical properties of the surfaces etc.[19].

Being a common matter, occurring to sliding and rolling surfaces, tribology is crucial to modern industry in which high speed-/precision finishing-machining is highly favoured. In fact, according to some studies, the consequence of ignorance of tribology related issues costs the United States about 6% of its gross national product [16]. Hence, it is of interest to understand the principles of tribology and find a way to reduce friction and combat wear.

2.1.2.2 Friction

Friction is the resistance to motion when one solid body moves tangentially over another contacting solid body [16]. The tangential forces required to initiate and

maintain the relative movement are defined as static friction force (F_s) and kinetic friction force (F_k), respectively. Accordingly, the coefficient of friction (μ), which is defined as the ratio between friction force and normal force, is also sub-categorised into the coefficient of static friction ($\mu_s = F_s/F_N$) and the coefficient of kinetic friction ($\mu_k = F_k/F_N$).

Two basic laws of friction were first observed by Leonardo da Vinci and rediscovered by Guillaume Amontons in 1699 [18]. They are described as following [19]:

The first law of friction: The friction force is directly proportional to the normal force.

The second law of friction: The friction force is independent of the apparent area of contact between the contacting bodies.

The two laws of friction, normally referred as Amontons' laws, are proved to exist under a wide range of conditions. However, a notable number of exceptions exist, especially when wear is involved, where the changing of surface topography, adhesion between counter surfaces, generation of wear debris, deformation of both bodies and increasing of temperature of contacting surfaces often occur and affect the friction.

It is worth noting that low friction is generally favoured for tribological pairs; however, it does not necessarily lead to a low wear rate [19].

2.1.2.3 Wear

Wear is well known as loss of material during relative motion between two solids (ASTM G40-05). Wear causes poor working tolerances, loss of efficiency and may ultimately lead to premature failure of the tools [20, 21].

Different wear mechanisms have been described by many researchers [18, 22-24], based on different classifying criteria. It is now widely accepted that major wear mechanisms can be categorised into five groups: adhesive, abrasive, oxidational, fatigue, and impact [19, 25]. In a tribological system, it is common that one mechanism initiates wear while more than one mechanism is responsible for the eventual failure[19].

Adhesive Wear

The adhesive wear mechanism was first proposed by Bowden and Tabor [26]. From a tribological point of view, all surfaces are rough on an atomic scale and when two surfaces are placed in contact, the contact only occurs at the tips of their asperities [27]. Accordingly, the real area of contact is much smaller than the apparent area of contact. Figure 2.1.2- 1 illustrates the process of adhesive wear. Under a normal applied load, the contacting asperities become flattened by plastic deformation and form a welded junction (cold welding). When sliding occurs, these cold welded junctions are sheared, and if the bond of the two asperities is stronger than the strength of either asperity, the junction will break from the weak point and thus be transferred to the counter surface [25]. Further transfer of material to one asperity causes the particle to grow in size and may finally break off from the surface and form wear debris, or else be transferred back to the original surface. Holm [28] proposed a relationship between the wear volume loss for adhesive wear v, the applied normal

load W, the sliding distance x, and the hardness of the softer material in the tribological pair H:

$$V = \frac{k_{adh}Wx}{H}$$ Eq. 2.1.2-1

Where k_{adh} is a non-dimensional wear coefficient which depends on the properties of the mating material.

Rabinowicz [29, 30] and Ohmae et. al [31] proposed a theory to correlate low k_{adh} with low metallurgical compatibility, which is the degree of solid solubility of two metals melted together [19].

Abrasive Wear

Abrasive wear takes place when asperities of a hard surface slide on a softer surface (two-body abrasion) or when hard particles are caught between two sliding surfaces (three-body abrasion), causing material removal in the softer one or both mating surfaces. In many cases, debris generated during the adhesive wear mechanism (as described above) are trapped at the interface of the mating pair and cause three-body abrasive wear [32].

In the case of ductile material (with high fracture toughness), abrasive wear occurs via plastic deformation, leading to deep grooves on the worn surfaces due to removal and/or redistribution of materials. Whereas in the case of brittle materials, abrasive wear takes place via fracture; hence significant cracking can be found in the worn surface [19].

An equation similar to that of adhesive wear is found to be obeyed in a wide range of abrasive wear situations via plastic deformation [19]:

$$v = \frac{k_{abr} W x}{H}$$

Eq. 2.1.2-2

where k_{abr} is a non-dimensional wear coefficient, which mostly depends on the geometry of the asperities and the probability of the given asperities to cause material removal rather than redistribution.

In the case of abrasive wear via fracture, a generally agreed equation, used to predict wear volume loss, has been created by Evans and Marshall [33]:

$$v = \alpha N \frac{(E/H)W^{9/8}}{K_c^{1/2}H^{5/8}}$$

Eq. 2.1.2-3

where α is a material-independent constant, N is the number of asperities in the contacting surface and K_c is fracture toughness. Since the E/H value does not greatly vary for hard brittle materials, the wear rate is proportional to the number of asperities and applied normal load$^{9/8}$, and inversely proportional to fracture toughness$^{1/2}$ and hardness$^{5/8}$.

Oxidational Wear

In case of dry sliding, the temperature of the contact areas (i.e. the asperities of mating surfaces that are in contact, noted as T_C) were reported to be the summation of the general surface temperature (T_S), which is more or less steady during the wear process, and the "hot-spot" temperature or flash temperature (θ_m), which is generated by the interactions between asperities, which is instantaneous [34]. A similar estimation for lubricated systems was proposed by Bolk [35]. Experiments performed by Bowden and Ridler [36] on constantan-mild steel sliding couple revealed that T_C increases with increasing normal load and the sliding velocity can easily reach 1000°C. Experiments on other metal-metal and ceramic-metal sliding couples performed later

13

also support the findings of Bowden and Ridler [22, 37]. Although the duration of the flash temperature is equivalent to the time period for which the asperities are in contact (usually of the order of a few microseconds as suggested by De Gee [38]), they can introduce appreciable changes to the contact zone of the surfaces, including metallurgical transformations, mechanical property degradation and especially surface oxidation [39, 40].

At T_C, protective oxide films may form at the asperities of metal or ceramic surfaces, which have low shear strength and consequently is responsible for reducing the friction coefficient. The oxide films grow under the parabolic law and eventually after reaching a critical thickness, break up to form wear debris.

Fatigue Wear

During repeated sliding and rolling, the cyclic loading and unloading, subjected to the mating surfaces, may induce the initiation and prorogation of surface or sub-surface cracks, which after a critical number of cycles will result in the break-up of the surface forming large fragments. Fatigue wear occurs to the surface region and sub-surface region during repeated sliding and rolling, respectively. In the cases where rolling contact is accompanied by sliding or slip, the maximum shear stress is moved nearer to the surface due to the friction stress caused by sliding (see Figure 2.1.2- 2) [19].

Impact Wear

Impact wear can be further categorised into two major classes of erosive and percussive wear, which originate from jets and/or streams of particles, droplets and implosion of bubbles formed in the fluid, and from repeated solid body impact,

respectively [16]. Erosive wear can be treated as a form of abrasion where the contact stress arises from the kinetic energy of particles, droplets or bubbles as it touches a surface. Whilst percussive wear is a hybrid process which involves all the aforementioned wear mechanisms.

Summary

The cutting process can be divided into continuous and interrupted cutting, based on the continuity of the process [13]. As shown in Figure 2.1.2- 3 [13], at low cutting speeds, both adhesive wear and abrasive wear are dominant. Under working conditions, a high temperature at the location of the chip formation promotes adhesion, which leads to the built-up cutting edges and the micro-welding between the chips and the tool [6] and further causes edge break-out and chip-off, especially for interrupted cutting [13]. The broken-off will then act as abrasive particles and cause flank wear of the cutting tools. As the cutting speed rises, the environment at the cutting edge become very aggressive, which leads to very high temperature and more complex wear mechanism. For continuous cutting, tribochemical reactions (such as mutual diffusion of tool material and work material, and oxidation of tool surfaces) dominates the tool life, while in the case of interrupted cutting, tribochemical wear, fatigue wear, as well as thermal shock all contribute to the wear of tools [5, 41-43].

2.1.2.4 Requirements of Machining Tools to Combat Wear

Both friction and wear are system responses instead of intrinsic material properties. The complex nature of friction and wear in addition to the complex and aggressive operating environment makes the wear of machining tools difficult to predict and prevent. However, from the understandings of the basic wear mechanisms that might

take place in the mating surfaces, some general requirements of wear-resistant tools can be drawn.

Surface Hardness

High hardness is generally favoured for tools, especially for the surface of tools to combat both adhesive wear and abrasive wear (see Eq. 2.1.2-1 to Eq. 2.1.2-3).

Fracture Toughness

As stated in Eq. 2.1.2-3, to reduce abrasive wear, it is of vital importance to gain high fracture toughness, in addition to high hardness, which prevents the fracture of tools.

Chemical Inertness

To reduce adhesive wear and avoid the mutual diffusion of tools and work materials, the surface of tools should have low metallurgical compatibility with most work materials. Oxidation resistance is also crucial to the surface of tools, especially for the high speed cutting process where extremely high temperatures can be achieved.

Surface Finishing

Surface roughness plays an important role in wear and friction. Low roughness indicates fewer asperities in contact during the sliding process, which leads to a smaller friction force and lower flash temperature, thus the wear loss can be reduced.

No single material is known to be capable of providing combined optimised properties which satisfy all the requirements to combat wear of cutting tools.

2.1.2.5 Potential Solutions

The recognition of surface properties as a key factor to the tribological performance of industrial machinery has led to the development of Surface Engineering (SE), with the most widely accepted definition by Bell [44, 45] : "Surface engineering involves the application of traditional and innovative surface technologies to engineering components and materials in order to produce a composite material with properties unattainable in either the base or surface material.".

The technologies that can be used for SE treatments are generally unified into two classes:

- Surface coating: where layer of material, which can be completely different from the substrate, is deposited on the substrate. Such as Physical Vapour Deposition (PVD), Chemical Vapour Deposition (CVD), thermal spray, etc.
- Surface modification: where the structure and/or chemical composition of the surface region of the substrate is modified. e.g. case hardening, short peening, thermal chemical diffusion, ion implantation, etc.

Appropriate selection of SE treatments can offer benefits such as flexible combination of substrate/surface properties and the possibility to use cheaper substrate. It is crucial to consider both the properties of the modified surface and the behaviour of the surface-substrate system during the selection of SE treatments, and in some cases several technologies can be combined to achieve the best performance.

2.2 Tribological Coatings

Today, the majority of cutting materials in use are coated with hard tribological coatings with different compositions and structures to achieve a longer tool life and/or improved productivity via higher cutting speeds. According to recent published

researches [13, 46], the use of techniques, such as CVD and PVD, to cement carbide tools has approached 70-75%.

Surface coatings can positively influence the performance of machining tools (as summarised in Figure 2.2- 1). The influences can be unified into two classes of: directly improving the wear resistance to specific wear mechanisms and indirectly alter the interactions between the tools and work material. Increasing level of understanding of the importance of tribological coatings to the performance of machining tools has led to the rapid development of coating technologies since the first introduction of tribological coating in 1969 [47, 48].

2.2.1   Compositions of Tribological Hard Coatings

2.2.1.1   Binary Coatings

Titanium carbide (TiC), which was deposited on cemented carbide inserts in 1969 [48], is the first tribological hard coating introduced to control friction and wear in industrial machinery.

Introduced in the late 1970s, TiN played an important role in the early development of hard coatings to improve the wear resistance of cutting and forming tools. It is one of the most widely accepted coating in engineering applications due to its noble golden appearance, excellent adhesion to substrates, high hardness, chemical inertness and high wear resistance [7, 49, 50].

Other binary coating systems, including HfC, ZrN, Al_2O_3 and CrN, were rapidly developed and commercialised since the early 1980s, among which CrN is the most widely used on cutting tools.

TiN is the most widely employed coating for engineering tribological applications because it exhibits a higher hardness and higher adhesion strength than CrN when deposited on the same steel substrate and is the most comprehensively researched and developed [51, 52]. However, in comparison to TiN, CrN coatings exhibit higher toughness, better corrosion resistance and better oxidation resistance (oxidation starts from 700 - 800 ℃ for CrN while TiN coatings oxidise readily at 550 °C in air [53-56]). Researches which adapted different test conditions have shown that CrN exhibit higher wear resistance than TiN in both dry and lubricated sliding wear tests [57-59]. Another advantage of CrN over TiN is that the target material is cheaper by the factor of 2 or 3. Recently, CrN has proved to be a successful alternative to TiN coatings for applications especially where a high working temperature is required [1, 50, 60-62].

2.2.1.2 Ternary

The development of advanced tribological hard coatings follows the major trend of synthesising multi-component coatings, mostly ternary or quaternary coatings, by alloying binary coatings [63-68]. While the number of multi-component coating systems explored grows rapidly, they share a few basic structural types. As shown in Figure 2.2.1- 1, a wide range of elements can be alloyed with TiN- and CrN-based coatings to achieve combined properties, of which the following are of great interest to both research and the industry due to their advanced properties and good accessibility:

Aluminium

Aluminium has high solubility in NaCl-structure materials, such as fcc-TiN and fcc-CrN, and is a popular candidate for alloying these coatings. According to theoretical calculations, approximately 60% and 77% AlN can be dissolved in TiN and CrN,

respectively [67, 69-71].When the solubility is exceeded, NaCl-structure AlN can be stabilised through the growth of AlN/TiN (0 0 1) nano-laminates with the thicknesses of AlN layer below 2 to 2.5 nm [72, 73]. Above this thickness, stable wurtzite AlN (w-AlN) with hcp structure precipitates [74].

Partial substitution of Me in MeN (where Me is a transition metal) with Al causes solid solution hardening and increases the hardness of the coating by up to 60% [75-77]. The formation of Al_2O_3-like film is considered to be responsible for protecting Al-containing coatings from further oxidation [78, 79]. High temperature hardness is also reported to be improved by the addition of Al in the coating, attributed to the decomposition of fcc-MeN and w-AlN to fcc-MeN and fcc-AlN, which can compensate the softening by residual stress relaxation [74, 80].

Silicon

Silicon as a light element is among the best candidate elements for introduction to transition metal nitride coatings. Introducing Si into MeN coatings was found to influence grain size, wear performance, as well as phase formation [81-84]. The solubility of Si in MeN is reported to be extremely low, which can be easily understood considering the fact that the mixing enthalpy of complex ternary nitride compounds is higher when compared with the free energy of MeN and α-Si_3N_4 phases [85]. Thus, Si is reported to intend to segregate along the grain boundaries as an amorphous phase in MeN coatings, which is deduced from the XPS spectra obtained by several research groups, showing Si-N bonding on different Me-Si-N systems [10, 86, 87]. However, there is a debate over the presence of α-Si_3N_4 phase in Me-Si-N systems, because in some researching works even high resolution TEM didn't reveal amorphous phase and the non-equilibrium state associated with low deposition

temperature was employed to explain the solution of Si in MeN [81, 88]. This debate will be discussed in further details in what follows.

Increase of hardness has been reported in transition metal nitride coatings with Si reinforcement, such as Ti-Si-N, W-Si-N, Cr-Si-N systems [83, 84, 89-94]. Two mechanisms have been proposed to explain the hardening effect of Si in Me-Si-N systems based on different viewpoints of the solubility of Si in MeN. The first mechanism adopts the theory of formation of α-Si_3N_4 phase along the grain boundaries, stating that the amorphous phase is responsible for the grain refinement, as well as the hardness increase. This model is the most widely accepted among the researchers of superhard (H $\geq$ 40 GPa) coatings and will be explained in detail in Section 2.2.2.1. The second mechanism is based on solid solution hardening, which attributes the hardening effect to the substitution of Me atoms by Si atoms in the MeN lattice [81].

The content of Si is proved to have a great influence to the hardness of the coatings, however, different values of maximum hardness were reported by several research groups for the same system with different Si contents. For example, for the Cr-Si-N system, the maximum hardness value was reported by Martinez et. al [95] and by Benkahoul et. al [96] independently to be ~23 GPa at the Si content of ~ 3 at.%, while the maximum hardness value of 30-34 GPa was reported by two different groups at the Si content of 4.1 at.% [81] and 9.3 at.% [82], respectively.

Si can also improve the oxidation resistance of coatings which is related to the blocked of intergranular diffusion channels by the segregation of Si_xN_y along the grain boundaries and the formation of SiO_2 as a diffusion barrier [97-99].

21

2.2.1.3 Quaternary coatings

Two ternary systems, alloying Al and Si to the MeN coatings, have been widely applied to the tooling industry: (1) MeAlN system and (2) MeSiN system. The high performance of these ternary coatings led to the investigation of the first quaternary coating system which introduced both Al and Si to MeN coatings: TiAlSiN, in late 1990s [100] followed by the rapid and thorough development of microstructure [101], mechanical properties [102, 103], tribological properties [104], oxidation resistance [55, 105] and applications [8].

Despite the fact that CrAlN and CrSiN coatings have been successfully introduced to replace TiN-based coatings in high temperature applications, research work on the quaternary CrAlSiN coatings is limited.

CrAlSiN

CrAlSiN coatings have been proved to have high hardness and good mechanical properties [88, 98, 106]. Settineri et. al and Rafaja conducted wear tests on CrAlSiN, CrAlN and TiAlSiN coatings with different chemical compositions and layer structures, respectively, and found that CrAlSiN coatings outperform both TiAlSiN and the ternary CrAlN coatings at room temperature [107, 108].

Thermal stability and oxidation resistance of CrAlSiN coatings are the most studied properties on account of the superior high temperature performance of Cr-based coatings. Air annealing has been adopted to evaluate the high temperature stability of CrAlSiN coatings with different chemical compositions and layer structures [9, 109-112], through which good oxidation resistance has been found up to 900℃ and is credited to the anti-oxidation properties of Si_3N_4 [10] and the formation of a dense

oxide layer consisting of Cr_2O_3, Al_2O_3 and SiO_2, and partial phase transformation from fcc-CrN to hcp-Cr_2N was found to be negligible under 900 ℃ [113]. Although the oxidation resistance has been proved to be superior, documented research work on the tribological performance of CrAlSiN coatings at high temperature has been carried out by only two groups of researchers [107, 110, 113]. Both reported that despite their good oxidation resistance, during high temperature wear tests CrAlSiN coatings with different chemical compositions begin to fail at temperatures from 400 to 600℃.

Studies of the phase constituent of CrAlSiN coatings carried out by several research groups reported that when the ratio of Al/(Al+Si+Cr) is 0.7, which is near the solubility of Al in CrN (77 at%), even the least amount of Si could cause the separation of w-AlN and Si-containing amorphous phase from fcc-Cr(Al,Si)N [114]. Regarding coatings with a smaller ratio of Al/ (Al+Si+Cr), similar to ternary coatings, different viewpoints are held by researchers on the local environment of Si. Hasegawa et. al and Rafaja et. al found definite grain boundaries and no evidence of an amorphous phase in a series of (Cr,Al) N based multi-component coatings [115, 116]. Soldán et. al and Zhang et. al found signals of Si-N bonding using XPF technology [88, 98], however, it is not conclusive for the identification of the Si_3N_4 phase since the possibility of the Si-N bonding from a solid solution cannot be ignored. Recently, Endrino et. al [114] carried out X-ray absorption spectroscopy (XAS) tests which proved a certain solubility of Si in Cr(Al) N lattice (up to 2.5%), and a Si-N-X compound, with X being Cr or Cr and Al, forms when the solubility is exceeded.

2.2.2 Coating Structure

The alloying of MeN coatings have proved to be successful in increasing the hardness and oxidation resistance. However, further improvement of properties, such as hardness and wear resistance, is still driven by both scientific curiosity and technology requirement along with the increasing need for high speed cutting and dry machining of hardened materials [117, 118]. Coating concepts, such as metastable coatings, gradient coatings, multilayer coatings, nano-multilayer coatings and nano-composite coatings, have been adapted and developed during the last decades [6, 69, 119]. Among these concepts, nano-composition and nano-multilayer coatings are the most advanced and promising.

2.2.2.1 Nano-composite Coatings

In the case of polycrystalline materials, grain size plays an important role in the strength and hardness of the material. Most polycrystalline material obey the Hall-Petch relationship [120, 121] which can be mathematically described as:

$$\sigma_y = \sigma_0 + K/d^{1/2}$$

where K is a constant and d denotes grain size.

The equation suggests that the yield strength of a material increases with decreasing grain size. This can be easily understood by the fact that with smaller grain size there are more grain boundary regions per grain. In addition, dislocations can be hindered at grain boundaries due to the different orientations of the adjacent grains and the discontinuity of slip planes in different grains.

However, if the grain size is smaller than a critical value (~15 nm), as shown in Figure 2.2.2- 1, the hardness decreases as the grain size decreases. This is due to a

change of deformation mechanism when the grain size decreases to a point where the number of atoms in the boundary regions is comparable or bigger than that in the grains. Under this condition, the formation of dislocation is prohibited by the grain boundaries [122] and the dominant deformation mechanism of the material becomes grain boundary sliding [123].

Nano-composite is an advanced concept which enables materials to maintain high strength and hardness with a grain size smaller than the critical value. It should be noted first that although conventionally nano-composite can be 2D or 3D (as shown in Figure 2.2.2- 2), the 2D system is often called "nano-multilayer" and discussed separately. Nano-composite (3D systems) coatings are defined as coatings which have "at least two separated phases with nano-crystalline (nc-) and/or amorphous (a-) structure or their combination"[124], and can be classified into the following groups: 1. nc-MeN/nitride, 2. nc-MeN/metal, 3. nc-MeC or nc-MeN/a-C, 4. nc-MeC/a-C + nitride [125]. Among these nano-composite coating systems, nc-MeN/a-Si$_3$N$_4$ coatings have become the most frequently studied and used.

As discussed in the former section, Si tends to segregate along the grain boundaries as the amorphous phase when alloyed in MeN coatings. Many researchers have succeeded in synthesising nano-composite nc-MeN/a-Si3N4 coatings, such as TiSiN [126, 127], TiAlSiN [128-130], CrSiN [131, 132], which show high hardness or even superhardness (>40 GPa). The high hardness can be related to their unique structure: nc-MeN crystallites embedded in an a-Si$_3$N$_4$ matrix. Under applied stress, nano-crystallites are constrained by the amorphous phase; hence grain boundary sliding can be suppressed (see Figure 2.2.2- 2).

Toughness can be significantly enhanced by hindering crack initiation and propagation. The design concept of nc-MeN/a-Si$_3$N$_4$ [133, 134], where the Si$_3$N$_4$ phase, segregated around the nano-crystallites, are very thin (usually less than 1 nm thick), is able to limit the flaw size which is crucial to the hindrance of crack initiation. With regard to crack propagation, the increased grain boundary region in nc-MeN/a-Si$_3$N$_4$ systems maximises the interface complexity, which decelerates the propagation of cracks by prolonging the path [135].

2.2.2.2 Nano-multilayer Coatings

It has been widely accepted that multilayer structures can have advantages over monolithic structures (also called monolayer when discussing about coatings), which can be summarised as follows: 1) multilayer coatings can achieve combined or improved properties and functions of corresponding monoliths, 2) adhesion between the coating and substrate can be enhanced by the design of multilayer structure, 3) residual stress of multilayer coatings can be reduced in comparison to corresponding single layer coatings [119, 136-138].

Many multilayer coating systems, such as TiN/Ti(C,N) [139], TiN/CrN [140] and TiAlN/Al$_2$O$_3$[141], have achieved higher hardness than corresponding monoliths due to the hindrance of dislocation motion by interfaces between sublayers which have different elastic properties. The interfaces contribute beyond hardness to the enhancement of toughness by acting as energy dissipation and crack deflection sites [119].

It is obvious that the interfaces are of vital importance to the properties of multilayer coatings, hence today most efforts made on multilayer coating systems have been devoted to nano-multilayer coating where the periods (also called bilayer thickness)

are in the nanometer range [142, 143]. With such a small bilayer thickness, the interfaces are very effective in grain size and texture adjustment, which in turn affect the mechanical and tribological properties of the coatings [119].

The most widely studied MeN-based multilayer coatings to combat wear are the AlTiN coatings [76, 144]. From Figure 2.2.2- 4, it is obvious to see that AlTiN coating with multilayer structure lasts longer in a machining test than the same coating with monolayer structure, whereas the nano-multilayer coating outperformed the multilayer coating.

Most recently, nano-multilayer CrAlSiN coatings have gained attention due to better oxidation than Ti-based multilayer coatings. Mechanical and tribological tests were carried out on nano-multilayer CrAlSiN coatings and the results showed the improved hardness, oxidation resistance, wear resistance and cutting performance [90, 91, 106, 111]. However, little information about the microstructure and phase constituents of nano-multilayer CrAlSiN coatings can be found in literature. Ding et. al. [91] discussed the possibility of formation of a-Si_3N_4 and w-AlN phases when the ratio of (Al+Si)/Cr >1.62, based on the sudden drop of mechanical properties of coatings when the ratio exceeded 1.62. Based on XPS spectra, Hoet. al. [145] proposed that the phases, existing in nano-multilayer CrAlSiN coating, are fcc-CrN, fcc-AlN accompanied by crystallised Si_3N_4. However, both proposals were made with no direct evidences from XRD or TEM analysis.

2.2.3 Deposition of Tribological Coatings

Tribological hard coatings can be deposited by physical vapour deposition (PVD) or chemical vapour deposition (CVD). CVD was the first technique used to deposit TiN

in 1970s [146]. However, the application of CVD process is limited to ceramic substrates due to the high deposition temperatures (up to 1000°C). This is due to the fact that HSS suffers from softening and possible distortion at temperatures above 550°C [13, 146]. During the last two decades, PVD coatings have attracted more and more interest because of two main reasons: (i) PVD coatings can be deposited at low temperatures (under 500 °C), which not only effectively reduces tool softening and distortion, but also facilitates the use of sharper cutting edges [1, 3, 146], and (ii) the compressive residual stress in PVD coatings may prohibit thermo-mechanical cracking.

2.2.3.1 Physical Vapour Deposition (PVD)

PVD processes involve vaporising target materials from solid or liquid state and transferring the materials in the form of vapour through a vacuum or low pressure gaseous/plasma environment to the substrate, where the materials condense and form a film [147].

In terms of the transfer of the target materials from condensed state to vaporous state, PVD processes can be divided into two general categories: sputtering and evaporation, of which the most commonly used two methods in industries are magnetron sputtering and cathodic arc evaporation deposition.

Sputtering is a non-thermal vaporisation process, which uses energetic particles (usually gaseous ions generated from plasma) to bombard a solid or liquid target, resulting in the ejection of atoms or molecules from the target surface through momentum transfer [6]. A potential is applied very near the cathode to form plasma. By applying a high negative voltage to the target, positive ions in the plasma are accelerated and directed towards the target, gaining energy from the electron field

which is sufficient to bombard the target and initiate sputtering [6, 147]. Magnetic fields have been introduced to deflect and elongate the trajectories of electrons near the cathode, in order to approach a higher ionisation rate of the sputtered material.

Compared to cathodic arc evaporation (CAE) deposition, magnetron sputtering has a low ionisation rate, low deposition rate and also requires high power supply, which makes the CAE process a more popular choice in the industry.

2.2.3.2 Cathodic Arc Evaporation Deposition (CAE)

Arc is defined by Karl T. Compton as "a discharge in a gas or vapour that has a voltage drop at the cathode of the order of the minimum ionizing or exciting potential of the gas or vapour". Vacuum arc was first suggested as a source for metallic coatings by Wroe et al. [6] in 1958 and has then been commercialised to deposit TiN at low temperature.

Cathodic arc is usually initiated by touching and separating the cathode (target material) with a high voltage auxiliary electrode (the trigger shown in Figure 2.2.3- 1) [147]. Once initiated, the arc moves around the cathode randomly in nature until it is extinguished and then reinitiated due to the inductance in the arc power supply. Along with the movement of the arc, a "cathode spot" is formed on the surface of the cathode with current density more than 104 A/cm^2 [148], which causes the melting and vaporization of cathode material. The voltage drop near the cathode surface enables the ionisation of the evaporated atoms. During the deposition process, the substrate is usually biased to attract positive target ions.

The most severe limitation to cathodic arc is the formation of macro particles (also called macros in some text books) due to thermal shock and hydrodynamic effect in

the molten spot on a solid cathode surface [147] (see Figure 2.2.3- 2). The diameter of macro particles is material dependent and the macro particles tend to solidify as they travel towards the substrate. On arrival at the substrate, the macro particles might stick and be incorporated into the coating (as shown in Figure 2.2.3- 3), or it might be reflected by the substrate surface, leaving a defect in the coating [6].

The macro particles do not have good adhesion with deposited coating hence can easily spall off under some working conditions and degrade the performance of the coating. They are also responsible for high surface roughness of CAE deposited coatings.

The number of macros can be reduced by several means: using suitable filters; using a magnetron field to control the trajectories of the arc; and heating up the cathode to form a substantial vapour pressure.

In summary, CAE is the most widely used PVD technique in the industry due to the following reasons: (1) high ionisation rate; (2) high deposition rate; (3) generally good to very good adhesion of coatings; and (4) low power supply needed [6, 76].

Optimised production parameters to deposit nano-multilayer CrAlSiN coatings using CAE technique, such as cathodic arc current, working pressure, substrate temperature and bias, have been investigated by several group of researchers. These researches have been based on the mechanical and tribological properties of the coatings deposited [91, 106, 149]. To achieve the multilayer structure, the substrate is usually in rotation; however; no information can be found from the literature on the optimisation of substrate rotation speed, which has the greatest effect on the bilayer thickness.

2.2.4   Properties and Characterisation of Nano-multilayer Coatings

2.2.4.1 Wear Behaviour of Coated Surfaces

As aforementioned, wear process during cutting is complex. When coated with tribological coatings, the wear resistance of tools is expected to improve because tribological coatings usually have high hardness and can be treated as diffusion barriers. However, the complexity of wear at the cutting interfaces is further increased by introducing a hard yet often brittle layer on top of a relatively soft substrate.

Hamilton [150] derived the distribution of σ_x in the surface of a semi-finite plane in contact with a spherical indenter and considered the effect of tangential force which is induced by friction. From Figure 2.2.4- 1, two effects of coefficient of friction (μ) can be noticed.

Firstly, with greater μ, the tensile stress built up at the back edge of contact increases drastically, which is suggested to be responsible for partial ring cracks formed in the wear track [151]. Since ceramic coatings are brittle, partial ring cracks are likely to form well below the nominal uniaxial yield stress and develop into through-thickness cracks which subsequently may lead to delamination [152].

Secondly, the presence of a tangential force intensifies the compressive stress at the front edge of contact, which promotes buckling at any poorly adhered area and easily leads to spallation [153, 154].

Cohesive failure, i.e. break-up of the coating, and adhesive failure, i.e. delamination or spallation, caused due to the failure of adhesive bond between the coating and substrate, are the most common failure modes of tribological coatings [152].

2.2.4.2 Desired Properties of Tribological Coatings for Cutting Tools

General requirements for materials to exhibit high wear resistance, such as high hardness, high fracture toughness and chemical inertness at both room temperature and elevated temperature, apply also to tribological coatings. Among these requirements, high fracture toughness is of vital importance to ceramic coatings based on the discussion in the former section.

Adhesion between the coating and substrate is also of importance to tribological coatings, which is crucial in preventing buckling and subsequently reducing adhesive failure of the coating.

2.3 Active Screen Plasma Nitriding and Duplex Surface Engineering Treatment

2.3.1 Nitriding of Steels

Nitriding is a well-known technique which improves the surface hardness and load bearing capacity (LBC) of steel through the formation of fine nitride precipitates and enhances their fatigue properties due to the introduction of compressive residual stress [155-158]. It can be achieved through a variety of means, such as gas nitriding, direct current plasma nitriding (DCPN) and active screen plasma nitriding (ASPN).

2.3.1.1 Gas Nitriding and DCPN

Gas nitriding is the first well-developed technique for nitriding. The work pieces are heated to the nitriding temperature (usually between 480℃ and 650℃) in a chamber with an atmosphere of ammonia. The ammonia dissociates by the following reaction:

$$2NH_3 \rightarrow 2N + 3H_2 [159]$$
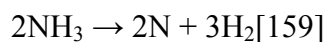
The nitrogen diffuses into the steel due to a concentration difference while hydrogen is exhausted. The main disadvantages of gas nitriding are the prolonged operation time (usually more than 10 hours) and the formation of a brittle white layer which in most cases is detrimental [159, 160].

In comparison to conventional gas nitriding, plasma nitriding offers additional advantages such as reduced emission and improved energy efficiency [157, 158, 161].

DC plasma nitriding is carried out in a chamber where the work pieces are placed on (and connected to) a cathodic worktable [162] with an atmosphere of ammonia or hydrogen and nitrogen gas mixture. A glow discharge will be generated when a high voltage (up to 1000 V) is applied between the cathode and the anode, which will ionise the gas to produce plasma. The positive nitrogen ions are attracted towards the work piece, with most of their energy generating heat and a small part of energy transferring nitrogen into the surface of the work piece [158, 162].

The plasma nitriding process can effectively improve the surface properties of steel at temperatures lower than that of gas nitriding, usually in the range of 350℃ to 550°C, which results in unchanged core properties after treatment. Thus, this technique is used extensively by the industry as a final treatment of tool steels or as a pre-treatment prior to the PVD process.

2.3.1.2 Active Screen Plasma Nitriding (ASPN)

The inherent shortcomings of conventional DC plasma technology (e.g. parts to be treated must be electrically conductive, instability of the plasma and potential of surface damage caused by arcing, difficulties in maintaining a uniform chamber temperature, non-uniform nitriding due to edge effect [156] and potential of overheating owing to hollow cathode effect [163-165]) lead to the development of active screen plasma nitriding (ASPN) also known as through cage (TC) technology in the late 1990s. The novel ASPN with all its technological and environmental advantages can be used to treat low alloy steels, tool steels, stainless steels and polymeric materials [166-168]. In the ASPN vacuum process, the components to be treated are placed in a floating potential or subject to a small cathodic bias power on a central worktable which is insulated from a surrounding screen which makes the cathode and the vacuum chamber wall the anode. A bias power supply is independently connected to the worktable to be used if and when appropriate. Such an electrical configuration allows plasma to be formed on the metal screen surface rather than on the component surface. The plasma discharges appearing on the metal screen are responsible for heating up the components on the worktable to the required nitriding temperature by radiation. Moreover, these plasma discharges also contain a mixture of ions, electrons and other active species for nitriding treatment [166, 167, 169].

Up to today, no dedicated study regarding the effects of process parameters (i.e. time and temperature) on AISI M2 tool steel (frequently used for cutting tools, dies and punches) using active screen plasma nitriding and their relationship with microstructure and mechanical properties including residual stress state have been reported.

2.3.2 Duplex Surface Engineering Treatment

The behaviour of a thin coating depends not only on its own properties, but also on the mechanical properties of the substrate and the bonding between the substrate and the coating. Plastic deformation of the substrate under a heavy load can lead to the premature failure of thin coating i.e. so-called "thin-ice effect" [156].

Duplex surface engineering treatment is defined by Bell. et. al [170] as "the sequential application of two (or more) established surface technologies to produce a surface composite with combined properties which are unobtainable through any individual surface technology". Among the concepts of duplex surface engineering treatment, ceramic coating-nitrided steel systems became a favourite method to avoid the thin-ice effect due to the mechanical support of nitrided steel to the hard coating.

One issue that should be born in mind when designing a ceramic coating-nitrided steel system is that the nitrogen diffusion zone with an unduly high thickness and nitrogen saturation was also reported to lower the compressive stresses and cause embrittlement of work piece [155]. Gawronski [156] suggested that, due to embrittlement, the diffusion layer of tool steels should be kept below 50μm.

2.4 Summary

As discussed above, CrAlSiN nano-composite/nano-multilayer coatings possess high mechanical and tribological properties at room temperature, while they have the potential to outperform the TiN-based nano-composite/nano-multilayer coatings at high temperature due to improved oxidation resistance. However, no systematic work has been carried out on the microstructure development and the high temperature tribological performance of CrAlSiN coatings.

Chapter 3   Materials and Experiments

3.1   Sample Preparation

3.1.1   Substrate Materials

M2 high speed steel (HSS) was selected as the substrate material for this study in view of its wide applications and importance in the tool industry. The chemical composition of the M2 steel is shown in Table 3.1- 1.

The hardness of 910 Hv (67.5 HRC) was achieved after the following heat treatments for the M2 HSS: 1) stress relieving at 600 °C for 2 hours followed by slow cooling down to 500 °C and fast cooling down to room temperature, 2) heating to 1200 ℃ , followed by quenching in N_2 atmosphere and 3) two stage tempering for 2 hours at 520 ºC and 550 ºC, respectively.

The material was supplied as an one inch rod bar and was cut into 5 mm thickness samples, which were ground with SiC abrasive papers and polished with 6 μm and 3 μm diamond pastes to a smooth surface finish with Ra=14.1 nm for both active screen plasma nitriding and coating deposition. The ASPNed samples were also polished with 3 μm diamond pastes to a similar Ra value to that of the untreated M2 substrate before being sent to Asociación de la Industria Navarra (AIN) for surface coating deposition.

3.1.2   Preparation of Cross-sectional Samples

All surface engineered samples were electroplated with a thin layer of nickel (about 1-3 μm) on the surface for protection before the samples were cut in to cross-sections.

The sectioned sample was then mounted with conductive bakelite, ground with SiC grinding paper and then polished with diamond paste up to 1μm for microstructural observation.

3.1.3 Preparation of Samples for Tribological Tests

The coated specimens were ground with#1200 SiC paper for 10 seconds to achieve Ra of 30-50 nm for all tribological tests. This was in accordance to an industry practice for CAE coating specimens [171]. The tribological pair was ultra-sonically degreased for 3 minutes prior to each test.

3.1.4 Preparation of TEM Samples

Figure 3.1.4- 1 shows a schema of the first two steps of cross-sectional TEM sample preparation [172] and the steps can be fully described as follows: (1) Two slabs were cut and glued together using G-1 epoxy with the treated surfaces facing each other, forming an assembly with a cross-sectional area of 3 x 3 mm^2; (2) The assembly was cut to a thickness of less than 1mm followed by fine grinding and polishing to ~50 μm in thickness; (3) This thin assembly was then carefully parted in to two slices. (4) This slice was then transferred to a Quanta 3D FEG focused ion beam (FIB) miller for final thinning to less than 100 nm. Prior to milling, a layer of tungsten was deposited along the surface of the region where the sample was to be thinned (refer to Figure 3.1.4- 2) in order to preserve the integrity of the coating structure. Rough milling was performed with ion beam currents from 50 nA to 5 nA at 30 KV and a final polish was conducted at 5 KV 48PA following fine milling at 1 nA to 0.1 nA, 30 KV.

3.2 Surface Treatment

3.2.1 Active Screen Plasma Nitriding

The nitriding process was carried out using an active screen (AS) Plasma Metal 75kVA +15kVA industrial scale plasma nitriding furnace. To optimise the most suitable nitriding conditions for M2 steel, the specimens were treated at different temperatures (400°C to 525°C) and with varied time durations (0.5 h to 2.5 h) under a total pressure of 75 Pa (0.75mbar) and 10% substrate bias. The matrix of treatment parameters regarding time and temperature are summarised in Table 3.2- 1. The maximum treatment temperature (i.e. 525°C) selected was concerning the tempering temperature of 550°C used for the heat treatment of AISI M2 HSS substrate, whereas the maximum treatment time was restricted to 2.5 hr considering the toughness performance as the toughness of the nitrided layer decreases with increasing treatment time. The furnace was heated to 300℃ in H_2 atmosphere as the first step (pre-cleaning and heating) and then to the treatment temperature in an atmosphere of 25% N_2 and 75% H_2 gas mixture as the second step. When nitriding was finished, the samples were cooled in the furnace to room temperature.

Two samples were treated under each condition in the investigation phase and 9 samples were treated for the duplex treatment purpose with the selected optimum parameters. All samples were degreased with acetone using an ultra-sonic device before treatment.

3.2.2 Surface Coating

Cathodic arc evaporation (CAE) deposition processes of designed coatings were conducted using a commercial METAPLAS MZR-323 PVD, which is equipped with

two opposing columns each holding three vertically aligned target cylinders with the diameter of 10 cm as cathodes. Three Cr (99.8% purity) targets were place in one column while the other column was left empty for the production of CrN coatings. For the deposition of multilayer coatings, three Cr (99.8% purity) (Ti with 99.5% purity in the case of TiAlSiN coatings) and three AlSi (70 at.% Al–30 at.% Si) targets were used and two types of arrangement of the targets, named as Mode I and Mode II, were employed as illustrated by Figure 3.2.2- 1. For Mode I coatings, three Cr targets were placed on one column and three AlSi targets were placed on the opposite column. Whereas for Mode II coatings, the Me (i.e. Cr or Ti) and AlSi targets were placed alternatively (i.e. one Me target was adjacent to one AlSi target on the same column and faced an AlSi target on the opposing column).

Substrate materials were placed on the sample holder so that the surface was vertical and facing the target. During the whole process, the samples were in two fold rotation as indicated in Figure 3.2.2- 1 as R_1 and R_2. Arc enhanced glow discharge (AEGD) process was run for 33 minutes in an argon atmosphere to clean the sample surface before each deposition process. The deposition process was carried out in a pure nitrogen atmosphere with a working pressure of 4 Pa. The substrate was subjected to a continuous DC bias of −50 V and the substrate temperature was set to 450°C.

Sample code and corresponding deposition parameters are summarised in Table 3.2- 2, where the sample rotation speed refers to R_1. TiAlSiN and CrN coatings were adopted as bench markers for the investigation of effect of composition difference on the mechanical and tribological properties.

3.3 Characterisation and Evaluation

3.3.1 Microstructure and Phase Identification

3.3.1.1 Optical Microscopy

An Axioskop 2 MAT mot optical microscopy was employed to examine the cross-sectional microstructure of the nitrided zones of the ASPNed samples.

3.3.1.2 Scanning Electron Microscopy (SEM)

A Philips XL-30 scanning electron microscope (SEM) and a JOEL 7000F SEM were used for surface and cross-sectional morphological and microstructural observation, as well as the post-examination of load bearing capacity and wear tested samples. Both SEM are fitted with Oxford Instruments inca energy dispersive X-ray spectroscopy (EDX) detector which enables quantitative measurements of elements.

3.3.1.3 X-Ray Diffraction (XRD)

The phase constituents of the M2 substrate and selected coatings were analysed using Philips X'pert X-Ray Diffractometer with a Cu-K$_\alpha$ radiation (λ=1.540598Å) using 30 mA current and 40kV accelerating voltage. A monochromatic X-ray beam was projected on the surface of the sample at incident angles 2θ over the range of 20° and 100°with of step size of 0.02° and for the time duration of 1 sec per step. The diffraction patterns obtained were analysed and indexed using X'pert High Score analytical software.

To analysis the phase constituents of thin coatings without the influence of the substrate, a glancing angle XRD with the incident angle of 1° was carried out using

a Panalytical X-Pert Pro MPD X-ray defractometer with Cu Kα radiation (λ=l.540598 Å).

3.3.1.4 Glow Discharge Optical Spectroscopy (GDOES)

The composition-depth profiles of the both ASPN samples and coated samples were measured using a LECO GDS-750 QDP Glow Discharge Optical Emission Spectrometry (GDOES). During the test, the sample surface was bombarded by argon ions and the material was sputtered layer by layer into the plasma where they were excited through the collision with electrons and argon atoms. The photons emitted during the de-exciting process were analysed by an optical spectrometer and compared with standard spectra to provide information about the composition along the depth. For each test, a circular area of 4 mm diameter was sputtered and analysed.

3.3.1.5 Transmission Electron Microscopy (TEM)

A JEOL JEM-2100 LaB6 transmission electron microscope with the operating voltage of 200kV was used to characterise the phase constituent and cross-sectional microstructure of selected coatings.

3.3.2 Surface Topography Measurement

3.3.2.1 Vertical Scanning Interferometry (VSI)

A vertical scanning interferometry was employed to produce topographic map of wear surface after high temperature wear test. During the measurement, a white light beam is directed towards the sample surface, which will be reflected and interfere with a reference light. The interference pattern (i.e. interferogram) is analysed and with a

vertical scanning with nanometre precision, a 3-D map of the surface can be produced with high vertical and lateral resolution.

3.3.2.2 Stylus Profilometer

The surface roughness of samples and 2-D profiles of wear tracks after room temperature wear tests were measured using an Ambios XP-200 stylus profilometer.

3.4 Mechanical Property Measurement

3.4.1 Hardness

3.4.1.1 Micro-hardness

A Mitutoyo MVK-H1 durometer fitted with Vickers indenter was used to determine the surface hardness of the received and nitrided M2 samples under a load of 500 g. At least five indents with a large interspacing to avoid plastic zone effect were made and measured for each sample and the average value of hardness was calculated and reported.

3.4.1.2 Nano-hardness

The schematic configuration of the Nanotest system (Micro Materials Ltd, Wrexham, UK) employed to measure the hardness and Young's modulus of the coatings is shown in Figure 3.4.1- 1. The current in the coil at the top of the pendulum generates a magnetic field which interacts with the permanent magnet and causes the pendulum to rotate around the frictionless pivot. The diamond Berkovich indenter (refer to Figure 3.4.1- 3 for the geometry of the indenter) moves towards the sample which is vertically mounted on the sample holder and the displacement is measured by a parallel plate capacitor with the resolution of sub-nm.

The maximum load used in this study was 25 mN with fixed a loading and unloading rate of 1.25 mN/s, and the system was held for 20s at the peak load. 50 repeats were carried out on each sample for consistency and the average value was calculated accordingly. Hardness (H) and reduced elastic modulus (Er) were calculated from the unloading slope of the load-displacement (P-h) curves using the equations below, following the Oliver – Pharr method [30] :

$$H = \frac{P_{max}}{A}$$

$$E_r = S\frac{1}{2h_c}\frac{1}{\beta}\sqrt{\frac{\pi}{24.5}}$$

$$A = f(h_c)$$

$$h_c = h_{max} - h_s$$

$$h_s = \varepsilon\frac{P_{max}}{S}$$

$$S = \frac{dP}{dh}$$

where S is the stiffness derived from the partial fitting of the first 20% unloading curve, β is the geometry correction factor, h_c is the calculated plastic depth and ε is a geometric constant. The schematic illustration of the P-h curve showing the quantities used in data analysis is presented in Figure 3.4.1- 2 [16].

The reduced modulus Er is related to the elastic modulus by the following equation.

$$\frac{1}{E_r} = \frac{1 - v_c^2}{E_c} + \frac{1 - v_i^2}{E_i}$$

Where E_c, ν_c and E_i, ν_i refer to the Young's modulus and Poisson's ratio of the coating and the indenter, respectively. From this equation the Young's moduli of tested specimens were calculated.

3.4.2 Load Bearing Capacity Evaluation

3.4.2.1 Indentation Test

The load bearing capacity of ASPNed samples was characterised by making indents using a Mitutoyo MVK-H1 durometer on the surface of samples under a series of loads (from 10 g to 1kg) and observing the crack initiation and propagation around indents under SEM.

3.4.2.2 Scratch Test

Scratch tests were carried out on all coating systems using a REVETEST® Scratch Testing instrument fitted with a Rockwell diamond indenter with the radius of 200 μm. A maximum normal force of 100 N was reached progressively from an initial load of 1N at the loading rate of 100 N/min and speed of 9.59 mm/min. The test was repeated thrice on each sample. Frictional force, i.e. transversal force (Ft), was recorded against applied normal load (Fn). The scratch wear track on the sample surface was examined under SEM.

3.4.2.3 Nano-impact tests

Nano-impact tests were conducted employing the same Nano Test system with that for nano-indentation test (refer to Figure 3.4.1- 1). The indenter used for nano-impact test is cube corner as shown in Figure 3.4.1- 3. The impact load was precisely controlled by the coil at the top of the pendulum, while a solenoid near the lower end of the pendulum, which is

connected to a time relay, enables repetitive impacts to be produced at regular intervals from a constant initial distance from the sample surface. The experimental configuration used in this study is summarised in Table 3.4- 1.

3.5 Tribological Property Evaluation

3.5.1 Room Temperature Reciprocating Sliding Wear Tests

The wear resistance of the surface treated samples was assessed employing a custom-made reciprocating sliding wear tester as shown in Figure 3.5.1- 1. The tests were conducted at room temperature in a laboratory dry condition. During the test, the surface treated samples were mounted on a sample holder which slides in one direction reciprocatingly with the frequency of 0.56 cycles per second and the stroke length of 4 mm. A ball with the diameter of 12.7 mm was held stationary against the sample surface with an normal applied force of 50 N. Two types of balls were used in the tests: WC-Co ($Hv_{0.03}$ 1420) and Al_2O_3 ($Hv_{0.03}$ 1700). Each test lasted for 8 hours, accumulating a total number of cycles of 16128 (for the sample) or total sliding distance of 129.024 m (for the ball).

Before each test, the tribological pair was mounted on their respective holders and put into contact gently. After applying the load, the system was stabilised for one minute before the test started. After the test, the wear debris was collected from the ball surface using a carbon sticker for SEM observation. The tribological pair was dismounted from their holders, cleaned with acetone before any post-test examination was carried out. Wear test under each condition was repeated for three times to ensure repeatability. The morphology of wear track was observed using SEM and the profile of wear track was measured by means of an Ambios XP-200 stylus profilometer. The

profile of each wear track was measured at 10 different positions, and the average value was used to calculate the total worn volume.

3.5.2 High Temperature Reciprocating Sliding Wear Tests

A Schwingungs-, Reibungs- und Verschleisstest (SRV) high temperature tribotester as shown in Figure 3.5.2- 1 was employed to access the tribological performance of the coated samples at 400℃ and 500℃. The sample was mounted on a stationary holder which was connected to a heater, and a WC-Co ball with the diameter of 10 mm was held against the sample surface. During the test, the testing chamber was sealed and heated to maintain a stable temperature; the ball slid reciprocatingly under the condition listed in Table 3.5- 1. Each test condition was repeated for three times on every sample to ensure repeatability.

The friction coefficient was recorded, with a data collection frequency of 1.21 Hz. After the test, the chamber was cooled in air. The morphology and volume change of the wear track was measured by means of SEM and vertical scanning interferometry.

3.5.3 Rolling-sliding Wear Tests

Rolling-sliding wear tests were carried out on selected samples, employing an Amsler Wear Test Machine TypeA135 with wheel-on-wheel configuration (refer to Figure 3.5.3- 1 for the picture and sketch of the configuration and geometry of samples). Two wheel specimens with the same size and geometry (i.e. with inner diameter of 16 mm, outer diameter of 45 mm, and thickness of 10 mm) were used for each test. During the test, a M2 wheel was placed as the lower specimen, which was driven by a motor to rotate with the speed of 200 rpm, and a coated wheel was placed as the upper specimen, which rotated with the speed of 180 rpm. Thus, a sliding ratio $(V_L-V_U)/V_L$

of 10 % were achieved, where V_L and V_U are the cylindrical speed of the lower and upper wheel, respectively.

Before each test, both wheels were degreased with acetone using an ultra-sonic machine for 5 minutes and weighed using a digital balance with the precision of 0.1 mg. The wheels were then carefully fixed to the sample holder, with the surfaces gently touching. The rotation of the wheels was started before a normal load of 750 N was gradually applied to ensure a smooth running-in. The test was carried out semi-continuously. After every hour, the test was stopped and both specimens were weighed following ultra-sonic cleaning for 20 minutes in acetone. Extra care was taken to ensure the wheels were put back in the original arrangement after weighing so the contact situation of the wheels would not change significantly during each test. At least three tests were carried out for each type of coated wheel.

3.6 Thermal Oxidation Treatment

An ELITE BRF15/5 furnace was used to conduct the thermal oxidation treatment of the selected coated samples. The furnace was firstly heated to 200℃ below the treatment temperature at the rate of 40°C/minutes and held for one hour, and then the samples were put into the furnace, followed by a slow heating rate of 8°C/minutes to the treatment temperatures. The dwell time was 2 hours and, after the treatment, the samples were cooled to room temperature in the furnace. 28 samples, 4 from each type of coating, were cut into surface sizes of 1cm x 1cm and ultra-sonically degreased for 3 minutes before each treatment.

Due to the fact that the samples were not fully covered with the coating (only coated on one surface), the severe oxidation of substrate made the treatment at temperatures

higher than 900℃ impossible. Hence, the oxidation treatments were conducted between 700℃ and 900℃ with an increment of 100℃. After the treatment, SEM was employed to investigate the change of surface morphology and chemical composition.

Chapter 4   Experimental Results

In this chapter, the experimental results will be presented in the following order: Section 4.1 firstly describes the characterisation results of ASPNed samples, based on which an optimal treatment condition was identified and used to treat the substrate for duplex treatments. Section 4.2 reports the effect of deposition parameters and coating compositions on the microstructure of coatings. Mechanical properties, such as hardness, scratch resistance and nano-impact resistance of coated samples, are presented in Section 4.3. The tribological properties of different surface systems at room temperature are reported in Section 4.4. In Section 4.5, the effect of high temperature on the performance of the surface systems is investigated.

4.1 Substrate Material

4.1.1 As-received M2 Material

The typical microstructure of as-received M2 steel (M2-unt) is presented in Figure 4.1.1- 1, showing relatively small spherical carbides distributed throughout the tempered martensite matrix. In addition to large carbide-colonies, some needle-like carbides were segregated along the prior austenite grain boundaries. It is noted from Figure 4.1.1- 1 that the majority of the carbides are in light grey and a small portion is in dark grey.

EDS elemental mapping analysis (Figure 4.1.1- 2) demonstrated that the carbides in light grey were rich in tungsten and molybdenum, while the carbides in dark grey were rich in vanadium. It is also noted that chromium, despite being a relatively strong carbide forming element, is uniformly distributed throughout the matrix and

carbides, most probably due to the presence of a high concentration of very strong carbide-forming elements, such as W, Mo and V.

XRD phase identification (refer to Figure 4.1.1- 3) revealed major peaks for the tempered martensite phase. Peaks of two types of carbides were also identified, among which peaks of M_6C (M= Fe,W,Mo) are more pronounced than peaks of VC. Combining with the microstructural observation, it can be concluded that the light grey coloured carbide is M_6C and the dark grey coloured one is VC.

4.1.2 Active Screen Plasma Nitrided (ASPNed) M2

4.1.2.1 Layer Structure

After ASPN, surface of the ASPNed samples were slightly polished and then etched in 2% Nital solution for SEM observation of the surface microstructure. As presented in Figure 4.1.2- 1,similar microstructure to that of M2-unt (Figure 4.1.1- 1) was observed, with the only difference being that the tempered marten site laths/plates in ASPNed samples are slightly coarsened (Figure 4.1.1- 1 vs Figure 4.1.2- 1).

Cross-sectional microstructures of the ASPNed samples were observed under optical microscope and SEM. It was found that the ASPN treatments, under the conditions designed, led to the formation of a nitrogen diffusion zone at the surface of the samples as indicated by the dark colour after etching, in optical microstructure (see Figure 4.1.2- 2). No clear compound layer (which is often referred to as "white layer" due to the bright colour after etching) could be observed on any of the treated samples.

Figure 4.1.2- 3 shows a cross-sectional SEM microstructure of ASPN 525-2.5, which was nitrided at the highest temperature and for the longest time adopted in this study, where no compound layer was evidenced.

4.1.2.2 GDOES Analysis and Thickness of Nitrided Layer

The GDOES composition-depth profiles of the ASPNed sample revealed that the interstitial alloying elements exhibited a virtually constant content throughout the nitrogen diffusion zone and the substrate, most probably due to the low diffusion rate at the temperatures chosen for the treatments. On the other hand, the content of nitrogen and carbon changes greatly with increasing distance from the sample surface.

Figure 4.1.2- 4 shows typical GDOES elemental depth profiles for nitrogen and carbon content. As evidenced from the graphs, the concentration of nitrogen decreases gradually, which is in line with a typical diffusion profile. The carbon was redistributed along depth, which is low at the outer surface and piled up in front of the nitrogen diffusion zone. The depth at which the nitrogen atomic percent reaches 0.4 was taken as the thickness of the nitrogen diffusion zone, as suggested by Kwietniewskiet. al [156], and the thickness data for all ASPNed samples are summarised in Table 4.1- 1. It can be seen that the thickness of hardened layer increased with both time and temperature, which is in good agreement with the microstructural observation (Figure 4.1.2- 2), and cross-sectional hardness profile (Figure 4.1.2- 7), corroborating the veracity of the GDOES profile as a reasonable indicator of nitrogen diffusion depth. It is worth noting that three samples, ASPN 500-2.5, ASPN 525-1 and ASPN 525-2.5, developed a deep (>50 µm) nitrided zone, with poor toughness, which could not be used for duplex treatment.

4.1.2.3 Phase Constituents

The XRD patterns of ASPNed samples treated for 2.5 hours at different temperatures are presented in Figure 4.1.2- 5 and compared with the M2-unt pattern. All ASPNed samples exhibited α'-martensite peaks which were broadened and shifted towards the

smaller angle when compared to the peaks for the M2-unt. This could be related to the expanded lattice parameters of the iron lattice caused by interstitial nitrogen atoms. For samples when treated at 450°C and above, peaks of γ'-Fe$_4$N and ε-Fe$_3$N can be identified, and the intensity of these peaks increased with increasing treatment temperatures.

4.1.2.4 Micro-hardness and Load Bearing Capacity

The surface hardness of M2-unt and all ASPNed samples, measured under the load of 50g is plotted in Figure 4.1.2- 6. Compared with the surface hardness of M2-unt (910 Hv), all the ASPNed samples showed improvement in surface hardness up to 1396 Hv for ASPN 450-2.5 sample. It is of interest to note that when treated at temperatures below 500℃ , the surface hardness is increased with increasing treatment time; when treated at 525℃ , the opposite was observed.

Figure 4.1.2- 7 depicts the cross-sectional hardness profile of a typical ASPNed specimen (sample ASPN 500-0.5). It can be seen that the hardness decreases gradually from the surface until it reaches the substrate hardness. This can be correlated to the nitrogen content distribution (Figure 4.1.2- 4). It can be noted from Figure 4.1.2- 6 & 7 that the core hardness was not affected by the ASPN process, mainly due to the relatively used low temperature.

To evaluate the load bearing capacity (LBC) of ASPNed samples, indentations were made on the ASPNed sample surfaces under a series of loads from 25 g to 1 kg using a micro hardness machine. The impressions left on the sample surface were examined under SEM. Figure 4.1.2- 8 demonstrates two typical types of cracks generated along the edges or at the corners of the impressions. Cracks in carbides, as shown in Figure 4.1.2- 8a, were found on all the samples under the load of 1 kg, the number and size

of which increased with increasing the nitriding time and temperature. This type of crack indicates the brittleness of carbides but is not an indication of low LBC or failure of the sample. Long cracks which initiated from the corner of the indentation and propagated well into the matrix (i.e. radial cracks) were found on ASPN 475-2.5 and all the samples treated at 500°C and above (refer to Figure 4.1.2- 8b) under the 1kg. The formation of this type of long cracks would be catastrophic, an indication of the embrittlement of the surface and low LBC of the samples.

The hardening mechanism through ASPN has been investigated by researchers around the world. Recently, it has come to agreement that the transportation of nitrogen from the atmosphere to the sample was accomplished through the deposition of metastable FeN on the sample surface followed by the decomposition of FeN into the more stable Fe_4N, Fe_3N and nitrogen atoms which subsequently diffuse into the sample [166, 168, 173].

The broadening and forward shifting of the α-Fe peaks indicate the formation of a solid solution, which leads to the distortion of the lattice and local stress field, slowing the movement of dislocations. Conjoining the GDOES profile, it is safe to suggest that the dominant mechanism of hardening is through the diffusion of nitrogen atoms and resultant interstitial solid solution.

The microstructural observation conducted in this study revealed a superficial layer of deposited particles which can be confirmed to consist mainly of γ'-Fe_4N by the XRD inspection carried out on the polished sample. The existence of ε-Fe_3N cannot be located by this study, which could be in the superficial layer as a product of the decomposition of FeN or as precipitations in the nitrided layer. Due to its limited quantity, evidenced by the minute intensity of peaks from the XRD spectra,

precipitation hardening is not considered to be the main mechanism of hardening in this study.

4.1.2.5 Optimal ASPN Condition for Duplex Treatment

Based on the results from microstructure and mechanical property evaluation, the optimal ASPN treatment was identified. As shown in Figure 4.1.2- 6, ASPN 450-2.5 sample possesses the highest surface hardness; indentation tests also revealed that this treatment can produce a hardened layer with good toughness. Hence, ASPN 450-2.5 treatment was chosen as the first step for duplex treatment, which will be deposited by coating as the second step of the duplex treatment.

4.2 Microstructure of Surface Coatings

4.2.1 Surface Morphology

The surface morphology of all the deposited coatings was examined under SEM and typified in Figure 4.2.1- 1. It was found that the surface morphology of the as-deposited coatings varied with their compositions and all CrAlSiN coatings showed a similar surface morphology.

Figure 4.2.1- 1 presents the surface morphology of CrN, T-II (TiAlSiN) and C-I-10 (CrAlSiN) coatings and all of them showed characteristics of CAE coatings: dispersed spherical macro particles and craters, although their size varied with the compositions. It can be seen that the surface of T-II (TiAlSiN) and C-I-10 (CrAlSiN) coatings seem to be rougher than that of CrN. In addition to the spherical particles, similar to those found in CrN coating, oblate particles in the size of 3-20 μm were also presented on the surface of TiAlSiN and CrAlSiN coatings. However, the surface roughness (Ra)

summarised in Figure 4.2.1- 2 revealed that CrN coating exhibited the highest Ra (215 nm) whilst the CrAlSiN coatings exhibited a much lower value (~150 nm). This could be related to the size and depth of the macro particles and craters formed on the coating surface, which will be discussed later.

EDS analysis (Figure 4.2.1- 3) confirmed that the oblate particles consisted mainly of Al and Si. This could be related to the lower melting point of Al and Si compared with Cr and Ti, which could increase the possibility of forming liquid droplets of Al and Si. This is backed up by the splash shape of the oblate particles. The spherical macro particles, however, are believed to be associated with chromium, as it was the only type of macro particles observed on the surface of CrN coating. The cross-sectional microstructure of the two types of macro particles will be presented in Section 4.2.2.

The craters could be related to the detachment of the macro particles, as suggested in reference [6]. It is noticed that the majority of the craters on all coatings could be associated with the Cr-rich particles, in view of the shape and size of the craters.

4.2.2 Layer Structures

To obtain an insight into the layer structure, fractography of the coatings on Si wafer substrate were studied, and the typical microstructures are shown in Figure 4.2.2- 1. It can be seen that the CrN coating exhibited a well-developed columnar structure, with a width of 100-200 nm. For all CrAlSiN and TiAlSiN coatings, a ~0.2 μm thick interfacial CrN and TiN layer, respectively, with fine columnar structure can be observed between the substrate and the coating. T-II (TiAlSiN) and C-II (CrAlSiN) exhibited similar fractural morphology and a typical layer structure of C-II is shown

in Figure 4.2.2- 1. Near the interface layer, a columnar structure with the width similar to that of the interfacial layer (30 – 50 nm) grew straight upwards till 1 μm and then the growth direction were altered to a small angle to the surface normal.

C-I coatings exhibited relatively flatter fractural surfaces than CrN, C-II and T-II coatings, which may indicate fine column size and strong bounding between the columns. Multilayer structure can be seen from the fractured samples of C-I-2, C-I-5 and C-I-8, and the thickness of intervals decreased with increasing sample rotation speed. For C-I-10, no multilayer layer structure was observed under SEM.

Figure 4.2.2- 2 shows the cross-sectional microstructure of the two types of macro particles found in all coatings (marked as A and B). Particle A exhibits the shape of a droplet, with a spherical "head" (the lower part) which showed bright colours in the BSE image, indicating a large atomic number. EDS analysis suggested a high chromium content; however, it could only be used as a semi-quantitive indicator of the elemental compositions because the size of the particle was smaller than the resolution of the EDS equipped with SEM. The "tail" (the upper part) of the droplet shows a similar colour as the coating, indicating similar chemical composition with the coating. This is evidence that the macro particles which stick to the coating were incorporated into the coating, as discussed in Section 2.2.3.2. The part of the tails exposed to the surface of the coating corresponds to the "spherical" particles observed in Figure 4.2.1- 1. Particle B, which corresponds to the "oblate" particles in Figure 4.2.1- 1b&c, is flat and exhibits dark colour in the BSE image, which is in agreement with the composition (i.e. rich in light elements Al and Si, refer to Figure 4.2.1- 3). The defects noted by the arrow in Figure 4.2.2- 2a are suggested to be related to the type B particles, due to the same contrast and shape observed. TEM, due to the high

resolution, was employed to confirm the composition of the spherical head of type A particles and the abovementioned defects, which will be discussed in Section 4.2.5.

It can be seen that the type A particles (Cr-rich) has a larger effect on the surface roughness than type B particles (Al- and Si-rich), due to the height of the particle and the depth of craters. Therefore, the relatively low surface roughness of the CrAlSiN coatings compared with T-II (TiAlSiN) coating could be attributed to the higher melting point of Cr than that of Ti.

The thickness of the coatings was measured using a calo tester and validated by cross-sectional SEM micrographs. As summarised in Figure 4.2.2- 3, all the coatings have a thickness in the range of 2.3 μm to 2.6 μm.

4.2.3 Chemical Composition

Glow discharge optical emission spectroscopy (GDOES) was used to determine the composition of the CrAlSiN coatings. As summarised in Table 4.2- 1, CrAlSiN coatings revealed a consistent average composition ratio for all the designed coatings with no influence of the deposition parameters used, and an average value of stoichiometric formula was calculated as $Cr_{32}Al_{13}Si_4N_{51}$. However, the elemental depth profiles of the selected C-I samples (refer to Figure 4.2.3- 1) exhibit composition fluctuations along depth, which coincides with the multilayer structure observed from the fractured samples. The decreasing amplitude with depth was due to the uneven coating surface introduced by the ion bombardment during the testing process, which led to the poor resolution of elements along the discharge distance. As for the fine interval multilayers, such as C-I-10 sample, no fluctuations could be observed as evidenced in Figure 4.2.3- 1c. The elemental depth profile of C-II is also

presented in Figure 4.2.3- 1, despite the fact that it shared the same sample rotation speed with C-I-5, no regular fluctuation feature could be observed. The details will be discussed in Section 4.2.5.

4.2.4   XRD Analysis

The XRD pattern of CrN coating is presented in Figure 4.2.4- 1 together with M2-unt pattern for comparison. It can be seen that the dominant phase is fcc-CrN, where the highly intensed peak of (200) planes indicates a preferential orientation of (200) planes parallel to the coating surface. Hcp-Cr_2N peaks were also identified, the strongest peaks of which, locating at 40.12 º and 42.61 º, overlap with the carbide peaks from the substrate, leading to a shift towards the higher angle.

Glancing angle XRD was employed to examine the CrAlSiN coatings deposited on M2 substrate. The spectra of all CrAlSiN samples are plotted in Figure 4.2.4- 2. A CrN-like fcc phase with NaCl-structure was identified for all CrAlSiN coatings. The C-II coating showed partial preferred orientation of (200) and (111), while for C-I coatings, the C-I-2 and C-I-5 coatings with low sample rotation speed showed the preferred orientation of (200) and the high sample rotation speed coatings, C-I-8 and C-I-10, showed the preferred orientation of (111). The intensity ratio of (200) to (111) planes decreased as the sample rotation speed increased. All the peaks of the fcc phase were broadened. No peaks of a second phase were identified, although it cannot be excluded that the peaks of an AlN-like hcp phase could overlap with the (111) peak of CrN and subsequently lead to the left shift in diffraction angle of the latter peak.

Glancing angle XRD test was also carried out on the duplexed treated samples, and as shown in Figure 4.2.4- 3, the XRD pattern from C-II coatings on M2 substrate and on ASPNed M2 are very similar. This implies that there should be no significant changes in their phase constituents and texture.

4.2.5 TEM Analysis

To confirm and further clarify the microstructure and phase constitutions of the coatings, cross-sectional TEM examination was conducted on some selected samples.

4.2.5.1 C-II Coating

Figure 4.2.5- 1 presents the typical TEM microstructure and corresponding SAD patterns of the C-II coating. A thin (~200 nm) CrN interfacial layer with a columnar structure was observed. The SAD pattern (Figure 4.2.5- 1c) revealed two sets of fcc-patterns which were identified as CrN: one pattern showed a preferred orientation of (200) plane parallel to the sample surface, the other pattern showed a preferred orientation of (220) plane almost normal to the coating surface, with the zone axis of 112].This indicates that the CrN interface layer was not textured. The main coating of C-II was also columnar structured, and the growth directions were consistent with the CrN grains. As shown by a bright field image at higher magnification (Figure 4.2.5- 2a), the a nano-multilayer structure with the bilayer thickness in the range of 11 - 22 nm was superimposed with the columnar structure.

The SAD ring pattern taken from the main C-II coating (Figure 4.2.5- 1b) could be indexed to an CrN-like fcc-MeN phase with partial preferred orientation of (200) and (111), and the lattice parameter calculated from the SAD pattern is 0.4126nm, which slightly smaller than 0.4149 nm for CrN. This drop in lattice parameter of MeN could

be related to the substitution of Cr atoms by Al and Si atoms, since no other phases could be detected by SAD from TEM analysis.

4.2.5.2 C-I-5 Coating

The TEM microstructure and corresponding SAD patterns of C-I-5 are shown in Figure 4.2.5- 3. The bright field image of the coating revealed a CrN interface layer similar to that of C-II, and for the main coating, a nano-multilayer structure with the bilayer thickness in the range of 16 - 27 nm was observed. Fine columnar structure, in the width of 70 -100 nm, was observed in addition to the nano-multilayer structure, which is in agreement with the fractograph shown in Figure 4.2.2- 1.

Although the TEM microstructure and the fractograph both revealed uniform through-thickness structure, SAD patterns showed different features when taken from the lower part (bottom layer) and the upper part (top layer) of the coating (Figure 4.2.5-3b&c).

The SAD patterns taken from both parts of the coating revealed similar patterns. However, a slightly larger scattering angles for both $(200)_{fcc}$ and $(01\bar{1}0)_{hcp}$ was found for the SAD pattern of the top layer. This indicates that the top layer coating structure is less oriented, which was to keep the surface energy to a low level.

It can be seen from Figure 4.2.5- 3c that a CrN-like fcc-MeN phase and an AlN-like hcp-MeN phase could be indexed. The fcc-MeN pattern consists of a set of continuous rings, indicating fine grains of nano size, as evidenced in Figure 4.2.5- 4. Two sets of fcc-MeN planes with the zone axes of [011] and [001], as indicated by the yellow and blue patterns in Figure 4.2.5- 3b, were indexed in the SAD pattern. These two fcc patterns were orientated in such a way that $[110]_a//[001]_b$,

$(200)_a//(200)_b//surface$, with a scattering angle of $\pm 17°$. The hcp-MeN pattern is relatively weak and consists of a set of $(01\bar{1}0)$ arcs with the scattering angle of $\pm 20°$, perpendicular to the surface of coating.

The lattice parameter of theoretical CrN and AlN, as well as the calculated lattice parameters for the two MeN phases are summarised in Figure 4.2.5- 3d, from which a drop and an increase in lattice constant for fcc-MeN and hcp-MeN phases was observed, respectively, which will be discussed next.

Figure 4.2.5- 4 shows the high resolution TEM image from the top layer of the C-I-5 coating and the FFT (Fast Fourier Transformation) of two nano-layers with different contrast; the regions from which the FFT was obtained are marked as A and B. Nano-crystallites with different orientation of lattice fringes could be seen from both nano-layers, while no sign of amorphous phase was observed. The FFT from the dark contrast nano-layer showed the presence of an fcc phase with the preferred orientation of (200) parallel to the coating surface, which is consistent with the CrN-like fcc-MeN phase, identified in the ring pattern (Figure 4.2.5- 3c). The corresponding EDS elemental analysis revealed a high content of chromium, nitrogen and low content of aluminium and silicon. Indexing of the FFT from the bright contrast layer revealed that it corresponded to the hcp-MeN phase identified in Figure 4.2.5- 3, with the preferred orientation of (0002) plane parallel to the sample surface. And the EDS analysis confirmed a higher content of Al and Si than in nano-layer A. This indicates that the bright contrast nano-layer corresponds to the AlN-like hcp-MeN phase.

It is worth noting that Al and Si with a concentration lower than an average value was detected in the dark contrast layer and Cr was also detected in the bright contrast layer.

This indicates that both the Cr-rich dark layer and the Al/Si-rich bright layer are not stoichiometric compounds, but solid solutions of fcc- and hcp-MeN with some substitutional alloying elements, which is believed to be responsible for the change of lattice parameter of both phases.

4.2.5.3 C-I-10 Coating

Figure 4.2.5- 5 shows the TEM microstructure and corresponding SAD patterns of C-I-10 coating. It can be seen that the coating was comprised of two distinct sublayers: the bottom layer (i.e. near the CrN interfacial layer) with a parallel columnar structure which is similar to that of C-I-5, and the top layer showing a small angle mismatched platter columnar structure with reduced column width. This is in good agreement with the fractographic observation (refer to Figure 4.2.2- 1). A nano-multilayer structure was observed throughout the coating thickness, with a bilayer in the range of 7 nm to 10 nm thickness.

The SAD pattern of the bottom layer revealed a set of AlN-like hcp-MeN patterns with the one axis of 2110] and three sets of CrN-like fcc-MeN patterns (two of them with the zone axis of [001] and one with [011]), which is similar to that of the bottom layer of C-I-5 (refer to Figure 4.2.5- 3d). The preferred orientation of (200) parallel to the sample surface was observed for fcc-MeN phase.

Figure 4.2.5- 5c shows the SAD pattern of the top layer of C-I-10 consisting of a set of AlN-like hcp-MeN and two sets of CrN-like fcc-MeN patterns. The zone axis of the hcp-MeN pattern was 2110] and the two fcc-MeN patterns shared the zone axis of [011], as indicated by Figure 4.2.5- 5c. The fcc-MeN and hcp-MeN phases showed respectively the preferred orientation of (111) and (0002) parallel to the coating surface. The scattering angle of both fcc and hcp patterns reduced to ~30˚comparing

to that of the bottom layer, indicate a stronger tendency of orientation. Figure 4.2.5- 6 shows the dark field image of the fcc-MeN phase, from which the size of the columns can be clearly seen in the width of 50 nm to 80 nm.

Figure 4.2.5- 7 presents the high resolution TEM image of the top layer of C-I-10 and the FFT of two nano-layers with different contrast; the regions from which the FFT was obtained are marked as A and B. The FFT of A (the dark contrast layer) and B (the bright contrast layer) revealed an fcc phase and anhcp phase, respectively. The preferred orientation of $[110]_{fcc}$ $2110]_{hcp}$, and $(111)_{fcc}//(0002)_{hcp}//$coating surface was found, which is in good agreement with the SAD pattern shown in Figure 4.2.5- 5b.

4.2.5.4 CAE Coating Defects

It is noted that some defects were observed in all the examined coatings, and two typical types of defects are demonstrated in Figure 4.2.5- 8, both of which are caused by the macro droplets produced during the cathodic arc evaporation process.

As discussed in Section 2.2, if the macro droplets solidified before arriving at the sample surface, it might be attached and incorporated into the coating. The defect marked as "A" in Figure 4.2.5- 8 could be related to such macro droplets, where the spherical "head", confirmed to be pure chromium by EDS, was the solidified macro droplet from the Cr target.

The defect marked as "B" in Figure 4.2.5- 8 was a flat droplet, and the EDS analysis revealed the composition of more than 95% of Al and traces of Si. This is most probably because that the macro droplets containing Al did not solidify when arriving at the sample surface, owing to the low melting point and splashed into flat droplet.

It is noted that the number of type B defects are much larger than that of type A defects, which could also be related to the low melting point of Al.

4.3   Mechanical Properties of CAE Coatings

4.3.1   Nano-hardness and Young's Modulus

Nano-indentation tests on the coatings were conducted under the load of 25 mN to ensure that the impression depth was less than 10% of the coating thickness in order to avoid the influence from the substrate to the hardness values. The measured raw data exhibited large scattering and the post-test SEM observation revealed that the extremely low values were related to the macro particles and craters on the surface of the coating (see Figure 4.3.1- 1). Based on SEM observations, the low value data corresponding to defects were eliminated and an average value was calculated from the filtered data of more than 20 measurements for each coating (see Figure 4.3.1- 2). As proven from the figure, all multi-component coatings show higher hardness than that of CrN coating (19.65 GPa). The C-II and T-II coatings possessed the highest hardness of 33.97 GPa and 31.15 GPa, respectively. The hardness of C-I multilayer coatings is slightly lower than that of the mode II coatings (C-II and T-II). Among the C-I coatings, except for the C-I-5 sample, the hardness marginally increased with the increase of the sample rotation speed.

The Young's modulus of all coatings were calculated and plotted in Figure 4.3.1- 3, which follows the same trends as the hardness.

4.3.2   Scratch Resistance

4.3.2.1 Coatings Deposited on M2 Substrate

Figure 4.3.2- 1 shows three typical curves of friction force and the first derivative of friction force against the incremental normal scratch load for CrN, C-II and C-I-10 coatings. It can be seen that for CrN coating, the friction force increased smoothly until a detectable fluctuation in the first derivative occurred, which indicates a sudden change in friction force. The normal scratch load under this point is defined as the first critical load (Lc_1). For C-II coatings, Lc_1 was detected at an early stage, and a drastic increase of friction was observed when the normal load reached a critical value: the so-called second critical load (Lc_2). For C-I-10 coating, only Lc_1 was observed in the scratch test, and it appeared at the early stage. The amplitude of fluctuation in the friction force was larger in comparison to that of CrN.

The friction force – load (Ft-Fn) curves of all coatings deposited on M2 substrate are summarised in Figure 4.3.2- 2. As can be seen from the figure, the Lc_2 value of C-II, C-I-5 and C-I-8 coatings ranged from 85 N to 95 N, while all other multi-component coatings showed a similar curve to that of C-I-10 coating with only Lc_1 detected. The Lc_1 and Lc_2 values of all the coating systems are summarised in Table 4.3- 1, from which it can be seen that CrN coating possessed the highest value of Lc_1, while the lowest value was for C-II coating. The Lc_1 of C-I mode coatings generally increased with increasing sample rotation speed.

4.3.2.2 Coatings Deposited on ASPNed Substrate

Figure 4.3.2- 3a shows the Ft-Fn curves of C-II and C-II-PN, from which it can be seen that the scratch resistance of the C-II coating was enhanced by duplex treatment, as evidenced by the fact that Lc_2 was not detected up to the maximum 100 N normal load. The values of Lc_1 (refer to Table 4.3- 1) for all duplex treated systems are higher than that of the corresponding coatings deposited on M2 substrate.

Figure 4.3.2- 3b-c depicted the back scattered (BS) SEM images of the entire scratch tracks formed on C-II and C-II-PN surfaces, and the bright coloured areas are the regions where the substrate was exposed. Conjoining the high magnification BS images inserted in Figure 4.3.2- 3 a, it can be seen that small craters appeared in the scratch wear track of the C-II coating on M2 substrate corresponding to Lc_1point, followed by spallation along the edge of the track and eventual gross spallation at the point of Lc_2. In the case of duplex treated C-II-PN (C-II coating on ASPNed M2), similar craters appeared in the scratch wear track at Lc_1 followed by a limited number of chipping along the edge of the track. Cracks parallel to the trailing edge of the indenter were observed as a result of tensile stresses present behind the indenter as discussed in Section 2.2.1.2.

4.3.3 Nano-impact Resistance

The nano-impact test is a noble method to assess the impact resistance and toughness of thin coatings. Tests under different loads were carried out and detailed test conditions can be found in Table 3.4- 1. The final depths of impact impressions after 75 impacts are summarised in Figure 4.3.3- 1.

Under the load of 1 mN, there is a high degree of correlation between the final depth of impact impression and the hardness of the coatings, i.e. the penetration depth decreases by increasing the surface hardness of coatings. The only exception is for C-I-10 coating, which possessed a lower hardness than the C-II and T-II coatings but revealed the shallowest penetration depth.

When increasing the impact load to 5 mN and 10 mN, the shallowest penetration depth was found for the C-II coating, and the superiority increases with increasing

load. T-II exhibited the second smallest penetration depth under 5 mN, however, further increase in impact load led to large scattering and a drastic increase in the penetration depth. Under the impact load of 5 mN, the C-I type coatings exhibited similar penetration depths regardless of the sample rotation speed. The depths are comparable to that of CrN, whereas under 10 mN their penetration depths are smaller than that of CrN, and the impact depth marginally reduced with increasing sample rotation speed.

C-I-8-PN was selected to investigate the effect of duplex treatment on the impact resistance of coatings. As can be seen from Figure 4.3.3- 1, the ASPNed layer under the coating would not affect the impact resistance until the load of 10 mN was applied.

Figure 4.3.3- 2to Figure 4.3.3- 4 show the real time change of indenter position (i.e. the depth of impression) of selected samples under different impact loads and the corresponding SEM images of the impact impressions. It is noticed that under the impact load of 1 mN, the depth of the impressions on CrN increased readily to a critical value at the running-in stage (Dc), and then increased gradually with a slow rate. This reflects the propagation of small cracks within the coating. Under the loads of 5 mN and 10 mN, an abrupt jump appeared in the curve for CrN, which mirrored the removal of coating material by fracture as shown in the SEM images.

Under the impact load of 1 mN, the depth of impact impression on C-II remained virtually constant after the running-in stage, indicating that the C-II coating has better resistance to crack propagation than CrN. The depth-time curves of C-II under impact loads of 5 mN and 10 mN resembled the curve for CrN under the load of 1 mN, while the Dc and the slope of the curve increased with increasing impact load. SEM images

of the post-impact impressions showed shallow and confined delamination of the coating on the edge of the impression (see Figure 4.3.3- 3, as indicated by the arrows).

The C-I-5 coating behaved in a similar manner to the C-II coating under the impact load of 1 mN and 5 mN, with a greater Dc as evidenced by the depth-time curve and a bigger delamination region as shown in the corresponding SEM image (see Figure 4.3.3- 4). Under the impact load of 10 mN, a series of small jumps were observed from the curve, which corresponded to multiple fracture/delamination of the coating as can be seen in the SEM image of the impression (Figure 4.3.3- 4).

4.3.4 Load Bearing Capacity

Indentations were made on the coating surfaces under a series of loads ranging from 10 g to 1 kg using the micro hardness machine with a Vickers indenter. The impressions left on the sample surfaces were examined under SEM. The two mode II coatings (i.e. C-II and T-II) showed similar behaviour while all C-I coatings showed a similar trend. Thus, the SEM images of the impressions under selected loads are typified in Figure 4.3.4- 1 using CrN, C-II and C-I-10 as examples. It can be seen that even under the highest load of 1kg, no radial cracks, as described in Section 4.1.2.4, were observed in all samples, indicating generally good toughness. Under a relatively low load of 100g, the impression left on the CrN coating revealed well-developed ring cracks, and for C-II coatings a small number of ring cracks were observed along the edge of the impression. However, for C-I-10, the impression was shallow and no cracks were observed. The critical load above which ring cracks were formed was observed to be 10g, 100g and 200g for CrN, mode II coatings, and C-I coatings, respectively.

The hardness values of selected coatings are plotted against different applied loads in Figure 4.3.4- 2. It can be seen that at low loads (i.e. less than 50 g), the coatings maintained high hardness, while a further increase in applied load led to a dramatic drop in hardness, which is attributed to the increasing contribution of the substrate in the hardness of the coating-substrate system. All the CrAlSiN coatings behaved in a similar way, showing a higher hardness than the CrN coating. However, under the highest load of 1kg, the difference in hardness between all coatings became negligible because the main contributor changed from the coating to the substrate.

4.4 Tribological Behaviour

4.4.1 Room Temperature Reciprocating Wear

Reciprocating sliding wear tests were performed at room temperature with WC-Co and Al_2O_3 balls as counterparts to form two types of wear couples. Selected coatings deposited on the M2 substrate were tested, and C-I-8 PN was selected to investigate the effect of duplex treatment.

4.4.1.1 Sliding Against WC-Co Ball

The cross-sectional area loss of all the tested samples after the reciprocating sliding wear test against WC-Co ball was calculated by integrating the 2-D profile of the wear track. The results are summarised in Figure 4.4.1- 1. Among all the coatings deposited on the M2 substrate, C-I-2 and C-I-10 showed a marked improvement in wear resistance over CrN with the lowest wear loss for the C-I-10 sample, which was 10 times smaller than that of CrN and 19 times smaller than that of T-II. However, the samples coated with C-II and C-I-8 coatings showed wear loss of up to 6 times more than that of CrN. It is worth mentioning that a significant amount of wear debris was

produced during the wear test of the C-II and C-I-8 samples, in contrast with the virtually unobservable amount of wear debris produced by CrN, T-II, C-I-2 and C-I-10 coatings. For C-I-8 PN, the duplex treated sample, a significant reduction by 47 times in wear loss in comparison to C-I-8 coating on M2 was observed.

Figure 4.4.1- 2 shows the SEM observation of the wear track on T-II coating, which revealed that large amount of material agglomerates on the wear track, especially on the end of the wear track. EDS analysis confirmed that the agglomerates are mainly the oxidation product of the coating. It is also worth noting that extremely high iron content was found in the wear track (i.e. marked as B in Figure 4.4.1- 2), indicating the remaining coating is very thin, which is in agreement with the high volume loss of T-II. No abrasive groove was observed on the surface of the wear track, thus it is clear that the wear mechanism of the T-II coating is severe oxidational wear.

It is noticed that the Cr-based coatings exhibited different morphologies for samples which produced a different amount of debris. Figure 4.4.1- 3 shows the SEM images of typical wear tracks in the SE and BSE modes. The wear track on C-I-8 coating was characterised by two regions: the near-edge areas are rough with a light grey colour in the BSE image, where spallation/attachment of material could be observed in the SE image; the centre of the wear track was relatively smooth and showed a slightly brighter colour in the BSE image in comparison with the edges. EDS line scan confirmed that the coating was totally removed from the wear track, exposing the substrate. A slight increase in the intensity of W, O and elements from the coating was observed in the near-edge areas, which indicates the attachment of a mixture of tungsten oxide and oxide of the coating material. This is in line with the slightly brighter colour of the near-edge area in the BSE image. In contrary with C-I-5, the

71

wear track on the C-I-10 coating was uniform, smooth and shallow. Backscattered electron image revealed some bright spots in the wear track which were confirmed by EDS analysis to be a mixture of oxides of coating and counter ball materials.

4.4.1.2 Sliding against Al_2O_3 ball

The wear area loss of all tested coating systems after reciprocating sliding wear test against Al_2O_3 ball are depicted in Figure 4.4.1- 4. Among the coatings deposited on the M2 substrate: C-I-2, C-I-5 and C-I-10 exhibited a similar area loss of 2.8 x 10^8 nm^2, whereas C-I-8 and C-II showed higher wear loss by two orders of magnitude compared to CrN. The C-I-8 PN sample possessed the best wear resistance under the current wear condition.

The 2-D cross-sectional wear track profiles presented in Figure 4.4.1- 5 clearly demonstrate that the wear track on the C-I-10 surface is narrow and shallow, while that one on C-I-8 is wide and deep (up to 17 μm). SEM images of these two samples are shown in Figure 4.4.1- 6. They represent two typical types of wear tracks, corresponding to the high and low wear loss.

The wear tracks of the M2 samples coated with C-I-8 and C-II are wide and the substrate was exposed, with abrasive grooves along the sliding direction. CrN and other C-I mode coatings exhibited similar wear track morphology (refer to Figure 4.4.1- 6 for the SE and BSE images of wear track on C-I-10), with the appearance of abrasive wear grooves along the sliding direction, indicating that abrasive wear mode is the main mechanism of material removal. The SE image revealed some black spots in the wear track. A similar shape and colour were also observed in the BSE image (Figure 4.4.1- 6d), which are believed to be the macro particles within the coating.

72

To investigate the mechanism of material removal in the C-II and C-I-8 coatings, FIB was employed to cross-section "cut" the edge of the wear track. Similar features were observed for both samples. Figure 4.4.1- 7 shows the cross-sectional view of the wear track in C-II, from which it can be seen that cracks originated at the interface of the coating and substrate, leading to delamination of the coating.

4.4.1.3 Comparison of WC-Co and Al_2O_3 Counterpart

The average wear area loss of samples sliding against WC-Co and Al_2O_3 balls are plotted in Figure 4.4.1- 8. As can be seen, more significant wear loss for all the samples was observed when sliding against the Al_2O_3 ball than against the WC-Co ball, which could be related to the higher hardness of Al_2O_3 in comparison to that of WC-Co. In both cases, C-I-2 and C-I-10 showed improved wear resistance over CrN, while C-I-8 and C-II showed much more severe wear loss than the other coatings.

Coefficient of friction (CoF) of samples sliding against both balls was evaluated with a load of 10 N and summarised in Table 4.4- 1. Generally the CoF is higher when slide against Al_2O_3 ball than against WC-Co ball. An increase in CoF with sample rotation speed was also observed.

4.4.2 Rolling-sliding Wear Test

4.4.2.1 Weight Change during the Test

Rolling-sliding wear tests were carried out on the CrN, C-II and C-I-10 coated wheels against the M2 wheel under the conditions described in Chapter 3. The weight change of the CrN and M2 wheels against time are shown in Figure 4.4.2- 1. A virtually linear relationship between the weight change and time was observed for both wheels, and a linear fitting on the data was calculated as indicated in Figure 4.4.2- 1. The

gradient represents the wear rate in the unit of gram per hour and the negative value refers to the reduced weight. It is clearly shown in the graph that the wear rate of the CrN coated wheel is 20 times lower than that of the M2 wheel.

The wear rate of the M2 wheel against the CrN, C-II and C-I-10 coated wheels was calculated to be -0.0183,-0.0187 and -0.0147 g/hr, respectively. Due to the similarity of these data, only the weight change of all the coated samples against time was summarised in Figure 4.4.2- 2 to evaluate the wear behaviour of the coated samples.

It can be seen that the wear rate of all the coatings changed with time to a different extent. CrN showed low wear rate (i.e. -0.0004 g/hr) during the first two hours, and a further increase in test's time led to an increase in wear rate to -0.0012 g/hr. C-II exhibited the same low wear rate as CrN for the first hour of the test, while upon a further increase of time, a drastic increase to -0.0083 g/hr (~20 times larger than that for the first hour) was observed. The test was stopped after 3 hours due to a large weight loss (0.017 g) since it was suspected that the coating layer had been worn off. In the case of the C-I-10 coated wheel, the smallest wear rate of -0.0001 g/hr was achieved. Also, a weight gain was found for the first two hours of the test, which will be discussed next.

4.4.2.2 Morphology of the Worn Surface

The tribology pairs were ground using the #1200 silicon carbide paper before the wear test. The typical morphology is shown in Figure 4.4.2- 3. It can be seen that under visual observation the coated wheel shows a smooth matt finish while the M2 steel shows a metallic finish with visible abrasive wear marks due to the grinding process. SEM observation of the coated wheel also found abrasive grooves on the surface.

A digital camera was used to record the morphology of the tribology pairs after each hour and some typical photos are presented in Figure 4.4.2- 4.

Figure 4.4.2- 4a demonstrates the morphologies of the CrN/M2 tribological pair after 1 hour. The CrN surface exhibited a matt brownish colour, and a small amount of spallation of the coating was observed as indicated by the arrow. The surface of the M2 wheel against CrN coating was covered with stripes with mixed brown and dark grey colours, which was identified as iron oxide through EDS analysis. Both the quantity and the size of spallation on the surface of the CrN coating increased as the test time increased. After the test of five hours, the fraction of spallation on the surface of the CrN coated wheel reached 30% (refer to Figure 4.4.2- 4b) which is considered as a failure of the coating. The stripes on the surface of the M2 wheel were changed to a smooth matt metallic colour with a small amount of dark spots distributed on the surface.

In the case of the C-II coated wheels against the M2 wheel (Figure 4.4.2- 4c-d), after one hour a relatively large area of delamination was observed near the edge of the coated wheel and after three hours the coating was completely removed, leaving the wheel surface virtually identical to that of the M2 wheel. This observation is in agreement with the large weight loss of the C-II coated wheel after two hours. The M2 wheel against C-II wheel behaved in a similar manner with that against CrN.

No visible wear mark was found on the surface of the C-I-10 coated wheel after a one hour test against the M2 wheel, although the surface became slightly darkened (Figure 4.4.2- 4e). After five hours, a few delamination sites were observed at the edge of the wheel, as denoted by the arrows in Figure 4.4.2- 4f, while the centre of the wheel remained in good condition.

SEM observation on the worn surfaces after testing for one hour (Figure 4.4.2- 5a-c) revealed the existence of agglomerate on the surface of all coated wheels, which was proved through EDS analysis to be iron oxide. EDS analysis indicated higher oxygen and iron content on the worn surfaces than on the unworn area, indicating the transfer of iron from the M2 wheel to the surface of the coated wheel and possible oxidation of the coating material. This indeed caused the slight weight gain of the C-I-10 coated wheel at early stages as shown in Figure 4.4.2- 1. The weight loss of the M2 steel and the coated wheels could be related to abrasive wear and delamination/spallation of the coating, respectively.

Post-test SEM morphologies of different coating surfaces are presented in Figure 4.4.2- 5d-f. It was found that the CrN coating showed surface spallation, as well as cracks perpendicular to the sliding direction within and around the site of spallation. The C-II coating was completely removed after a test of 3 hours and the SEM image was taken from the 2 hour tested surface. As it can be seen in Figure 4.4.2- 5e, around 50 % of the coating was removed, leaving sharp edges of the coating and abrasive grooves on substrate surface. On the C-I-10 coated wheel, spallation sites and cracks are similar to those on the CrN coated wheel but on a much smaller scale of ~50 μm (Figure 4.4.2- 5f). For all the coated samples, iron oxides were often observed on the edge of the spallation site.

4.5 High-temperature Performance

4.5.1 Structure and Stability of the Oxidised Layers

4.5.1.1 Surface Morphology and Chemical Composition

Thermal oxidation treatments were carried out on all coating systems at 700℃, 800℃ and 900℃ with a dwelling time of 2 hours. Post-treatment examination was conducted under SEM for surface morphology observation and chemical composition analysis.

It was found that after thermal oxidation treatments at 700, 800 and 900°C, an oxide layer was formed on the surface of all the coatings; however, the morphology of the oxide layers varied with different specimens and temperatures (Figure 4.5.1- 1).

As can be seen in Figure 4.5.1- 1, after oxidation at 700°C, dispersed oxide particles of 60 nm to 140 nm were formed on the surface of the CrN coating. After oxidation at 900°C, an oxide layer with large particles/plates in the size of 200 - 600 nm was formed.

The oxide layer formed on T-II after oxidation at 700℃ showed a similar morphology to the as-deposited coating. Upon an increase of temperature to 900℃, an oxide layer was formed, which was characterised by particles in the size 100 nm to 200 nm.

In the case of C-II, after oxidation at 700℃, "plaques" with the size of ~200 nm were distributed throughout the coating surface with a relatively low density, and a closer observation at higher magnification revealed the existence of a dense layer with small (10 – 20 nm) homogenous particles. A further increase of temperature to 900℃ led to

the development of "plaques" into irregular plates, as well as an increase in the size (to ~50 nm) and in the density of the homogenous particles.

The oxide layer formed on C-I type coatings was characterised by a mixture of many homogenous small (10 to 20 nm) particles and a few large (60 to 100 nm) particles. When oxidised at 900℃, the surface morphology of all the C-I mode coatings showed a very small difference, if any, which were characterised by homogenous particles between 40 to 100nm.

An EDS analysis, as summarised in Figure 4.5.1- 2, revealed a drastic increase in oxygen content with increasing oxidation temperature for CrN and T-II coatings. It is also noticed that the oxygen content of T-II was higher than that of CrN treated at the same temperatures. The CrAlSiN coatings, however, exhibited a marginal increase of oxygen content with increasing temperature, and the value remained moderately low throughout the temperature range, indicating a good oxidation resistance, which is in good agreement with the morphology observation (Figure 4.5.1- 1).

4.5.1.2 Phase Constituents

XRD analysis was conducted on all the samples oxidised at different temperatures, and generally the C-I mode coatings showed a similar oxidation behaviour, thus C-I-5 was selected to represent the C-I mode coatings.

Figure 4.5.1- 3 depicts the XRD patterns of CrN, T-II, C-II and C-I-5 after oxidation at 700℃. For CrN coating, the formation of a mixture of various chromium oxides (denoted as Cr_xO_y) was evidenced by the peaks at 35.9 °, 42.1 ° and 42.3 ° with appreciable intensity. Whereas for the T-II (TiAlSiN) and CrAlSiN coatings, oxidation at 700℃ led to the formation of Al_2O_3 as well as Ti_xO_y and Cr_xO_y,

respectively. The intensity of oxide peaks for the multi-component coatings was much lower than that of the CrN coating. It is also interesting to notice that in the XRD pattern for C-II, a minor peak at 39.3 ° identified itself as SiO_2, while the peak is absent in the patterns for all other coatings.

For CrN and T-II coating, the oxide peaks exhibited an increase in both quantity and intensity with increasing oxidation temperature, while the intensity of oxide peaks of the CrAlSiN coatings only showed a slightly increase. This mirrors the surface morphology observation (Figure 4.5.1- 1) and the surface oxygen content of the coatings (Figure 4.5.1- 2).

The XRD patterns of CrN, C-II and C-I-10 after oxidation at 900℃ are depicted Figure 4.5.1- 4. It can be seen that the intensity of the chromium oxide peaks increased drastically with time for the CrN coating. A close observation on the XRD pattern of C-II and C-I-5 coatings revealed that both coatings showed similar behaviour. In addition to the slightly stronger Cr_xO_y peaks than the 700℃ oxidised coating, Al_2O_3 and SiO_2 peaks with appreciable intensity were also observed. The only difference being C-II shows slightly stronger Cr_xO_y peaks.

4.5.2 Mechanical Properties

4.5.2.1 Surface Hardness

Surface hardness of the samples after oxidation treatment at 900℃ was evaluated via nano-indentation test and summarised in Figure 4.5.2- 1. The surface hardness of the coatings reduced after oxidation treatment and the T-II sample showed the lowest hardness value (7.34 GPa). C-II coating experienced a dramatic drop of surface hardness from 34 GPa to 14.2 GPa after oxidation at 900°C. In contrast, a small

reduction in hardness was observed for C-I type coatings (maintained around 20 GPa), indicating the high stability of these coatings at 900℃ .

4.5.2.2 Impact Resistance

Impact tests were carried out with impact loads of 1, 5 and 10 mN on selected samples after oxidation treatment at 900℃ . Since the final impact depth showed the same trend for a different impact load, the impact depths of the different samples after impact tests under 5 mN are summarised in Figure 4.5.2- 2 as a representation. As it can be seen from the figure, the oxidation treatment led to a dramatic increase of impact depth for the CrN and T-II coatings, while it had no real influence on the impact depth of the CrAlSiN coatings.

4.5.3 High Temperature Reciprocating Wear

High temperature reciprocating sliding wear tests were carried out on selected coating systems at 400°C and 500°C, and the details of the test conditions can be found in Table 3.5- 1. It is necessary to note that preliminary work was carried out where samples were tested against the WC-Co ball for 5000 cycles at 400°C.

Figure 4.5.3- 1 demonstrated the 3-D profiles of the wear tracks of selected samples after the preliminary wear tests. As it can be seen, an early failure was observed for CrN and T-II, thus a reduced cycle of 1000 was employed for the wear test. In this study, unless specifically stated, the high temperature wear test of CrN and T-II refers to the tests performed for 1000 cycles.

To evaluate the wear resistance without the influence of the number of cycles employed, the wear factor K was calculated using the following equation:

$$K = \frac{V}{F \times N}$$

where V is the wear volume loss measured using a vertical scanning interferometry, F and N are the applied normal force and the number of cycles for the wear test, respectively. The K values of all coatings tested at different temperatures are summarised in Figure 4.5.3- 2 and post-examination of wear tracks and the wear scars on the counterpart balls were carried out using SEM.

4.5.3.1 CrN and T-II

In terms of the K value, the T-II coating suffered from more severe wear (~ 7 times) than CrN at both temperatures. The increase of temperature from 400℃ to 500℃ had little effect on the wear behaviour of both coatings.

The SEM image of the wear track of CrN, as shown in Figure 4.5.3- 3a, indicated that the coating remained functional after sliding against the WC-Co ball for 1000 cycles at 400°C, judging from the integrity of the coating (Figure 4.5.3- 3). EDS analysis (refer to Table 4.5- 1 for atomic percentage of main elements in the wear track of selected coatings) revealed just over 14 at% of oxygen and nearly 2 at% of tungsten in the wear track, indicating a certain degree of oxidation of the coating and possible transfer of the ball material to the wear track. The backscattered electron image in higher magnification (Figure 4.5.3- 3b) revealed lateral cracks over the full length of the wear track running perpendicular to the reciprocating motion of the WC-Co ball, as well as grooves along the motion of the ball indicating the occurrence of abrasive wear. Also, on the surface of the wear track, the uniform distribution of a layer of scale-like material with brighter colour than that of the coating can be observed. EDS analysis showed high content of oxygen and tungsten in these regions.

The SEM images (see Figure 4.5.3- 4) of the T-II wear track of in the SE and BSE mode revealed that most of the coating was worn off from the sample surface, and the substrate was exposed. As shown in Table 4.5- 1, the overall oxygen and tungsten contents in the wear track were high. Detailed EDS analysis revealed that the remaining coating in the wear track contributed most to the high oxygen content while most tungsten signal came from the substrate, indicating severe oxidation of the coating.

4.5.3.2 CrAlSiN Coatings

All the CrAlSiN coatings, both C-I mode and C-II mode, suffered from mild wear during wear tests at high temperature against the WC-Co ball, as evidenced by the small wear factor and the integrity of the coating in the wear track. In terms of the wear factor, when tested at 400℃ , C-II outperformed all the C-I mode coatings, and a further increase in the test temperature led to a reduction in the wear factor for all samples.

A SEM examination revealed similar wear features for these CrAlSiN samples, and a typical wear track of C-I-2 is presented in Figure 4.5.3- 5. As it can be seen, after 20000 cycles of sliding against WC-Co ball at 400℃ , the wear track on C-I-2 was shallow and smooth, with some bright spots visible at low magnification. The images at higher resolution in both SE and BSE modes (see Figure 4.5.3- 5b&c) revealed the adherence of plate-like materials on the wear track. EDS analysis indicated that these plate-like features contained a high level of oxygen and tungsten. Accumulation of rod-like oxide debris occurred at the spallation site. No cracks were observed in the wear track, while very shallow abrasive wear marks along the motion of the WC-Co

ball were observed. Low oxygen content (3.85 at%) was detected by EDS analysis in the wear track, which indicates that mild oxidation took place during the test.

C-II-PN was selected to investigate the effect of duplex treatment on the wear resistance of coatings at high temperature. As shown in Figure 4.5.3- 2, C-II-PN exhibited an improvement in wear resistance over all coatings deposited on the M2 substrate at both temperatures. The SEM observation of the wear track revealed similar features to C-II deposited on M2.

As discussed in Figure 4.5.3- 2, increasing the test temperature to 500°C introduced a slight decrease in the wear factor of all samples which maintained the integrity after the test. By comparing the BSE images of the wear tracks of C-I-10 after test at both temperatures (Figure 4.5.3- 6), it can be seen that the wear track formed at 500°C was covered with more fine particles, indicating more severe oxidation of the ball and/or the coating.

4.5.3.3 Morphology of the Ball Worn Against the Samples

To further investigate the wear modes taking place during the reciprocating sliding wear test at high temperature, the wear scars of the counterpart balls worn against the coatings were examined under SEM. The morphology of the wear scars on the counterpart balls could be categorised into four types corresponding to the morphology of the wear tracks on the coatings described earlier. It should be noted that for all the samples the differences in the wear scar for both testing temperatures were negligible, thus only the wear scars after the 400℃ are presented.

CrN Coating

The wear scar on the WC-Co ball after sliding against CrN for 5000 cycles was examined to investigate the wear mechanism responsible for the failure of the coating. As shown in Figure 4.5.3- 7, adhesion of material was found on the surface of the wear scar, which was more severe on the edge in comparison to the centre. An EDS analysis confirmed that the material attached in both regions of the wear scar was mainly chromium oxide, indicating oxidational and adhesive wear modes.

T-II Coating

The wear scar of the ball worn against T-II for 1000 cycles (Figure 4.5.3- 8) also showed a high tendency of material adhesion, which was revealed by the BSE image and EDS to be tungsten carbide particles in sub-microns embedded in the matrix of oxidised coating material, indicating oxidational and adhesive wear modes. The BSE image of the centre of the wear scar on the WC-Co ball revealed WC grains of triangular shape, which was found in the adherent material as indicated by A in Figure 4.5.3- 8d.

CrAlSiN Coatings

As shown in Figure 4.5.3- 9, the surface of the wear scar on the ball worn against C-I-2 was smooth, with material accumulation mainly occurring around the edge of the wear scar. An EDS analysis confirmed that the accumulation mainly consisted of the oxidation products of the ball material (tungsten carbide), while in the centre of the wear scar oxygen was also detected but at a much lower content. As evidenced in Figure 4.5.3- 9b, in BSE images, the oxides appeared to be slightly darker than the ball material, due to the lower atomic number element of oxygen. It is noticeable that

in the centre of the wear scar the colour is also dark with some lighter stripes, which further confirmed oxidation of the ball. Images at high magnification (Figure 4.5.3- 9c, d) revealed that the stripes in lighter colour in the BSE mode correspond to abrasive grooves, indicating that the oxidation products of the ball was removed by coating through abrasive wear, which exposed the substrate.

4.5.3.4 Summary

Generally, the CrAlSiN coating outperformed the CrN and T-II coating during the high temperature reciprocating sliding wear test. Combining the examination of the wear track and the ball, it can be concluded that the dominative wear mode of CrN and T-II was oxidational wear, and that of the CrAlSiN coatings was mild abrasive wear.

Chapter 5   Interpretation and Discussion

5.1 Microstructure and Phase Constituents of CrAlSiN Coatings

5.1.1   Formation of hcp-MeN Phase

As has been discussed in Section 2.2.2, there has been a debate on the phase constituents of CrAlSiN coatings. It has been widely agreed that the elemental composition of the coatings, especially the Cr/(Al+Si) ratio, is a key factor. A critical Cr/(Al+Si) ratio from 0.38 to 1.08 was reported for CrAlSiN coatings with a monolayer structure and fcc-MeN phase (i.e. homogeneous through-thickness chemical composition) [98, 115, 116], below which phase separation from fcc-MeN to a mixture of fcc-MeN and hcp-MeN would take place.

As reported in Section 4.4.2, an hcp-MeN phase based on AlN was formed in all C-I type CrAlSiN coatings. It is known that the crystal structure of AlN is in fact wurtzite (i.e. w-AlN), in which both Al and N atoms individually forms an hcp sublattice and are tetrahedrally coordinated. This is also considered to be an hcp structure on a two-atom basis and hence the diffraction pattern of the w-AlN resembles that of hcp phase. For the sake of simplicity the wurtzite type MeN will still be referred to as hcp-MeN hereafter.

The Cr/(Al+Si) ratio of all the CrAlSiN coatings deposited from this research was calculated based on the GDOES results (refer to Table 4.2- 1) to be 1.8 ± 0.1, which is greater than the suggested critical values. Thus it is expected that these CrAlSiN coatings should consist of a single fcc phase.

However, the indexing of their SAD patterns (Figure 4.2.5- 3b&c and Figure 4.2.5- 5b&c) confirmed the existence of hcp-MeN phase in the C-I type CrAlSiN coatings. This can be attributed to the nano-multilayer structure of the coatings, as revealed from TEM observations (Figure 4.2.5- 2). Despite the high Cr/(Al+Si) ratio calculated from the average composition of the coatings, for individual nano-layers the ratio could be different. This is supported by the fluctuation in the GDOES elemental depth profiles (Figure 4.2.3- 1), which revealed explicit difference in the elemental composition of the alternating nano-layers. This is further supported by the more direct evidence that the Cr/(Al+Si) ratios calculated from the TEM-based EDS analysis of C-I-5 (Figure 4.2.5- 4) are 0.52 and 4.92 for the Al-rich and the Cr-rich nano-layers, respectively. As a matter of fact, the Cr/(Al+Si) ratios in the Al-rich nano-layers of the C-I type coatings are so low that only the hcp-MeN phase was indexed from the FFT of the corresponding nano-layer (Figure 4.2.5- 4 & Figure 4.2.5- 7). Clearly, coating structure plays an important role in phase evolution, which is supported by the work by Zhang et. al [88] that phase separation occurred for nano-multilayer CrAlSiN coatings with a Cr/(Al+Si) ratio greater than 3.5.

For the C-II coating, however, although nano-multilayer structure was also observed under TEM (Figure 4.2.5- 1), only a single fcc-MeN phase was indexed from the both SAD patterns (Figure 4.2.5- 1b&c) and the GAXRD pattern (Figure 4.2.4- 2). This is probably because the composition difference between the alternating nano-layers in the C-II coating is not so prominent as for the C-I type coatings, which could be attributed to the target arrangement during the deposition process (refer to Figure 3.2.2- 1). The "semi-homogeneous" elemental distribution is evidenced by the almost flat GDOES elemental depth profile shown in Figure 4.2.3- 1, and by the indefinite contrast between the nano-layers as shown in Figure 4.2.5- 2a. It is reasonable to

assume that the Cr/(Al+Si) ratio in the individual nano-layers are not far from the calculated average of 1.8 ± 0.1. The high Cr/(Al+Si) ratio is believed to have led to the stability of the fcc-MeN phase in the C-II coating.

It is interesting to notice from the SAD patterns of C-I-5 and C-I-10 that the hcp-MeN pattern is not composed of continuous rings but arcs with a certain scattering angle, which indicates that the hcp-MeN phase is textured. The (01T0) planes which exhibit the strongest intensity do not cover the direction normal to the surface of the coatings. This suggests that no (for C-I-10) or a very small number (for C-I-5 coating) of (01T0) planes are oriented parallel to sample surface, which in turn explains the reason why no peak of the (010) plane was identified from the XRD spectra of the C-I type coatings. On the other hand, most (0002) planes are orientated parallel to the sample surface, suggesting that the intensity of the (002) peak from the XRD spectra should be strong. This is supported by the clear broadening of the peak at ~37.5 º.

5.1.2 Energetic driving force for coating growth

As discussed in the above section, the GAXRD patterns (Figure 4.2.4- 2) of all CrAlSiN coatings mainly revealed the information about the fcc-MeN. It is noticed that C-II coating showed partial preferred orientation of (200) and (111), while the former is more dominant than the latter. For C-I type coatings, the preferred orientation changed with sample rotation speed, from the intensive (200) orientation for C-I-2 coating to the intensive (111) orientation for C-I-10 coating.

Interestingly, within each coating, there is also an evolution of orientation with increasing the coating thickness. This is supported by comparing the SAD patterns of

the bottom and top layers of C-I-5 (Figure 4.2.5- 3b&c) and C-I-10 (Figure 4.2.5-5b&c). It can be found that for both the coatings the bottom layer showed a strong (200) preferred orientation parallel to the coating surface, while the top layer showed more pronounced (111) orientation than the bottom layer.

In terms of the hcp-AlN phase in C-I type coatings, the degree of texture increased with increasing sample rotation speed. This is evidenced by the reduced scattering angle for the hcp arcs in the SAD patterns of C-I-10 coating compared to that of C-I-5 coating.

Many factors are known to influence the preferred orientation during the coating growth, such as the deposition temperature, $N2^+$/Me flux ratio, substrate bias and adatom mobility, etc.[174, 175]. The large numbers of factors involved in the growth of the film make it impossible for systematic interpretation of the preferred orientation. However, a common approach could be adopted to explain the evolution of preferred orientation of coatings by considering the driving force for coating growth, which is minimising the overall energy (surface energy and strain energy) of the coating.

Hence, it is of vital importance to understand the nature of both surface energy and strain energy before the aforementioned observations can be discussed.

Surface Energy

The surface energy of coatings originates from the excess energies possessed by the surface atoms of a solid coating material due to the lack of bonding to neighbouring atoms. Assume the bonding strength between two atoms in a crystal is β, which can be considered to be a reduction in the internal energy of each of the neighbouring atoms by $\beta/2$, and then the surface atom with a broken bond gains the excess energy

of $\beta/2$. The number of broken bonds for each surface atom varies with (hkl) planes and will be denoted by N_{hkl}. Consider the sublimation of a mol of solid material, where Z x N_a bonds are broken, where Z is the coordination number and N_a is Avogadro number (6.023×10^{23}), and then β can be estimated from the sublimation energy (L_S) through the equation:

$$L_S = (Z \times N_a) \times \beta/2$$

<div align="right">Eq. 5.1.2-1</div>

Considering only the nearest neighbours, the surface energy per unit area (S_{hkl}) of a coating material can be defined by the equation:

$$S_{hkl} = (N_{hkl} \times L_S)/(Z \times N_a \times A_{hkl})$$

<div align="right">Eq.5.1.2-2</div>

where A_{hkl} is the occupied surface area by each surface atom.

The sublimation energy for CrN is currently not available; however, it is an isotropic energy and thus it is possible to compare the surface energy of different (hkl) planes of CrN by calculating the number of broken bonds per unit area for each orientation (N_{hkl}/A_{hkl}). Table 5.1- 1 presents the N_{hkl}/A_{hkl} values calculated for NaCl-type fcc structures with two components, from which it can be seen that the surface energies at different orientations are $S_{200} < S_{220} < S_{111}$ [176].

Strain Energy

The internal stresses of a PVD coating are usually composed of intrinsic stress, which results from the chemical and structural defects incorporated during the deposition process of the coating, and thermal stress, which is generated during the post-deposition cooling process due to the difference in thermal expansion coefficient of the coating and the substrate. It is the intrinsic stress that introduces a considerable

amount of strain energy which in turn affects the preferred orientation. For the two-dimensional case, the strain energy (U_{hkl}) is given by:

$$U_{hkl} = \varepsilon^2_{hkl} \times E_{hkl} \times (1 - v)$$

<div align="right">**Eq. 5.1.2-3**</div>

where ε_{hkl} is the strain in the (hkl) plane, E_{hkl} is the Young's Modulus of the (hkl) plane and v is the Poisson's ratio. It is interesting to note that unlike surface energy, which is independent of the coating thickness, strain energy is expected to increase with increasing coating thickness due to larger strain introduced by increased intrinsic stress. It is not possible yet to calculate the strain energy of fcc-Cr(Al)N as the anisotropic factors of Yong's Modulus is not available. However, detailed researches have been done on NaCl-type TiC and TiN, which proved that $U_{200} > U_{220} > U_{111}$ and that U_{200} has a higher increasing rate than U_{111} along with the thickness of coating [176, 177].

5.1.2.1 Effect of Surface and Strain Energy on the Preferred Orientation

The competition between the differences in surface energy (ΔS) and strain energies (ΔU) of various orientations would determine the preferred orientation of the coating. When the surface energy dominates, the preferred orientation of (200) with the lowest surface energy should be expected, while when strain energy dominates, the preferred orientation of (111) with the lowest strain energy should be expected.

Evolution of Preferred Orientation along the Thickness of Coating

At the initial stage of deposition, when the coating is thin and the intrinsic stress is minimal, the main source of differences in energy between various orientations is ΔS, and hence the preferred orientation of (200) should be expected. This is proved by the

SAD patterns of the bottom layer of C-I-5 (Figure 4.2.5- 3b) and C-I-10 (Figure 4.2.5-5b) coatings, both of which revealed fcc-MeN phases with (200) preferred orientation.

As aforementioned, the strain energy increases with increasing coating thickness, and the increasing rate at the orientation of (200) is larger than that at the orientation of (111). Thus, ΔU between the (200) and (111) orientations will increase with increasing coating thickness. This increase in ΔU will lead to the gradual change of preferred orientation from the surface energy favoured (200) to the strain energy preferred (111) along the coating thickness. An orientational crossover with increasing coating thickness was observed by Je et. al. for the binary TiN coatings within a thickness of 1500 nm [178].

Such an orientational crossover was not found for CrN coating in this work, probably due to the relatively high deposition temperature which has minimised the intrinsic stress. As aforementioned, the C-I type coatings showed increased intensity ratio of (111)/(200) with increasing sample rotation speed. This is mainly because as the sample rotation speed increased; the bilayer thickness deceased, thus forming more interfaces with lattice mismatch. The lattice mismatching interfaces introduced intrinsic stress. By rearranging Eq. 5.1.2-3 to: $U_{hkl} = \frac{\sigma^2}{E_{hkl}} \times (1 - v)$, it can be seen that the strain energy and hence ΔU increases with increasing intrinsic stress. It is most probably that for C-I-8 and C-I-10 coatings, the intrinsic stress reached a critical value which made ΔU large enough to dominate the growth of the coating.

As noted in Figure 4.2.5- 5c and Figure 4.2.5- 7, the AlN-like hcp-MeN and CrN-like fcc-MeN in C-I-10 are crystallographically related: {0001}$_{hcp}$//{111}$_{fcc}$//sample surface. The zone axes <2$\overline{1}\overline{1}$0>$_{hcp}$ and <110> $_{fcc}$ are also parallel. The crystal

structures of both phases are illustrated in Figure 5.1.2- 1. The labelled planes are $(0002)_{hcp}$ and $(111)_{fcc}$. The {111} plane group of fcc structure is well known for favouring the growth of {0001} plane group of AlN-like hcp phase (i.e. the wurtzite structure)[179] due to shared atomic structure of the plane (Figure 5.1.2- 1a), which in turn reduces the strain energy. The epitaxial growth of the hcp-MeN and fcc-MeN phase is also responsible for the fact that the hcp-MeN phase is more textured in the top layer of C-I-10 than in C-I-5.

Effect of Target Arrangement during Coating Deposition Process

Among all the CrAlSiN coatings deposited in this research, since C-I-5 and C-II coatings shared the same rotation speed during the deposition process, thus it is reasonable to deduct that any difference in the preferred orientation of fcc-MeN could be attributed to the difference in the target arrangement during deposition.

The deposition process of the coatings was controlled by power output, i.e. a pre-set power output was the trigger to terminate the coating process. Considering that in target arrangement mode I and mode II, the employed targets are both 3 Cr targets and 3 AlSi targets, the total amount of all elements in the coatings should be the same. However, the thickness of C-II coating is significantly smaller than that of C-I type coatings (Figure 4.2.2- 3), which implies that the density of the C-II coating would be higher than that of the C-I-5 coating. This is supported by the TEM observation as shown in Figure 4.2.5- 2, from which it can be seen that the bilayer thickness of the C-II is smaller than that of the C-I-5. This is probably due to the absence of the hcp-MeN phase in the C-II coating, and the high content of Al and Si atoms, which have smaller diameter than Cr atoms, in its fcc-MeN phase.

High density usually indicates high compressive internal stress, which, as discussed earlier, magnifies ΔU. Hence, this could push the orientational crossover forward, which is supported by the fact that the C-II coating exhibited a higher intensity ratio of (111)/(200) than the C-I-5 coating.

5.2 Mechanical and Oxidation Properties

As has been discussed in Section 2.2.2.4, the wear behaviour of tribological coatings, as a complex phenomenon, depends on mechanical properties such as hardness, fracture toughness and adhesion between substrate and the coating. In addition to combined mechanical properties, chemical inertness and oxidation resistance also play an important role in determining coating tribological behaviour especially under dry machining or unlubricated wear conditions. As a matter of fact, mechanical properties and oxidation properties are often used to predict the wear behaviour of tribological coatings. Thus it is of vital importance to analyse the mechanical and oxidation properties of the coatings developed from this project and to study their effect on the tribological performance of these coatings (see Section 5.3).

5.2.1 Hardness and Young's modulus

5.2.1.1 Effect of Composition and Deposition Conditions

As described in Section 3.4.1, the surface hardness of the coatings was measured using nano-indentation and the results have been summarised in Figure 4.3.1- 2. It is clear that all multi-component coatings exhibited a marked improvement in hardness compared to CrN coating, which could be attributed to the combination of solid solution hardening and the grain refining, as evidenced by the EDS analysis (Figure 4.2.5- 3) and cross-sectional microstructural observation (Figure 4.2.2- 1).

Among the CrAlSiN coatings, C-II coating showed a relatively higher surface hardness than all the C-I type coatings. The relatively low hardness of the C-I type coatings could be related to the formation of AlN-like hcp-MeN, which possesses a lower hardness (12-16 GPa [180, 181]) than fcc-CrN (19.7 GPa). This is in turn caused by the difference in target arrangement during the cathodic arc evaporation coatings process.

Generally the hardness of the C-I type coating increased with increasing sample rotation speed, with the exception of C-I-5, which showed marginal decrease of hardness compared to C-I-2. Since the phase constituents of all the C-I type coatings are similar, the main contributor of the difference in hardness is considered to be the bilayer thickness, which decreased with increasing sample rotation speed. The highest hardness was found for C-I-10, which exhibited the thinnest bilayer thickness of 7 -10 nm.

5.2.1.2 Strengthening Mechanisms

Two mechanisms have been proposed for the strengthening of nano-multilayer structure, namely, coherency strain effect and dislocation line energy effect [182].

Coherency strain effect was explained by Cahn, where the hardening of the multilayer structure is proportional to the coherency strain, resulted from lattice mismatch [182]. The coherency strain in a nano-multilayer system is related to the interplanar spacing modulation (ε_0), which decreases with increasing bilayer thickness, and the composition modulation amplitude (A_1), which increases with increasing bilayer thickness. The peak of the coherency strain corresponds to a critical bilayer thickness which is small enough that the strain is significant, yet large enough that the interdiffusion between neighbouring layers is minor. This critical bilayer thickness

was reported to be between 4 and 10 nm for many nano-multilayer systems [183-187]. In this study, the bilayer thickness of C-I-10 was measured to be in the range of 7 to 10 nm, which is in good agreement with the critical value to provide the highest strengthening effect by coherency strain effect.

The second mechanism for strengthening of nano-multilayer structure is based on the difference in dislocation line energy between neighbouring layers, which is given by $Gb^2 2$, where G denotes the shear modulus and b is the Burger's vector [182]. Assuming the shear modulus of the neighbouring layers $G_a > G_b$, then the maximum resolved shear stress (σ_{cr}) required for a dislocation to move from layer b to layer a can be approximated [137, 188] to be:

$$\sigma_{cr} \approx \sigma_r(h \approx 2b) = \frac{QG_b(t_b - 4b)\sin\theta}{8\pi(t_b - 2b)}$$

Eq. 5.2.1-1

where h is the distance that the dislocation moves, t_b denotes the thickness of layer b, and θ is the minimum angle between the interface and the glide planes of layer b. Q and G are given by

$$Q = \frac{G_a - G_b}{G_a + G_b}$$

Eq. 5.2.1-2

$$G = \frac{E}{2(1+v)}$$

Eq. 5.2.1-3

Different values of Young's modulus and shear modulus have been reported for CrN and AlN with different preferred orientations, and the data from literature [180, 189, 190] that agrees with the measured value in this study was adopted to calculate the shear moduli to be $G_{CrN(200)}$ = 97 GPa, $G_{CrN(111)}$ = 92 GPa, $G_{AlN(0001)}$ = 152 GPa. Considering the primary slip system in fcc structure: {111}<110>, θ = 0° for (111)-oriented coating and θ = 54.7° for (200)-oriented coating. Another slip system,

{110   110>, is also widely accepted to be an active slip system in nitride coatings [182, 186], for which θ is calculated to be 35.3º and 45º for (111)- and (200) oriented coatings. Keeping t_b constant, the variables in Eq. 5.2.1-1 can be defined as $K = G_b \sin\theta \frac{G_a - G_b}{G_a + G_b}$. And the K value is calculated and summarised in Table 5.2- 1 for different slip systems and different CrN orientations. It can be seen that for both slip systems, the (200) preferred orientation promotes more strengthening effect, which is consistent with the result observed in this study, i.e. the (200)-oriented C-I-8 and C-I-10 coatings possess a higher hardness than the (111) oriented C-I-2 and C-I-5 coatings. It should be noted that the bilayer thickness has an effect on the shear modulus of the individual layers: the smaller the bilayer thickness is, the smaller the difference in shear moduli between the neighbouring layers will be due to inter-diffusion. This could be responsible for the decrease in hardness for C-I-5 coating.

Another contributor to the hardness improvement with increasing sample rotation speed (i.e. decreasing bilayer thickness) would be the grain size reduction. This is supported by the TEM observation at high resolution (see Figure 4.2.5- 4 and Figure 4.2.5- 7) which proved that the nano-crystallites are confined within individual nano-layers, i.e. the size of the nano-crystallites decreases with decreasing bilayer thickness.

5.2.2 Toughness

Toughness, defined as the ability of a material to absorb energy before fracturing, refers to the resistance to both crack initiation and crack propagation. The accurate assessment of toughness of thin coatings is difficult. The indentation test using a Vicker's indenter, initially proposed by Evans et. al [191, 192] in the 1970s for brittle bulk materials, has been adopted to assess the toughness of thin coatings deposited on

hard substrate. In the case that well-developed radial cracks form around the corner of the indentation impression, the fracture toughness K_{IC} can be described as:

$$K_{IC} = \chi\left(\frac{H}{E}\right)^{1/2}\frac{P}{c^{3/2}}$$

Eq. 5.2.2-1

where χ is an empirical constant related to the indenter geometry, H and E are the hardness and Young's modulus of the coating, respectively, P is the applied force and c is the crack dimension.

To investigate the toughness of the CAE deposited coatings, indentation tests were carried out on all coating systems under the load up to 1 Kg. However, as described in Section 4.3.4, for all the coating systems investigated in this research, the cracks were confined within the indentation impression, and no radial crack was observed. Similar observation was reported by other researchers when the substrate is relatively soft compared to the coating. Hainsworth et. al [193] credited the absence of radial cracks to the good fracture toughness of the coating.

Despite the fact that fracture toughness cannot be quantified using Eq. 5.2.2-1, it can be seen from Figure 4.3.4- 1 that under the same applied load, the resistance to crack initiation and propagation increases in the order of CrN, C-II and C-I type coatings, indicating improved toughness.

Two mechanisms of the formation of the ring/nested cracks within the indentation impression were proposed, namely the tension-induced and shear-induced cracking mechanism. The former mechanism was described by Page and Knight [194, 195] in the 1980s: under the stress introduced by the indenter, the substrate, which is relatively ductile, deforms - at first elastically then plastically as the load increases. To conform into the indentation, the coating is bent and flexed, introducing intense

tensile stress under the contact area. Cracks then initiate from the pre-existing structural weak sites of the coating (e.g. inclusions, defects and grain boundaries) and propagate along the grain boundaries upon further increase of load. The latter mechanism was proposed by Jayaram et. al [196], which attributes the ring cracks to the inter-columnar shear at the grain boundaries as shown in Figure 5.2.2- 1.

It is noted that for both mechanisms, the initiation and propagation of the cracks are explained to be mainly along the grain boundaries. Although introducing Al and Si into the coating led to grain refinement and subsequent increase in grain boundaries, the crack propagation is interrupted by the multilayer structure due to different moduli of neighbouring nano-layers. Hence the multi-component coatings show increased toughness over the single-component CrN coating. In addition to the multilayer structure, the C-I type coatings are proved to have nano-crystallites by TEM observation (see Figure 4.2.5- 4&7). Figure 5.2.2- 2 shows a schematic of crack propagation in columnar grain structure and nano-crystallite structure coatings, from which it can be seen that the nano-crystallite structure complicates and elongates the path for crack propagation, which in turn slows down the crack propagation procedure.

5.2.3 Oxidation

5.2.3.1 Oxidation Behaviour

As reported in Section 4.5.1, CrN and T-II coatings showed poor oxidation resistance, which is evidenced by the large amount of oxides formed on the surface of the coatings even at 700°C (refer to Figure 4.5.1- 3 for XRD patterns and Figure 4.5.1- 2 for surface oxygen content). Whereas for the CrAlSiN coatings, limited amount of

Al$_2$O$_3$ and Cr$_x$O$_y$ were formed after oxidation at 700℃ and no obvious increase in the intensity of the oxide peaks was observed up to 900°C (Figure 4.5.1- 4).

It is noticed that the chemical composition have great influence on the oxidation behaviour of the coatings. This can be attributed to the affinity between different elements with oxygen, which can be estimated by the Gibbs free energy of formation of the corresponding most comment oxides.

The standard Gibbs free energies of formation at 25℃ for the oxides of the four alloying elements in the coatings are -700 KJ/mol, -900 KJ/mol, -1050 KJ/mol and -860 KJ/mol for Cr$_2$O$_3$, TiO$_2$, Al$_2$O$_3$ and SiO$_2$, respectively [197]. The free energy increases with temperature linearly and are calculated to be -563 KJ/mol, -764 KJ/mol, -914 KJ/mol, -724 KJ/mol at 900℃ for Cr$_2$O$_3$, TiO$_2$, Al$_2$O$_3$ and SiO$_2$, respectively [197]. Hence, the affinity of these alloying elements with oxygen can be estimated based on the free energy to be in the order: Al> Ti > Si >Cr.

According to the affinity with oxygen, at high temperatures up to 900℃ , Al$_2$O$_3$ would preferably form before other oxides appear, and thus it is expected that the formation of an Al$_2$O$_3$ layer can prohibit or retard the formation of Ti$_x$O$_y$ and Cr$_x$O$_y$. However, the XRD patterns shown in Figure 4.5.1- 3 and Figure 4.5.1- 4 suggested more complicated oxidation behaviour of the coatings.

The XRD patterns for T-II and CrAlSiN coatings after oxidation showed much stronger peaks for Ti$_x$O$_y$ or Cr$_x$O$_y$ than for Al$_2$O$_3$. There are two possible reasons for this seemingly abnormal behaviour: firstly, in the corresponding coatings, the content ratio of Al to Ti (for T-II) or Cr (for CrAlSiN) is ~0.39, which indicates that the activity of Al in the current coatings is not high enough to form a continuous layer due to the low content [111]. Secondly, the Al$_2$O$_3$ formed on the coating surface could

be partially amorphous, which results in low peak intensity in the XRD patterns. Similar observation was reported by Tien et. al [198] for CrN/AlN multilayer coatings, and the amorphous Al_2O_3 phase was reported to inhibit the diffusion of oxygen into the coating and subsequently supress the formation of crystallite oxides.

It is clear from Figure 4.5.1- 2 that C-II coating outperformed T-II in terms of oxidation resistance. The more severe oxidation behaviour of the T-II coating than the C-II coating can be partially attributed to the greater affinity of oxygen with Ti than with Cr, thus leading to faster oxidation of Ti when compared with Cr; this could also partially attributed to the integrity (density & adhesion) of the oxide layer formed at high temperature since Ti has a higher Pilling-Bedworth ratio (the ratio of oxide-to-metal molar volumes) than Cr. The dense and adherent chromium oxide can effectively retard the diffusion of oxygen and thus reduce oxidation rate. Similarly, the improved oxidation resistance of the CrAlSiN coatings over the CrN coating can be credited to the addition of Al and Si, which retards the formation of Cr_xO_y by forming very stable alumina and silica.

It is interesting to notice that despite the same chemical composition, SiO_2 formed in C-II at 700℃ while in C-I-5 no SiO_2 peak was observed until 900℃ . It is also noticed that when oxidised at 700℃ the C-II coating showed slightly stronger Al_2O_3 peaks and weaker Cr_xO_y peaks when compared with C-I-5 coating. An increase of temperature to 900℃ led to similar intensity of Al_2O_3 peak for both coatings, while stronger Cr_xO_y peaks were found in C-II. This difference in oxidation behaviour of C-II and C-I-5 at different temperatures can be supported by the surface oxygen content (Figure 4.5.1- 2), from which it can be noticed that at relatively low temperatures, the atomic percentage of oxygen in C-II is lower than that in C-I-5, indicating retarded

oxidation process due to the formation of Al_2O_3 and SiO_2. However, when oxidised at 900℃ , the opposite was observed.

Huber and Hofmann [199] proposed that at temperatures lower than 900℃ , the chromium-based nitride coatings oxidised through the inward diffusion of oxygen along grain boundaries. Al_2O_3 and SiO_2 will preferably form due to the high oxygen affinity of aluminium and silicon, while a part of chromium is also oxidised due to the high content. The possible reason for the high oxidation resistance of C-II at relatively low temperature is that the grain boundaries of the columnar structure, as shown in Figure 4.2.2- 1 and Figure 4.2.5- 1a, creates short diffusion path for oxygen. This promotes relatively fast growth of Al_2O_3 and SiO_2, which in turn retards the formation of Cr_xO_y. While for C-I coatings, the interfaces of nano-multilayer structure retards the inward diffusion of oxygen [9], which leads to a slightly more severe oxidation of chromium in the outer surface of the C-I coatings than for the C-II coating.

At high temperature, a different oxidation mechanism was proposed by Kacsichi et. al [200] and Zhu et. al [201] based on the Au marker experiment. They suggested that at high temperature, the oxidation mechanism is the combination of inward diffusion of oxygen, which results in the formation of an oxide scale containing the mixture of Cr_xO_y, Al_2O_3 and SiO_2, and the outward diffusion of Cr^{3+} through the oxide scale which results in the formation of Cr_xO_y at the outer surface of the oxide scale. SEM morphology observation confirmed the formation of large Cr_xO_y grains on the surface of C-II coating, as shown by the irregular plates in Figure 4.5.1- 1. These large grains are responsible for the increased peak intensity of Cr_xO_y at 900℃ . However no large Cr_xO_y grain was observed at the surface of C-I coatings at 900℃ , which can be attributed to the inhabitation of outward diffusion of Cr^{3+} by the sharp interfaces of

the nano-multilayer structure due to the large size of Cr^{3+} and significant composition difference between alternating bilayers.

Based on the XRD analysis and SEM observation, it is suggested that the sample rotation speed does not have significant influence of the oxidation resistance of the C-I coatings, and the oxidation resistance of different coatings follow this order: C-I > C-II>>CrN>T-II.

5.2.3.2 Thermal Stability

Lee et. al suggested that the annealing and oxidation of the CrAlSiN coatings favours the outward diffusion and the escape of nitrogen in the coating [111]. Similar observation was found in the present work. As can be seen from Figure 4.5.1- 4, the peak intensity of the fcc-MeN phase in both C-II and C-I-5 reduced after oxidation at 900℃ , while the peak intensity of Cr_2N and hcp-AlN increased, suggesting a decomposition of the fcc-MeN phase to hcp-Cr_2N and hcp-AlN. It is noticed that the reduction of the peak intensity of fcc-MeN for C-I-5 is not as drastic as that for C-II, which indicates that C-I-5 has better resistance to decomposition, i.e. better thermal stability. This could be attributed again, to the sharp interfaces of the nano-multilayer structure, which retards the outer diffusion of nitrogen. This is supported by the change of surface hardness caused by oxidation at 900°C.

As showed in Figure 4.5.2- 1, at room temperature the C-II coating is much harder than that of C-I type coatings. All samples after oxidation at 900℃ showed a reduction in surface hardness, which could be contributed by the formation of surface oxide layer, the relaxation of residual stress and the decomposition of fcc-MeN phase to Cr_2N and AlN phase with relatively low hardness. However, after oxidised at

900°C, the hardness of all C-I type coatings is much higher than that of C-II coating. Clearly, the clear nano-multilayer structure can effectively increase the thermal stability of CrAlSiN coatings.

5.3 Tribological Behaviour

5.3.1 Reciprocating Sliding Wear Test at Room Temperature

The results from reciprocating sliding wear tests at room temperature in air against WC-Co and Al$_2$O$_3$ balls have been reported in Section 4.4.1. Some interesting or seemingly abnormal experimental observations are worth further discussion in this section.

Wear of C-II and C-I-8 Coatings

It can be seen from Figures 4.4.1-1 & 3 that C-II and C-I-8 coatings are characterised by high wear loss and the examination of the wear track revealed coating delamination and subsequent abrasive wear induced by the coating fragments acting as abrasive particles. As a matter of fact, according to the study by Arnell [152] on the mechanics of the tribology of thin film systems, for hard coatings on relatively soft substrates, the most common failure mode is abrupt coating delamination.

As has discussed in Section 2.2.4.1, for a "ball-on-disk" sliding system, both the tensile stress built up at the back of the contact and the compressive stress generated at the immediate front of the contact can lead to coating delamination. The former will generate partial ring cracks and subsequent crack propagation under cycling loading and unloading of tensile stress field induced by the reciprocating sliding motion of the counterpart ball; and the latter will cause buckling at poorly adhered

area and the resultant tensile stress at the coating-substrate interface. As illustrated in Figure 2.2.4- 1, both stresses increases with increasing local friction coefficient.

According to Hamilton [150], who proposed this stress distribution model, when the local coefficient of friction exceeds 0.25, it is very likely that the tensile stress at the back of the contact will exceed the maximum surface and subsurface yield stress, causing the formation of partial ring cracks. As has been reported in Section 4.4.1, the coefficients of friction of all coatings exceeded 0.25 when sliding against both counterpart balls. Hence it is likely that the delamination of the coatings is due to the high tensile stress at the back edge of the contact with the ball.

However, a close observation of one end of the wear track of C-I-8 worn against WC-Co ball under SEM (Figure 5.3.1- 1) clearly showed spallation of coating outside the wear track, i.e. ahead of the contact with the counterpart ball. Partial ring cracks were found on the oxides attached near the edge of the wear track; however no crack was observed on the remaining coating near the edge of the wear track. This is probably due to the compensation of the tensile stress developed by the moving counterpart ball by the high compressive residual stress within the coatings, which is a characteristic feature of PVD coatings.

Similar observations were found for the wear tracks of both C-II and C-I-8 worn against WC-Co ball and Al_2O_3 ball, which put into evidence that the compressive stress developed ahead of the contact with the ball was responsible for the delamination of the coatings. This is in good agreement with the poor adhesion between these two coatings and the substrate, as indicated by the low Lc_1 and Lc_2 values from scratch test (Table 4.3- 1).

Wear mechanism of CrN, C-I-2 and C-I-10 Coatings

As reported in Section 4.4.1, after reciprocating sliding wear test against WC-Co ball and Al$_2$O$_3$ ball, the wear tracks left on CrN, C-I-2 and C-I-10 exhibited neither partial ring cracks nor delamination of the coating. The main wear mechanisms were found to be oxidational wear and mild abrasive wear.

Although the wear tests were carried out at room temperature, as discussed in Section 2.1.2.3, in case of dry sliding, the "hot-spot" temperature at the interacting asperities can easily reach 1000℃ . The high instant temperature may lead to the formation of oxide scales at the tip of the interacting asperities, which eventually break up from the contacting surfaces after reaching a critical thickness to form wear debris (see black spots Figure 4.4.1-2a), thus leads to material removal. It is obvious that in oxidational wear mode, the oxidation resistance of the coating is of vital importance.

As aforementioned, mild abrasion also took place during the sliding of the coatings against the counterpart balls. It has been widely accepted that high H/E^*, H^3/E^{*2} ratios have been proved to be reliable indicators for good wear resistance [202]. Eq. 2.1.2-3, which was proposed by Evans and Marshall [33] to predict the volume loss through abrasion wear, suggests that toughness also plays an important role in abrasion wear for relatively brittle materials. Musil [124] proposed that a ratio between the hardness and the reduced modulus (H/E^*) ≥ 0.1 indicates enhanced toughness and subsequently good wear resistance.

The H/E^* ratio of all deposited coatings are calculated and plotted in Figure 5.3.1- 2, from which it can be seen that all multi-component coatings possess H/E^* higher than 0.1, while the H/E^* ratio for CrN is 0.078, well below 0.1. The H/E^* ratio shows a strong correlation with the surface hardness, where the highest value was found for C-

II and T-II coatings, and for C-I type coatings, the value increases with increasing sample rotation speed.

The wear resistance of CrN, C-I-2 and C-I-10 depends on the combination of their oxidation resistance and H/ E*. As depicted in Figure 4.5.1- 1 and Figure 5.3.1- 2, C-I-10 shows the highest oxidation resistance and H/E*, while both C-I-10 and C-I-2 show significant improvement in both factors over CrN. This is in good agreement with the volume wear loss against both WC-Co ball and Al_2O_3 ball (Figure 4.4.1- 8).

Effect of Counterpart Ball

Figure 4.4.1- 8 summaries the wear volume loss of all tested coatings sliding against WC-Co ball and Al_2O_3 ball. It can be seen that more wear occurred to the coatings sliding against the Al_2O_3 ball than against the WC-Co ball. For example, the area loss of C-I-10 coating increased from about 0.25×10^8 nm^2 for sliding against a WC-Co ball to 2.5×10^8 nm^2 for sliding against an Al_2O_3 ball. Clearly, the counterpart ball has played an important role in determining the wear of CrAlSiN coatings.

There are two possible reasons for this observation: 1: In abrasive wear mode, the relative wear is correlated with the relationship between the hardness of the abrasive (Ha) and that of the coating (Hc). In case that Ha < K x Hc, where K = 0.7- 1, no wear will occur to the coating [203]. The hardness values of the WC-Co and Al_2O_3 balls are provided by the supplier to be Hv 1700 (~16.67 GPa) and Hv 1420 (~13.93 GPa), respectively. Considering the ball as the abrasive, then for CrN coating, Ha/Hc is calculated to be 0.83 and 0.69 for the WC-Co and Al_2O_3 ball, respectively. While for the high hardness C-I-10, the ratio is reduced to 0.58 and 0.48, respectively. This indicates that when sliding against the Al_2O_3 ball, abrasion wear does not contribute significantly to the material removal of the coating, while when sliding against WC-

Co ball, it is likely that abrasion wear does not occur to the coatings. This is supported by the shallower and smoother wear track of C-I-10 against WC-Co ball than against Al_2O_3 ball (see Figure 4.4.1- 3c and Figure 4.4.1- 6c). 2: The coefficient of friction generally is higher when a coating slides against Al_2O_3 ball than sliding against WC-Co ball, indicating higher "hot-spot" temperature due to the release of energy as heat. This suggests that the oxidation may be more severe when sliding against Al_2O_3 ball than sliding against WC-Co ball.

Effect of Duplex Treatment

The benefit effect of duplex treatment on the wear properties of hard CrAlSiN coatings can be demonstrated by comparing the wear of single CrAlSiN coated C-I-8 sample with duplex treated (CrAlSiN on plasma hardened substrate) C-I-8-PN sample. From Figure 4.4.1- 8 it can be seen that the duplex treatment can dramatically improve the wear resistance of the corresponding coatings sliding against both Al_2O_3 and WC-Co balls.

This effectively improved wear resistance by duplex treatment could be attributed to the enhanced surface damage resistance, which is supported by the scratch test results as summarised in (Table 4.3- 1).   It can be seen that the critical load Lc_1 increased from 22.1 N for single CrAlSiN coated C-I-8 surface to 40.3 N for duplex treated C-I-8-PN surface.

It is known that the load bearing capacity of a hard coating on relatively softer substrate can be very low due to the so-called "thin ice effect", which describes the phenomenon that under applied load, the soft substrate deforms plastically, leading to the premature failure of the hard and rigid thin coating. Duplex treatment was proposed by Bell et. al [170] in late 1990s to reduce the thin ice effect by producing a

deep hardened layer through surface modification. In the present work, an optimal active screen plasma nitriding (ASPN) process was selected to produce a relatively thick hardened layer (39 μm) with gradually changing hardness along the distance from the surface (Figure 4.1.2- 7). The increased substrate hardness can mitigate against plastic deformation and hence produce a mechanical support for the thin coating. This is supported by comparing the morphology of the scratch tracks of C-II and C-II-PN (Figure 4.3.2- 3b&c). It can be seen that the formation of the first spallation site is postponed for the duplex treated C-II-PN; while the C-II coating was completely removed at the applied load of 87.5 N, the duplex treated C-II-PN remained coating integrity up to 100 N.

5.3.2 Reciprocating Sliding Wear Test at High Temperature

Comparing the high temperature wear behaviour of the coatings (Figure 4.5.3- 2) with the room temperature wear behaviour (Figure 4.4.1- 8), two major differences can be observed: (1) The C-II and C-I-8 coatings, which exhibited extremely high wear loss at room temperature, showed small wear factors at high temperature which are comparable to those of C-I-2 and C-I-10; (2) The T-II and CrN coatings, which showed slightly higher volume loss than that of C-I-2 and C-I-10 at room temperature, exhibited wear factors more than 50 times larger than that of the C-I-2 and C-I-10 coatings.

Effect of High Temperature on the Wear Behaviour of C-II and C-I-8 Coatings

As shown in Figure 4.5.3- 2, the wear factor of C-II and C-I-8 at 400 and 500°C is comparable to that of C-I-2 and C-I-10 although the former showed much high wear than the latter when tested at room temperature. This change of wear behaviour could

be attributed to the low friction coefficient and low applied load for high temperature wear tests.

As discussed in Section 5.3.1, the main failure mode during room temperature wear test for these two coatings was the premature coating delamination mainly due to the poor adhesion with substrate and high stress induced by a high applied normal load and high friction coefficient (>0.25).

For the high temperature wear tests, a low load of 5 N was selected based on the high temperature tribological studies on similar coatings [110, 204]. According to the Hertz contact theory, the low normal load will reduce the stress in the coating. More importantly, the friction coefficient of these coatings sliding against Al_2O_3 or WC-Co balls at high temperature has been found to be reduced due to the formation low friction oxide film. Therefore, the shear stress acting at the coating/substrate interface could be effectively reduced. As a result, the wear of the C-II and C-I-8 coatings was reduced due to the reduced normal and shear stresses in the coating and at the coating/substrate interface.

Effect of High Temperature on the Wear Behaviour of T-II and CrN Coatings

A comparison between the H/E* ratio of as deposited coatings and that of the coatings after oxidation at 900℃ is shown in Figure 5.3.2- 1, from which a drop in H/E* can be observed for all coatings, with T-II showing the most drastic drop. However, the high temperature wear behaviour of these coatings cannot be correlated with the H/E* ratio after oxidation. This can be attributed to the fact that at high temperatures, oxidation wear would replace abrasion wear as the main wear mode. This is partially due to the ease of the formation of oxide films during high temperature and partially due to oxidation of WC-Co surface [205], which subsequently leads to the reduced

hardness of the asperities of the WC-Co ball surface and in turn the reduced abrasive wear.

As discussed in Section 5.2.3, the oxidation resistance and thermal stability of the T-II and CrN coatings are much lower than that of the CrAlSiN coatings since Cr, Si and Al can form very dense and stable oxide films to retard high temperature oxidation. Therefore, it is reasonable to correlate the high temperature wear of coatings with their oxidation resistance. To this end, the wear factor of selected coatings at 400℃ and the surface oxygen content of corresponding coatings after oxidation at 900℃ are summarised and put into comparison in Figure 5.3.2- 2. It can be seen that the wear factor K can be directly correlated with the oxidation resistance. The CrN and TiAlSiN (T-II) coatings, which show low oxidation resistance, suffered from early failure during high temperature wear tests. In contrast, the CrAlSiN coatings, which showed high oxidation resistance, displayed the best wear resistance at elevated temperature under current test conditions.

5.3.3   Rolling-sliding Wear Mechanism

Rolling-sliding wear testing, as described in Section 3.5.3, is an effective method to evaluate the wear behaviour of gears and rollers where the loading under working conditions generally takes place as a combination of rolling and sliding. Hence, it is important to understand the wear behaviour of these new coatings developed from this research under combined rolling-sliding conditions.

As shown by the visual and SEM observation of coated wheels after 1 hour (Figure 4.4.2- 4a,c,e & Figure 4.4.2- 5a,b,c), CrN, C-II and C-I-10 coated wheel behaved in a similar manner at the initial stage of rolling-sliding wear test. The M2 wheels, which

worn against the coated wheels, were covered with a thick layer of iron oxide after one hour, which was formed due presumably to the high "hot spot" temperature at contacting asperities induced by the high speed rolling and sliding motion between the tribological pairs. Preferential material transfer from the M2 wheel to the coated wheel was evidenced by the appearance of iron and oxygen on the surface of the coated wheels, which was confirmed by EDS analysis.

The spallation sites observed on the coated wheel after one hour have similar morphology with the ones observed at later stages (Figure 4.4.2- 5d,e,f), i.e. iron oxides are often found near the edge of the spallation sites. This observation agrees with the wear mechanism proposed by Dong and Bell [206], where the continuous material transfer from the steel wheel to the surface engineered wheel (with ceramic surface) leads to the change of contact, from steel against ceramic to steel against steel. This will result in the increase of tangential force between the contacting asperities due to the higher metallurgical compatibility between steel and steel than that between steel and ceramic. The increasing tangential force, as well as the elastic energy stored in the transferred material (i.e. the agglomerates), which builds up gradually with increasing thickness, will eventually lead to the break-off of the agglomerates. The break-off site could be either the interface between the agglomerates and the coating, or the interface between the coating and the substrate.

Another mechanism was reported by Neubrand and Weiss [207] and Akazawa and Kato [208], stating that the transferred material were welded with the coating surface, and led to an increased contact stress due to reduced contact area, which subsequently led to the formation of microcracks and delamination of the coating. This mechanism

is supported by the netted cracks found near the spallation site of CrN (Figure 4.4.2-5d).

Thus, it is most probably that both mechanisms have contributed to the wear of the coated wheels during rolling-sliding wear test.

The sudden increase in the wear rate of C-II after one hour indicates a change in the wear mechanism. Severe delamination of the coating took place, which could be attributed to the poor adhesion between the C-II coating and the substrate as suggested by the low Lc_1 and Lc_2 value obtained from the scratch test (Table 4.3- 1). As described in Figure 2.1.2- 2, the maximum intensive shear stress was pushed towards the subsurface of the coating system by the rolling motion, which is believed to be responsible for accelerating the delamination of the C-II coating.

Comparing C-I-10 and CrN coated wheels, at any stage, C-I-10 coated wheel always showed the smaller and less spallation sites than the CrN coated wheel. This is probably mainly due to the relatively high toughness, i.e. the inhibition of crack propagation which can be credited to the nano-multilayer and nano-crystallite structure as discussed in Section 5.2. In addition, the higher oxidation resistance (Figure 4.5.1-2) and thermal stability (Figure 4.5.2-1) of C-I-10 than CrN may have also contributed to the better sliding-rolling wear resistance of C-I-10 over CrN coating.

Chapter 6   Summary and Conclusions

The evidence produced throughout this project and the discussion presented in the last chapter can be summarised as follows:

Design and synthesis of new surface systems

1) A series of new multi-components and nano multi-layer coatings have been designed and successfully synthesised using a cathodic arc evaporation PVD equipment with pure Cr or Ti targets and powder metallurgy AlSi targets to investigate the effect of chemical composition, sample rotation speed and target arrangement on the microstructure and properties of the coatings.

2) An optimal active screen plasma nitriding process (ASPN-450-2.5) has been developed and used as the first step of novel duplex treatment, which shows high surface hardness, good load bearing capacity and moderate hardened case thickness. A novel duplex surface system has been developed by combining active screen plasma nitrided M2 with nano multi-layer CrAlSiN surface coatings.

3) Properties required for optimal tribological performance of nano-multilayer coatings have been established: high hardness, high toughness, strong bonding with the substrate, good oxidation resistance and blurred interfaces between nano-layers.

Microstructure of the Coating Systems

4) All multi-component coatings possess a nano-multilayer structure due to the rotation of the substrate during the deposition process, and the bilayer thickness decreases with increasing sample rotation speed. Coatings deposited employing the

Mode II target arrangement show a relatively uniform composition profile and blurred interfaces between individual nano-layers in comparison to those deposited using the Mode I target arrangement.

5) The binary CrN coating shows a typical columnar structure and introducing Al and Si using Mode II target arrangement can lead to the coarsening of the columnar structure. The coatings synthesised using Mode I target arrangement all have nano-crystallites, the size of which is confined by the individual nano-layers.

6) An CrN-like fcc-(Cr,Al,Si)N phase has been identified for all the CrAlSiN coatings developed from this research. While the C-II coating deposited using Mode II target arrangement exhibits only this fcc-MeN phase, all C-I type coatings deposited using Mode I target arrangement are composed of both an fcc-MeN phase and an AlN-like hcp phase.

7) For C-I type coatings, the preferred orientation of the fcc-MeN phase changes from (200) to (111) with increasing sample rotation speed, mainly due to the high strain energy induced by large number of interfaces.

8) The nitrided substrate of the duplex system has no significant influence on the microstructure of the surface coating.

Mechanical Properties of the Coating Systems

9) All multi-component TiAlSiN and CrAlSiN coatings exhibit a higher hardness than the binary CrN coatings, due to solid solution hardening and microstructure modification.

10) Among all the CrAlSiN coatings deposited, the C-II coating possess the highest hardness due to the lack of the soft hcp-MeN phase. In general, the hardness of the C-I coatings increases with increasing the sample rotation speed during the deposition process.

11) The C-I coatings show a better toughness than the C-II coatings, most probably due to the increased interfaces and complicated grain boundaries, which prolongs the crack propagation path within the coatings.

12) The adhesion between the coating and the substrate is dependent on a large number of variables. Under current test condition, C-I-5 and C-I-8 coatings suffered from gross spallation during scratch, whereas no gross spallation was observed for all other coatings under the normal load up to 100 N.

13) The load bearing capacity of nano-multilayer CrAlSiN coating can be effectively increased by hardening the M2 substrate using active-screen plasma nitriding i.e. duplex treatment.

Tribological Properties of Coating Systems

14) The nano-multilayer C-I-10 CrAlSiN, which is deposited using the Mode I target arrangement with the highest target rotation speed of 10rpm, possess the highest wear resistance when reciprocating against WC-Co and Al_2O_3 balls at room temperature under unlubricated (dry) conditions. This could be attributed to its nano-multilayer structure induced high H/E ratio, high toughness and good oxidation resistance.

15) Active-screen plasma nitriding of M2 substrate prior PVD coating (i.e. duplex treatment) can improve the wear resistance of nano-multilayer coating during the

reciprocating sliding wear test by two orders of magnitude due to improved load bearing capacity of the coating system.

16) Compared with the benchmark monolayer binary CrN coating, the new multi-component, nano-multilayer CrAlSiN coating possess a much better resistance to rolling-sliding wear mainly due to the improved toughness and oxidation resistance by the nano-multilayer structure and addition of Al and Si.

High Temperature Performances

17) The main contribution to the oxidation resistance of coatings is their chemical composition. By introducing Al and Si, which retards the diffusion of oxygen into the coating and form dense oxide films, all the CrAlSiN coatings show much better oxidation resistance over CrN coating.

18) The oxidation resistance of TiAlSiN (T-II) coating is not as good as C-II. This is partially due to the stronger affinity of Ti to O than that of Cr to O and partially due to the poorer integrity of titanium oxide film than chromium oxide film.

19) Sliding wear at high temperature of the coatings is dominated by the oxidation resistance of the coating, and hence all CrAlSiN coatings, independent of the microstructure, show better wear resistance than the CrN and T-II coatings.

Chapter 7   Proposals for Future Work

It has been established from this study that in terms of oxidation resistance and wear behaviour at both room temperature and elevated temperatures, CrN-based nano-multilayer coatings perform much better than TiN-based nano-multilayer coatings. To lead to a better understanding of the superiority of CrN-based coatings, it is suggested that wear test could be carried out with an expanded temperature range in future.

In this study, the effect of sample rotation speed on C-I mode coatings was investigated. However, the C-II coating happened to show poor adhesion with the substrate, which makes it impossible to conclude on the comparison of the wear behaviour of both type of coatings. It is suggested that the C-II coating should be deposited with different sample rotation speed to make a systematic study on the effect of target arrangement on the properties of the coatings.

Chapter 8   Appendix

8.1   List of Tables and Figures

8.2   Tables

Table 2.1- 1 Temperature ranges of tool material oxidation and structural change

Tool material	Oxidation	Structural change (and nature of change)
		Temperature range (°C) for:
High speed steel	–	> 600 (over-tempering)
WC-Co carbide	> 500	> 900–950 (solution of WC in Co)
Mixed carbides/cermets	> 700	–
Ceramics	–	> 1350–1500* (intergranular liquids)
PcBN	–	> 1100–1350 (change to hexagonal form)
PCD	> 900	> 700 (change to graphite)

*: very composition dependent – these temperatures indicate what is achievable.

Table 3.1- 1 Chemical composition (wt%) of M2 HSS

Element	C	Mn	Si	Cr	Ni	Mo	W	V
wt%	0.78-0.88	0.15-0.4	0.2-0.45	3.75-4.5	0.3 max	4.5-5.5	5.5-6.75	1.75-2.2

Table 3.2- 1 ASPN nitriding conditions and corresponding specimen code

Sample code	Temperature (°C)	Time (h)
M2-unt	N/A	N/A
ASPN 400-0.5		0.5
ASPN 400-1	400	1.0
ASPN 400-2.5		2.5
ASPN 450-0.5		0.5
ASPN 450-1	450	1.0
ASPN 450-2.5		2.5
ASPN 475-0.5		0.5
ASPN 475-1	475	1.0
ASPN 475-2.5		2.5
ASPN 500-0.5		0.5
ASPN 500-1	500	1.0
ASPN 500-2.5		2.5
ASPN 525-0.5		0.5
ASPN 525-1	525	1.0
ASPN 525-2.5		2.5

Table 3.2- 2 Sample code and corresponding deposition parameters

Sample code	Sample rotation speed	Substrate	Construction of targets	Current of Cr	Current of Ti	Current of AlSi
CrN	5 rpm	M2	I with only 3 Cr targets	70		
C-I-2	2 rpm	M2	I	70		40
C-I-5	5 rpm	M2	I	70		40
C-I-8	8 rpm	M2	I	70		40
C-I-10	10 rpm	M2	I	70		40
C-II	5 rpm	M2	II	70		40
T-II	5 rpm	M2	II		70	40
C-I-2-PN	5 rpm	ASPN M2	I	70		40
C-I-8-PN	5 rpm	ASPN M2	I	70		40
C-II-PN	5 rpm	ASPN M2	II	70		40

Table 3.4- 1 Technical specifications of nano-impact test

Applied Load (mN)	Impact Frequency (Hz)	Test time (s)	Impact number	Initial distance (nm)	Repetition per sample
1,5,10	0.25	300	75	12000	20

Table 3.5- 1 Technical specifications of high temperature wear test

Sample	Counter part	Load (N)	Stroke length (mm)	Frequency (Hz)	No. of cycles
CrN, T-II	WC-Co ball Φ=10 mm	5	1.5	17	1000/5000
C-II, C-I	WC-Co ball Φ=10 mm	5	1.5	17	20 000

Table 4.1- 1 Thickness of nitrogen diffusion zone of ASPNed samples

Sample	Thickness (µm)	Sample	Thickness (µm)
ASPN 400-0.5	9	**ASPN 475-2.5**	52
ASPN 400-1	11	**ASPN 500-0.5**	25
ASPN 400-2.5	14	**ASPN 500-1**	34
ASPN 450-0.5	17	**ASPN 500-2.5**	54
ASPN 450-1	24	**ASPN 525-0.5**	33
ASPN 450-2.5	39	**ASPN 525-1**	51
ASPN 475-0.5	19	**ASPN 525-2.5**	71
ASPN 475-1	29		

Table 4.2- 1 Elemental composition of all coatings obtained from GDS analysis

Sample	Composition (at%)			
	Cr	Al	Si	N
C-I-2	33.38186	12.42720	4.450915	49.74002
C-I-5	31.89727	12.90389	4.567109	50.63173
C-I-8	31.92645	12.37986	4.429586	51.26410
C-I-10	32.07094	11.95618	4.319249	51.65363
C-II	30.22617	12.67174	4.438808	52.66328

Table 4.2- 2 Theoretical value of lattice parameters for fcc-CrN and hcp-AlN, and corresponding parameters calculated for fcc-MeN and hcp-MeN from the SAD patterns

	FCC-MeN	HCP-MeN	
	a (nm)	a,b (nm)	c (nm)
CrN	0.4149		
AlN		0.3110	0.4980
C-II	0.4126	N/A	N/A
C-I-5	0.4120	0.3112	0.5039
C-I-10	0.4115	0.3121	0.5080

Table 4.3- 1 First and second critical load of all coating systems in scratch test

Sample	Lc_1 (N)	Lc_2 (N)
CrN	67.7	
C-II	14.7	87.5
T-II	34.0	
C-I-2	16.7	
C-I-5	21.4	88.0
C-I-8	22.1	93.4
C-I-10	35.1	
C-II-PN	20.6	
C-I-2-PN	24.8	
C-I-8-PN	40.3	

Table 4.4- 1 The coefficient of friction of coatings sliding against WC-Co and Al_2O_3 balls

Sample	WC-Co	Al_2O_3
CrN	0.25	0.31
C-II	0.34	0.40
T-II	0.30	
C-I-2	0.27	0.34
C-I-8	0.41	0.50
C-I-8-PN	0.41	0.50
C-I-10	0.47	0.55

Table 4.5- 1 EDS analysis showing the atomic percentage of major elements in the centre of the wear track after reciprocating sliding wear test at 400 °C

sample	Element (at%)						
	O	N	Fe	Cr	Ti	Al	W
CrN	14.10	29.23	0.22	49.74			1.91
T-II	17.36	7.14	31.63	2.20	19.21	12.04	2.56
C-I-2	3.85	38.5	0.45	33.11		17.01	0.26
C-I-5	43.40	0	44.69	4.05		0.67	2.45

Table 5.1- 1 Number of broken bond per surface atom (N$_{hkl}$), occupied surface area per surface atom (A$_{hkl}$) and number of broken bonds per unit area of a NaCl-type fcc crystal at different orientation

(hkl)	(111)	(200)	(220)
N$_{hkl}$	3	1	2
A$_{hkl}$	$\sqrt{3}a^2/4$	$a^2/4$	$\sqrt{2}a^2/4$
N$_{hkl}$ / A$_{hkl}$	$6.93/a^2$	$4/a^2$	$5.65/a^2$

Table 5.2- 1 K value of CrAlSiN system with different slip system and different preferred orientation of CrN phase

	K$_{[1]\,0>}$ GPa	K$_{0>}$ GPa
CrN$_{200}$	17.50	15.09
CrN$_{111}$	0	13.34

8.3 Figures
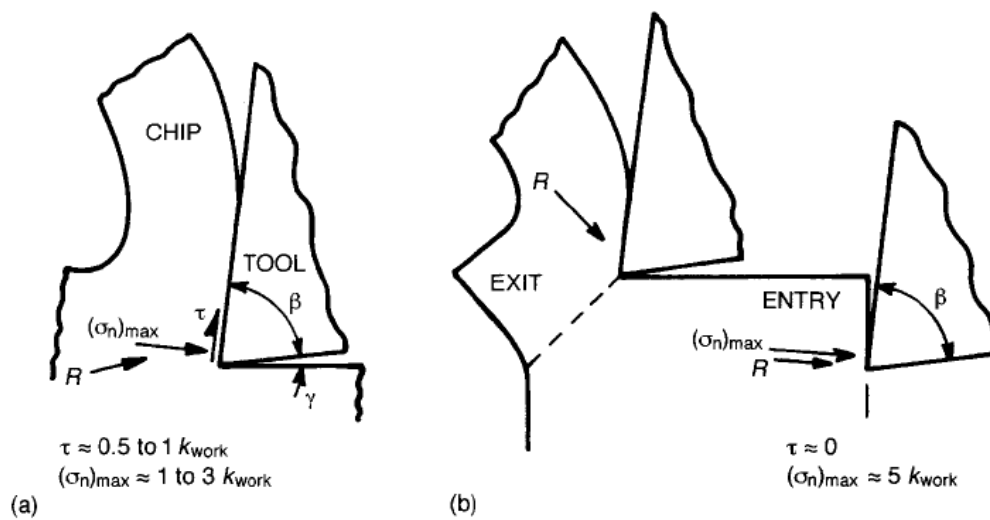
Figure 2.1.1- 1 Stress distribution at a tool rake in a) steady and b) work entry and exit conditions [11]
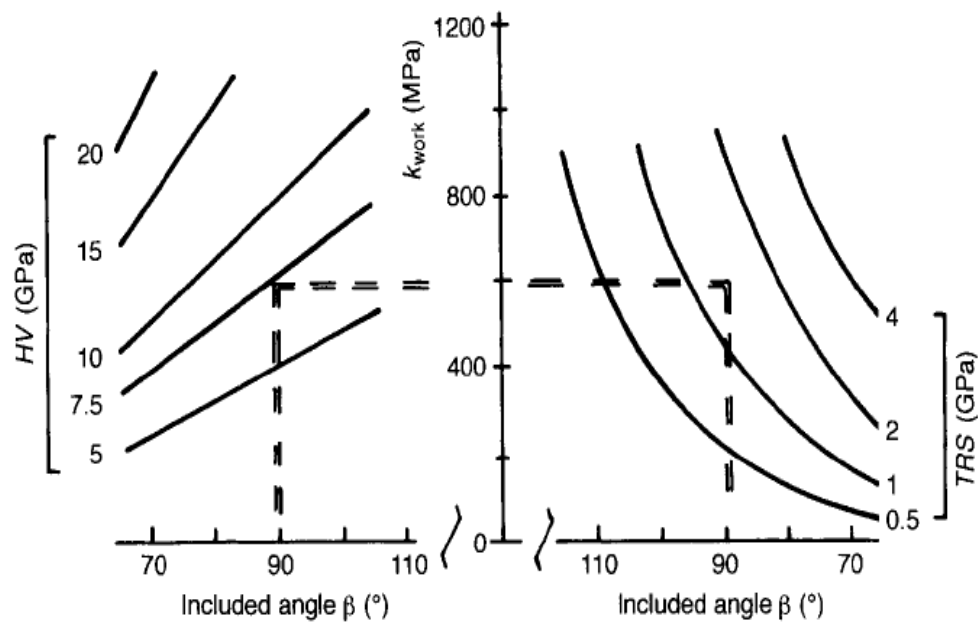
Figure 2.1.1- 2 Minimum hardness values (Hv) and tensile rupture strength (TRS) required for cutting tools, defined by the shear strength of the corresponding working material (kwork) and the included angle (β) of the tool rake [11]
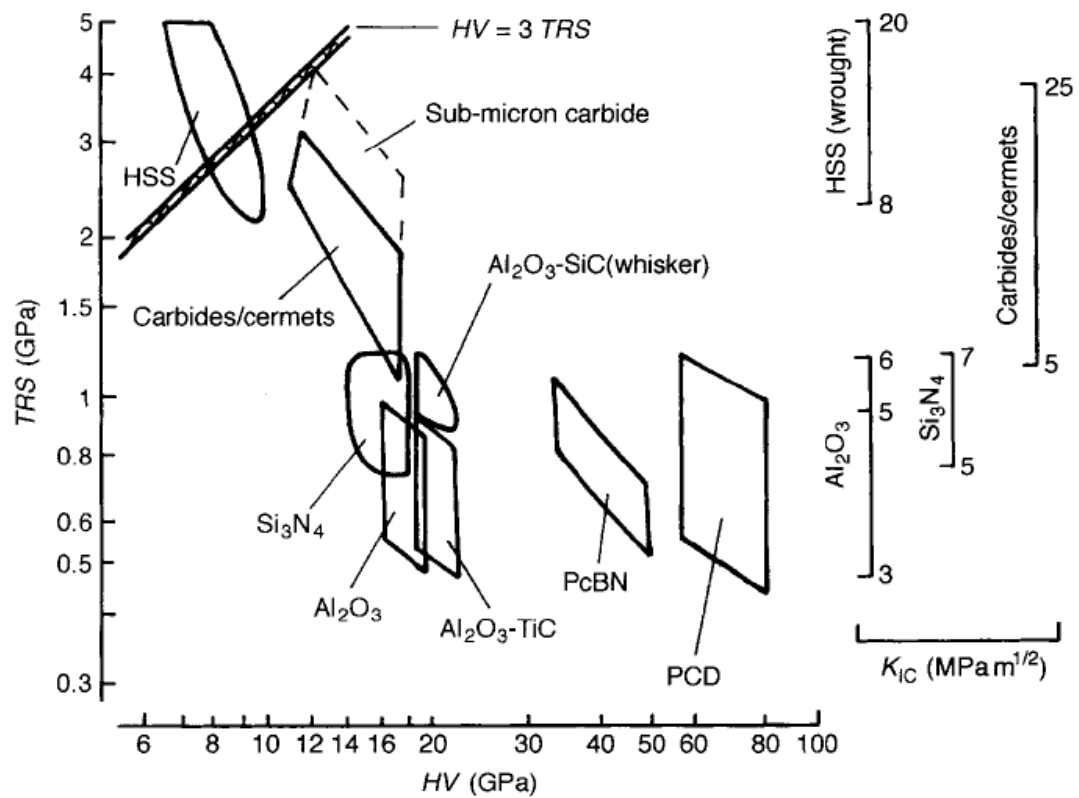
Figure 2.1.1- 3 Room temperature TRS and Hv ranges of commercial machining tool materials [11]
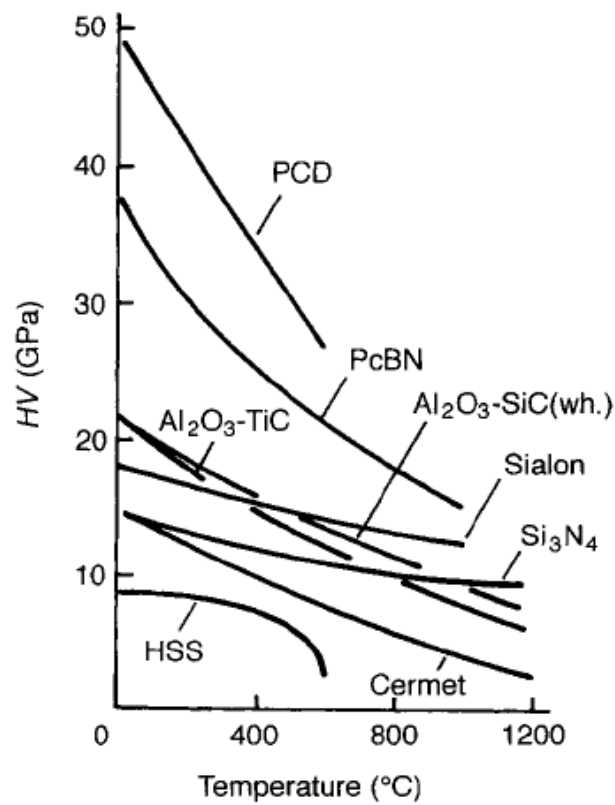
Figure 2.1.1- 4 Change of hardness with increasing temperature for tool materials [11]

132

Initial real contact area

Flattening of asperities and cold welding

Breaking of junction
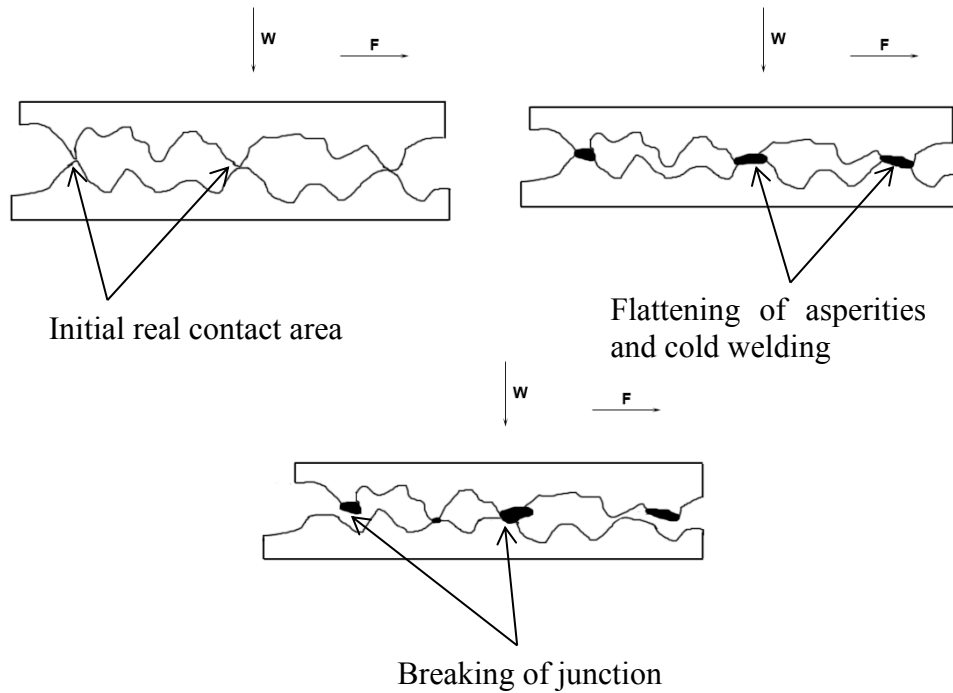
Figure 2.1.2- 1 Process of adhesion wear (F=tangential force)
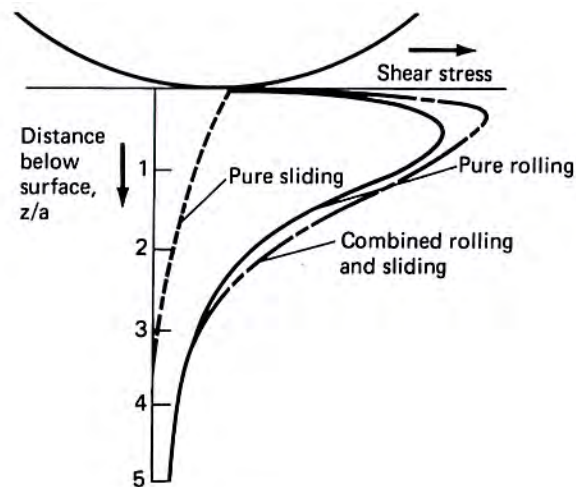
Figure 2.1.2- 2 Variation of principal shear stress at various depths directly below the point of contact of two hard surfaces in pure rolling, pure sliding and combined contact. The z is the distance below the surface in the vertical direction and a is half of the Hertzian diameter [19]
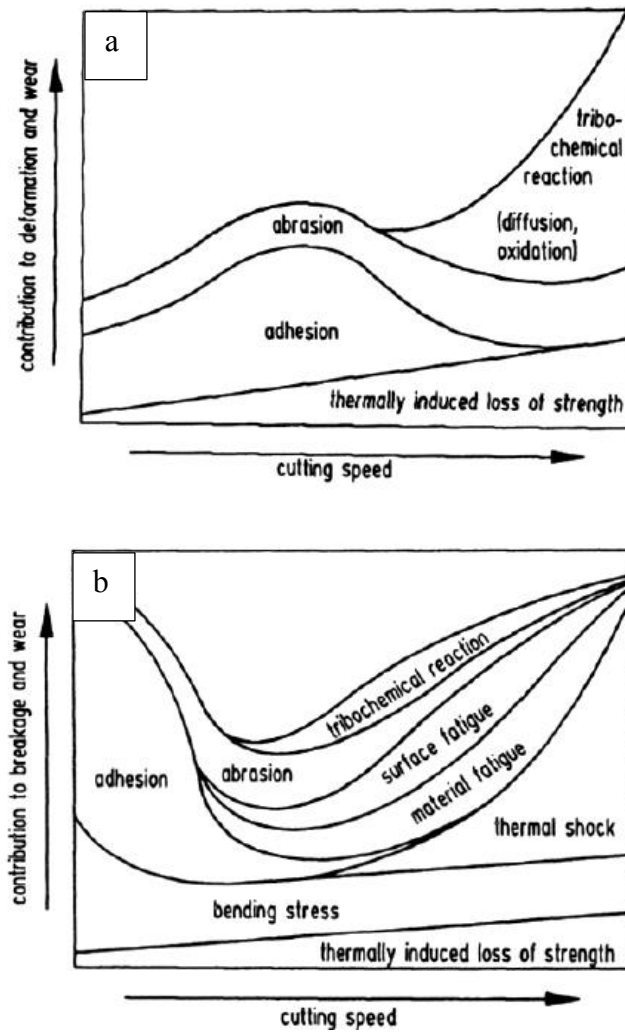
Figure 2.1.2- 3 Failure mechanisms in (a) continuous cutting and (b) interrupted cutting [13]
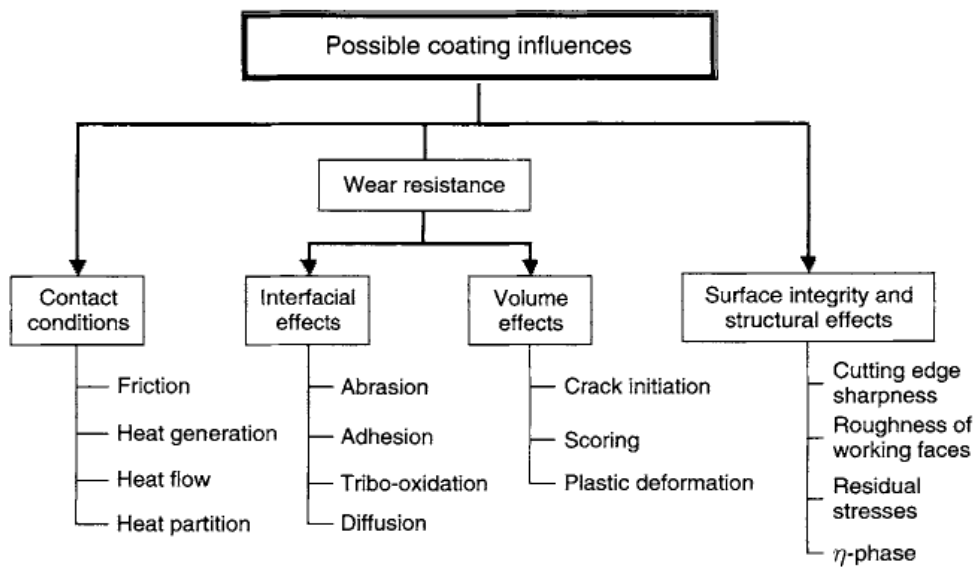
Figure 2.2- 1 The possible coating influences to performance of machining tools [47]

Figure 2.2.1- 1 Alloying elements of ternary Ti- and Cr-based nitride hard coatings [68]
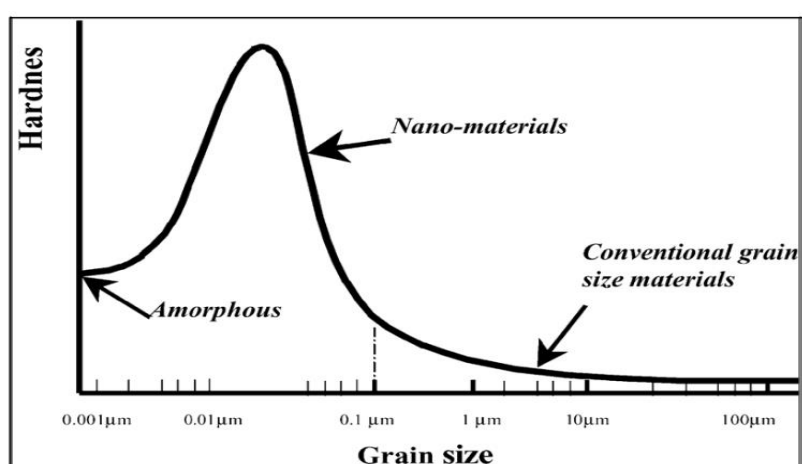
Figure 2.2.2- 1 Hardness of a material as a function of the grain size [210]
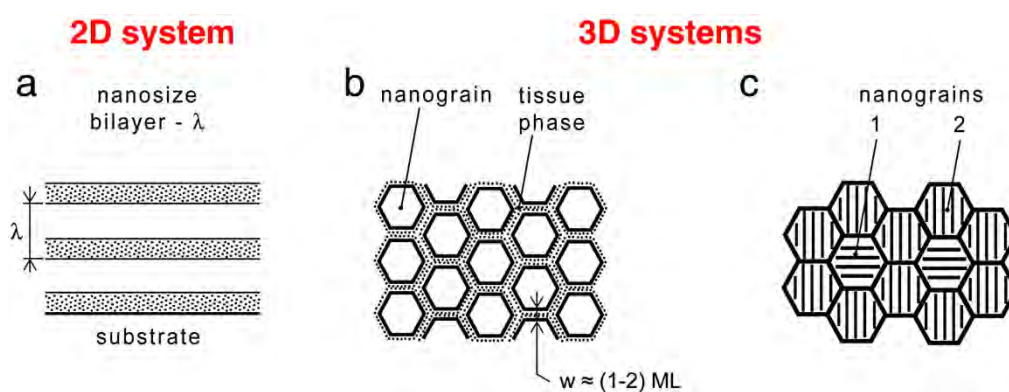
Figure 2.2.2- 2 Schematic illustration of 2D and 3D systems of nano-composite structures [125]
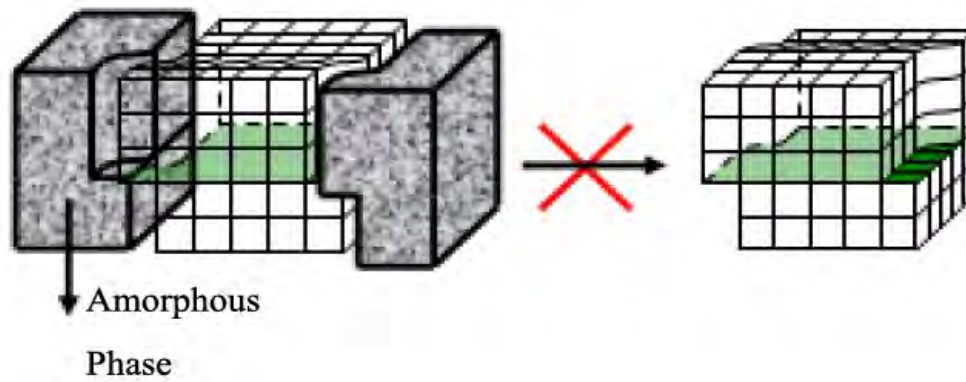
Figure 2.2.2- 3 Strengthening mechanism of amorphous phase in nano-composite materials [211]
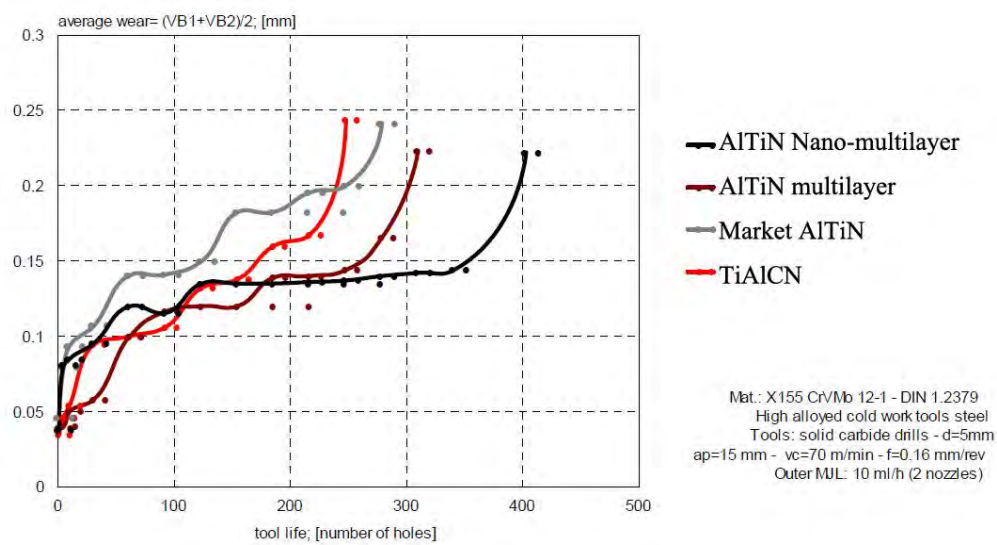
Figure 2.2.2- 4 Wear of AlTiN coatings with different structures [145]
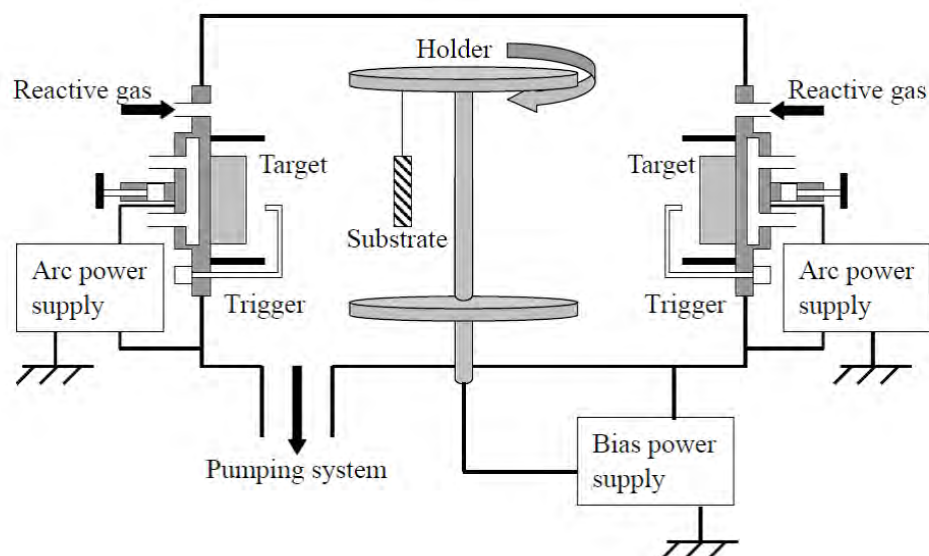
Figure 2.2.3- 1 Schematic of cathodic arc evaporation process [212]

136
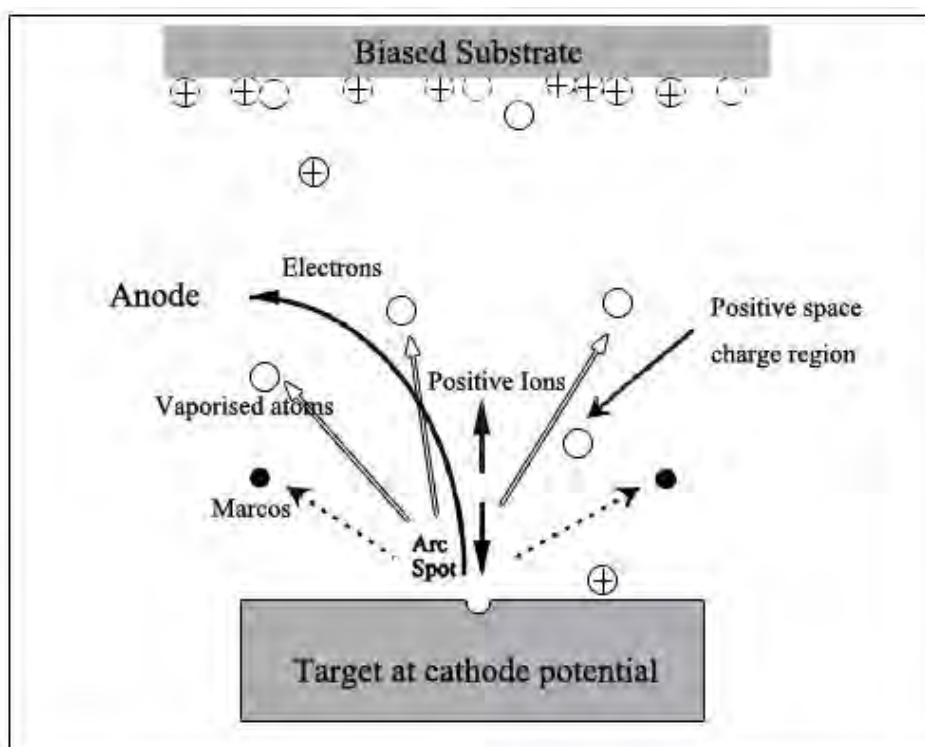
Figure 2.2.3- 2 Phenomena occurring at a cathodic arc spot
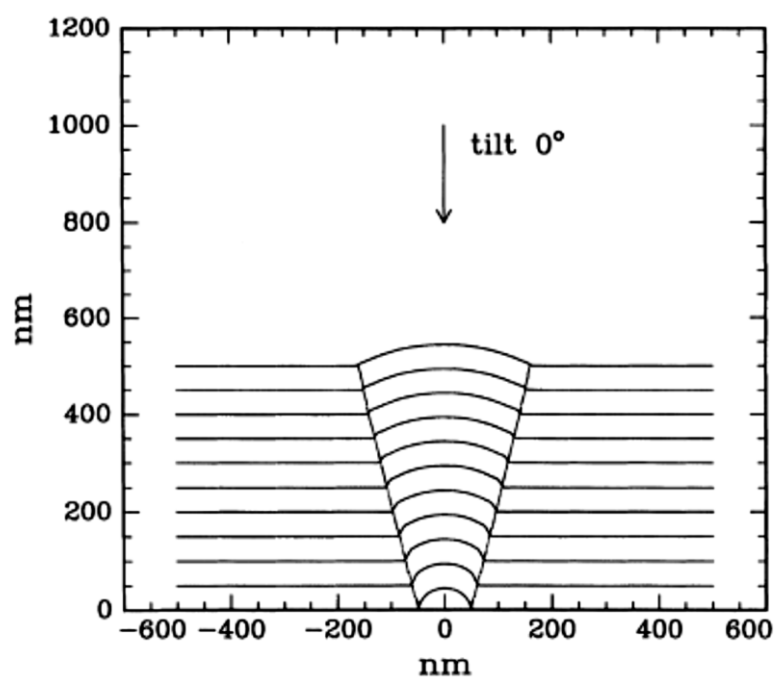
Figure 2.2.3- 3 Computer simulation of the proposed growth model at perpendicular ion incidence [213]
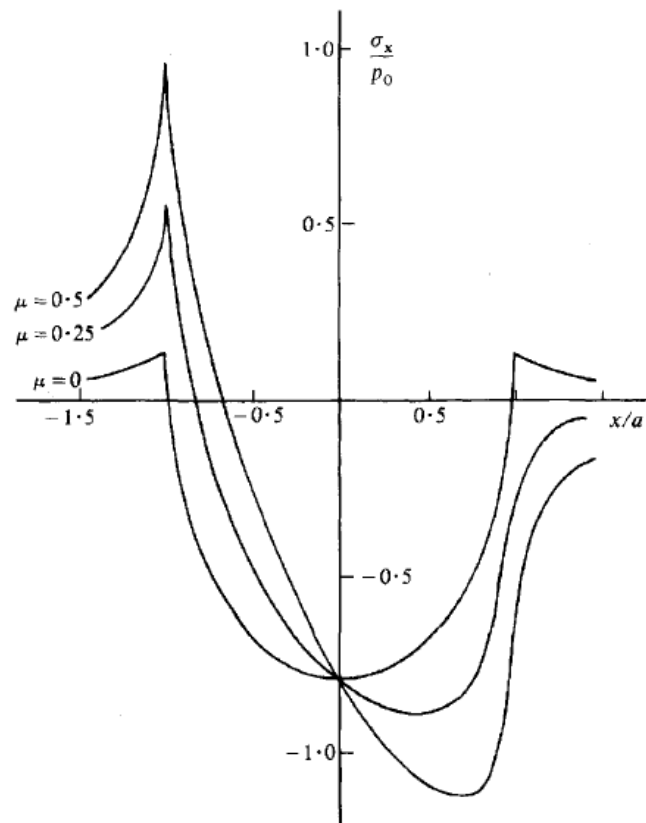
Figure 2.2.4- 1 The distribution of the stress σ_x in the surface of a semi-finite plane in contact with a spherical indenter of the radius a, for a range of coefficients of friction [151]
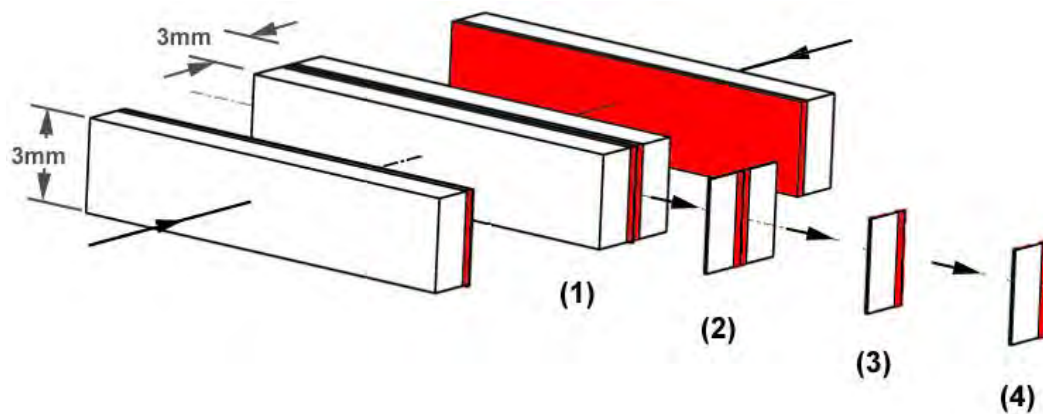
Figure 3.1.4- 1 Schematic of the steps involved in the preparation of a Cross-section TEM sample preparation
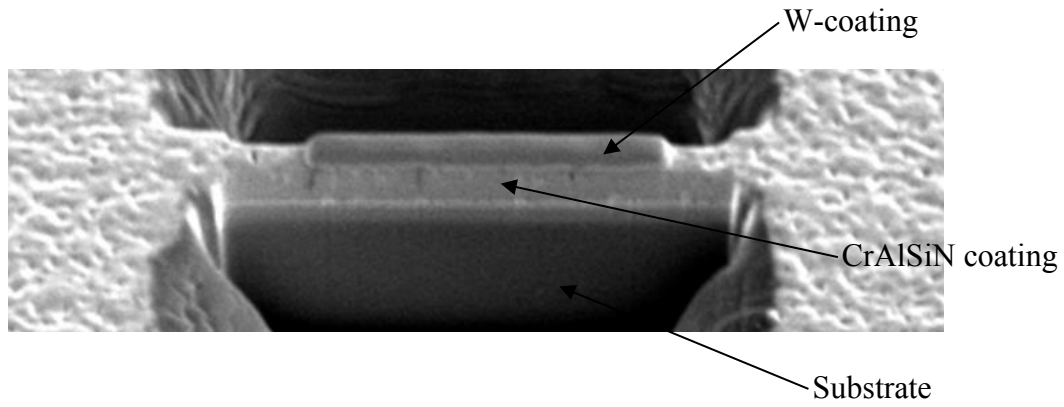
Figure 3.1.4- 2 Secondary electron image of FIB cross-section sample
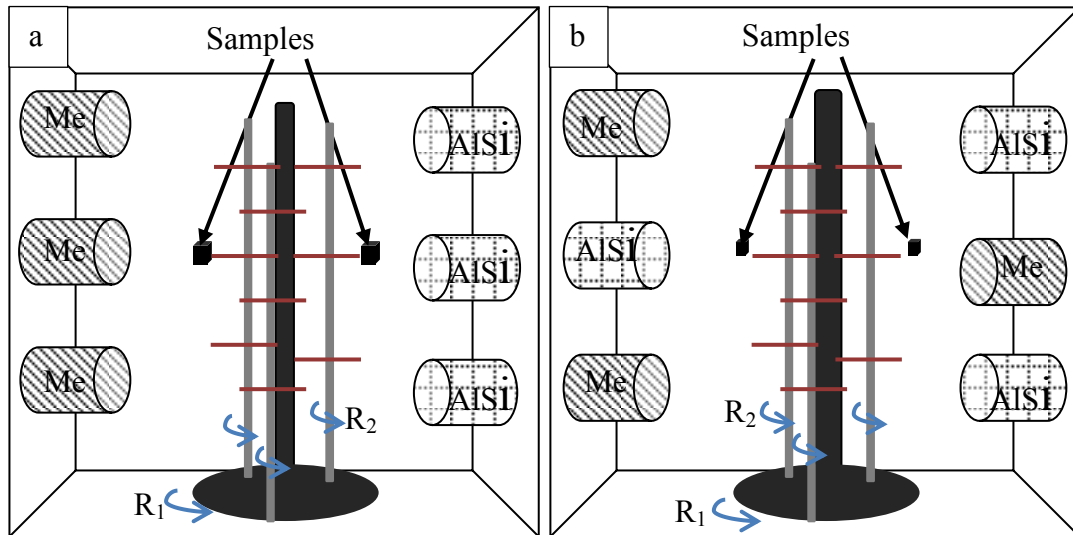
Figure 3.2.2- 1 Sketch of CAE furnace showing different arrangement of targets for the two types of multi-layer coatings, a) Mode I and b) Mode II, where Me=Cr or Ti
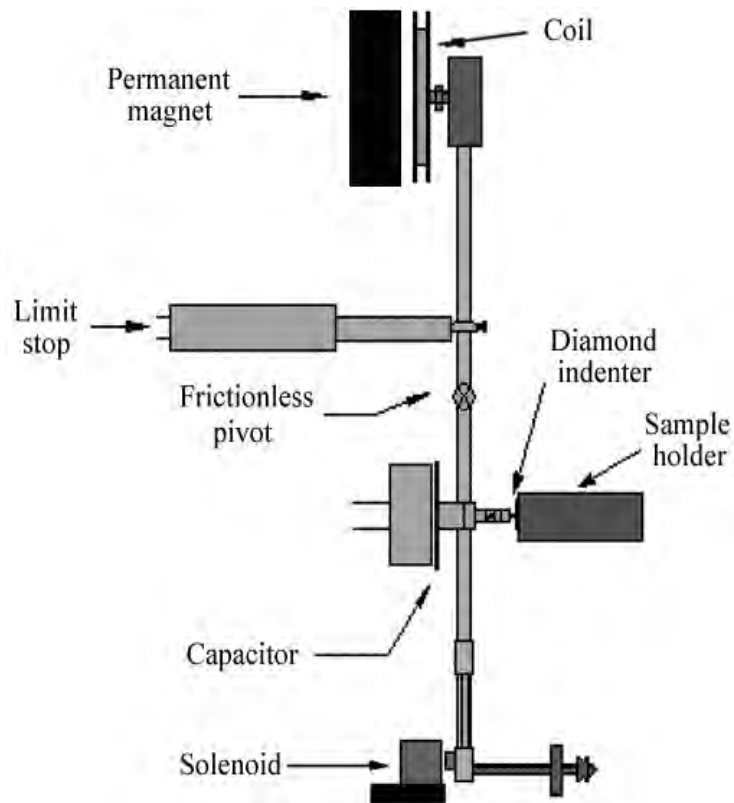
Figure 3.4.1- 1 Schematic illustration of NanoTest System used for nano-indentation and nano-impact tests
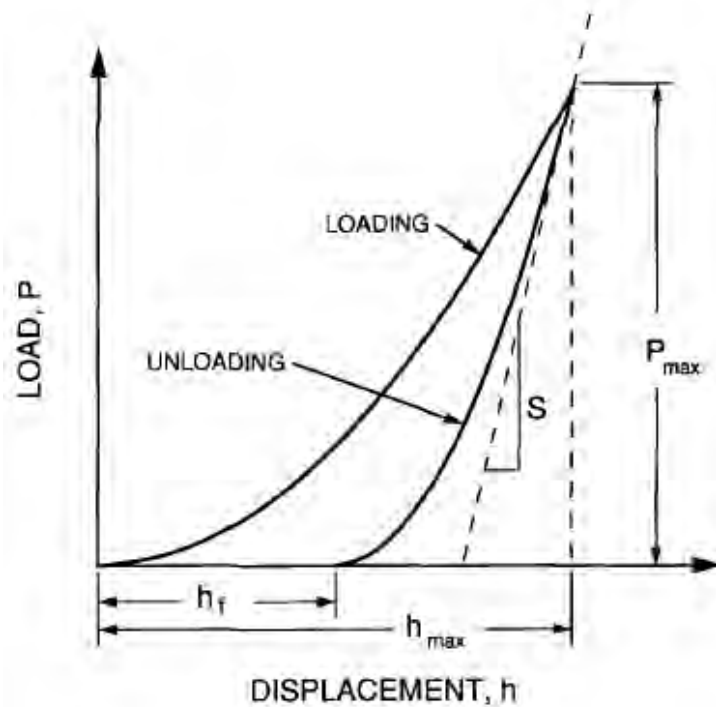
Figure 3.4.1- 2 Schematic illustration of a typical P-h curve of nano-indentation test, showing the quantities used in data analysis [16]

BERKOVICH TB	CUBE CORNER TC
a	a'
Berkovich: a = 65.03° Mod. Berkovich: a = 65.27° Available as **Traceable Standard**	Cube corner: a = 35.26° Available as **Traceable Standard**

Figure 3.4.1- 3 The schematic illustration of the geometry of Berkovich and cube corner indenter used by NanoTest System for nano-indentation test and nano-impact test, respectively
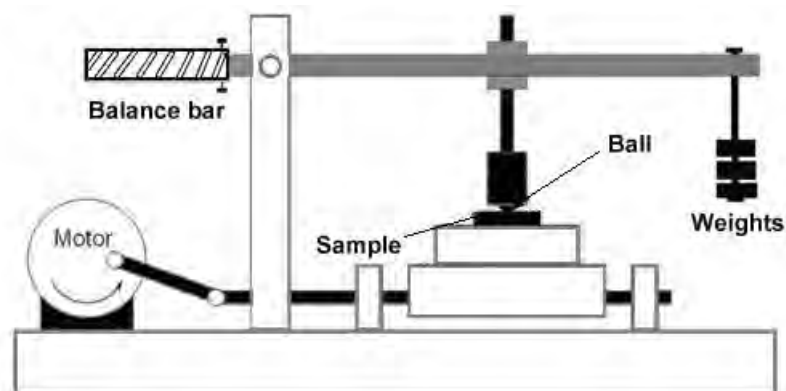
Figure 3.5.1- 1 Sketch of room temperature reciprocating sliding wear tester
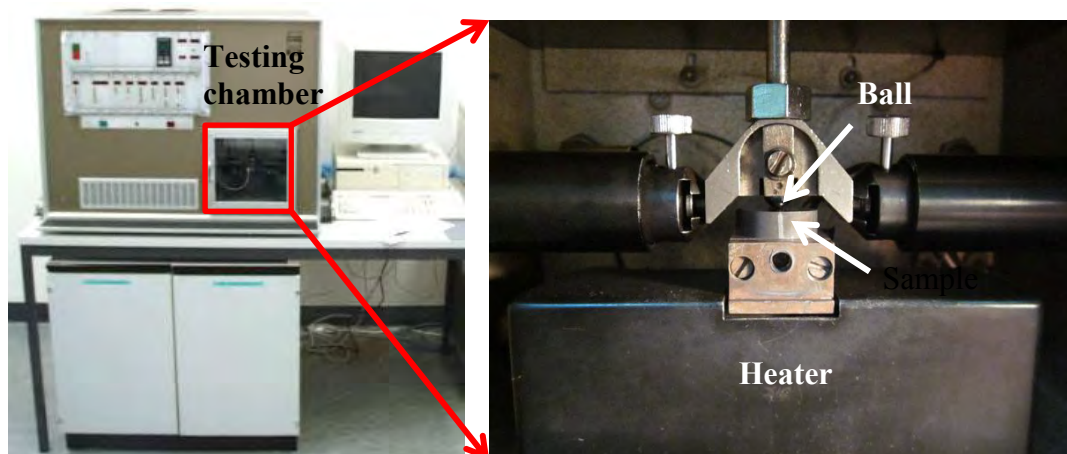
Figure 3.5.2- 1 SRV high temperature tibotester set-up
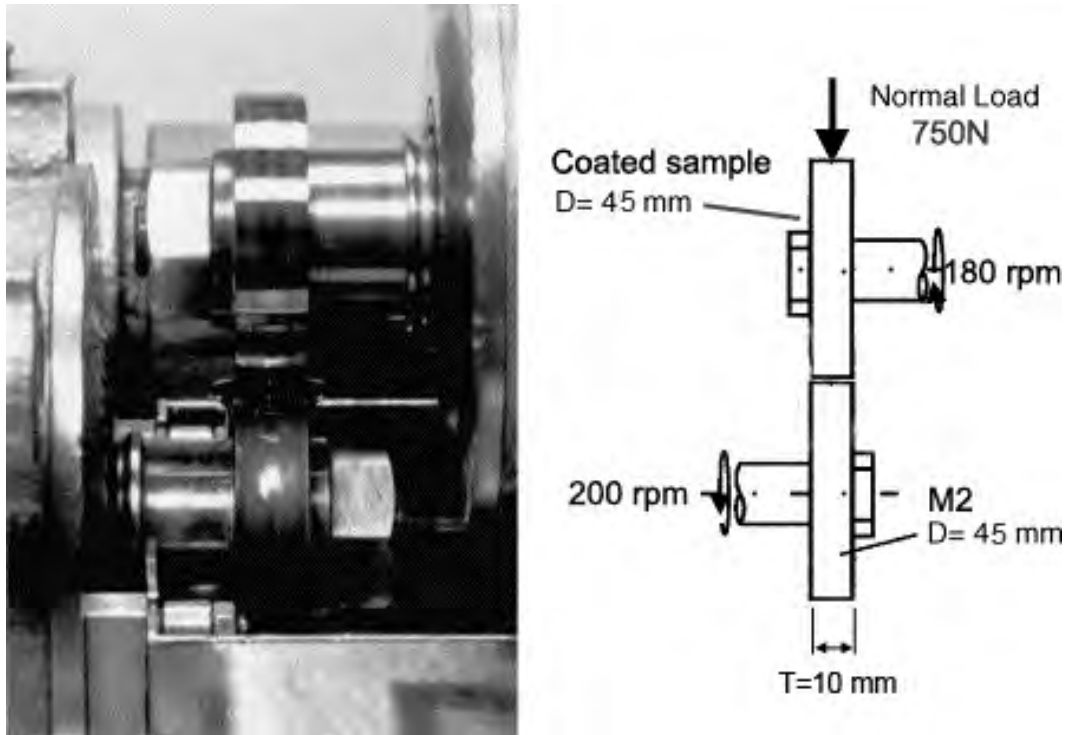
Figure 3.5.3- 1 Picture and sketch of the sample arrangement and dimension of an Amsler rolling-sliding wear tester with wheel-on-wheel configuration
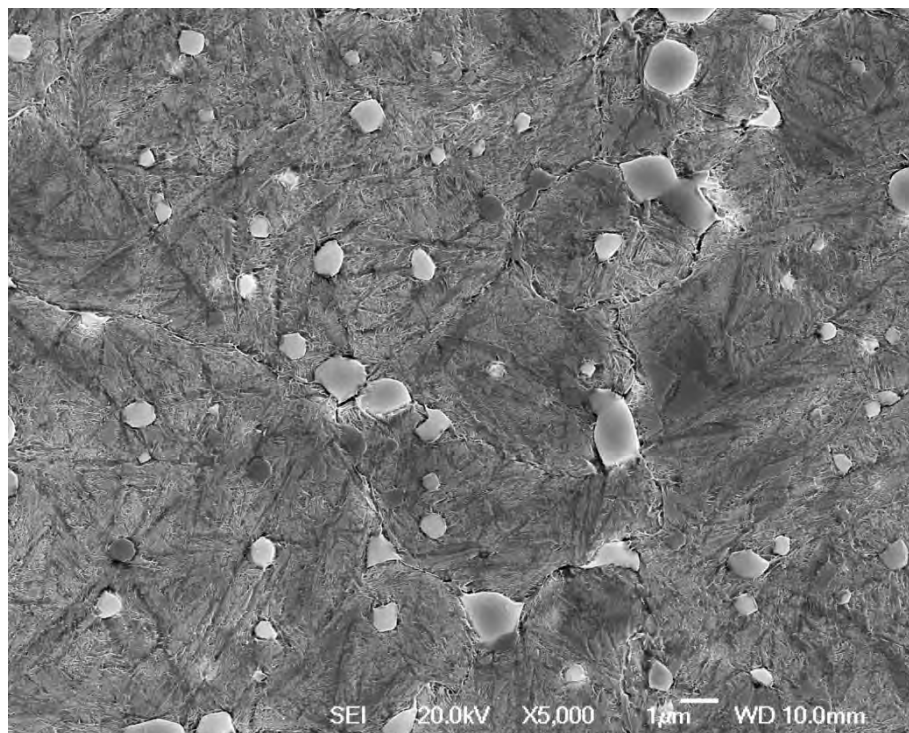
Figure 4.1.1- 1 SEM microstructure of M2-unt sample (2 % Nital etchant)
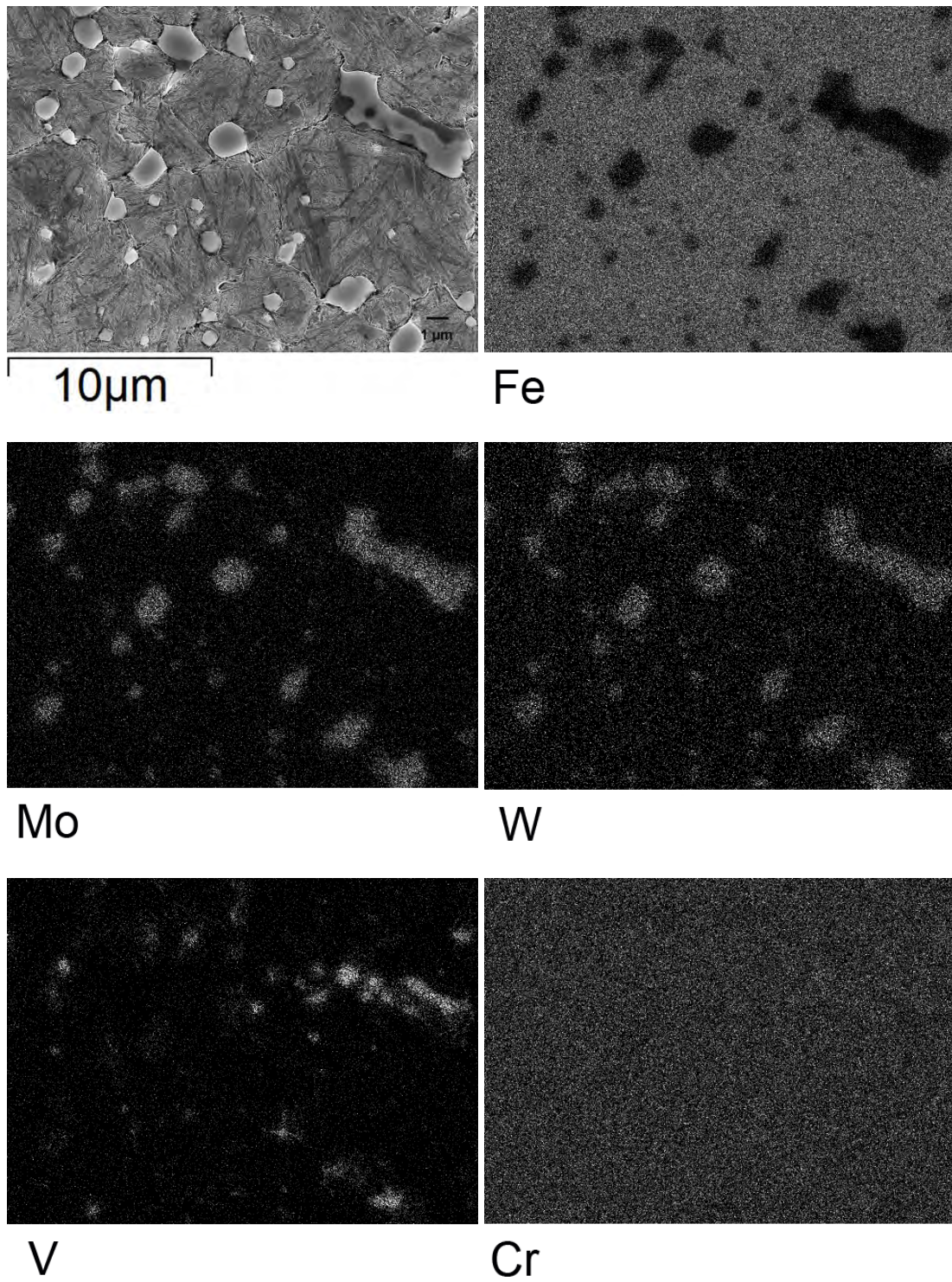
Figure 4.1.1- 2 EDS mapping showing the elemental distribution in M2-unt sample
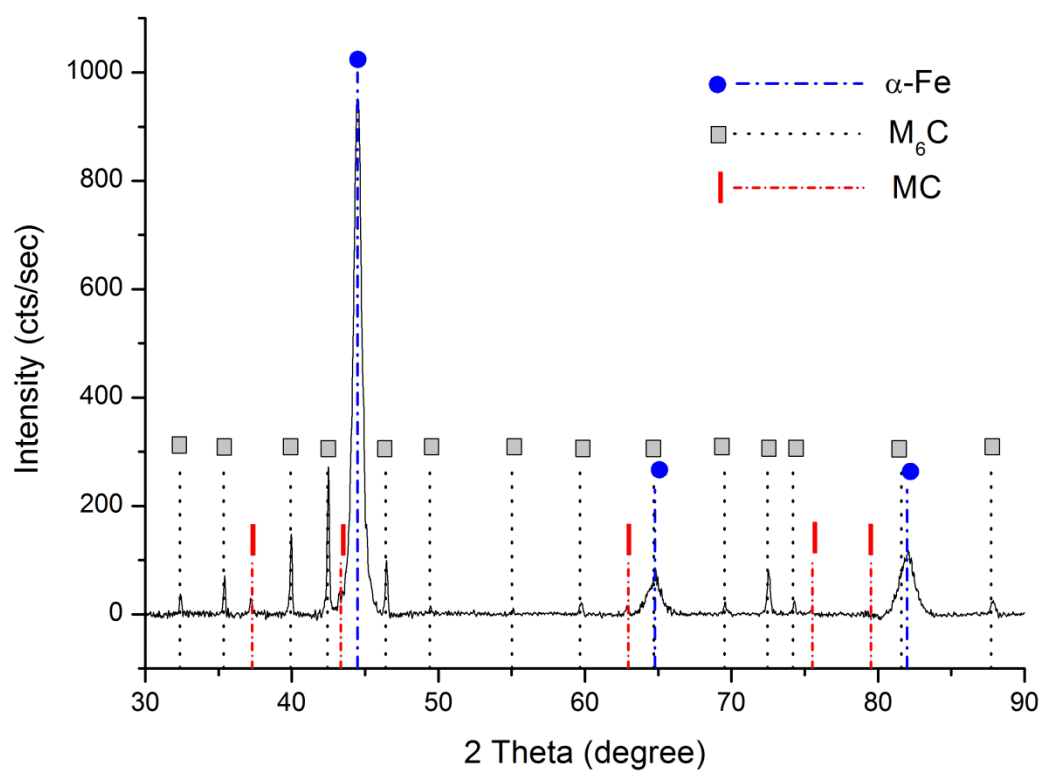
Figure 4.1.1- 3 XRD pattern of M2-unt inserted with peaks of indexed phases
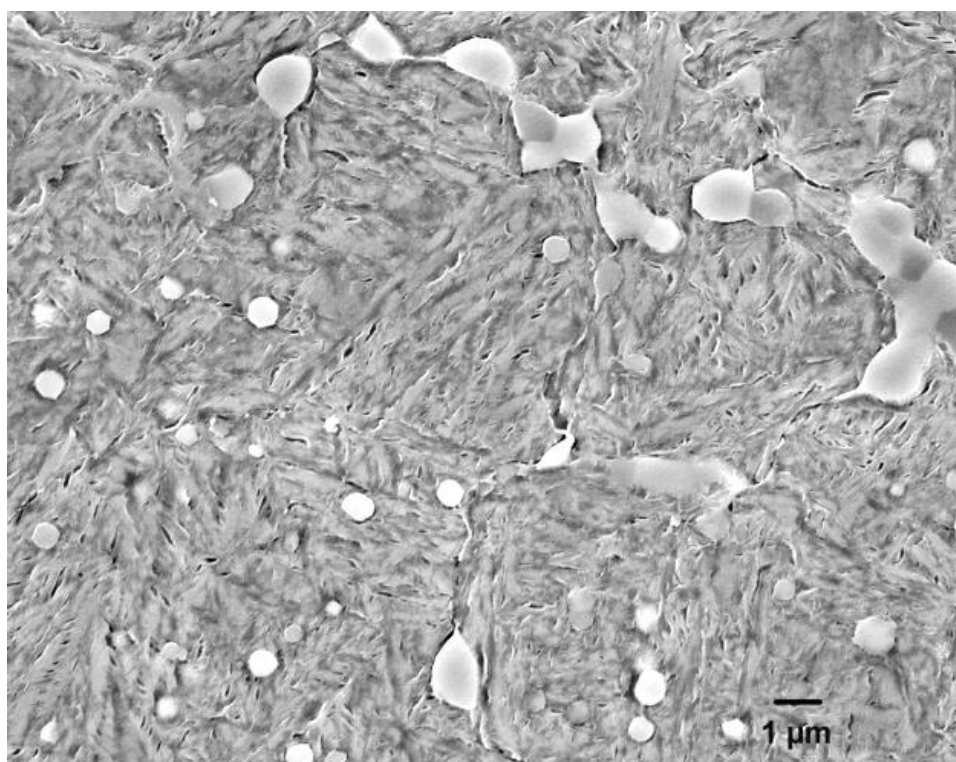
Figure 4.1.2- 1 Top view SEM images showing the microstructure of ASPN 450-2.5 sample, polished and etched using 2% Nital
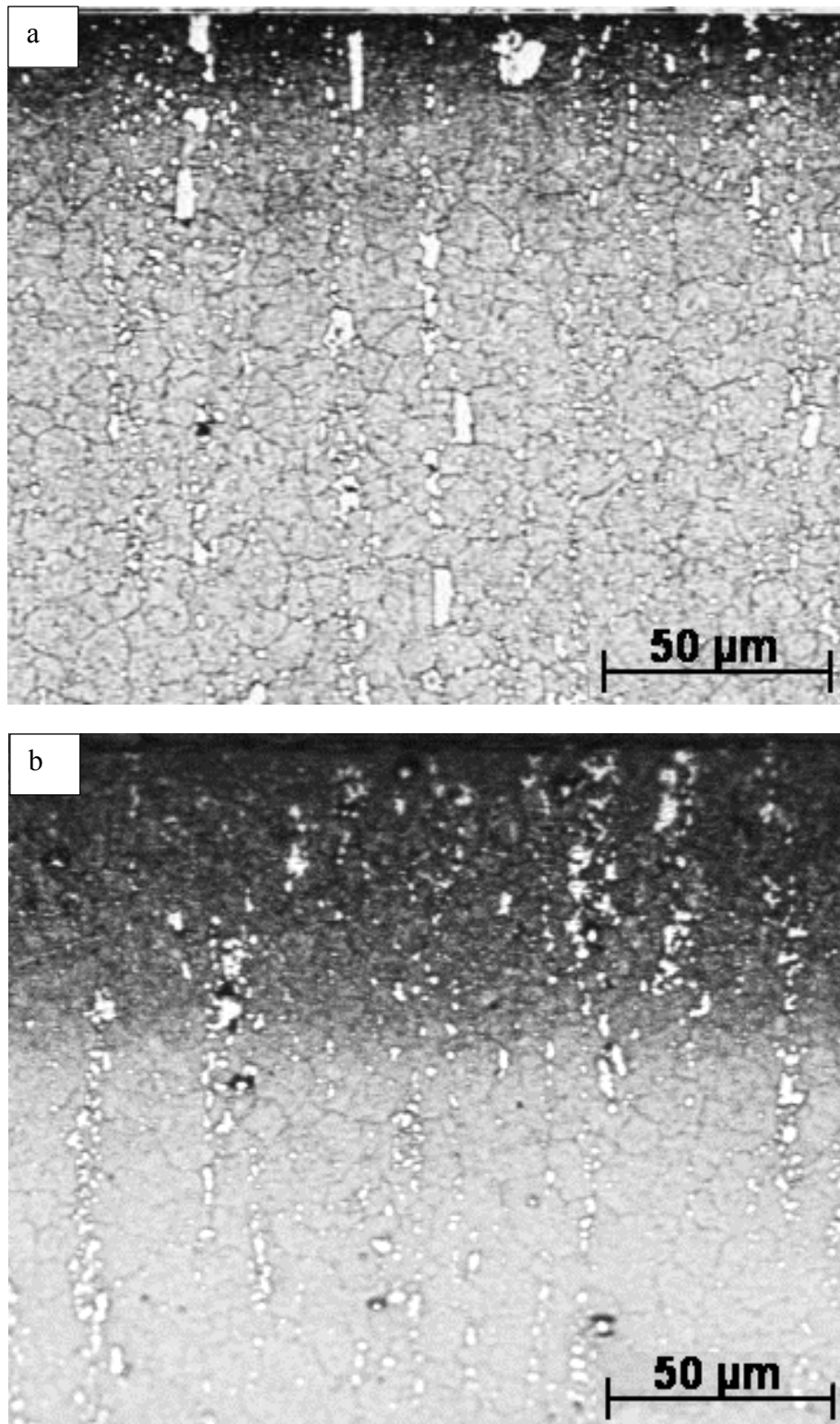
Figure 4.1.2- 2 Optical cross-sectional microstructures of a) ASPN 450-2.5 and b) ASPN 525-2.5 (etchant: 2% Nital)
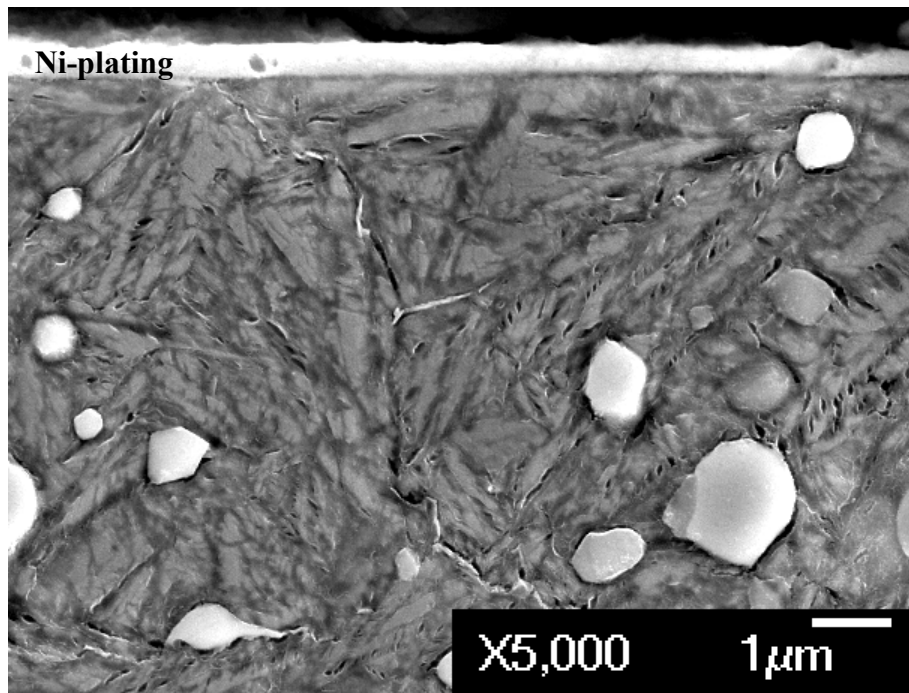
Figure 4.1.2- 3 Cross-sectional SEM microstructure of ASPN 525-2.5 (etchant: 2% Nital)
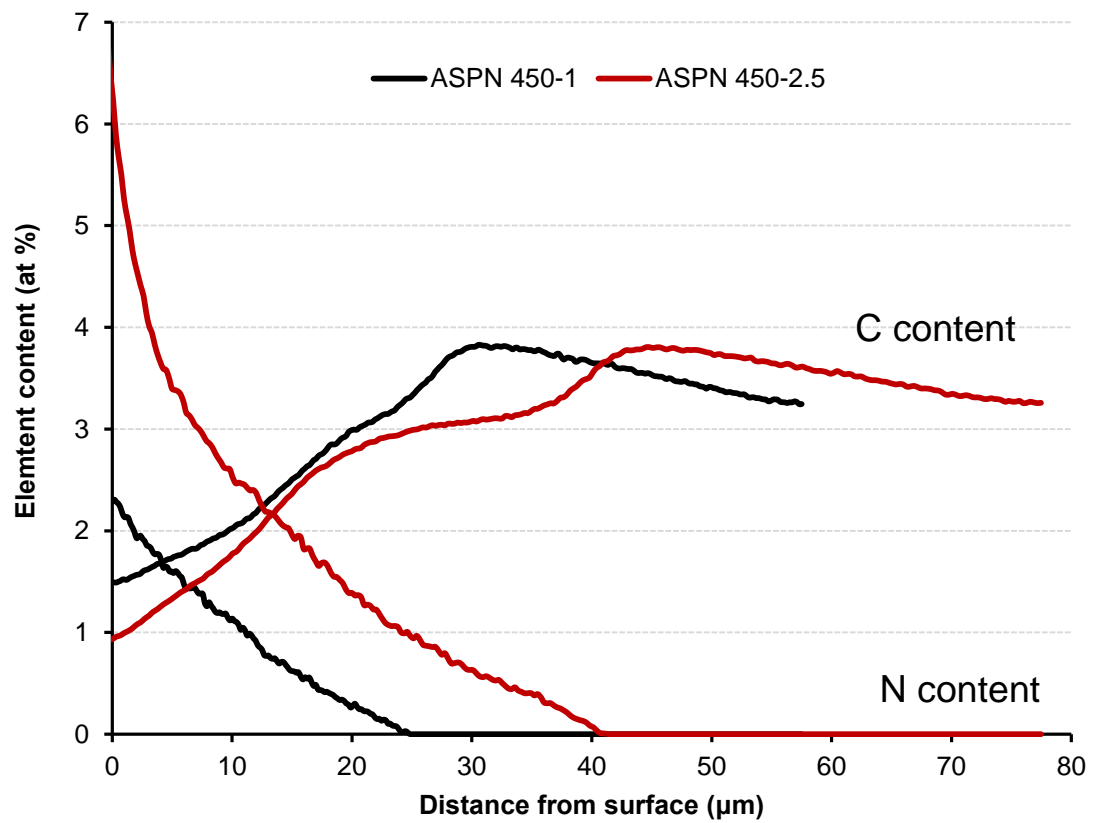
Figure 4.1.2- 4 GDOES elemental depth profiles of nitrogen and carbon for samples treated at 450 ℃ for different time periods
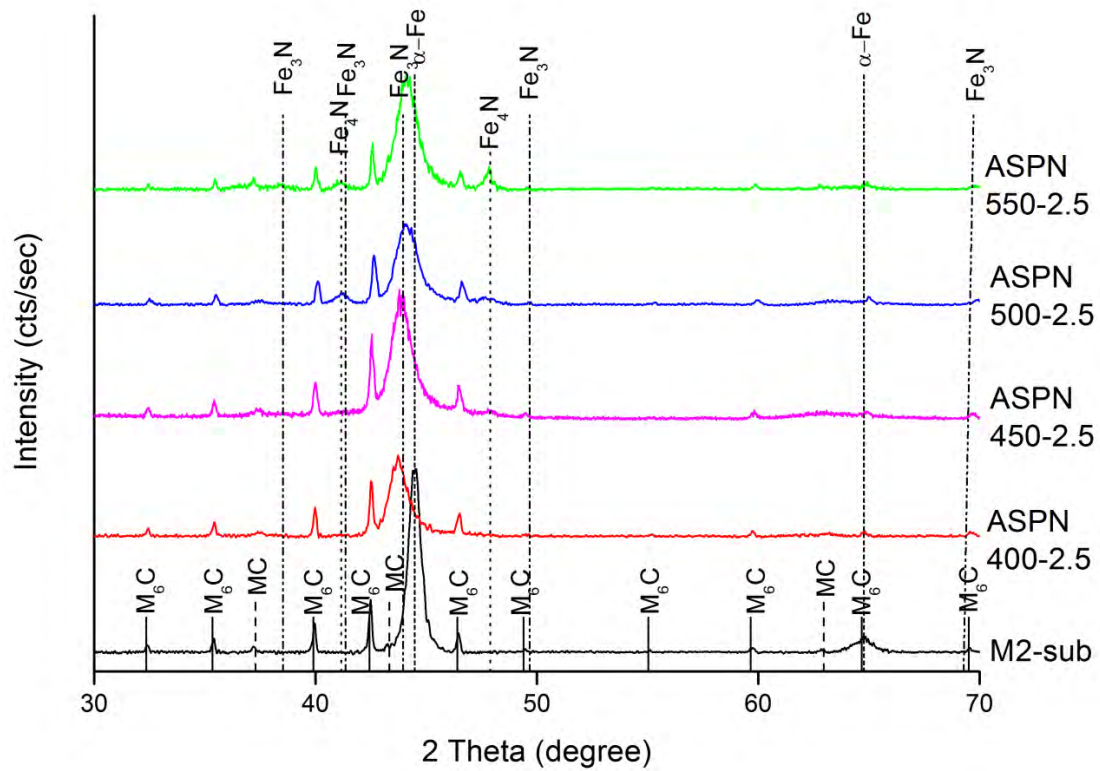
Figure 4.1.2- 5 XRD patterns of ASPNed samples treated for 2.5 hours
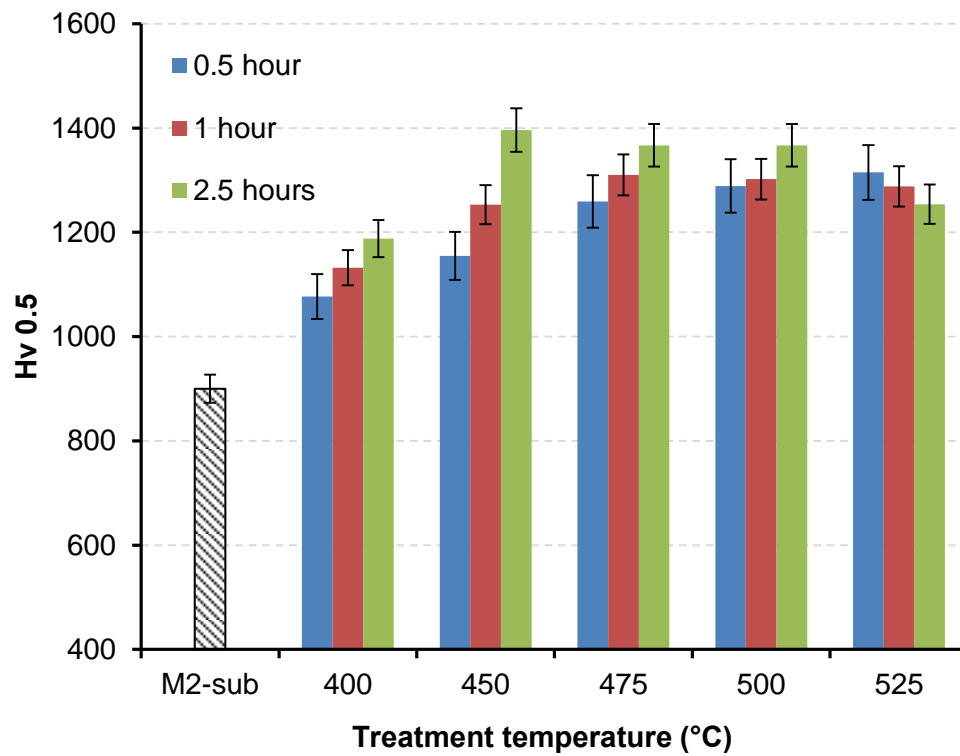
Figure 4.1.2- 6 Surface hardness of untreated M2 and ASPNed samples
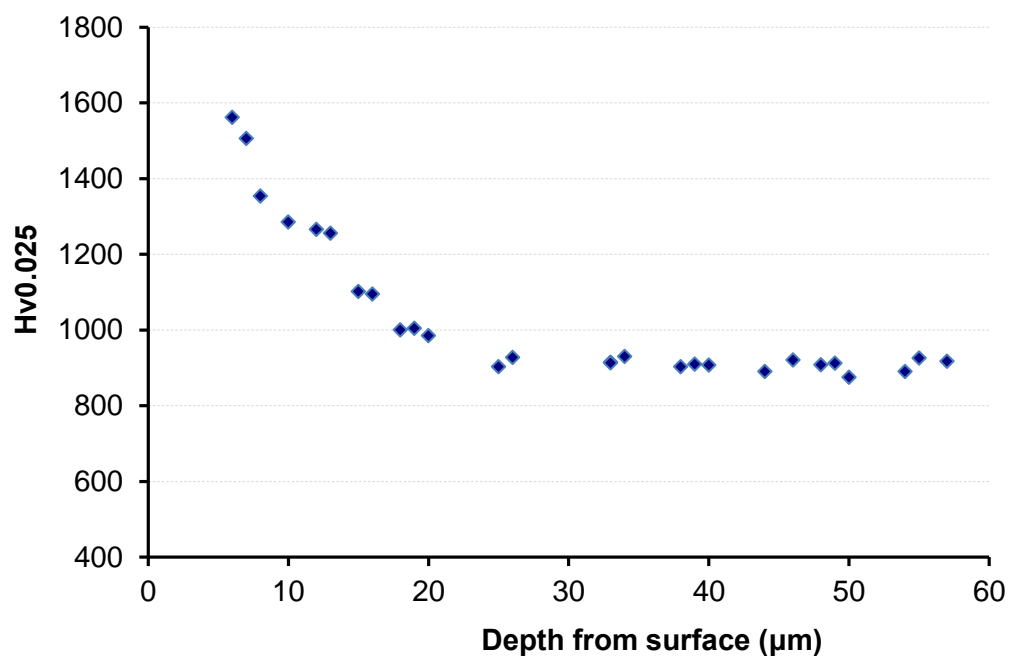
Figure 4.1.2- 7 Cross-sectional hardness profile of ASPN 500-0.5
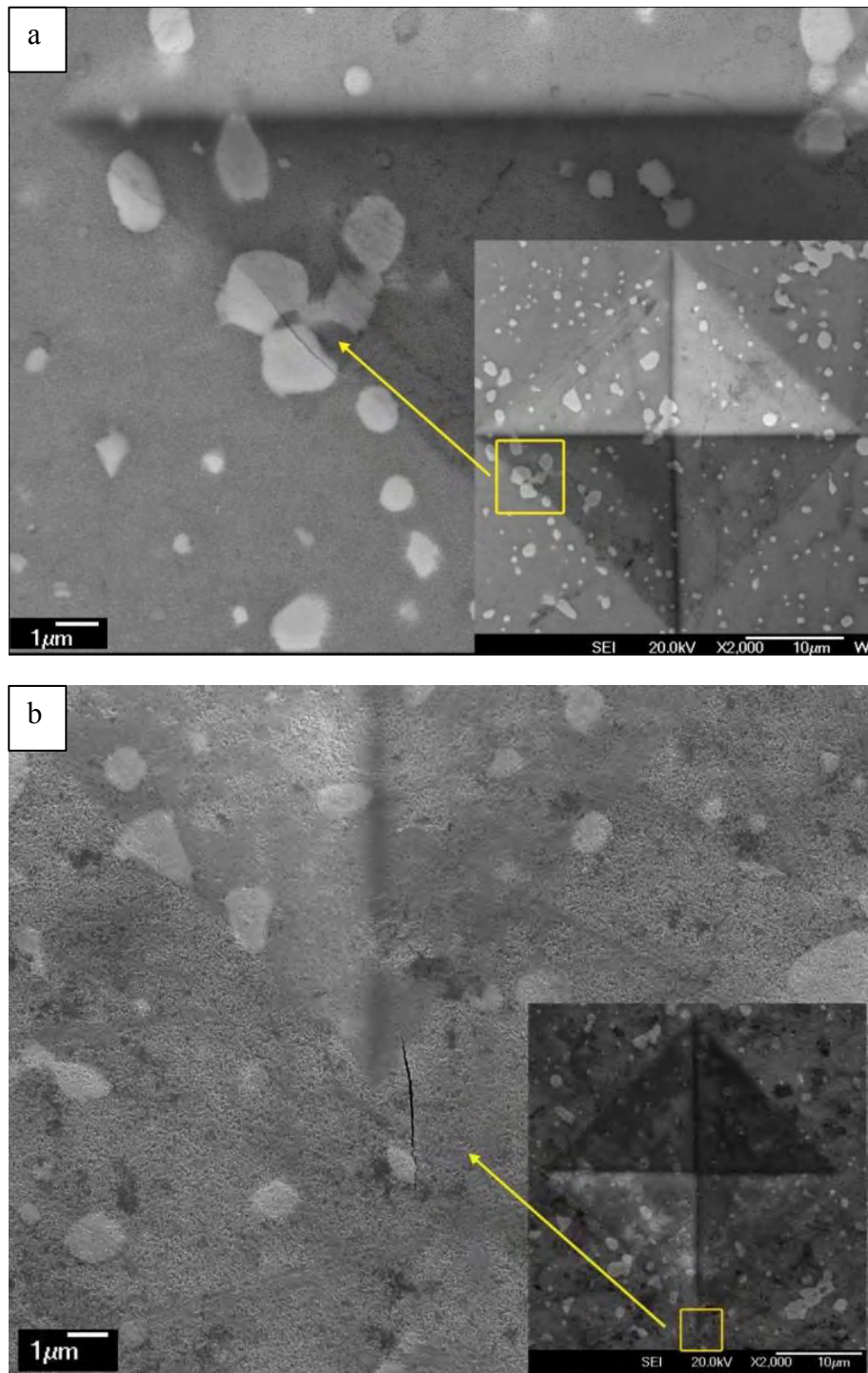
Figure 4.1.2- 8 Cracks generated around the micro-indentation on a) ASPN 500-0.5 b) ASPN 500-2.5 under a load of 1kg
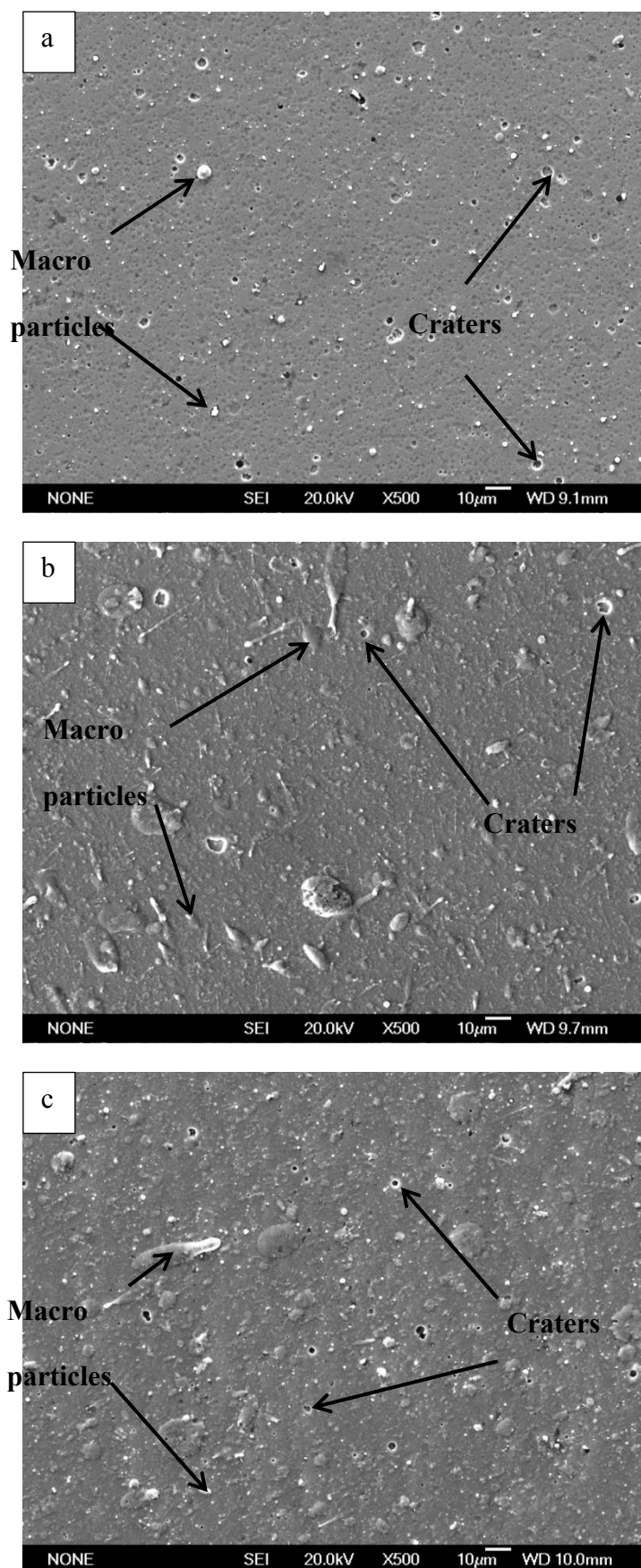
Figure 4.2.1- 1 SEM surface morphology of as deposited a) CrN, b) T-II and c) C-I-10 coating
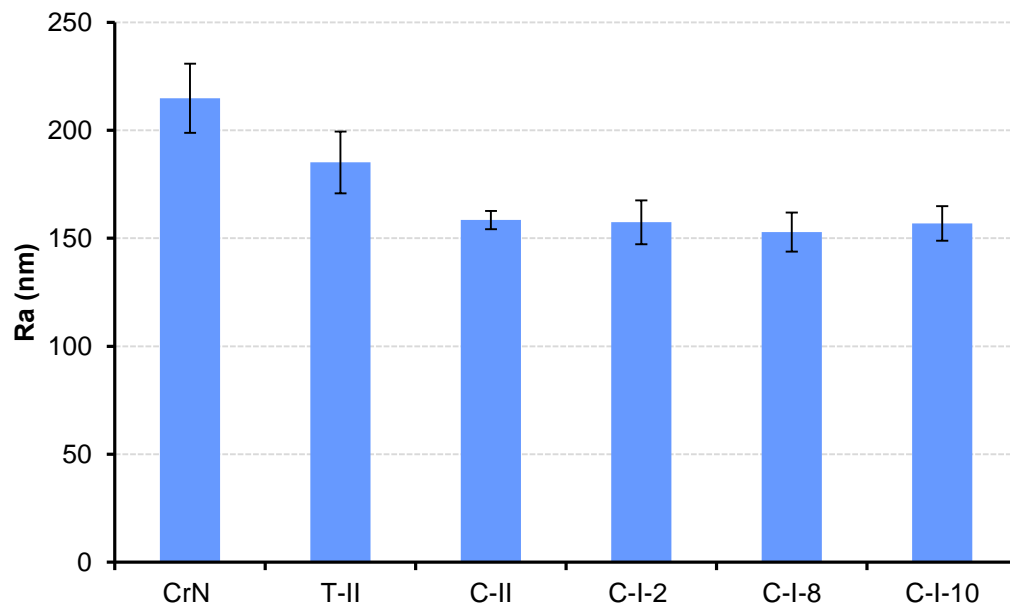
Figure 4.2.1- 2 Surface roughness of all coatings deposited on M2-unt substrate
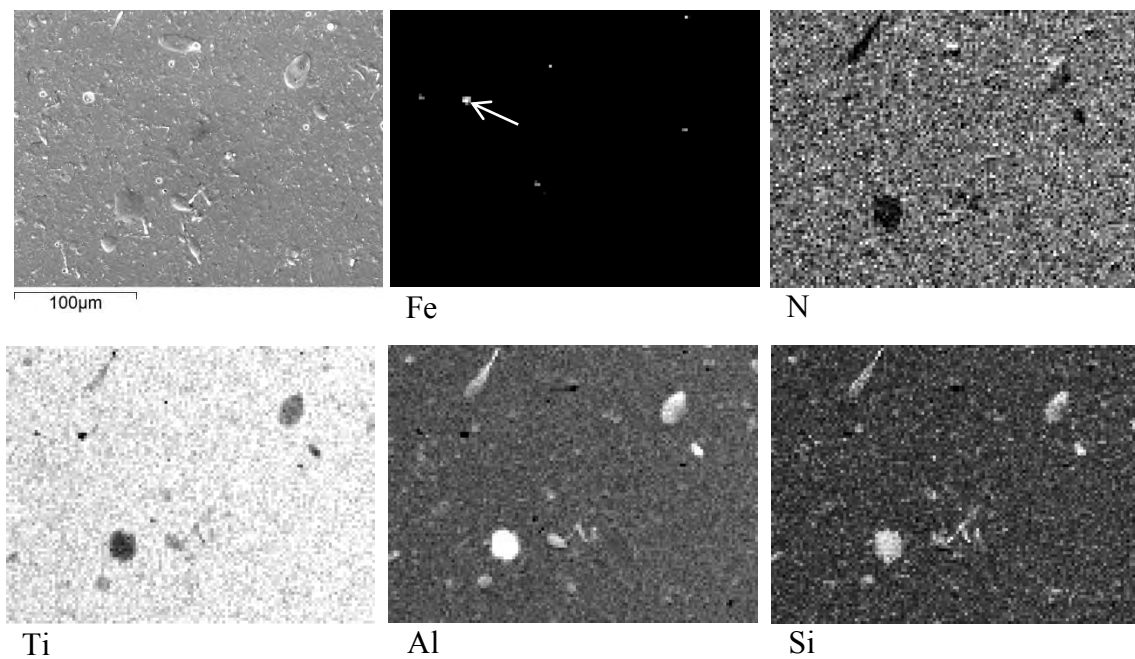
Figure 4.2.1- 3 SEM image of T-II top surface and corresponding EDS element mapping showing the composition of surface features
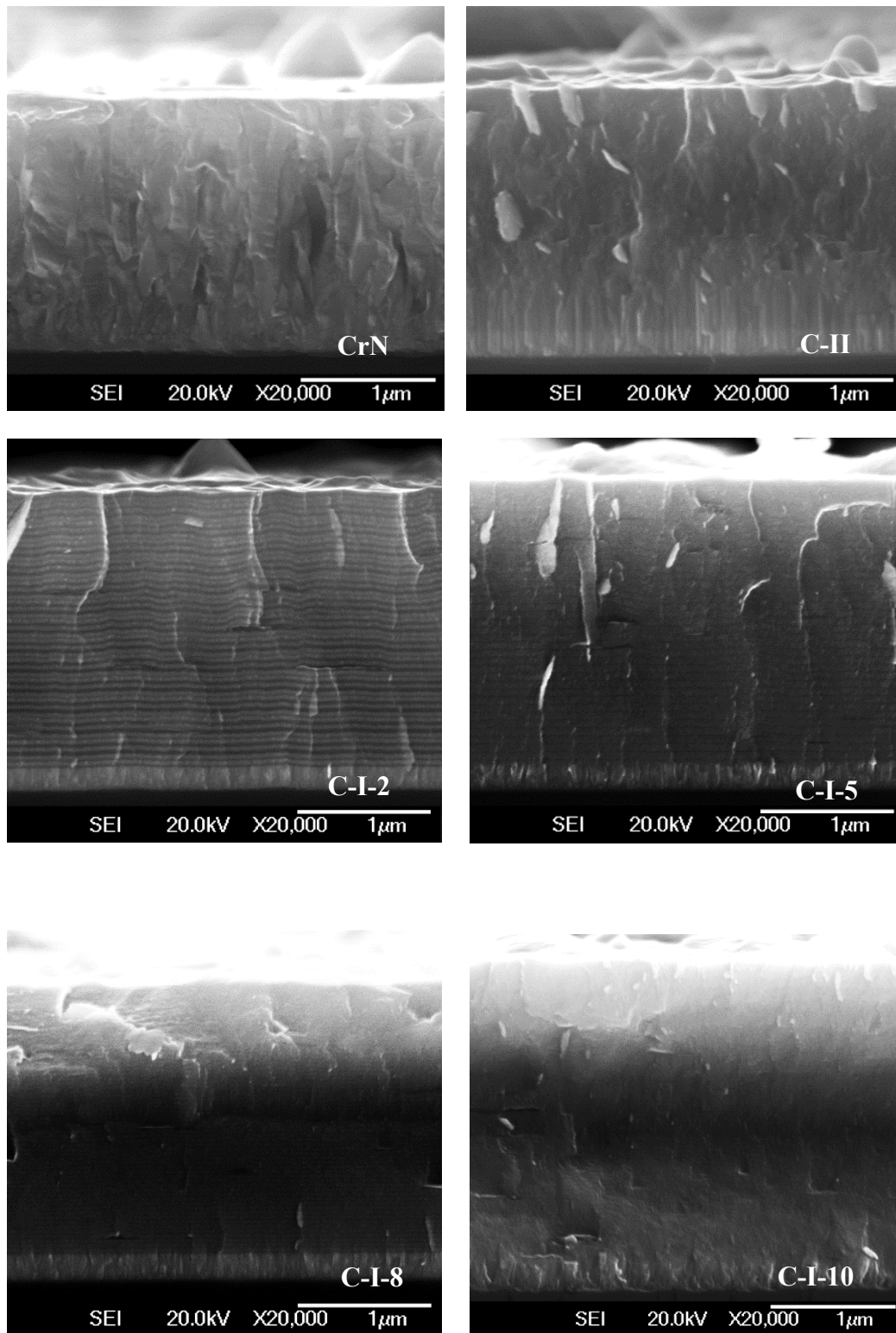
Figure 4.2.2- 1 SEM images of fractural surfaces of selected coatings
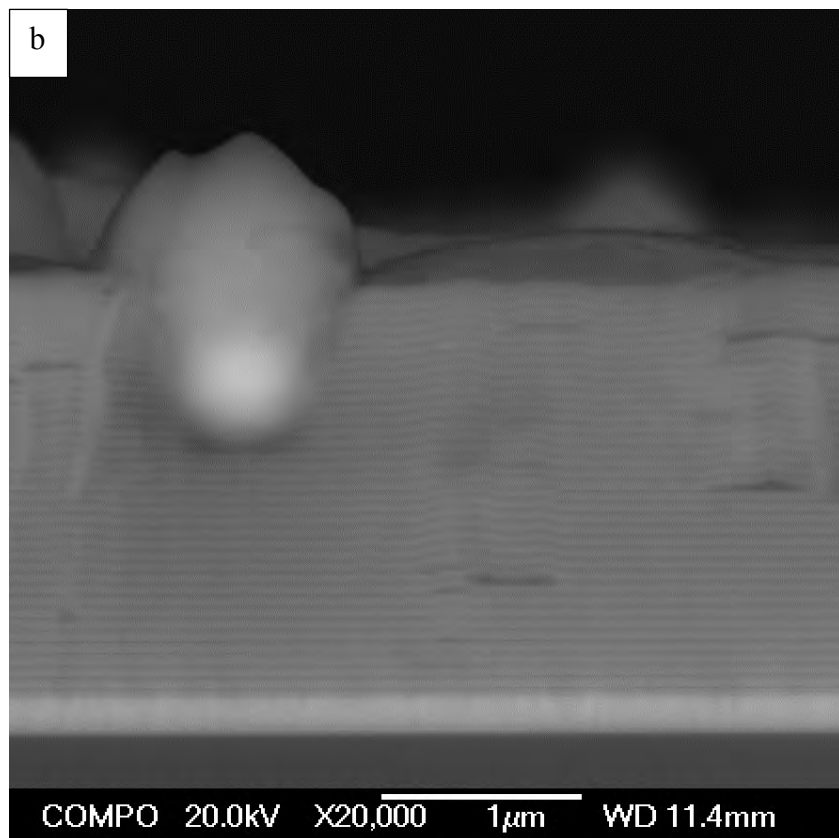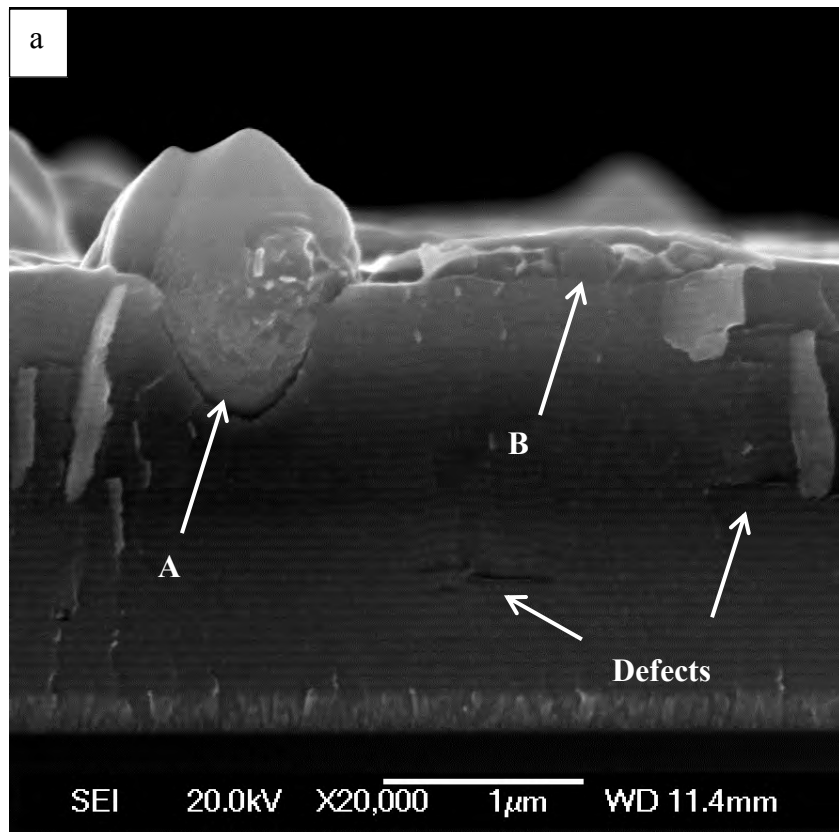
Figure 4.2.2- 2 a)Secondary electron image of fractrural surface of C-I-5 showing two types of microparticles and b) corresponding back scattered electron image

153
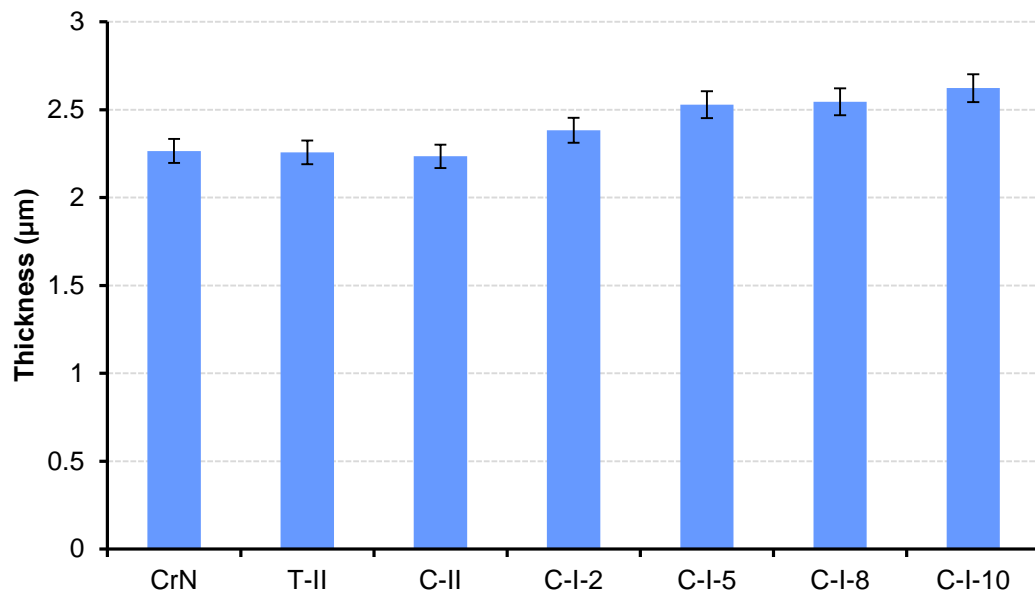
Figure 4.2.2- 3 Thickness of coatings deposited on M2-unt
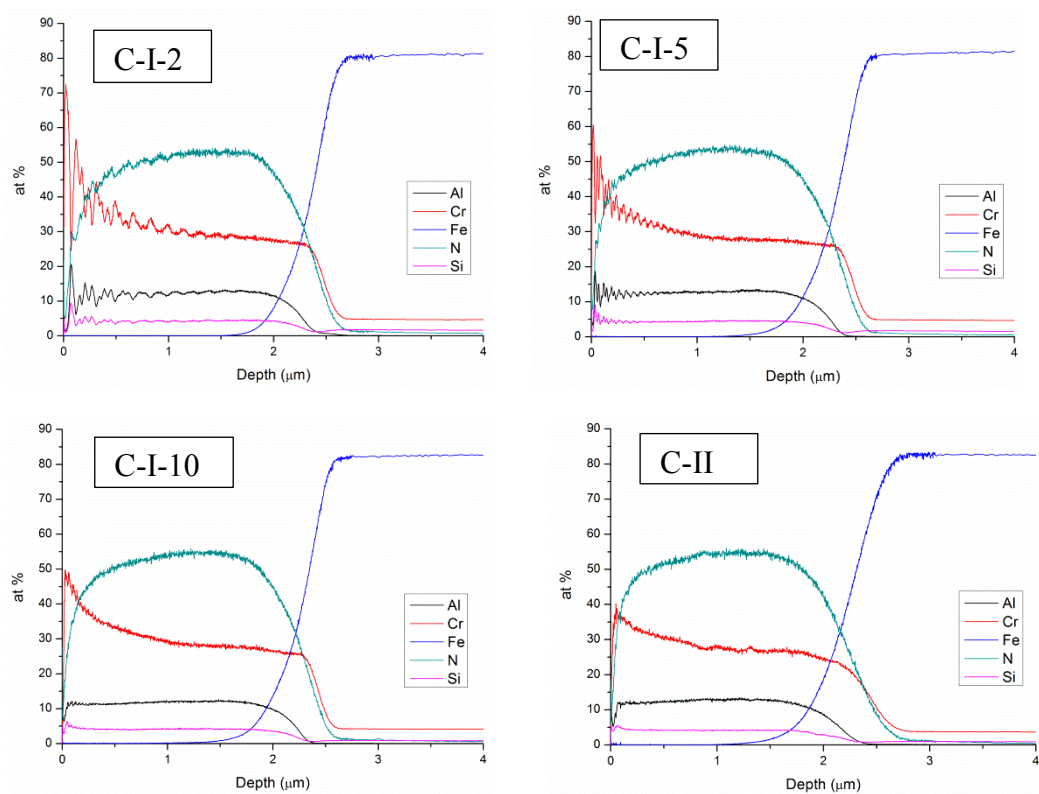
Figure 4.2.3- 1 Elemental depth profile of selected coatings obtained from GDOES analysis

154
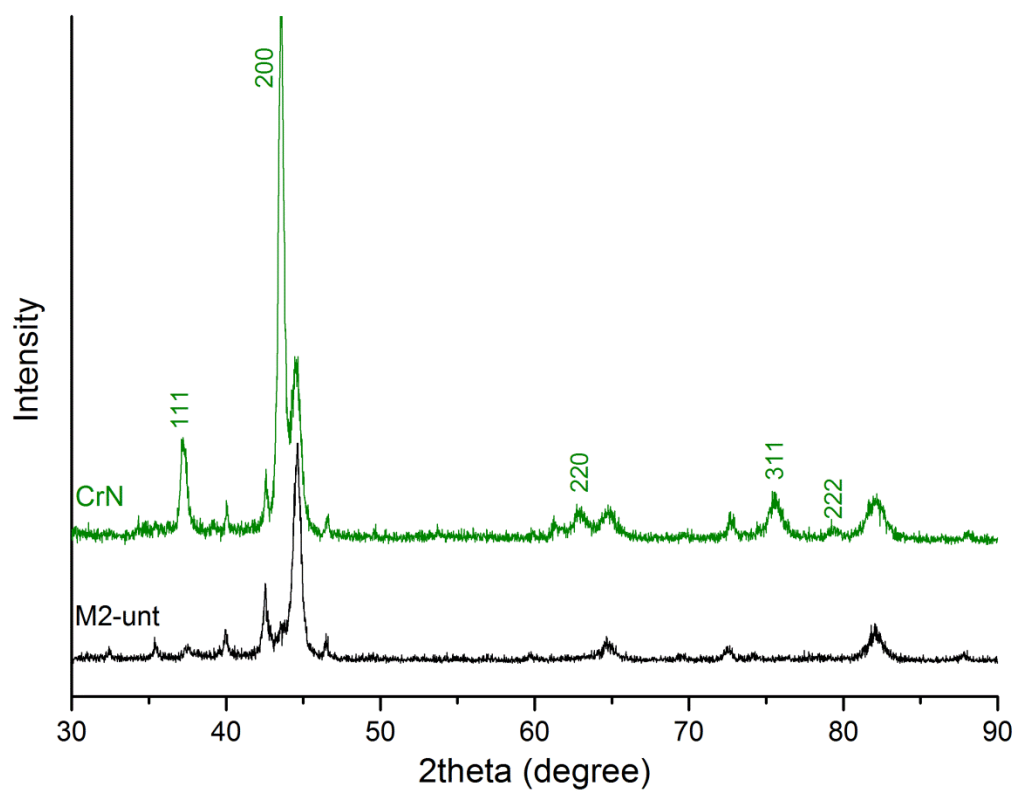
Figure 4.2.4- 1 XRD patterns of CrN and M2-unt
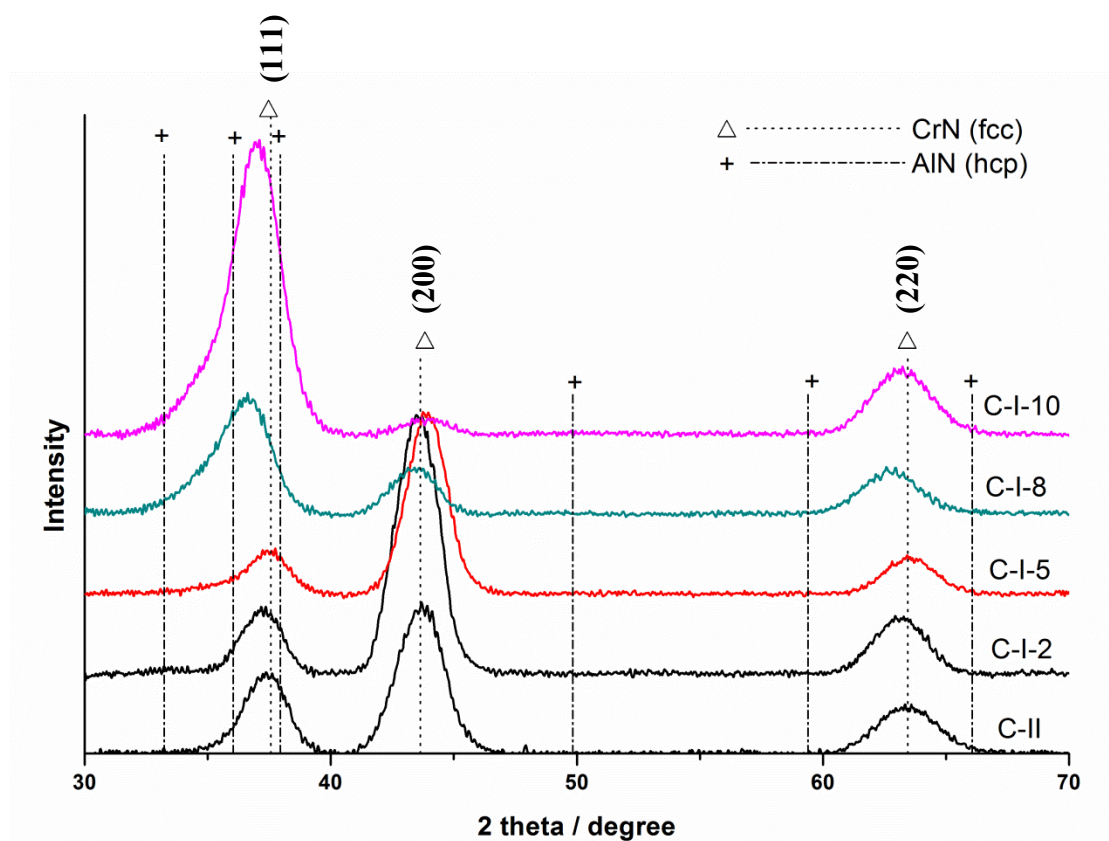
Figure 4.2.4- 2 Glancing angle XRD spectra of all CrAlSiN coatings
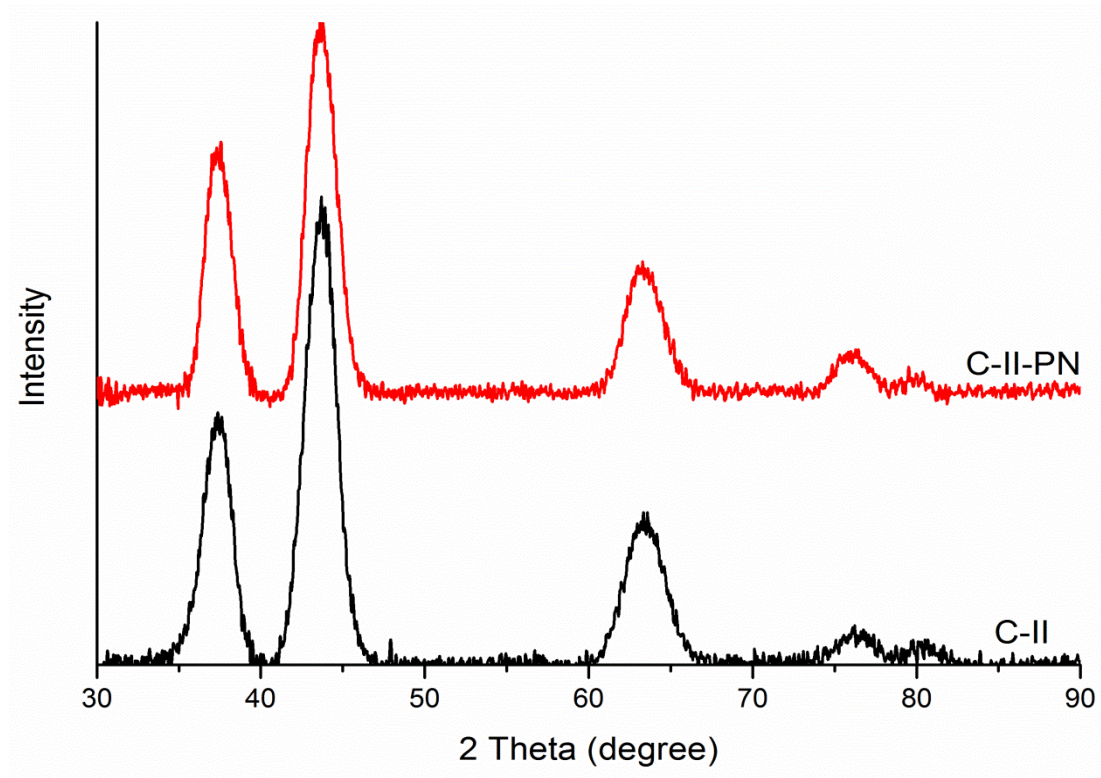
Figure 4.2.4- 3 Glancing angle XRD spectra of C-II coating deposited on M2 and ASPNed M2 substrate
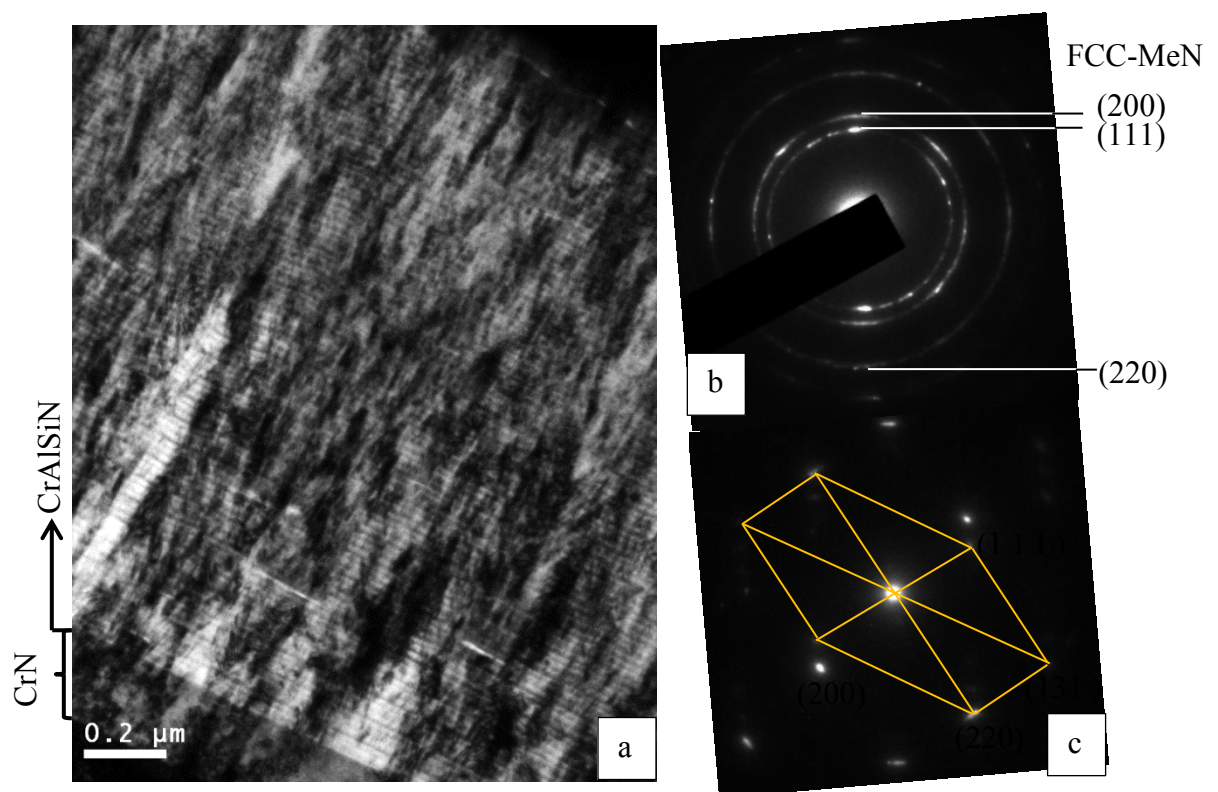
Figure 4.2.5- 1 a) Bright field image of C-II, with SAD patterns of b) the main C-II coating and c) CrN interfacial layer
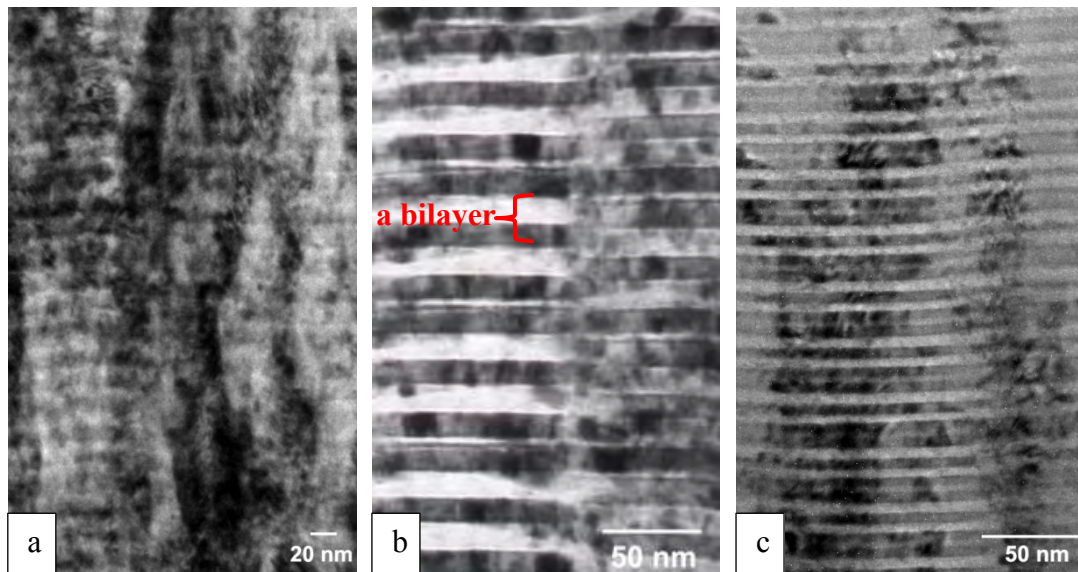
Figure 4.2.5- 2 Bright field image of a)C-II, b) C-I-5 and c) C-I-10, showing the columnar structure and multilayer structure

(200)

b

c

fcc hcp
(01$\bar{1}$0)
(0002)
(111)
(01$\bar{1}$1)
(200)
(01$\bar{1}$2)
(11$\bar{2}$0)
(220)
(11$\bar{2}$2)
(311)
(02$\bar{2}$2)
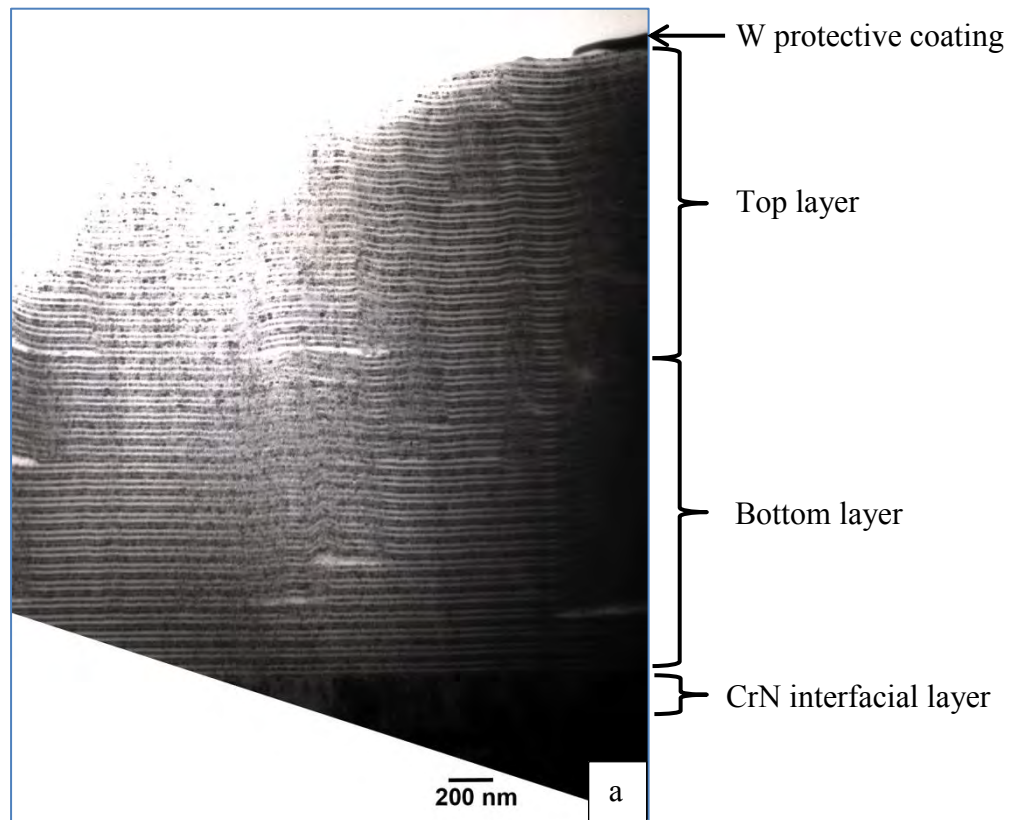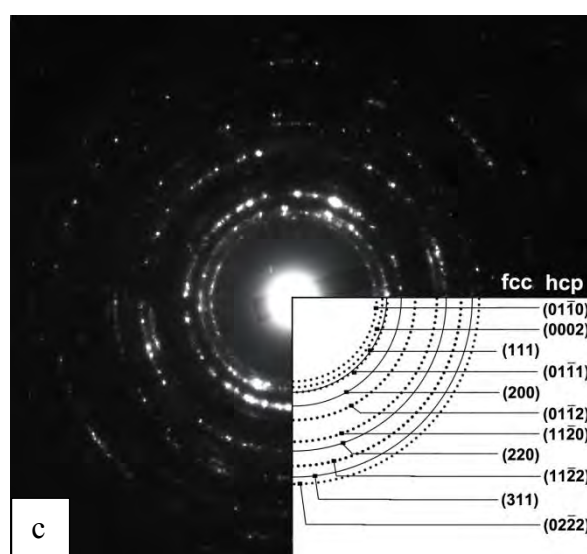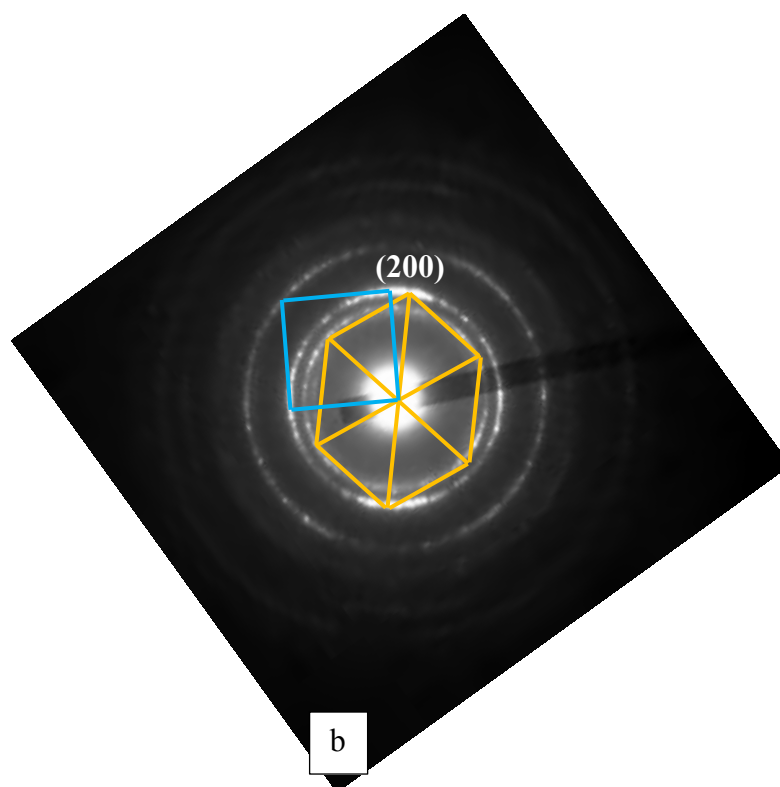
d	fcc-MeN	hcp-MeN	
Lattice Parameters	a (nm)	a,b (nm)	c (nm)
CrN	0.4149		
AlN		0.3110	0.4980
C-I-5	0.4120	0.3112	0.5039

Figure 4.2.5- 3 a) Bright filed image of C-I-5 and corresponding SAD patterns of b) bottom layer and c) top layer; d) Theoretical lattice parameters of fcc-CrN and hcp-AlN, and calculated lattice parameters of the fcc and hcp phase from the SAD pattern of C-I--5
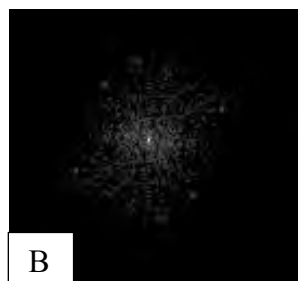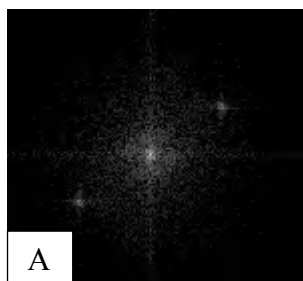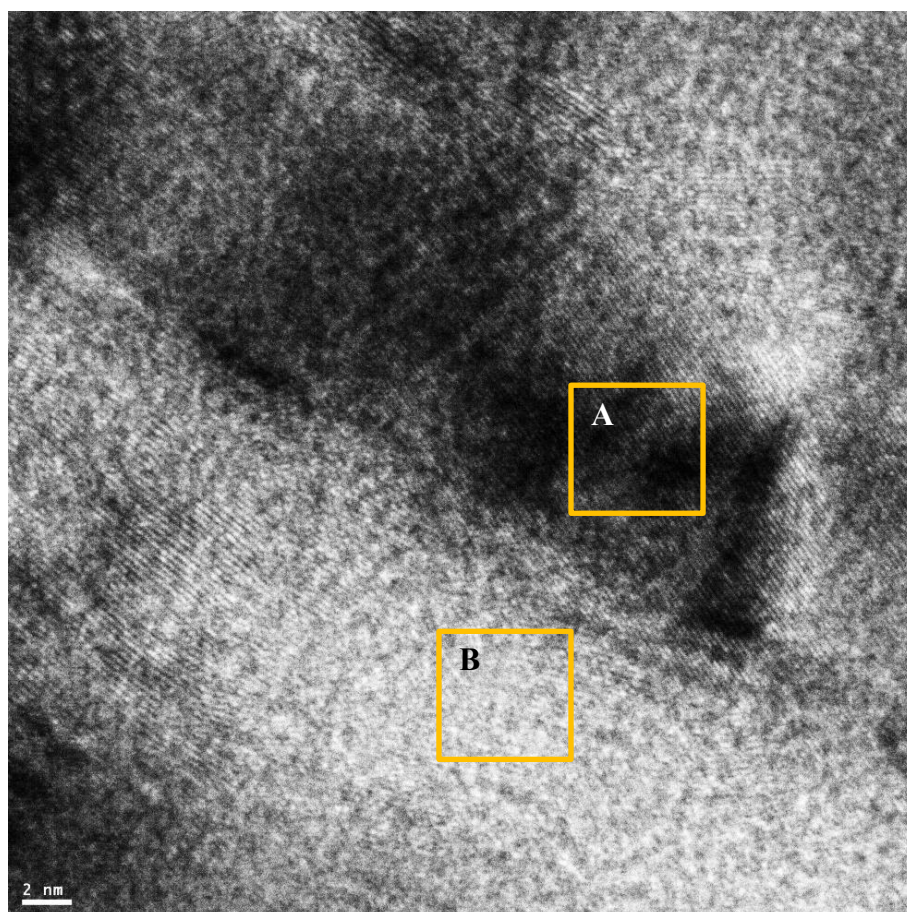
Location	Composition at%			
	N	Al	Si	Cr
A	36.14	7.98	2.80	53.09
B	38.66	29.51	10.77	21.06

Figure 4.2.5- 4 High resolution cross-sectional TEM images of C-I-5 and the FFT from the marked regions, inserted with the EDS compositional analysis of the marked regions

W protective coating

Top layer

Bottom layer

CrN interfacial layer

Substrate

500 nm

a

b

c
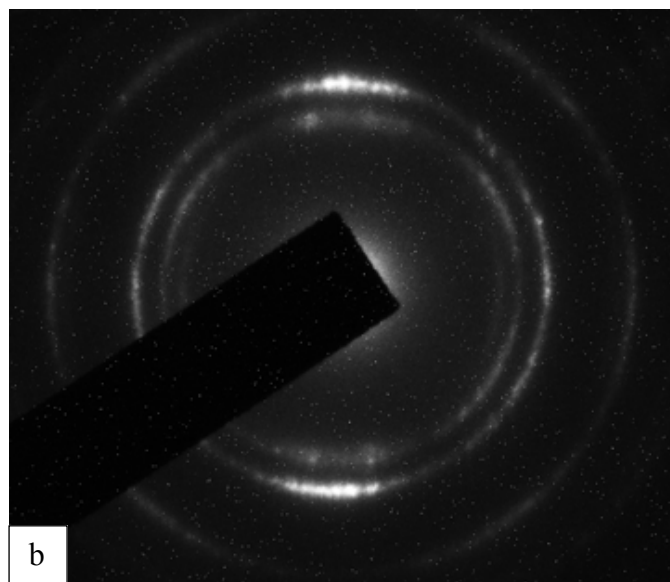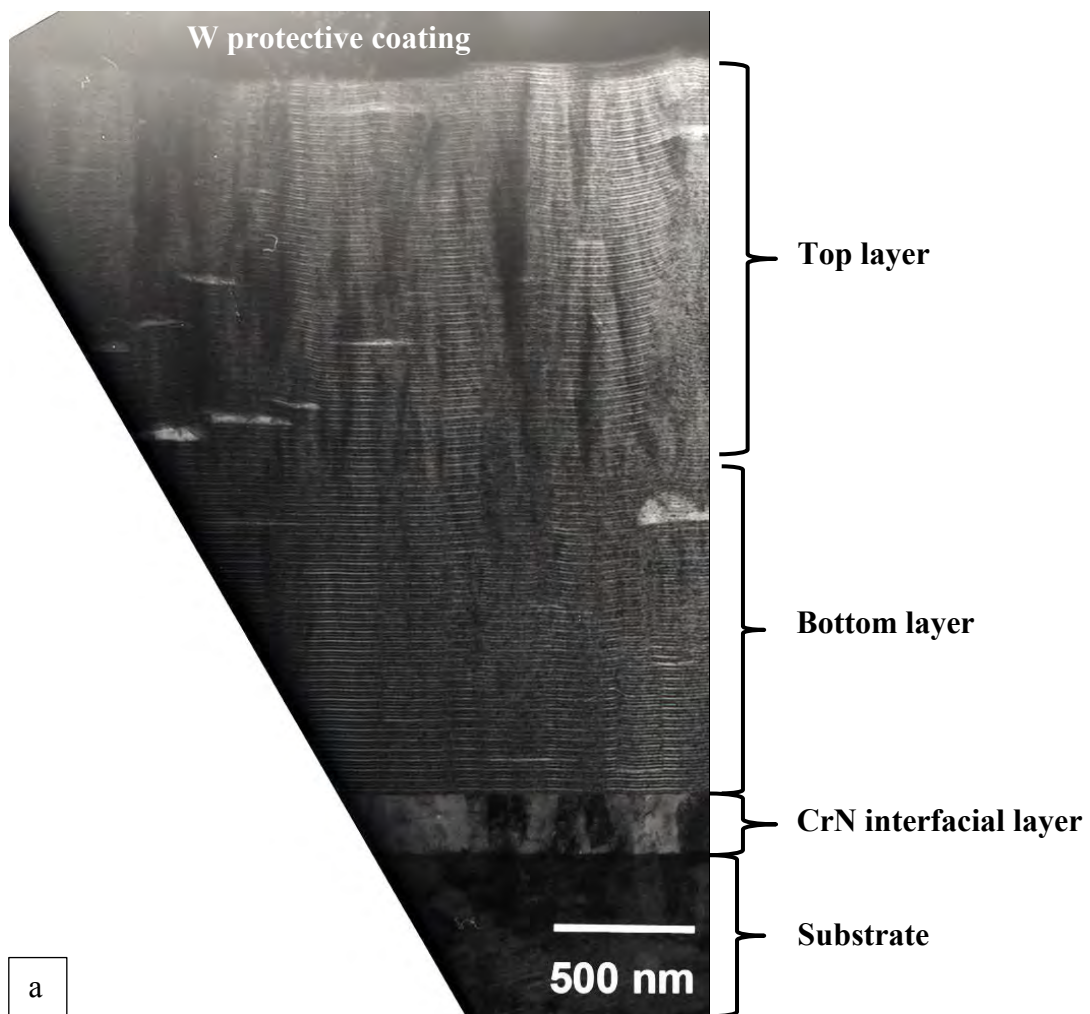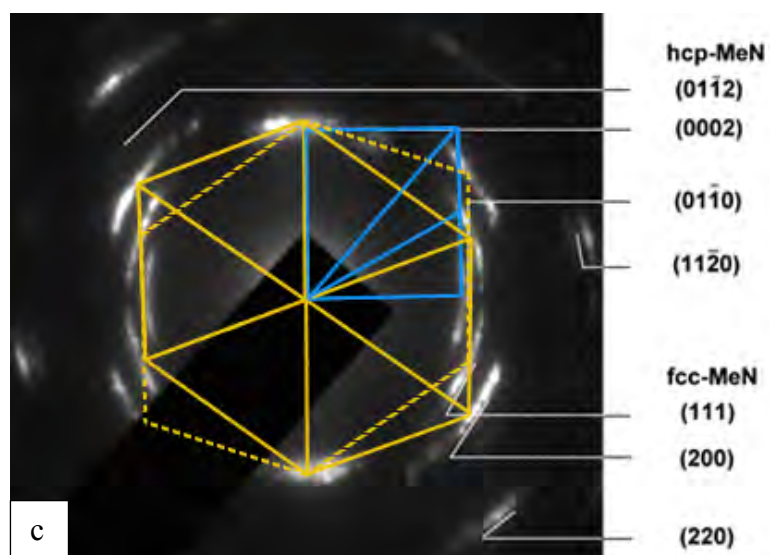
d	fcc-MeN	hcp-MeN	
Lattice Parameters	a (nm)	a,b (nm)	c (nm)
CrN	0.4149		
AlN		0.3110	0.4980
C-I-10	0.4115	0.3121	0.5080

Figure 4.2.5- 5 a) Bright filed image of C-I-10 and corresponding SAD patterns of b) the bottom layer and c) the top layer of the coating; d) simulated diffraction patterns of fcc-MeN phase in the top layer of the coating

Figure 4.2.5- 6 Dark field images of Sublayer II of C-I-10, showing the CrN-like fcc-MeN phase
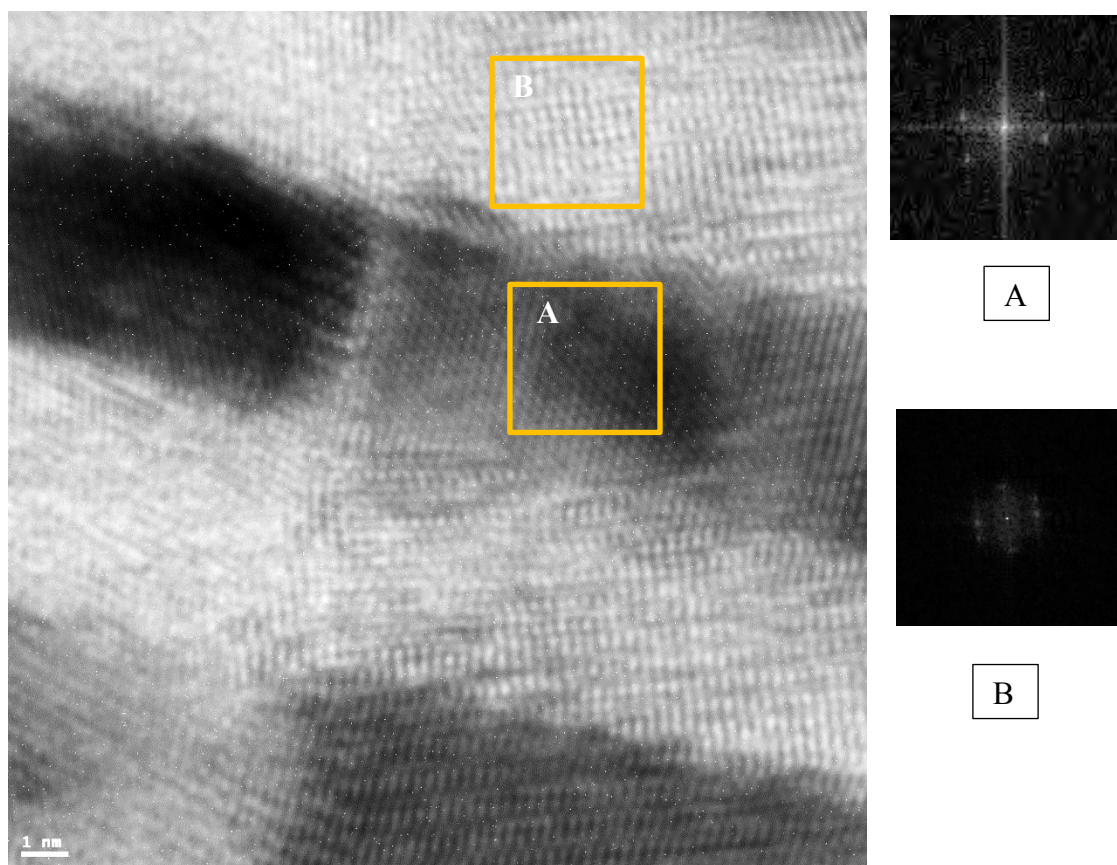
Figure 4.2.5- 7 High resolution cross-sectional TEM images of C-I-10 and the FFT taken from marked regions
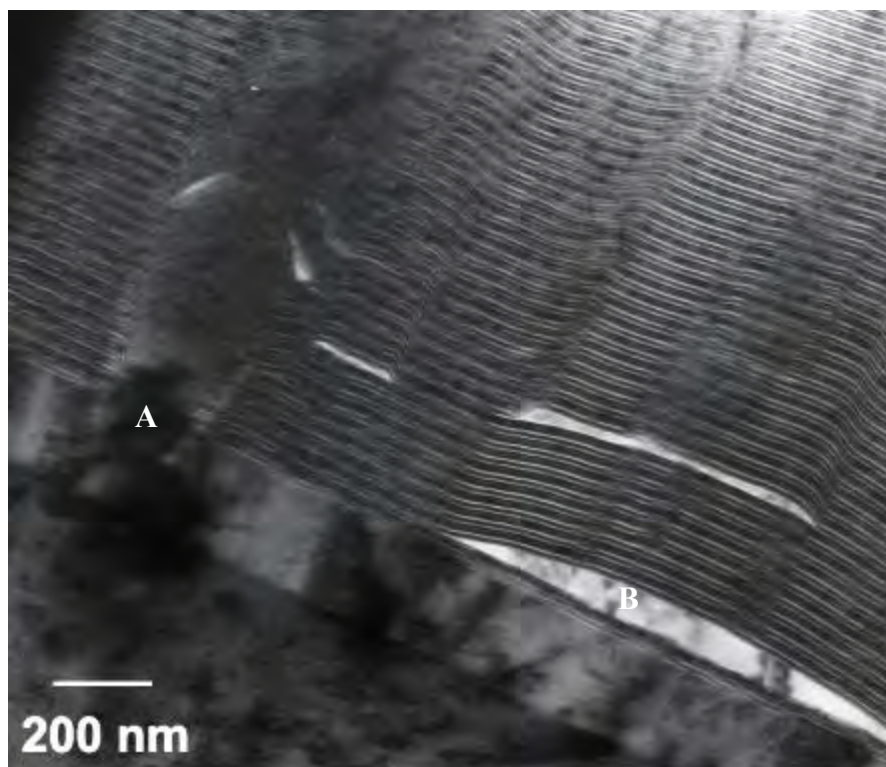
Figure 4.2.5- 8 Cross-sectional TEM image of C-I-10 showing two typical types of defects
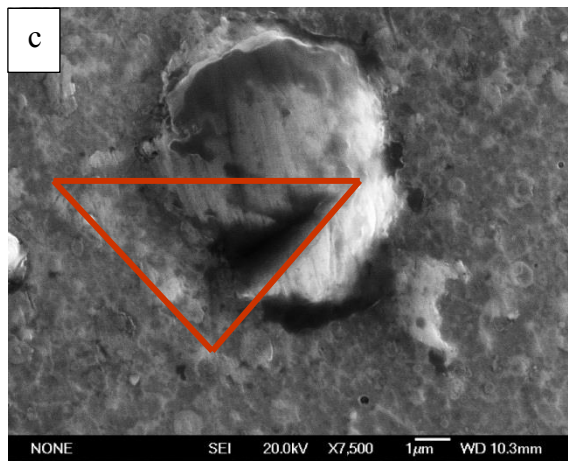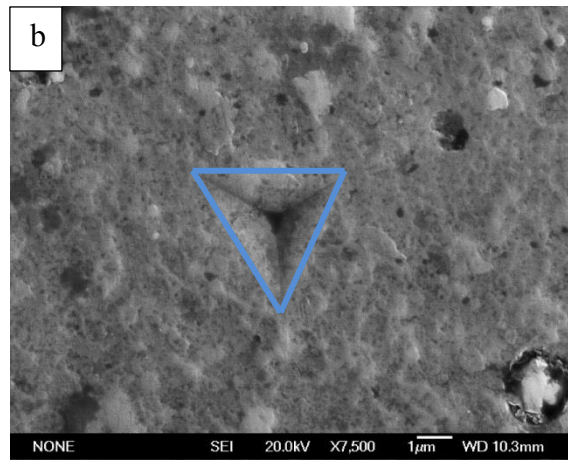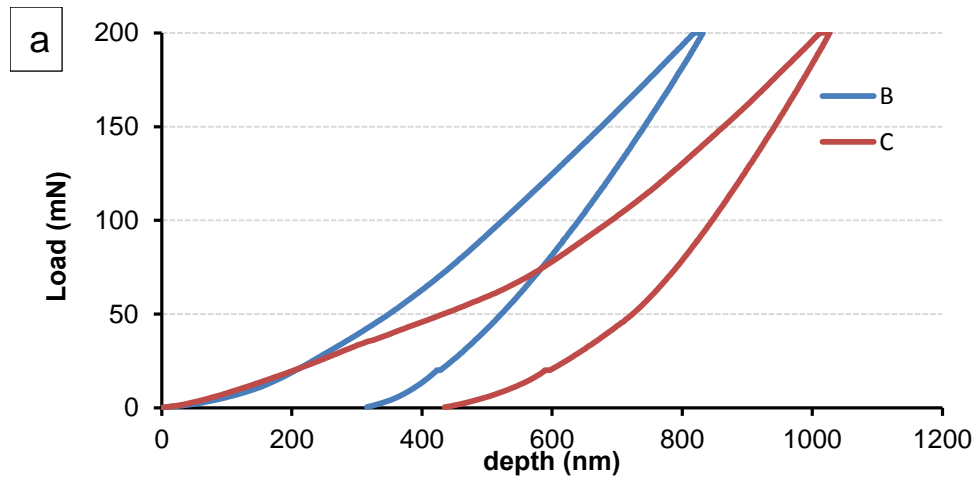
Figure 4.3.1- 1 a) Load-displacement curve of two indentations performed on the surface of C-I-10 using the load of 200 mN and corresponding SEM images of the indentation footprints, showing different shape and size of indentations on b) coating matrix and c) macro particles
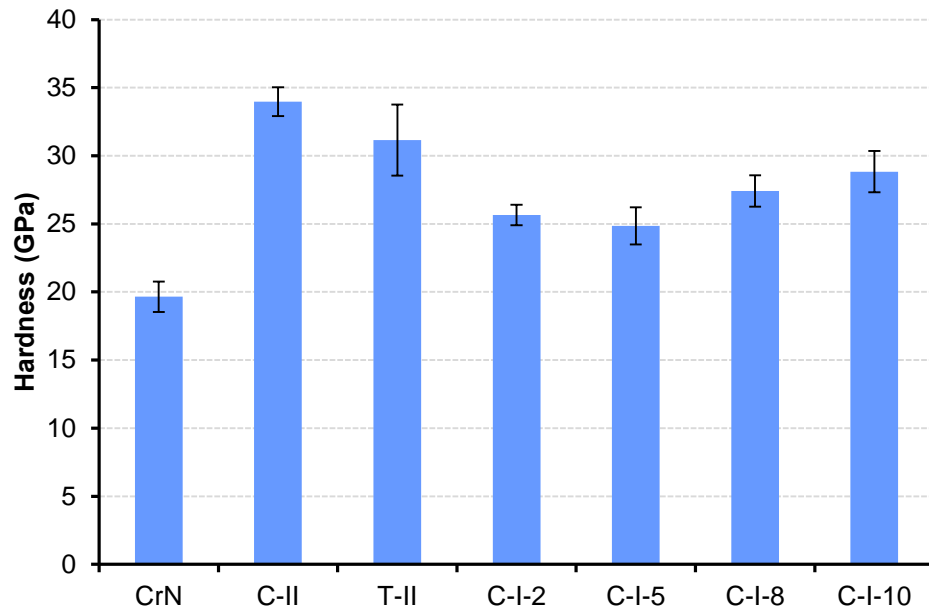
Figure 4.3.1- 2 Surface hardness of all coatings evaluated using nano-indentation at room temperature, under the load of 25 mN
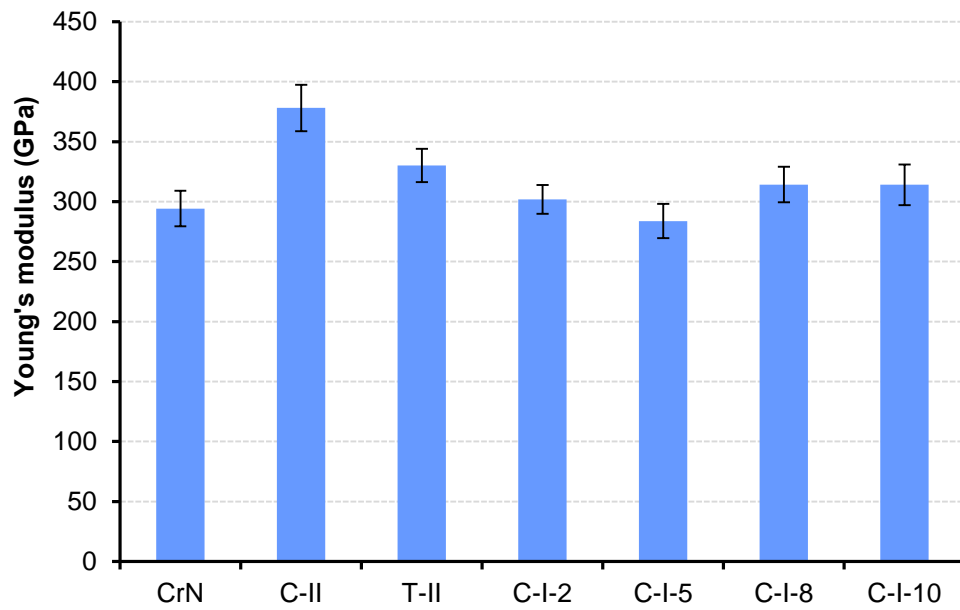
Figure 4.3.1- 3 Young's modulus of all coatings evaluated using nano-indentation at room temperature, under the load of 25 mN
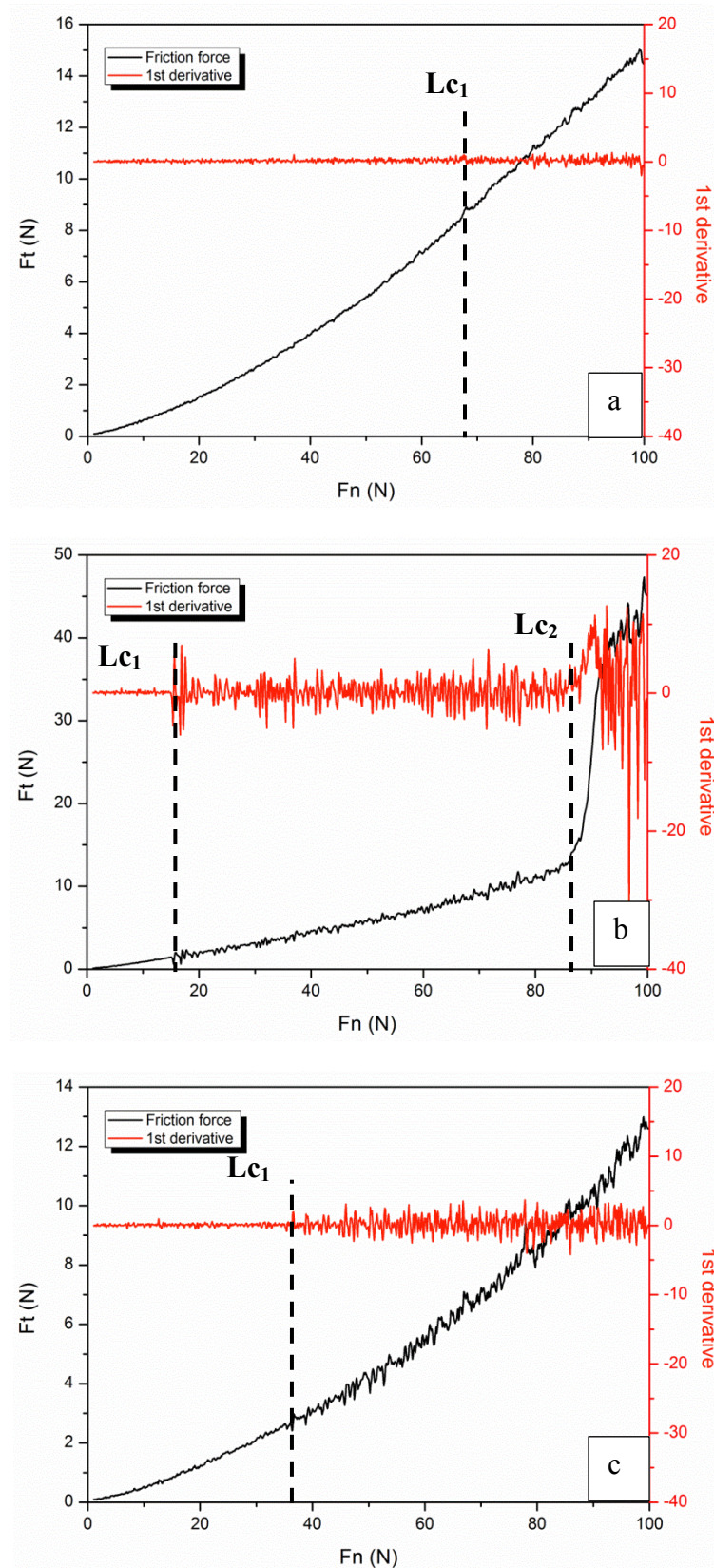
Figure 4.3.2- 1 Friction force and its first derivative against incremental scratch load for samples a) CrN, b) C-II and c) C-I-10
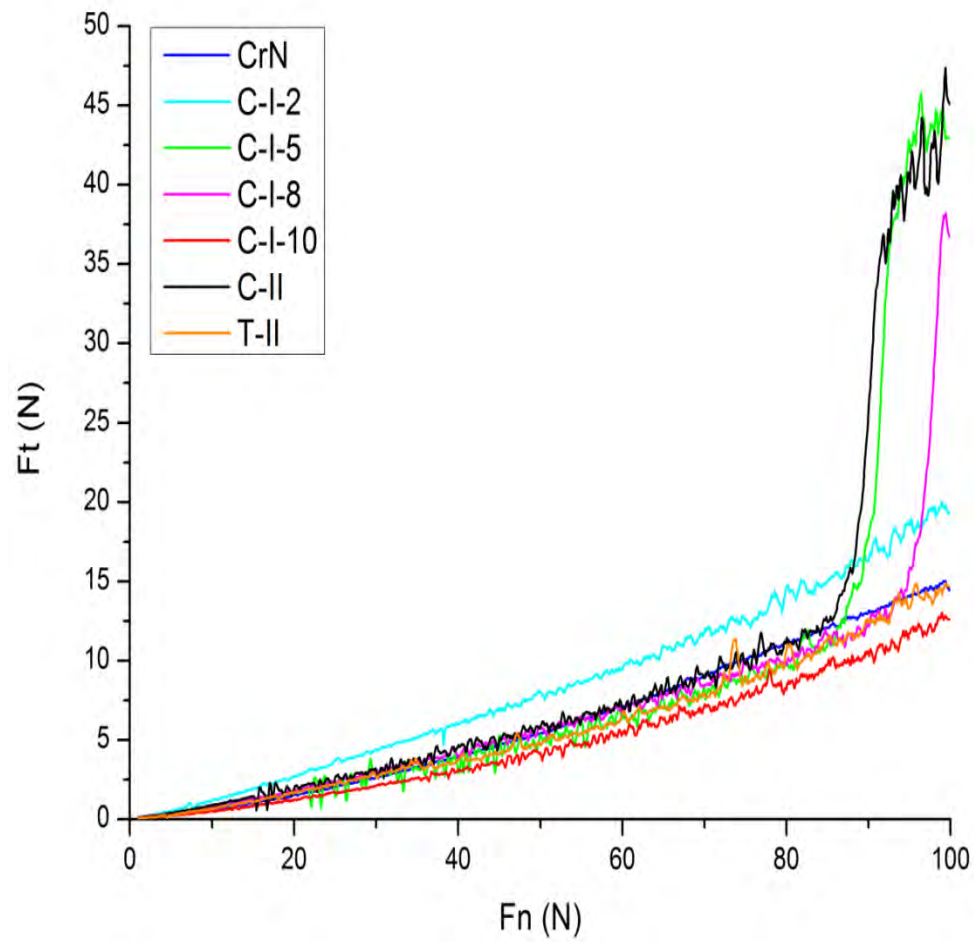
Figure 4.3.2- 2 Friction force against incremental scratch load for all coatings deposited on M2 substrate
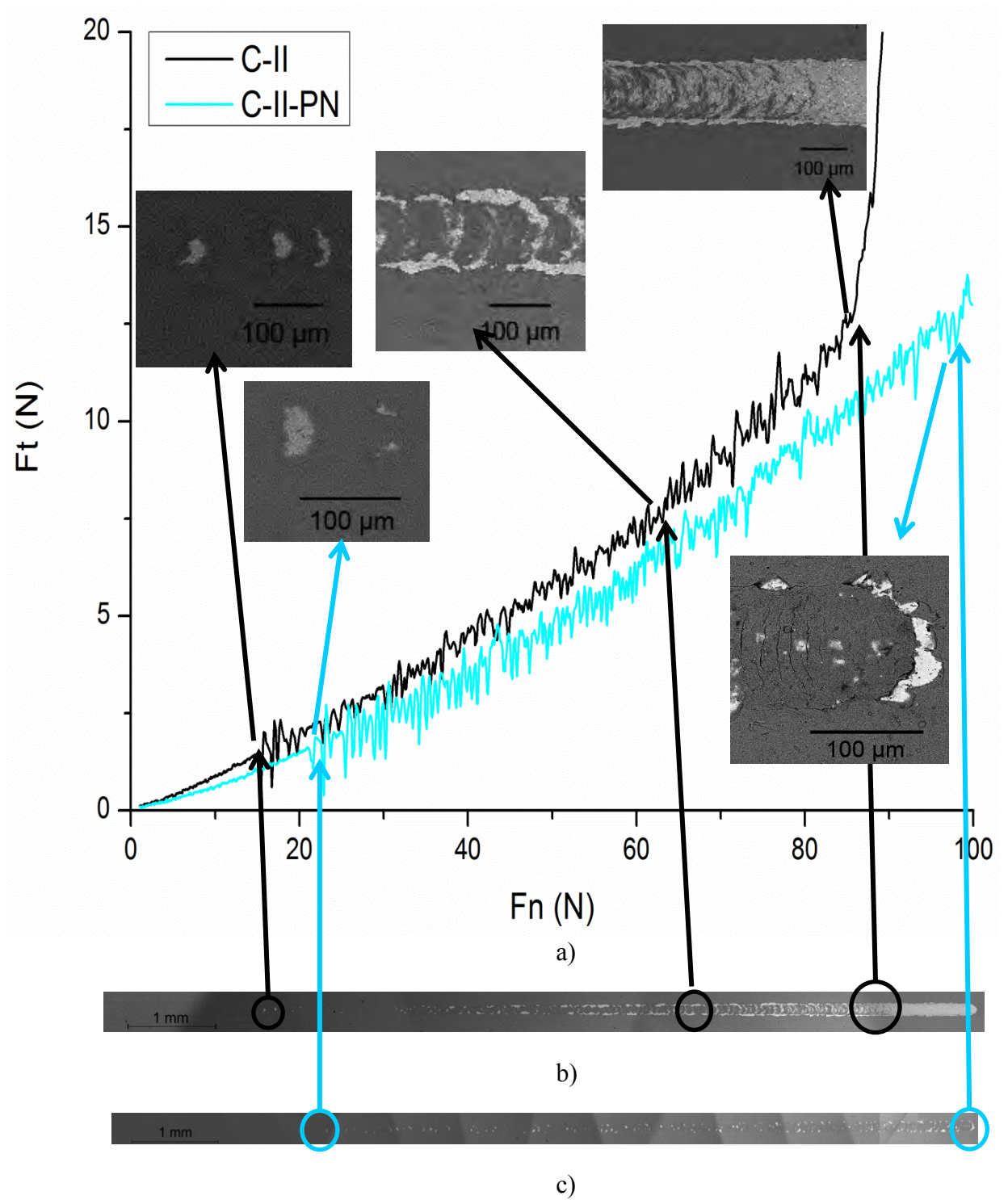
Figure 4.3.2- 3 a) Friction force against incremental scratch load of C-II and C-II-PN, and back scattered images of overview of the scratch wear track of b) C-II and c) C-II-PN, showing the influence of duplex treatment
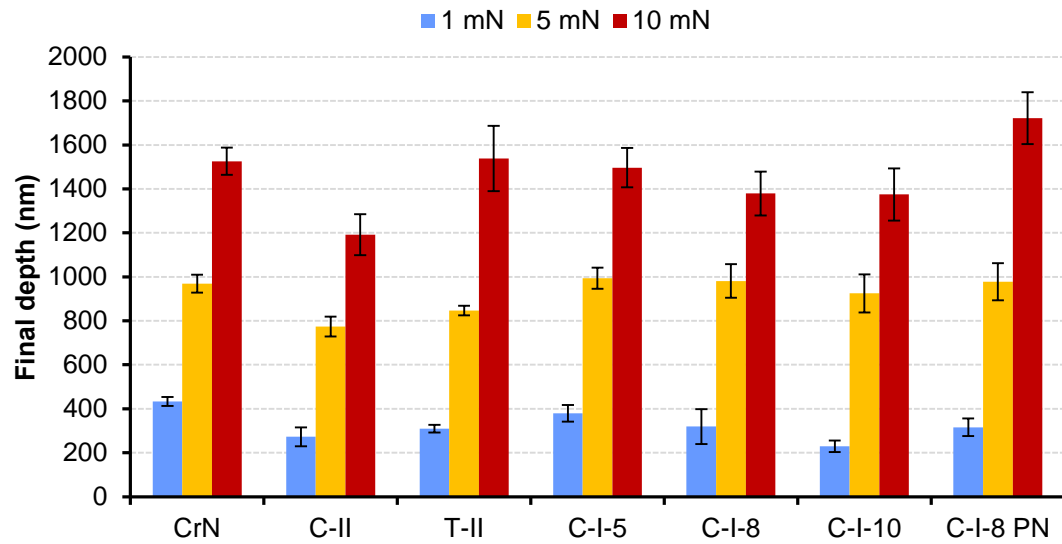
Figure 4.3.3- 1 Final impact depth of the coatings after 75 impacts on the coating surfaces with different impact load
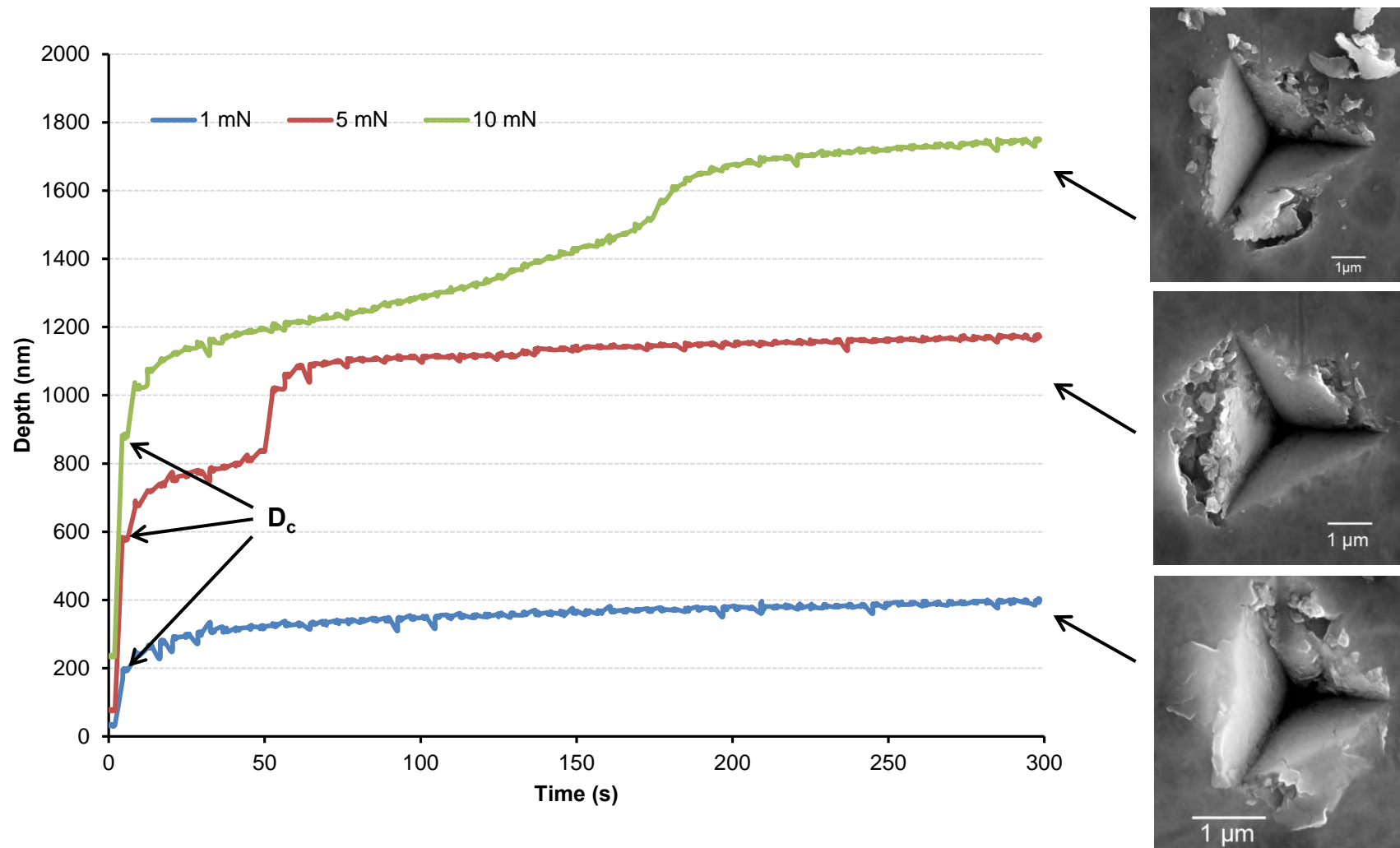
Figure 4.3.3- 2 Depth against time curve of CrN under different impact loads and corresponding SEM images of impact impressions
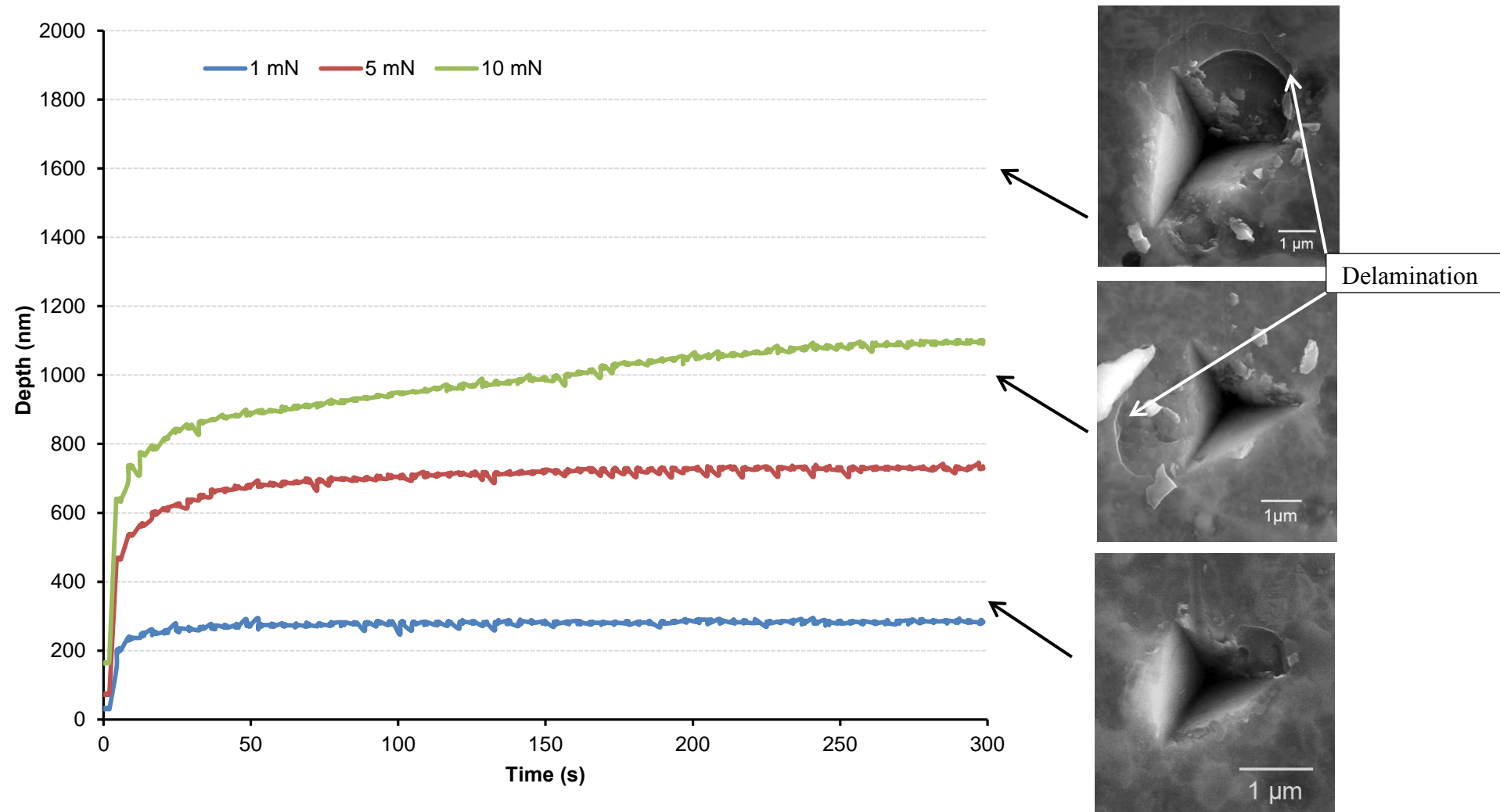
Figure 4.3.3- 3 Depth against time curve of C-II under different impact loads and corresponding SEM images of impact impressions
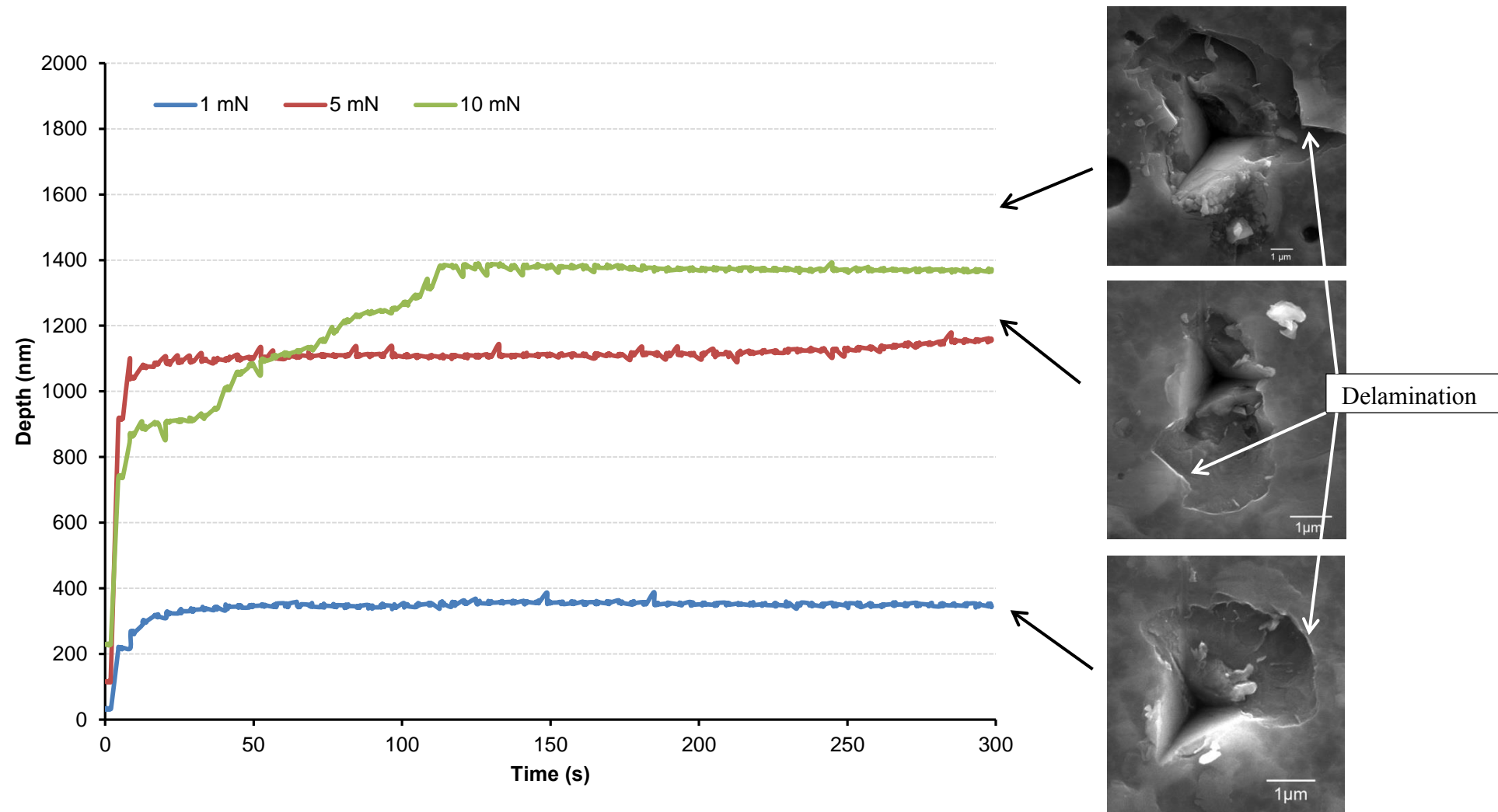
Figure 4.3.3- 4 Depth against time curve of C-I-5 under different impact loads and corresponding SEM images of impact impressions
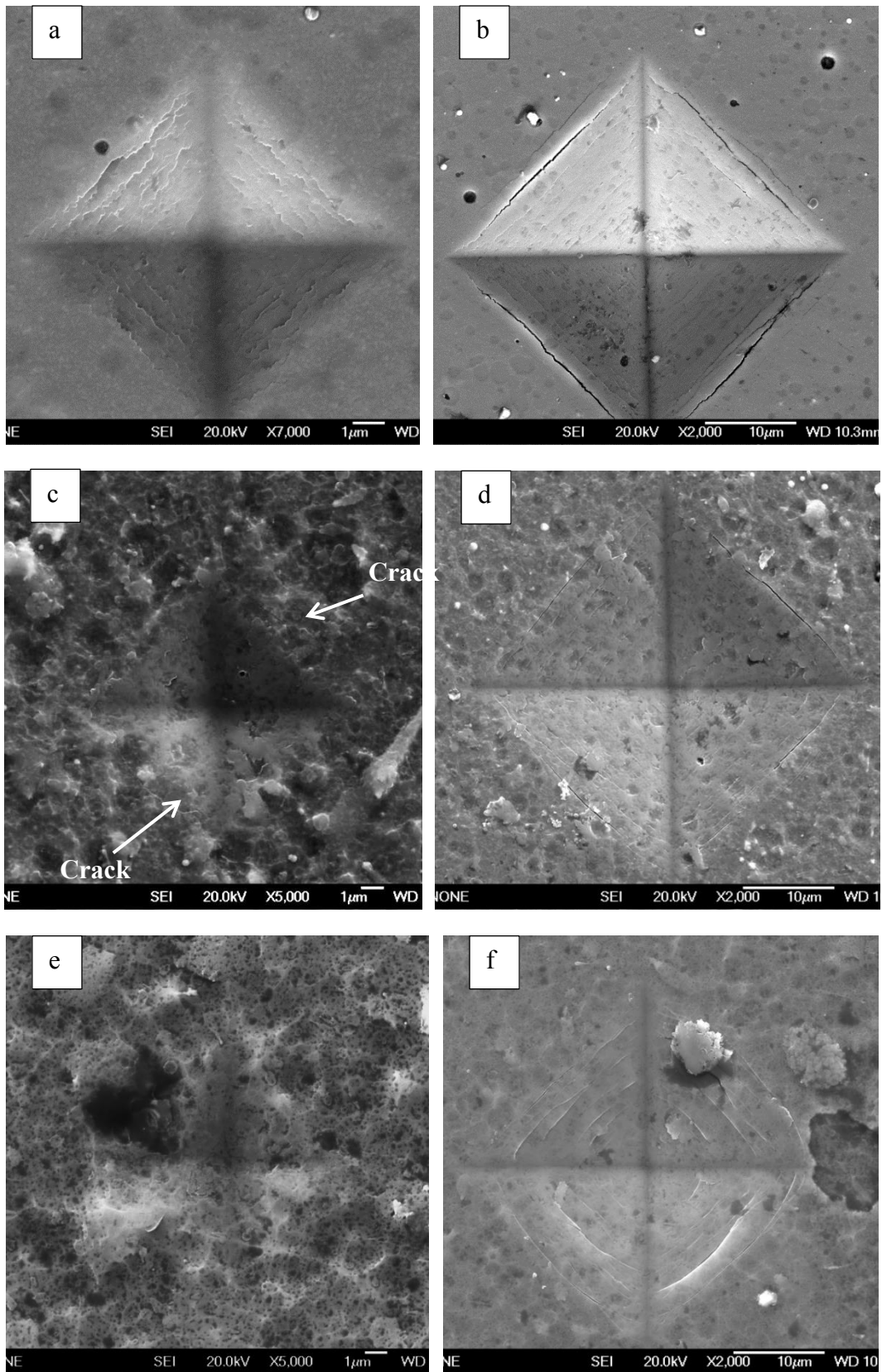
Figure 4.3.4- 1 Impressions of Vicker's indentations left on a,b) CrN, c,d) C-II and e,f) C-I-10, under the load of 100 g (left) and 1 kg (right)
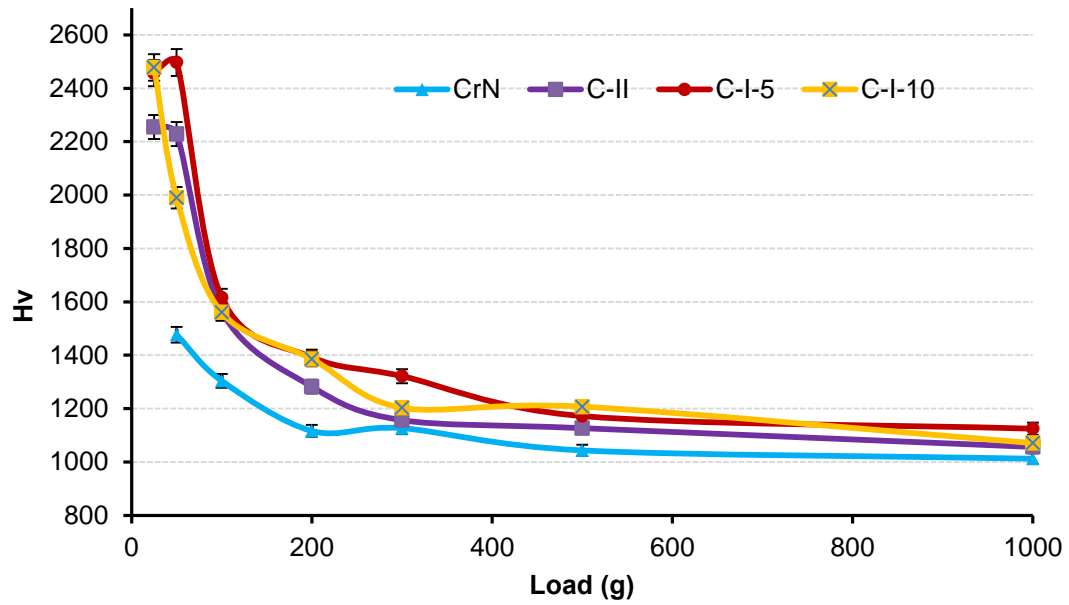
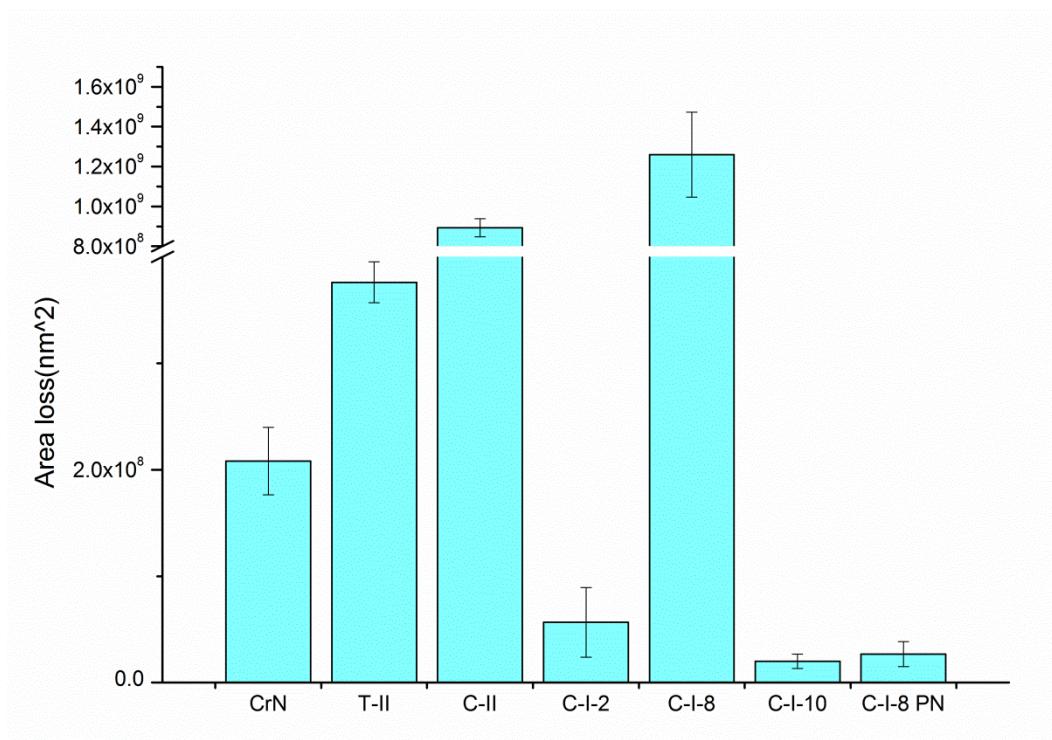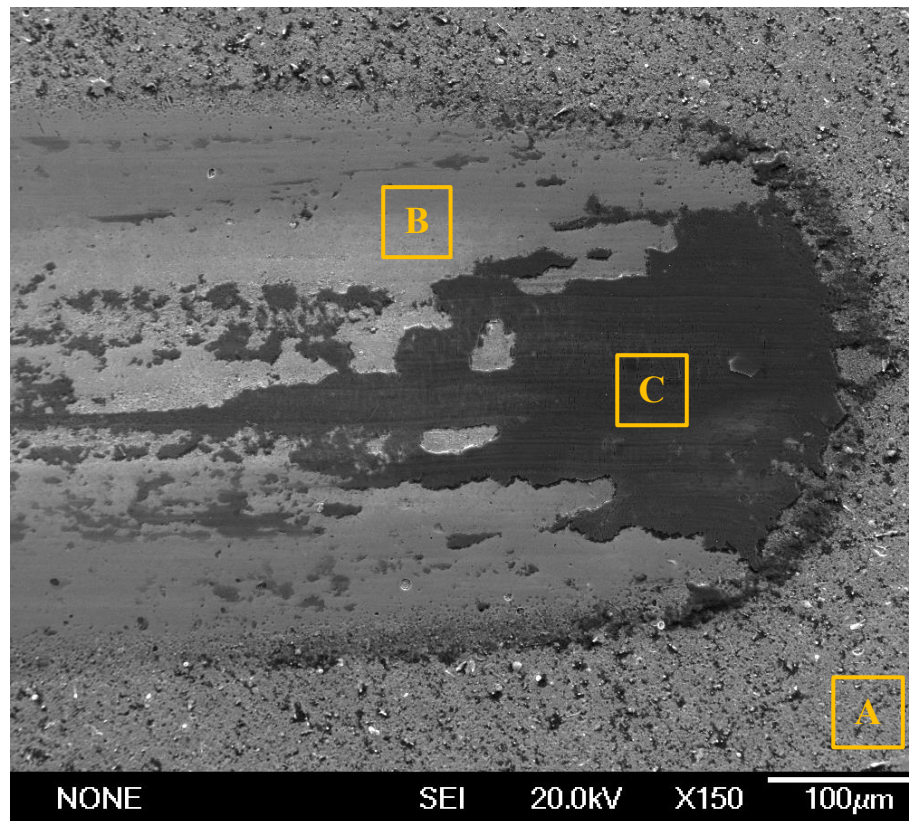**Figure 4.3.4- 2 Hardness of selected coatings under different loads**

Figure 4.4.1- 1 Average area loss of the wear track after room temperature reciprocating sliding wear test against WC-Co ball

at %	C	N	O	Al	Si	Ti	Fe	W
A	4.76	44.37		11.39	5.02	34.00	0.46	
B	4.53	40.47		5.48	2.00	13.73	31.68	0.31
C	4.63		65.01	5.67	2.50	18.43	2.86	0.68

Figure 4.4.1- 2 SEM morphology of one end of the wear track on T-II after room temperature reciprocating sliding wear test against WC-Co ball and EDS analysis on corresponding marked regions
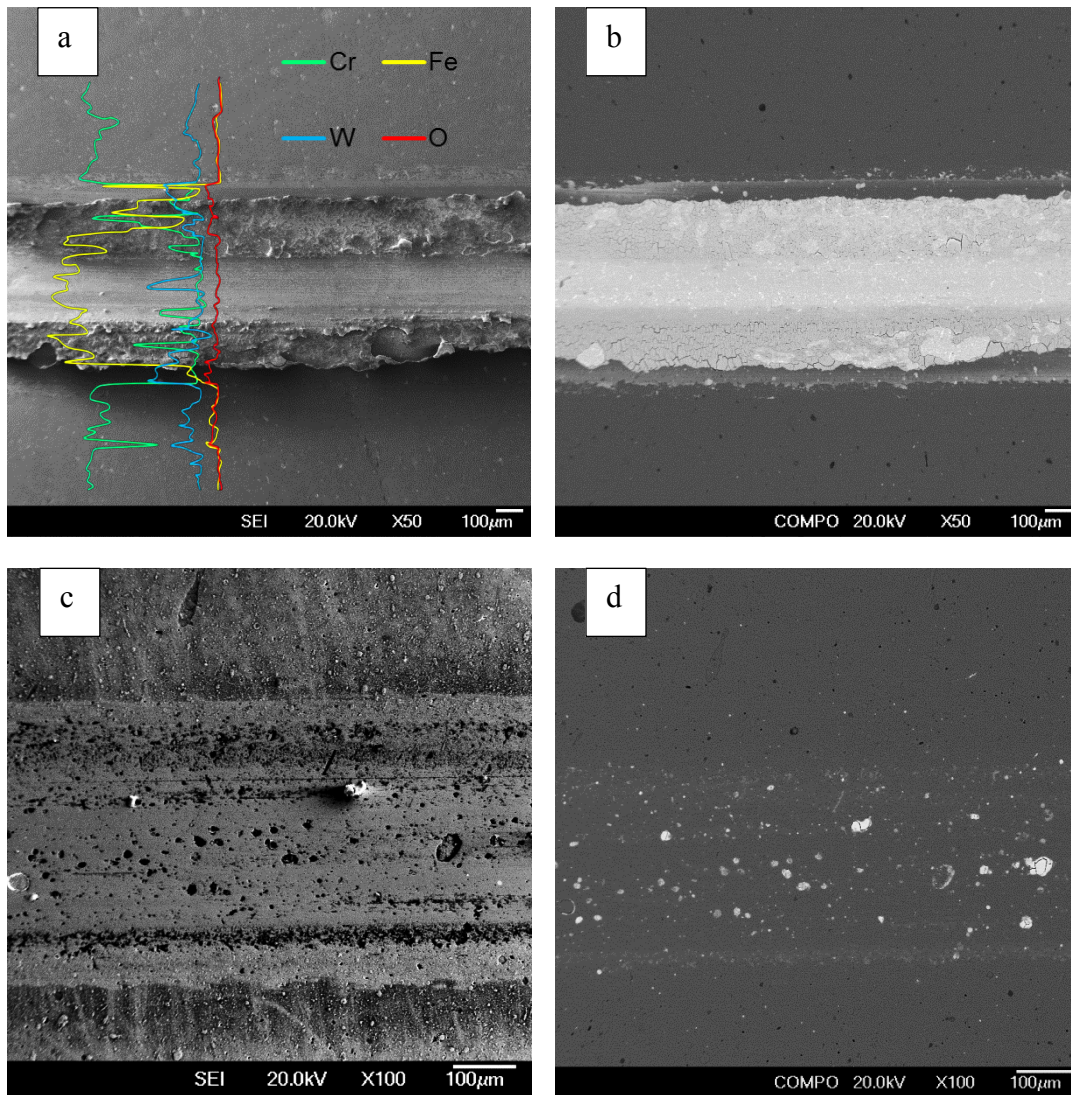
Figure 4.4.1- 3 SEM images in SE mode (left) and BSE mode (right) of the wear tracks on a,b) C-I-8 and c,d) C-I-10 sliding against WC-Co ball, with inserted EDS elemental line analysis for wear track of C-I-8
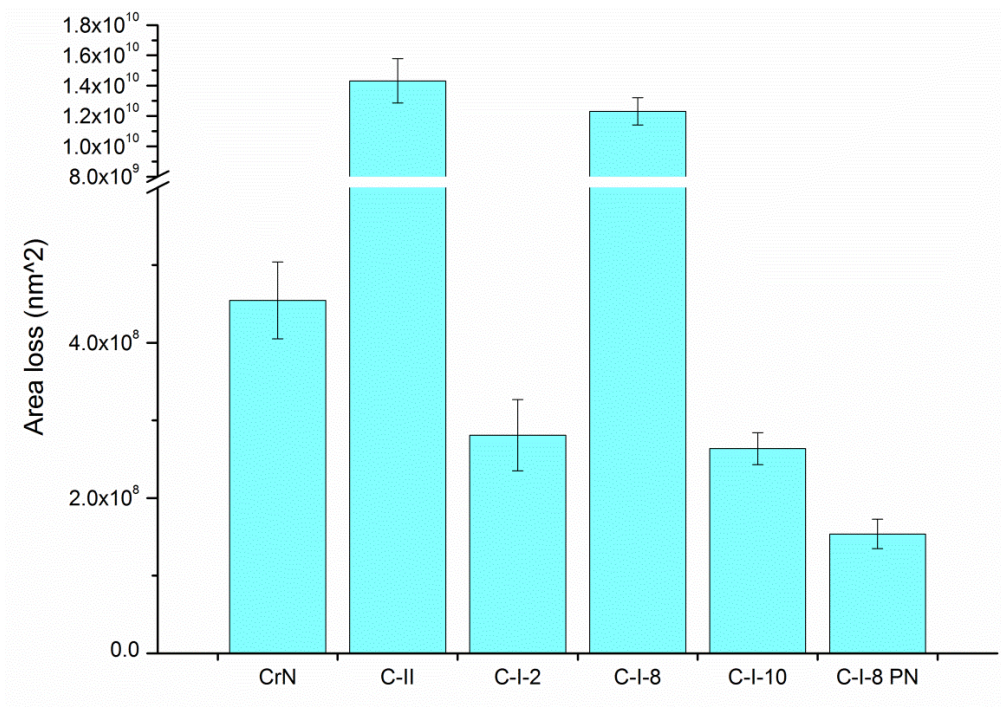
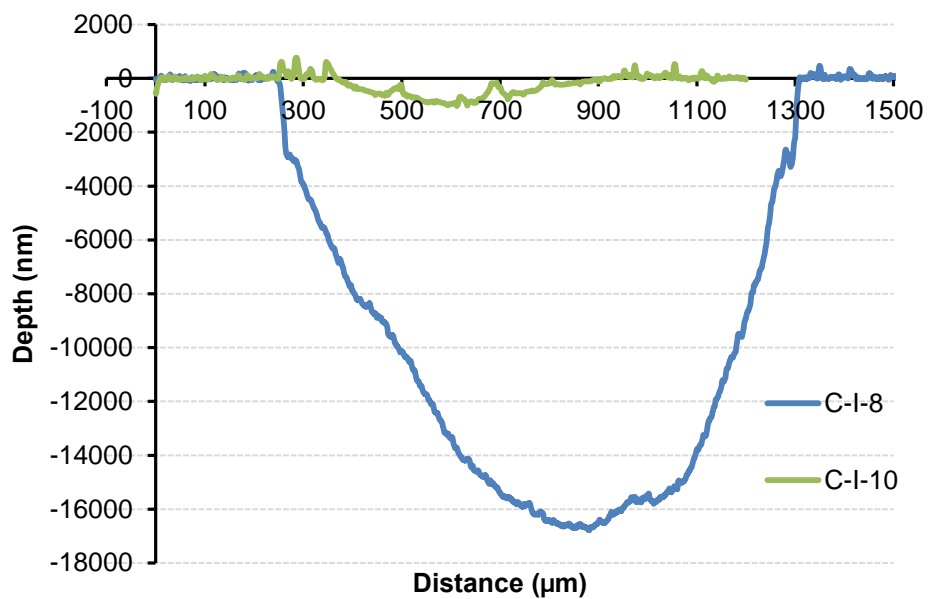**Figure 4.4.1- 4 Average area loss of the wear track after room temperature reciprocating sliding wear tests against Al$_2$O$_3$ ball**

Figure 4.4.1- 5 2-D profiles of the wear tracks on C-I-8 and C-I-10 after room temperature reciprocating sliding wear tests against Al$_2$O$_3$ ball
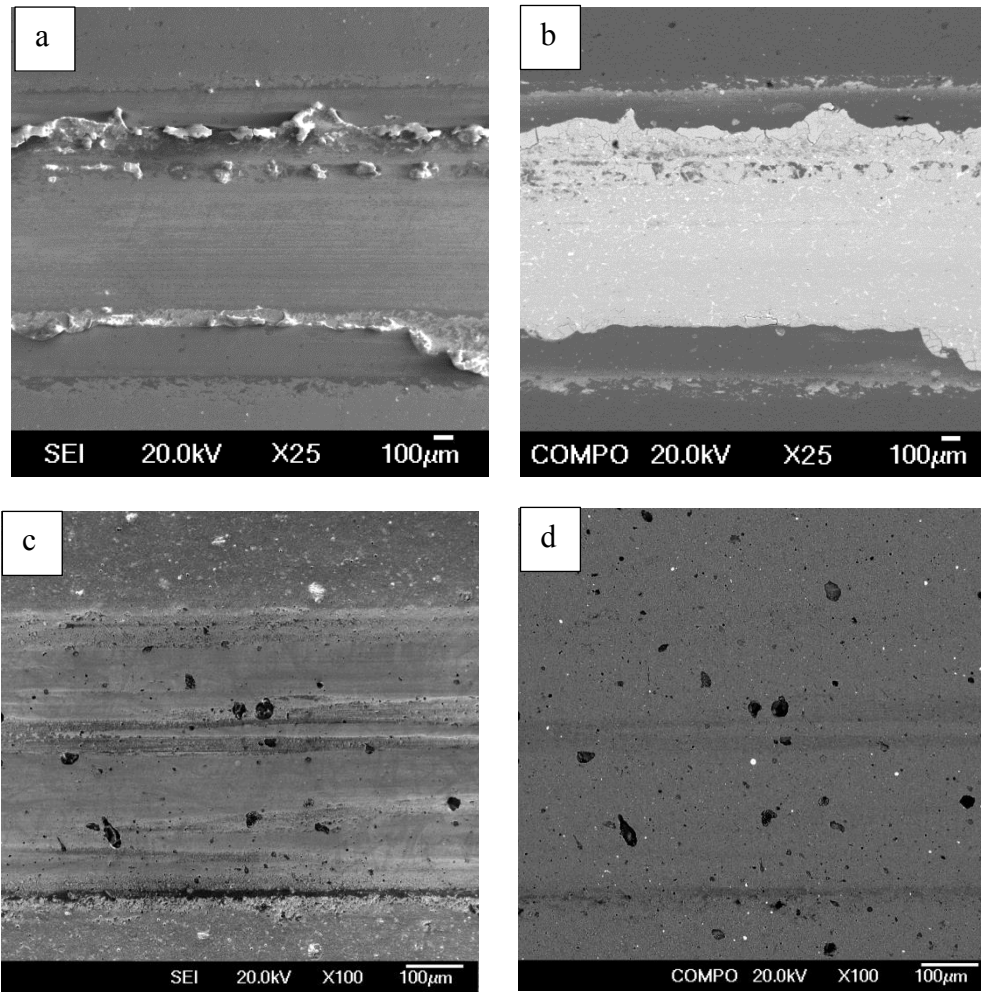
Figure 4.4.1- 6 SEM images in SE mode (left) and BSE mode (right) of the wear tracks on a,b) C-I-8 and c,d) C-I-10 sliding against Al$_2$O$_3$ ball

Figure 4.4.1- 7 a) FIB SEM topview of the edge of the wear track on C-II, the yellow line denotes the position that ion milling took place; and b) FIB SEM tilted view showing the crack leading to coating delamination
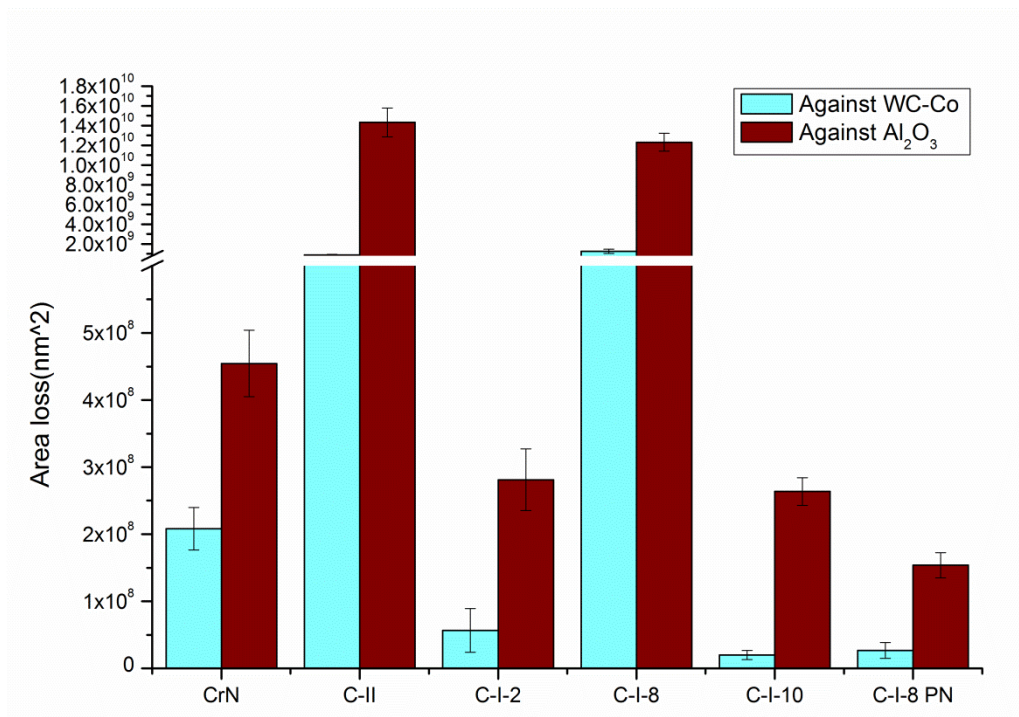
Figure 4.4.1- 8 Comparison of the average area wear loss of the wear tracks after reciprocating sliding wear test against two different counterpart
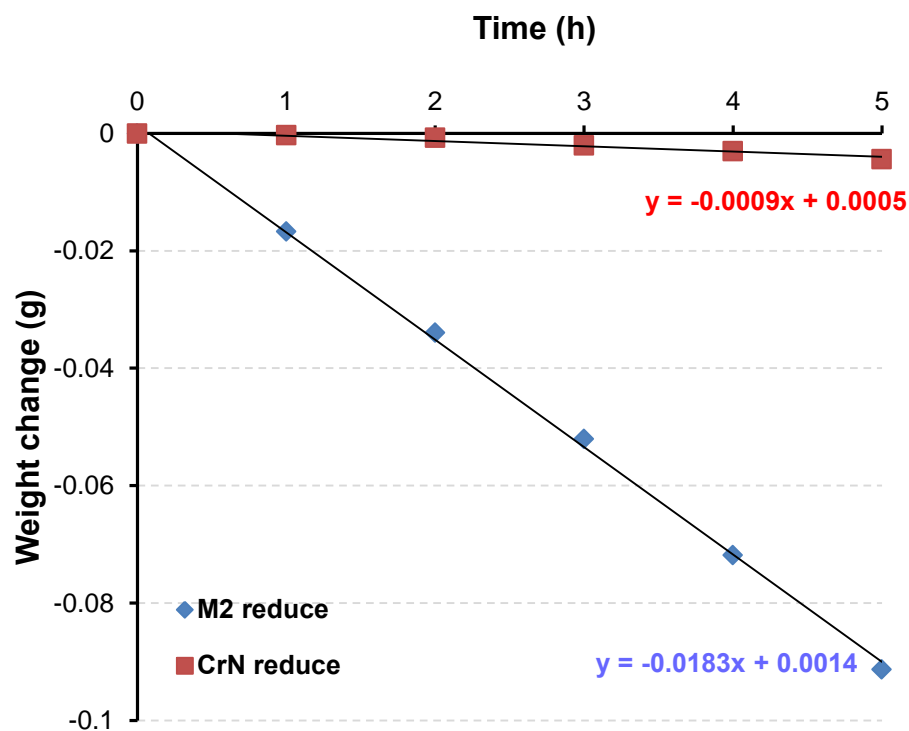

Figure 4.4.2- 1 The weight change of the tribological pair against time during the rolling-sliding wear test where CrN worn against M2
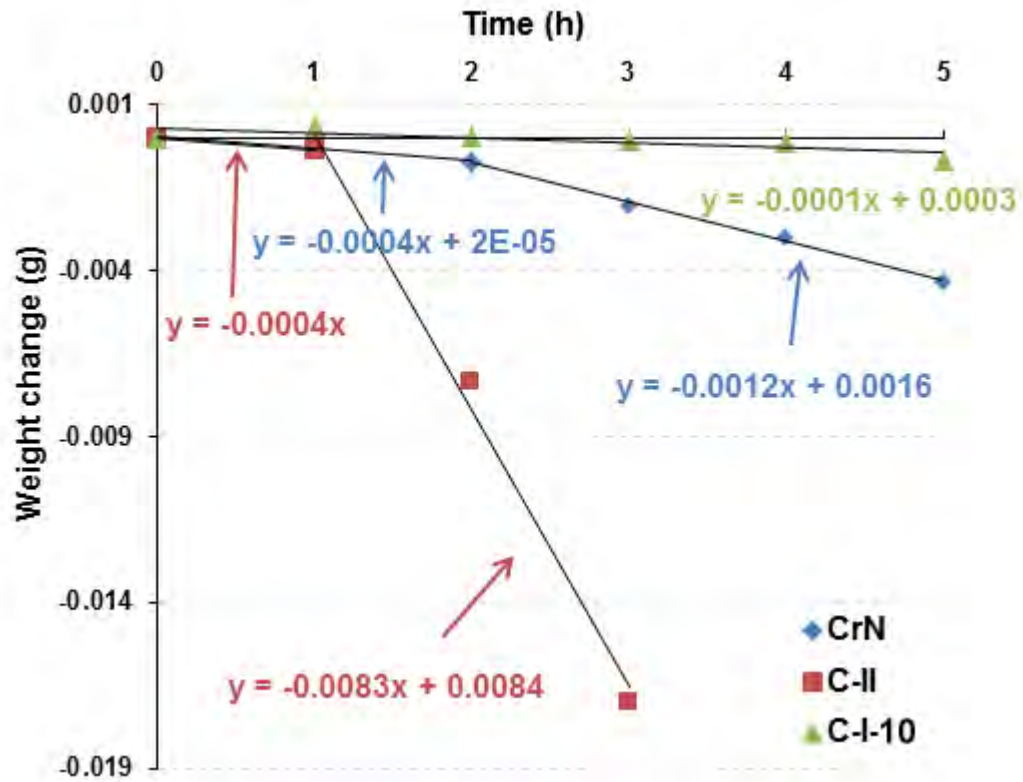
Figure 4.4.2- 2 The summary of weight change of coated samples against time during rolling-sliding wear tests with M2 counterpart
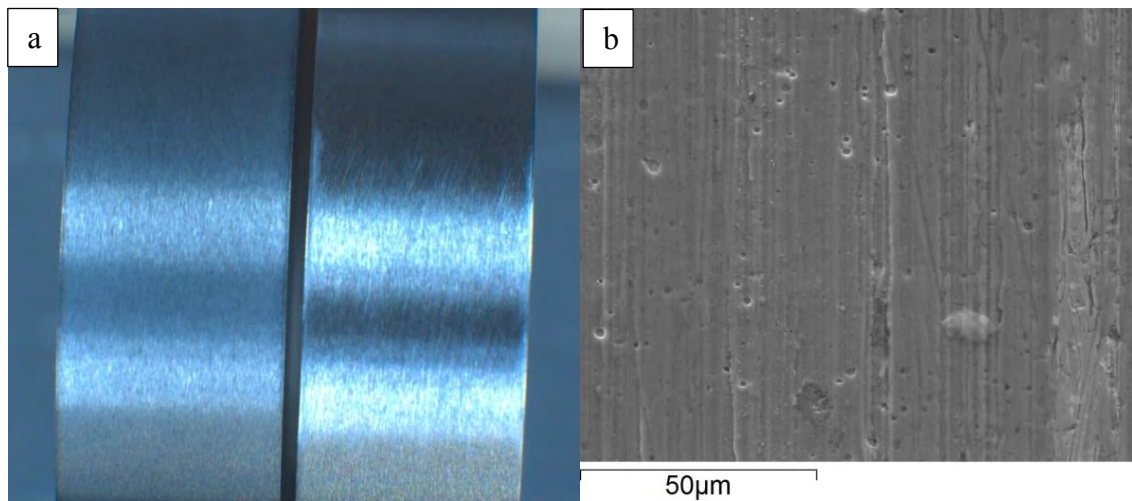
Figure 4.4.2- 3 a) The visual observation of the tribological pair of C-I-10 coated wheel (left) and M2 wheel (right) before the wear test and b) the SEM morphology of the C-I-10 coated wheel before the wear test
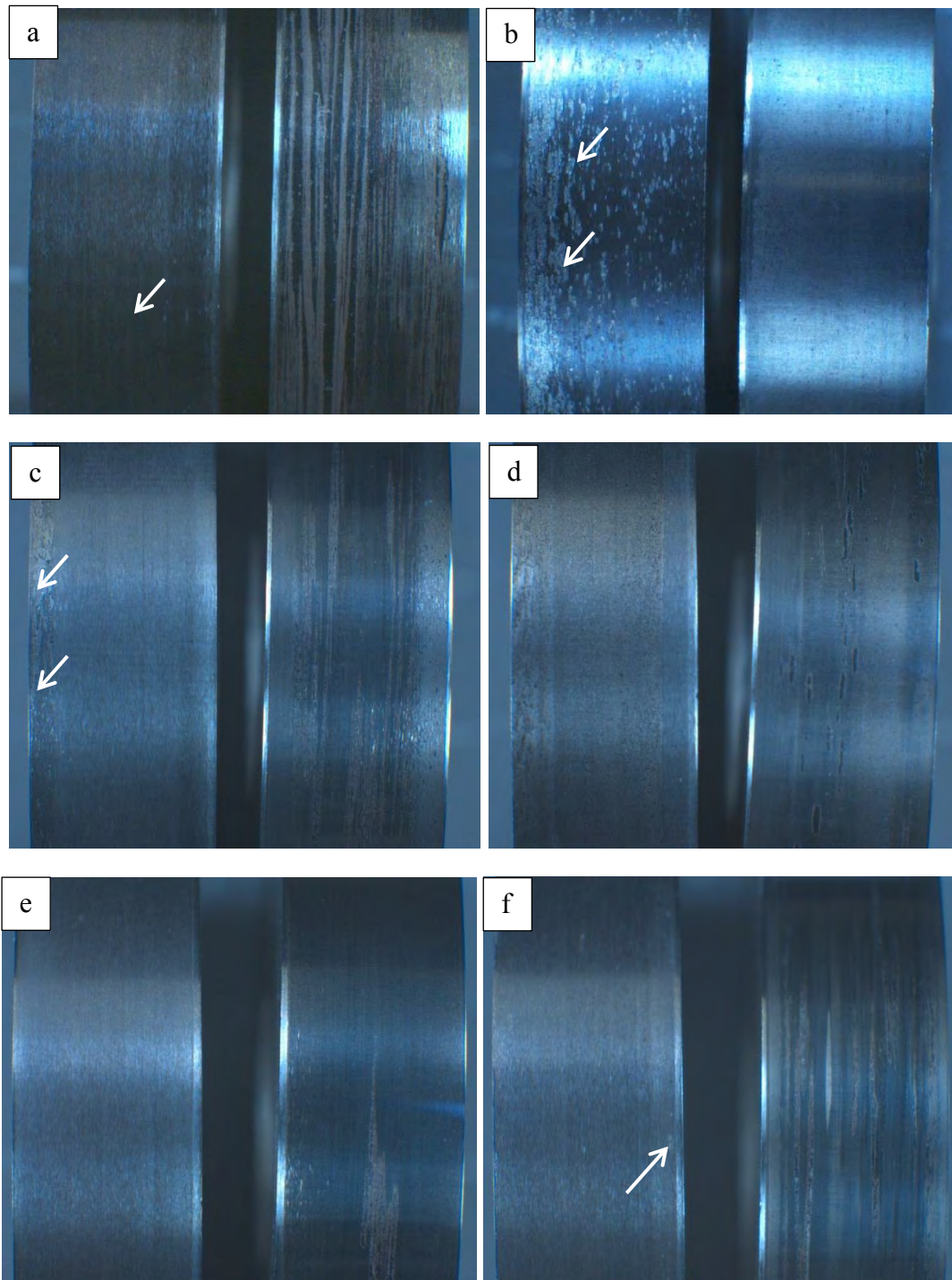
Figure 4.4.2- 4 Photos taken via a digital camera showing the morphology of the tribological pair with coated wheel on the left and M2 wheel on the right: CrN vs M2 after a) 1 hour and b) 5 hours; C-II vs M2 after c) 1 hour and d) 2 hours; C-I-10 vs M2 after e) 1 hour and f) 5 hours. The arrows denote areas of spallation or delamination
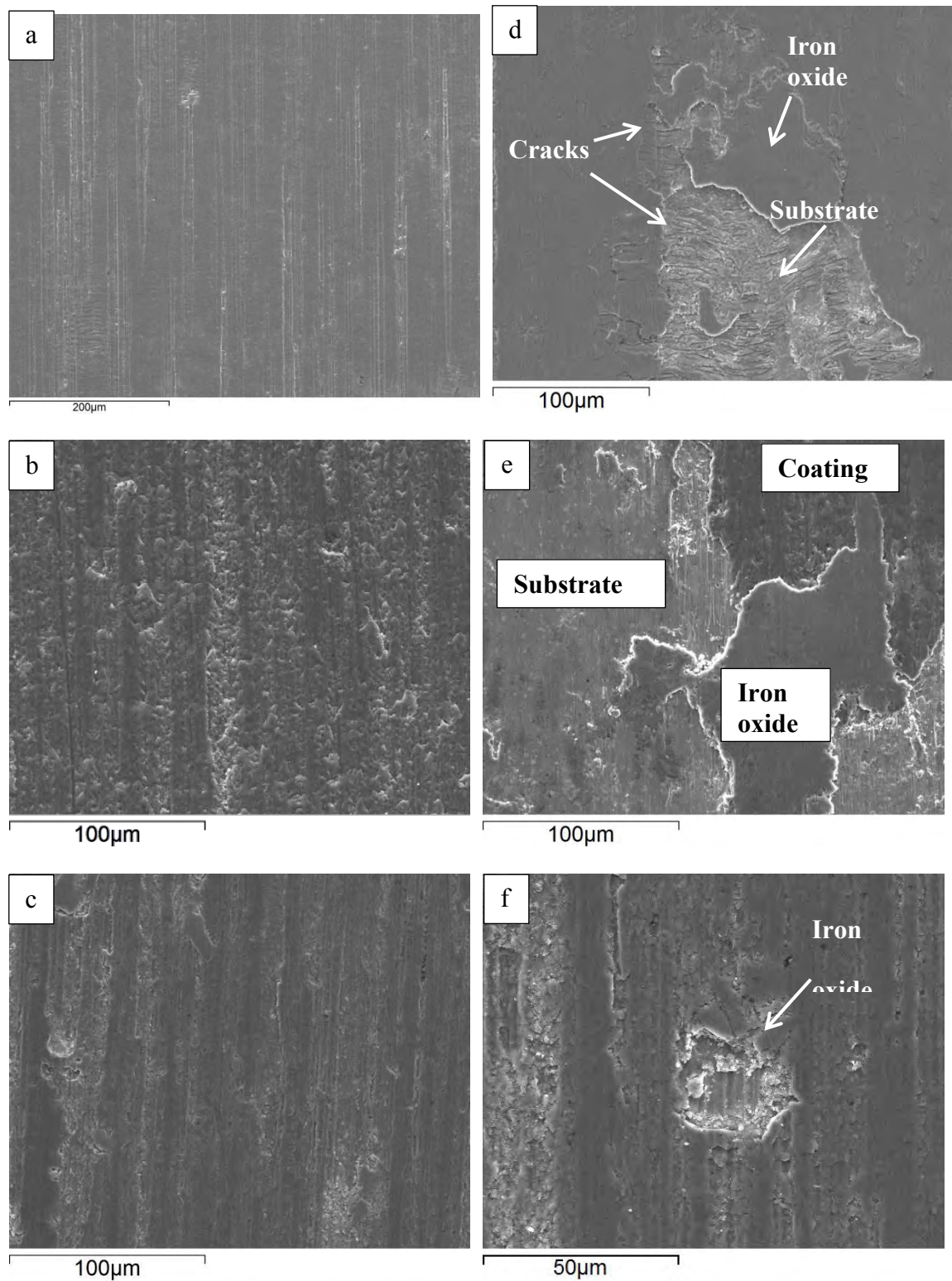
Figure 4.4.2- 5 SEM images showing the morphology of the worn surfaces after 1 hour (left) and after 5 hours (right, 2 hours for C-II) of a,d) CrN, b,e) C-II and c,f) C-I-10. The sliding direction was vertical in all images.

182

	As-deposited	**700 °C**	**900 °C**
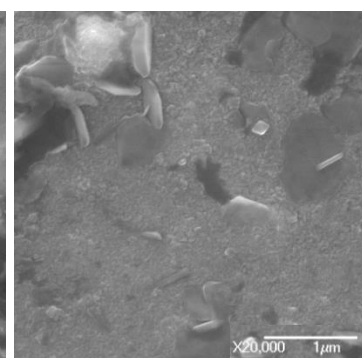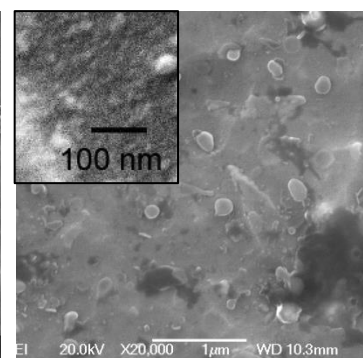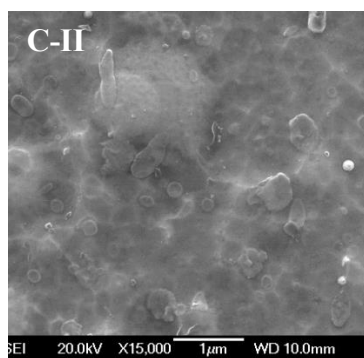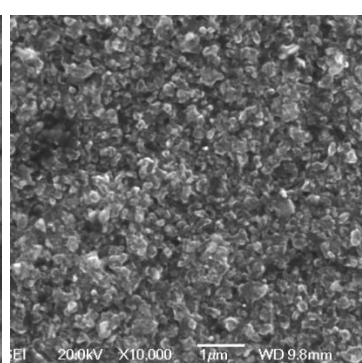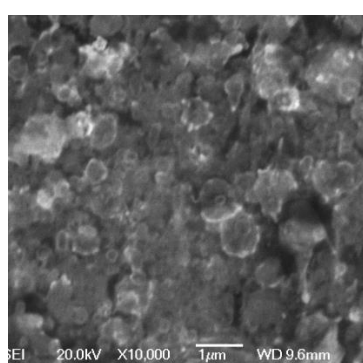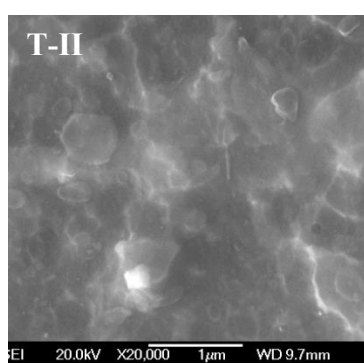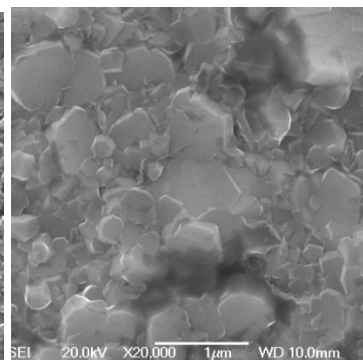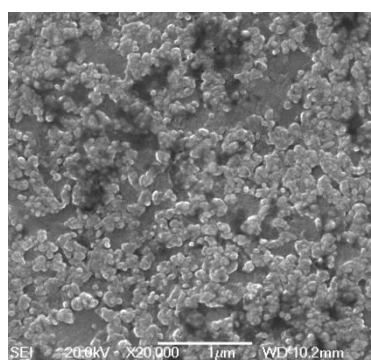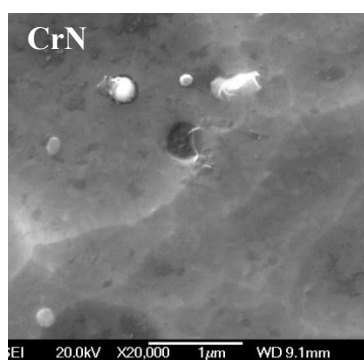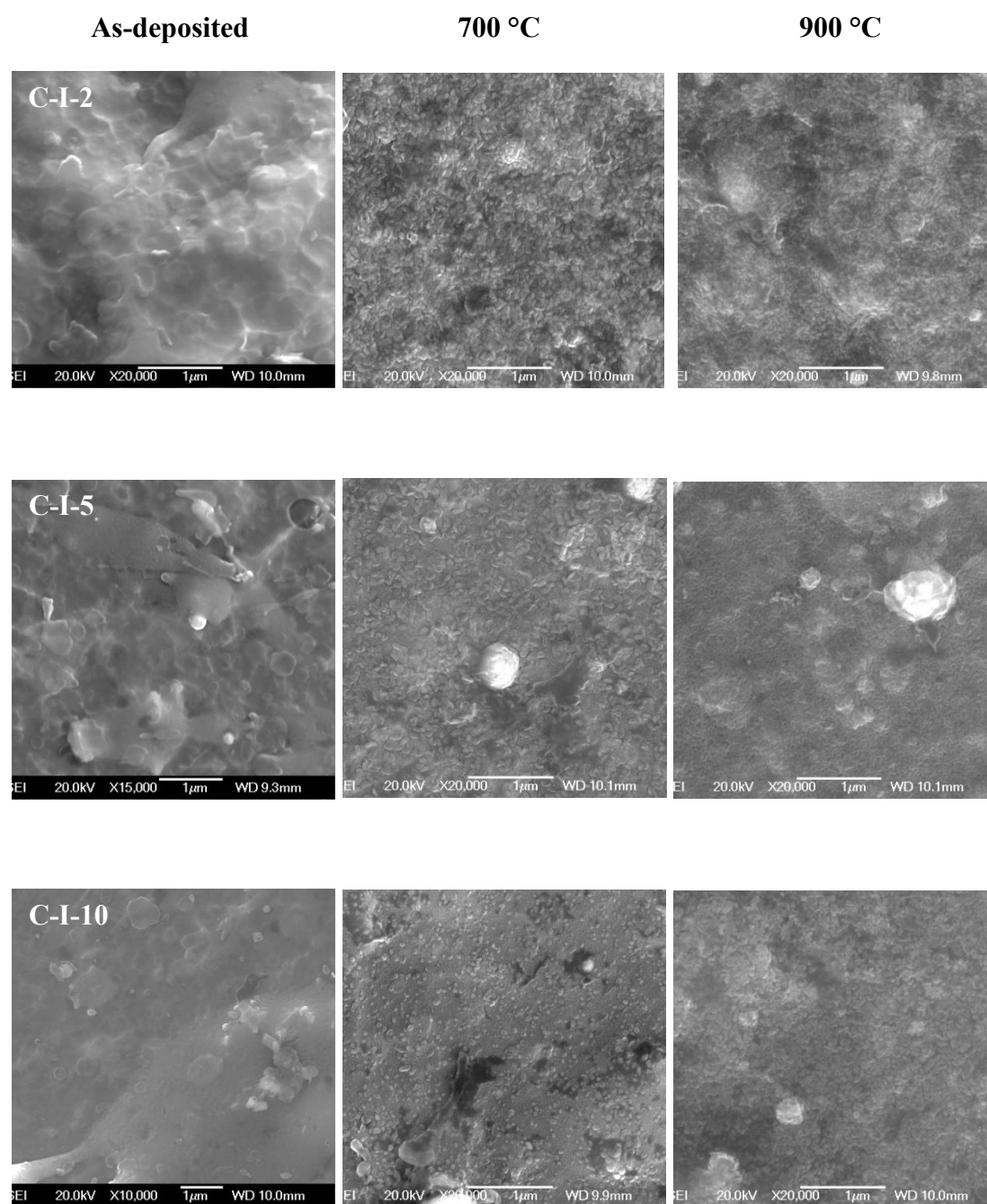
Figure 4.5.1- 1 SEM morphology of as-deposited coating (left), and morphology of coating surfaces after oxidation treatment for 2 hours at 700 °C (middle) and 900 ℃ (right)
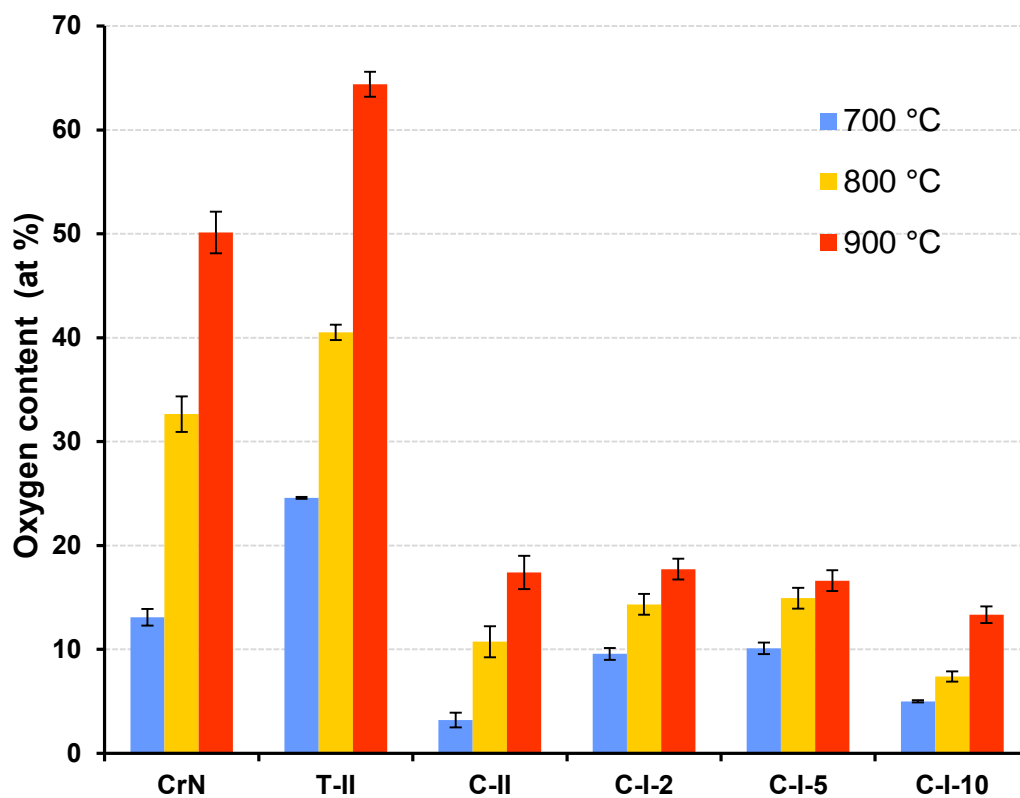
Figure 4.5.1- 2 Atomic concentration of oxygen in the coating surfaces after thermal oxidation treatment at different temperatures from EDS analysis
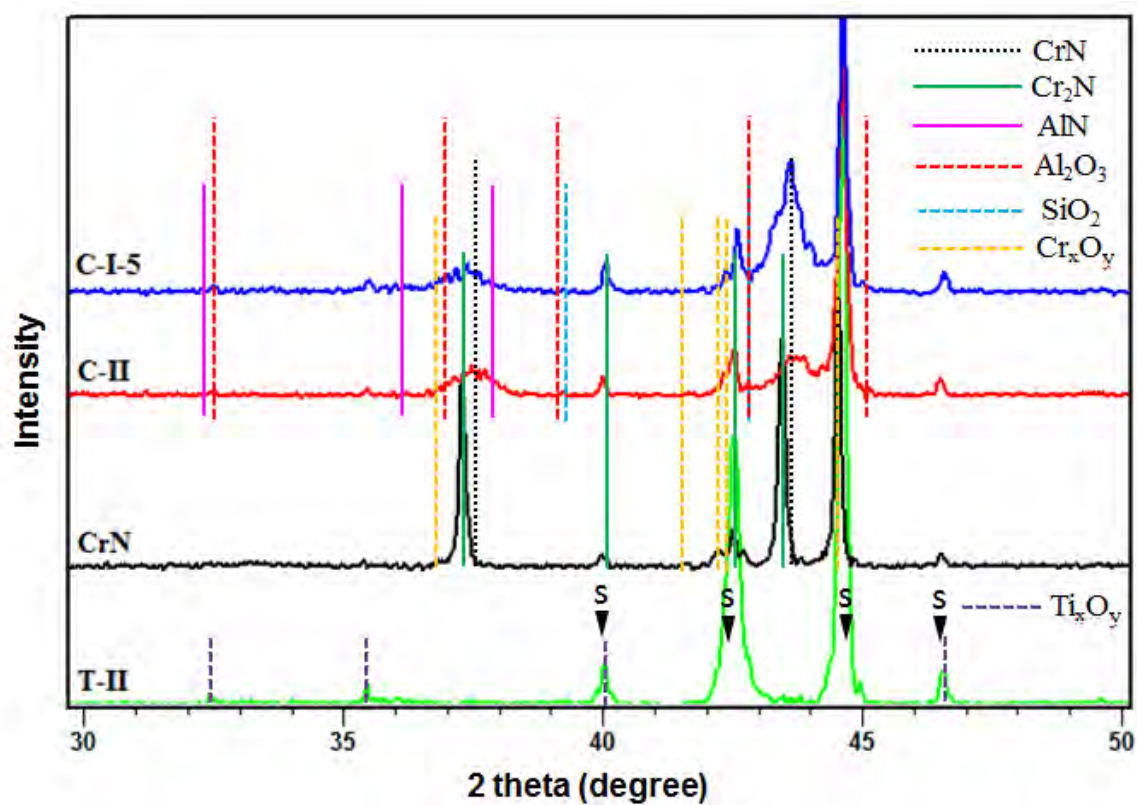
Figure 4.5.1- 3 XRD patterns of selected coatings after oxidation treatment at 700 ℃

185
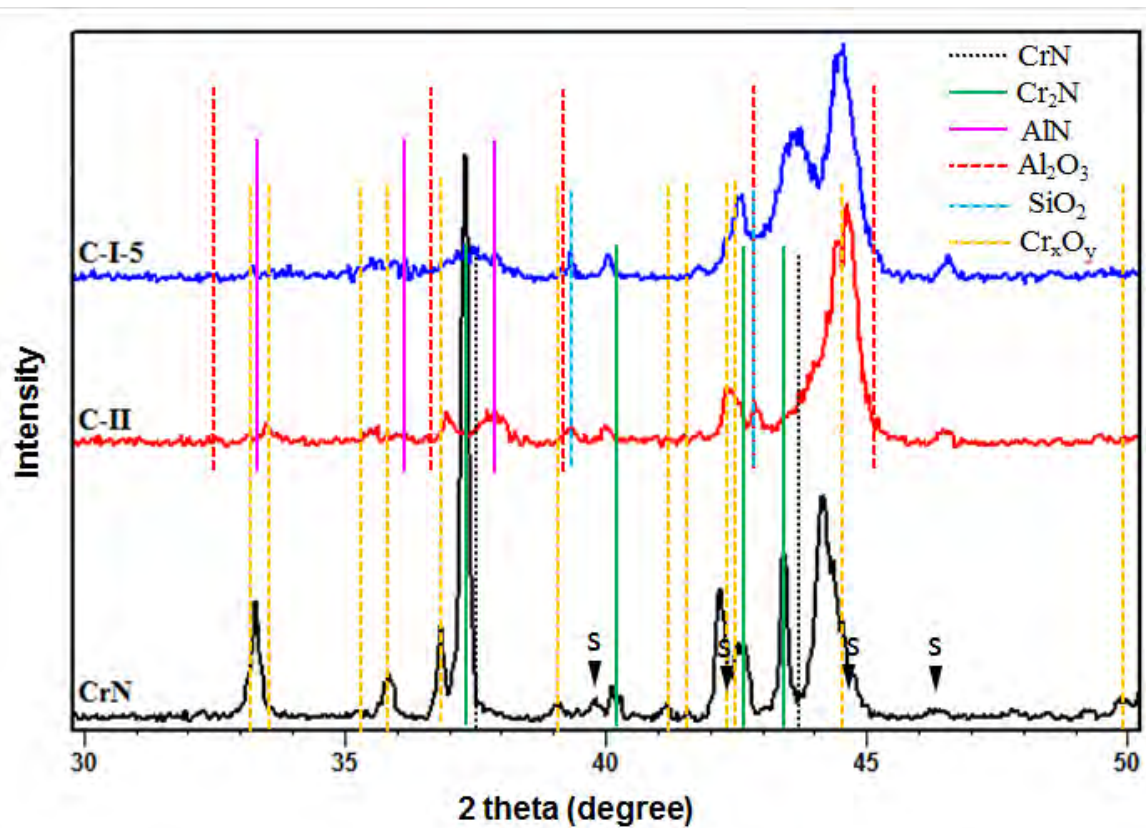
Figure 4.5.1- 4 XRD patterns of CrN, C-II and C-I-10 coatings after oxidation treatment at 900 ℃
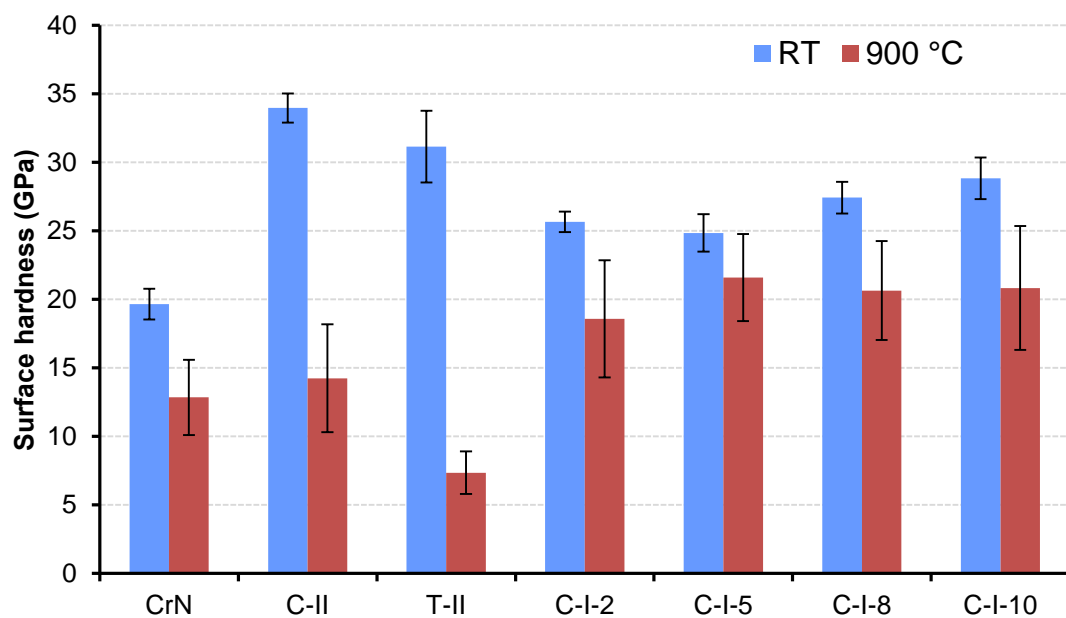
Figure 4.5.2- 1 Surface hardness coatings after oxidation treatment at 900 °C, in comparison to hardness of as deposited coating, evaluated using nano-indentation
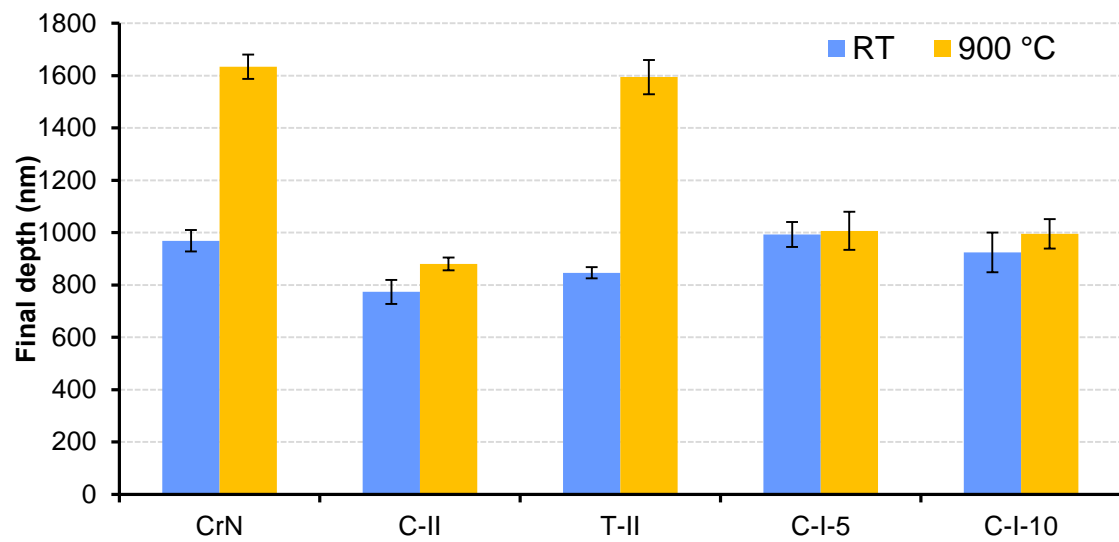
Figure 4.5.2- 2 Final impact depth of the coatings which were oxidised at 900 °C, after 75 impacts on the coating surfaces with different impact load
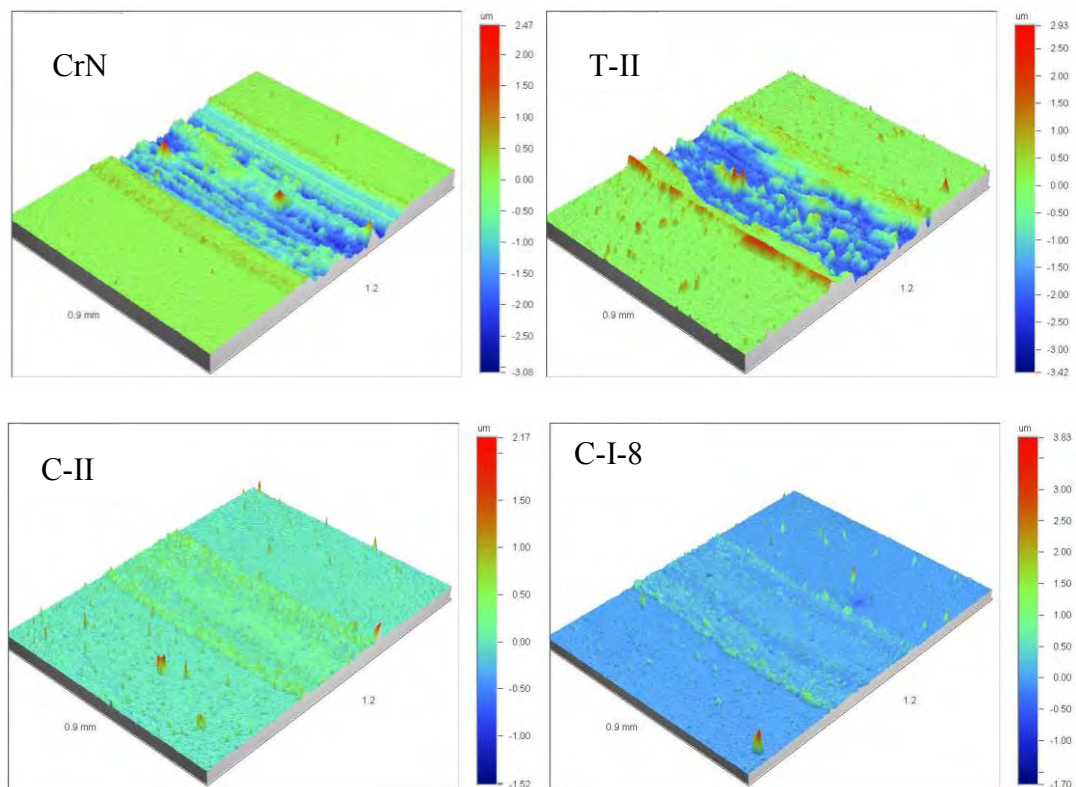
Figure 4.5.3- 1 3-D profiles of wear tracks on selected specimens after reciprocating sliding against WC-Co ball for 5000 cycles at 400 °C
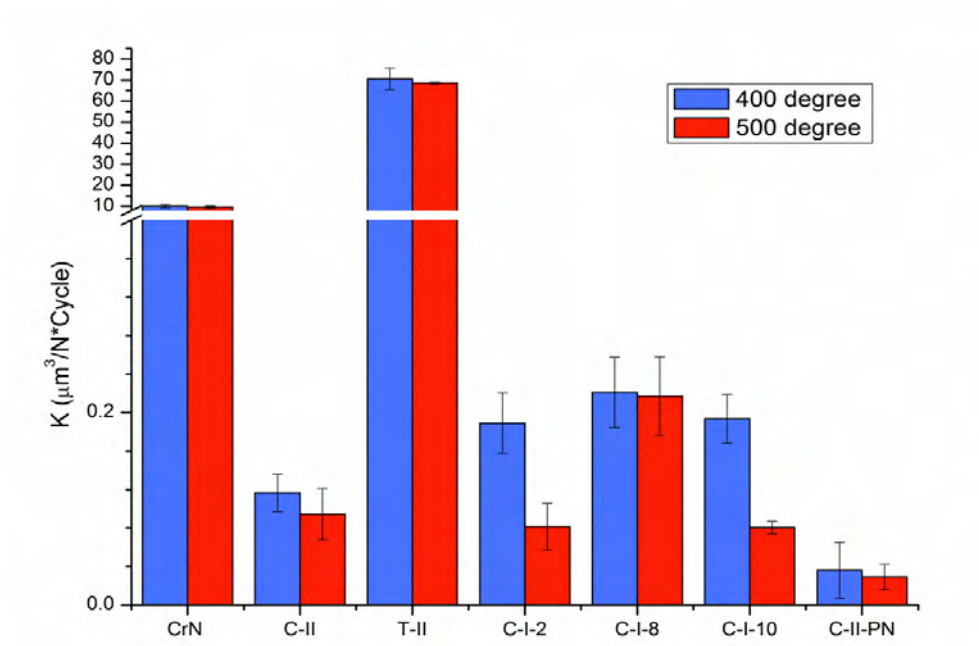
Figure 4.5.3- 2 Wear factor of all samples after reciprocating sliding wear test against WC-Co ball at 400°C and 500 °C
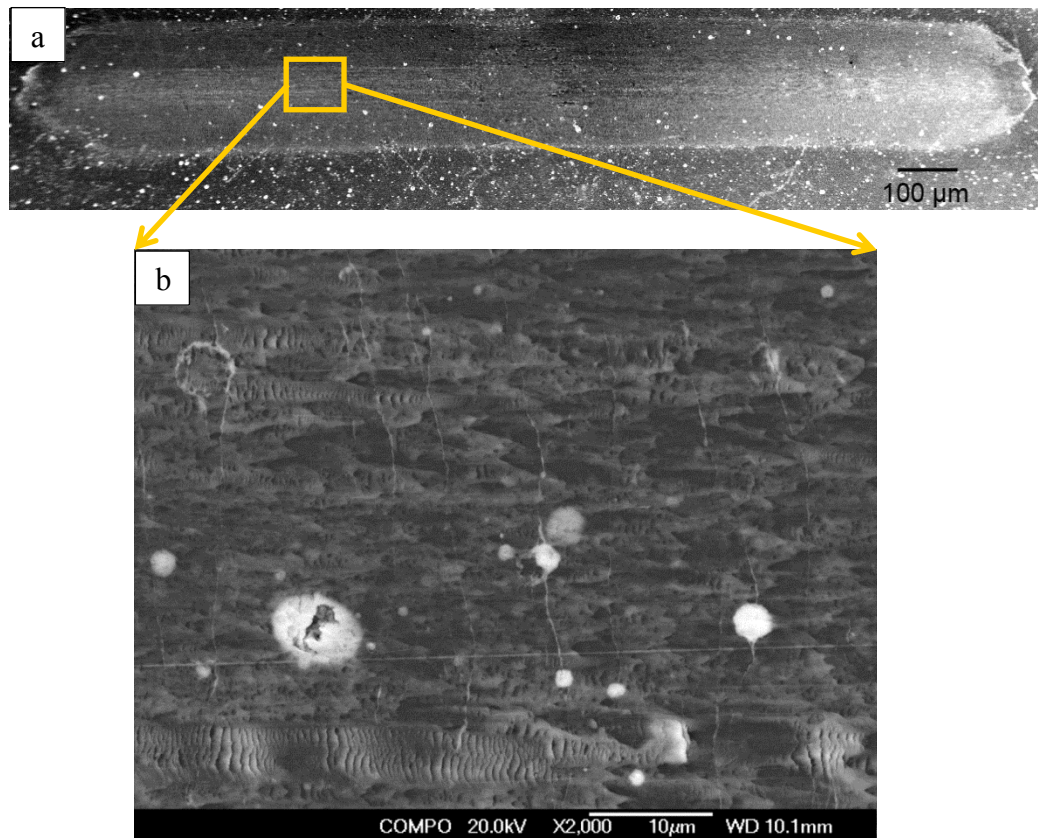
Figure 4.5.3- 3 a) Secondary electron image showing the overview of wear track of CrN after sliding against WC-Co balls at 400°C for 1000 cycles and b) backscattered electron image at high magnification of marked area
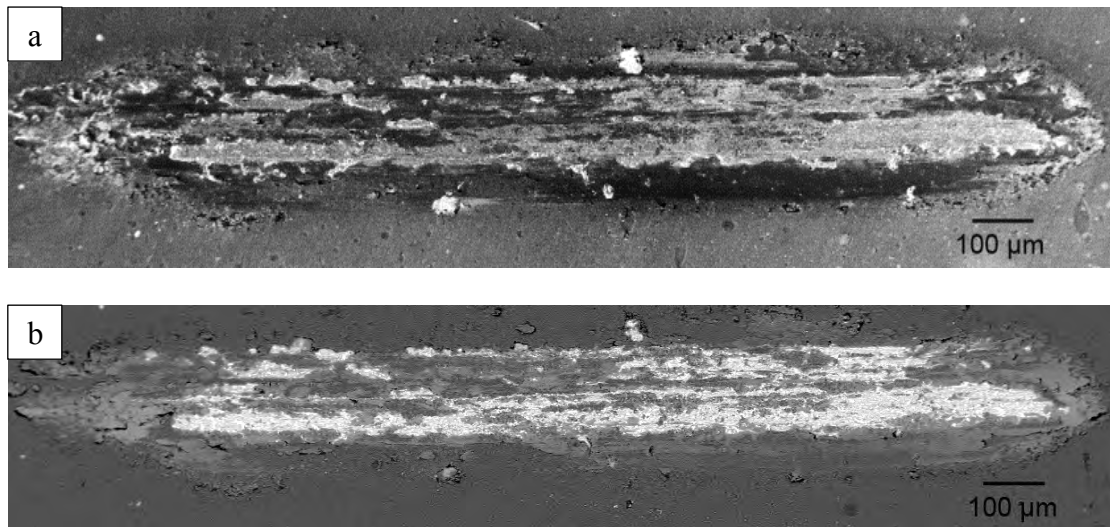
Figure 4.5.3- 4 a) Secondary electron image and b) corresponding backscattered electron image showing the overview of wear track of T-II after sliding against WC-Co balls at 400 °C for 1000 cycles
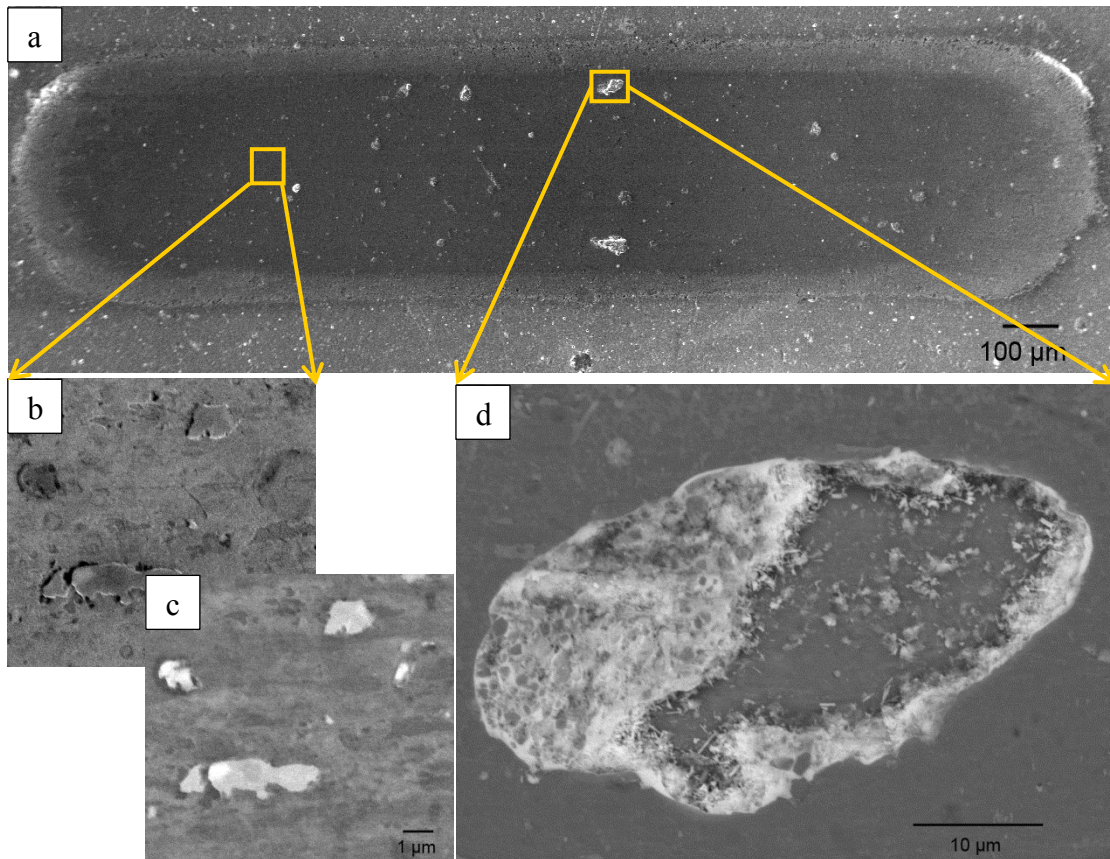
Figure 4.5.3- 5 a) Secondary electron image showing the overview of wear track of C-I-2 after sliding against WC-Co balls at 400°C for 20 k cycles, high magnification images in b) SE mode and c) BSE mode of the wear track and d) BSE image of the spallation site at high magnification
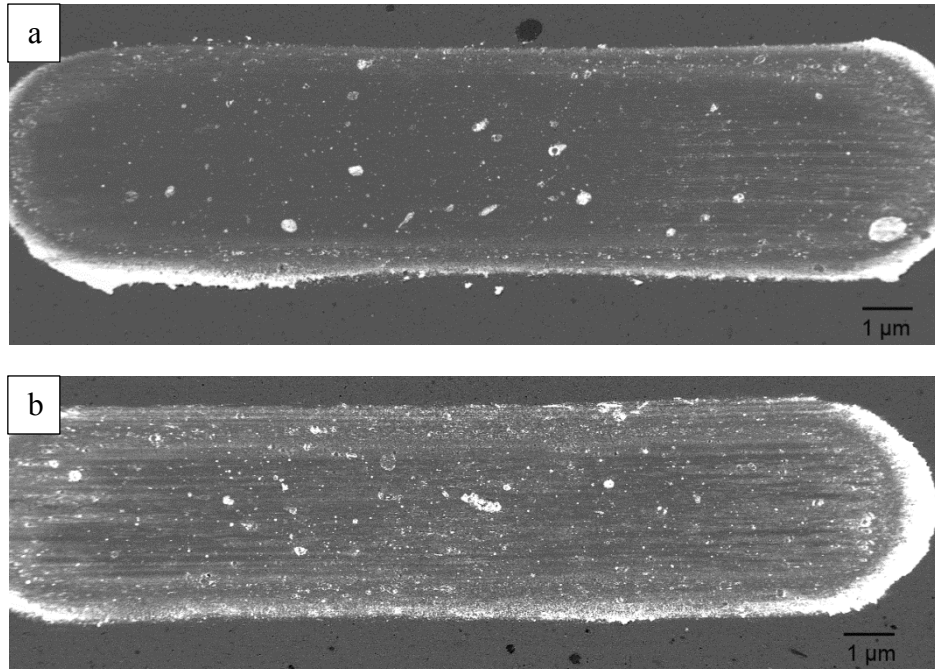
Figure 4.5.3- 6 BSE images of wear tracks of C-I-10 sample after sliding against WC-Co balls at a) 400°C and b) 500°C for 20 k cycles
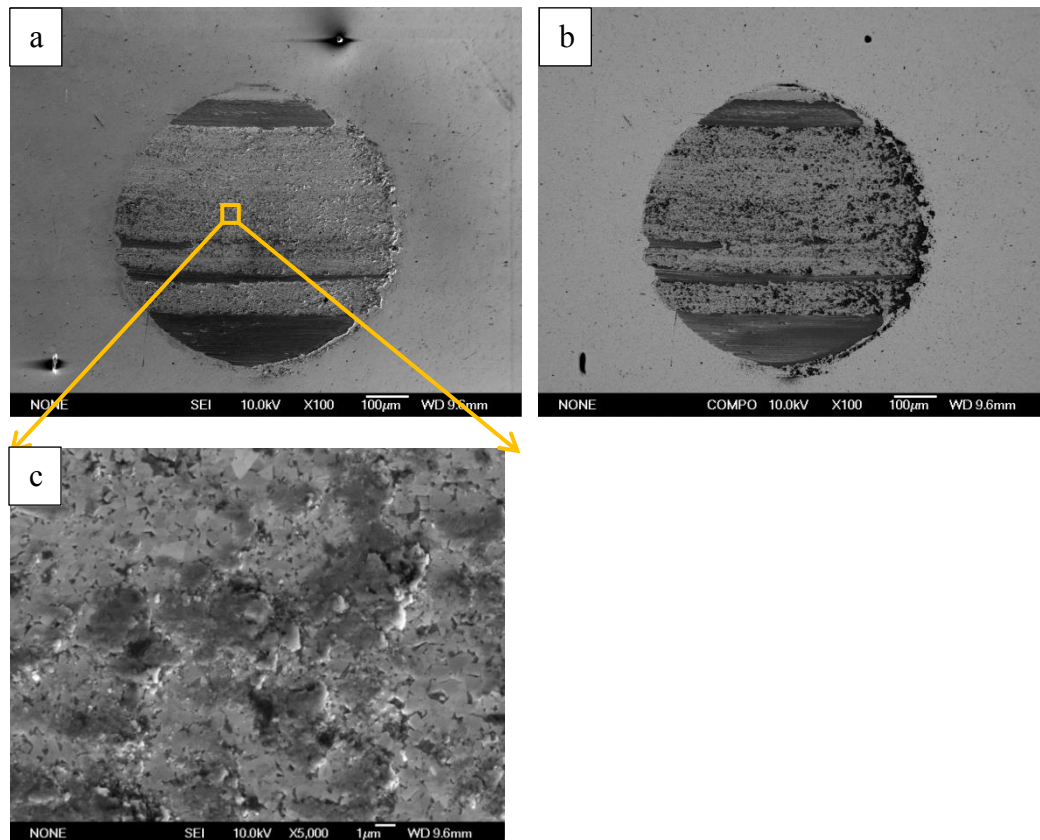
Figure 4.5.3- 7 SEM image in a) SE and b) BSE mode showing the morphology of the wear scar on the WC-Co ball after sliding against CrN at 400℃ for 1000 cycles, and SE images of c) the centre

at%	A	B
C	21.57	4.26
O	46.28	59.07
Al	7.87	11.49
Si		4.56
Ti	9.39	12.95
Fe	3.66	5.22
W	10.92	2.04
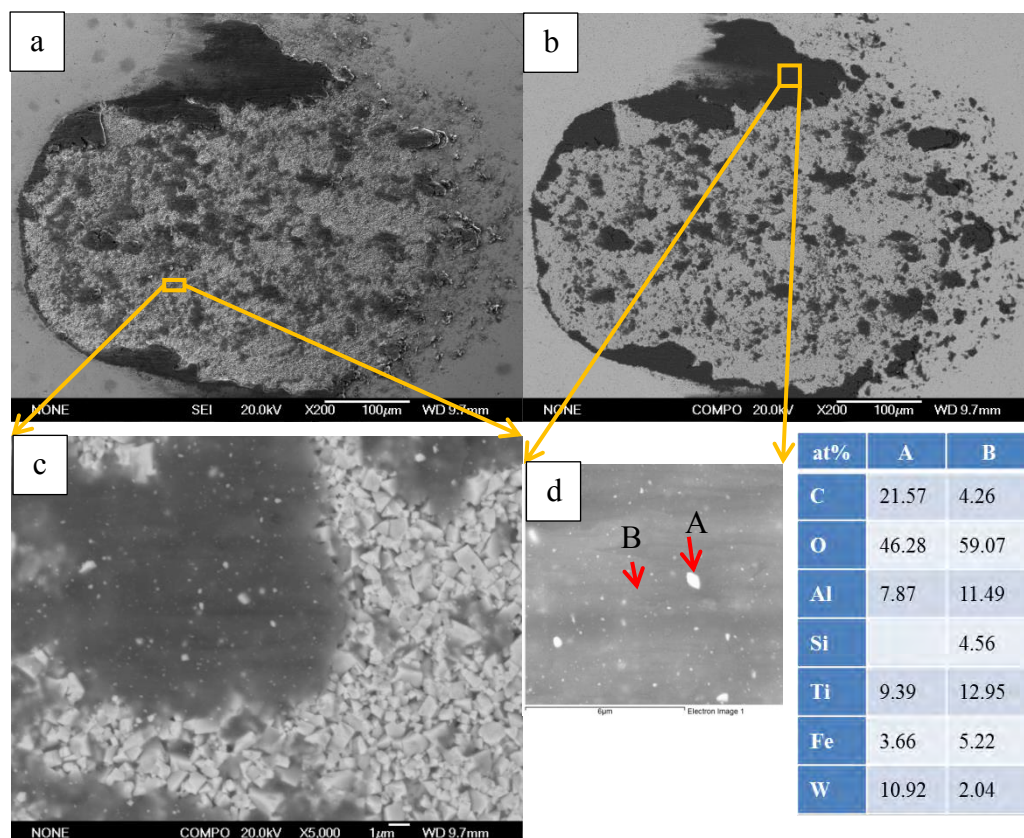
Figure 4.5.3- 8 SEM image in a) SE and b) BSE mode showing the morphology of the wear scar on the WC-Co ball after sliding against T-II at 400℃ for 5000 cycles, and high magnification images of c) the centre and d) the edge of the wear scar, inserted with the EDS compositional analysis of marked area in d)
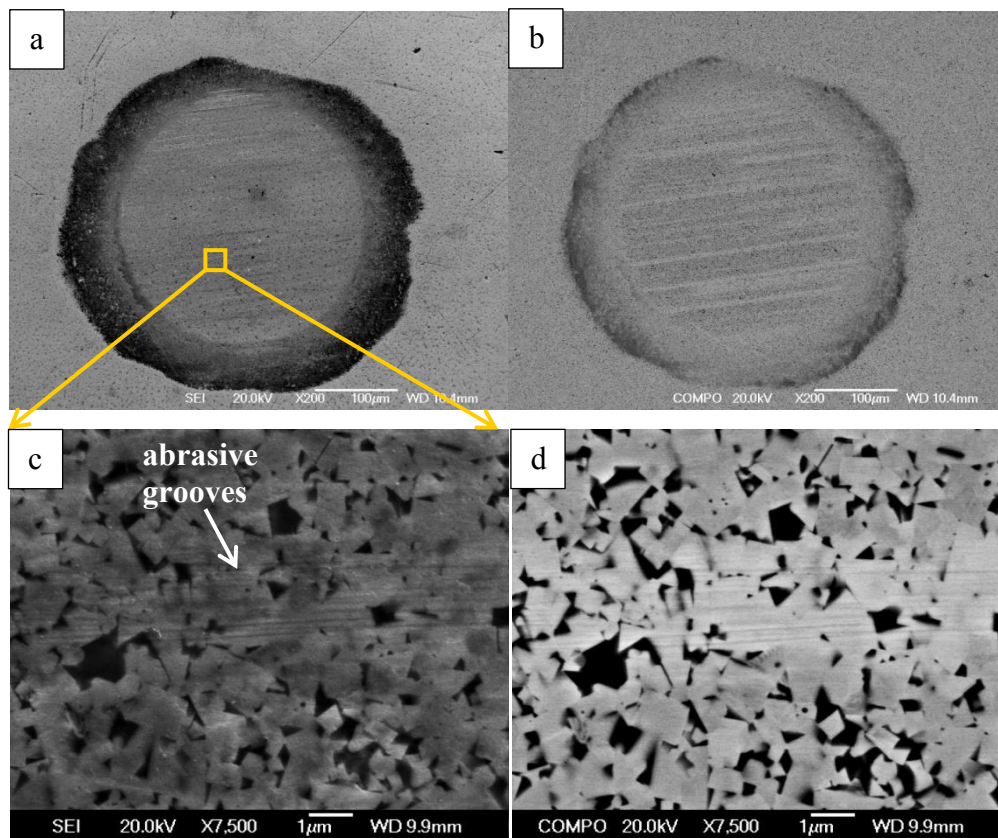
at%	C	O	Cr	Co	W
Centre	38.84	12.89		8.52	39.76
Edge	23.57	52.47	0.97	3.92	19.06

Figure 4.5.3- 9 SEM image in a) SE and b) BSE mode showing the morphology of the wear scar on the WC-Co ball after sliding against C-I-2 at 400°C for 20 k cycles, and high magnification images of the centre of the wear scar in c) SE and d) BSE mode, inserted with the composition analysis of the centre of the wear scar and the material accumulation around the edge
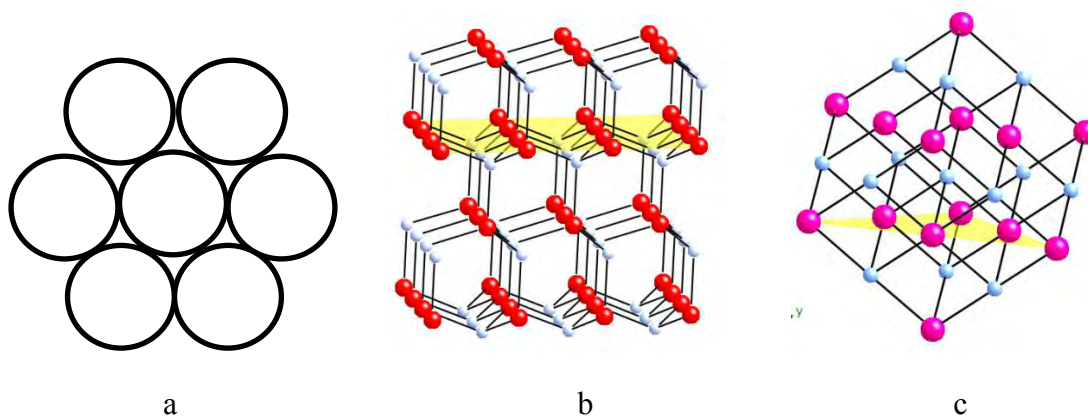
Figure 5.1.2- 1 a) Atomic structure of fcc (111) plane and hcp (0002) plane, b) crystal structure of AlN-like hcp-MeN phase and c) crystal structure of CrN-like fcc-MeN phase
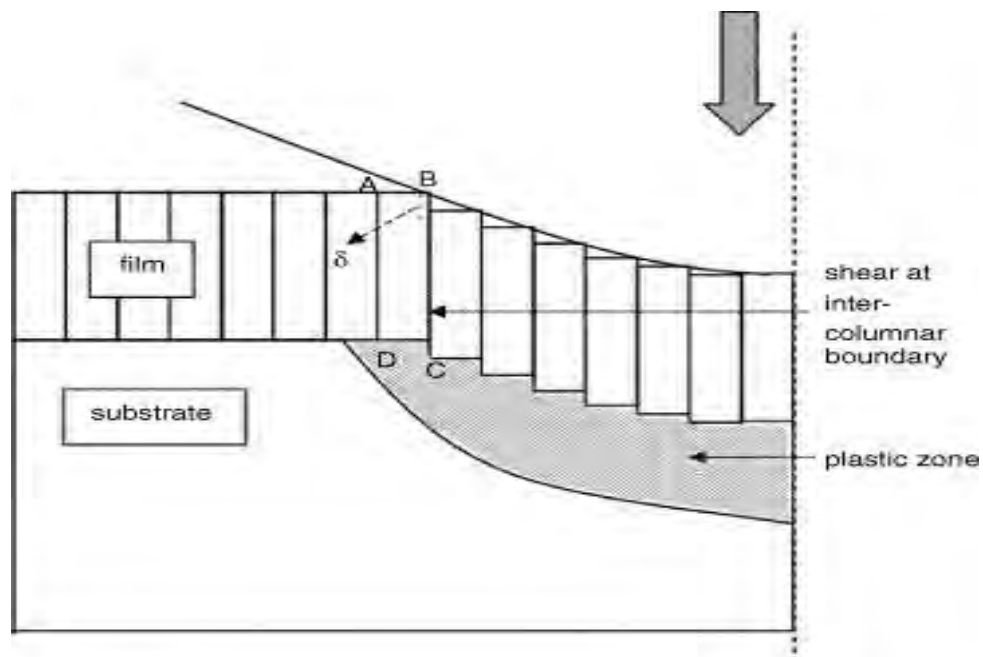
Figure 5.2.2- 1 the schematic of the shear at inter-columnar boundaries of a coating under indentation [197]
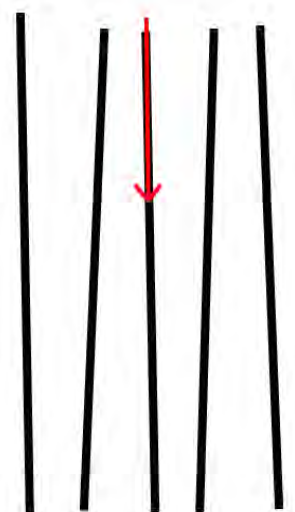
Columnar Grain
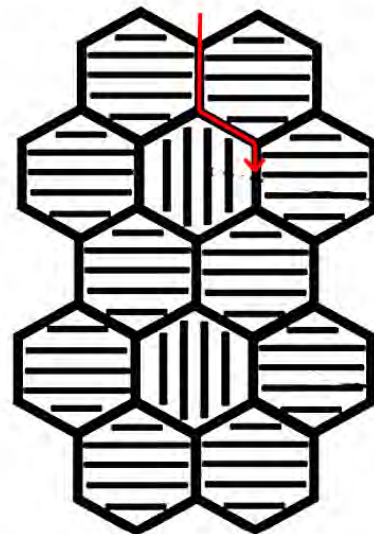
Nano Crystallites

Figure 5.2.2- 2 Schematic of crack propagation along grain boundaries for columnar grain structure and nano-crystallite structure coatings, the red arrow denotes the path of crack propagation
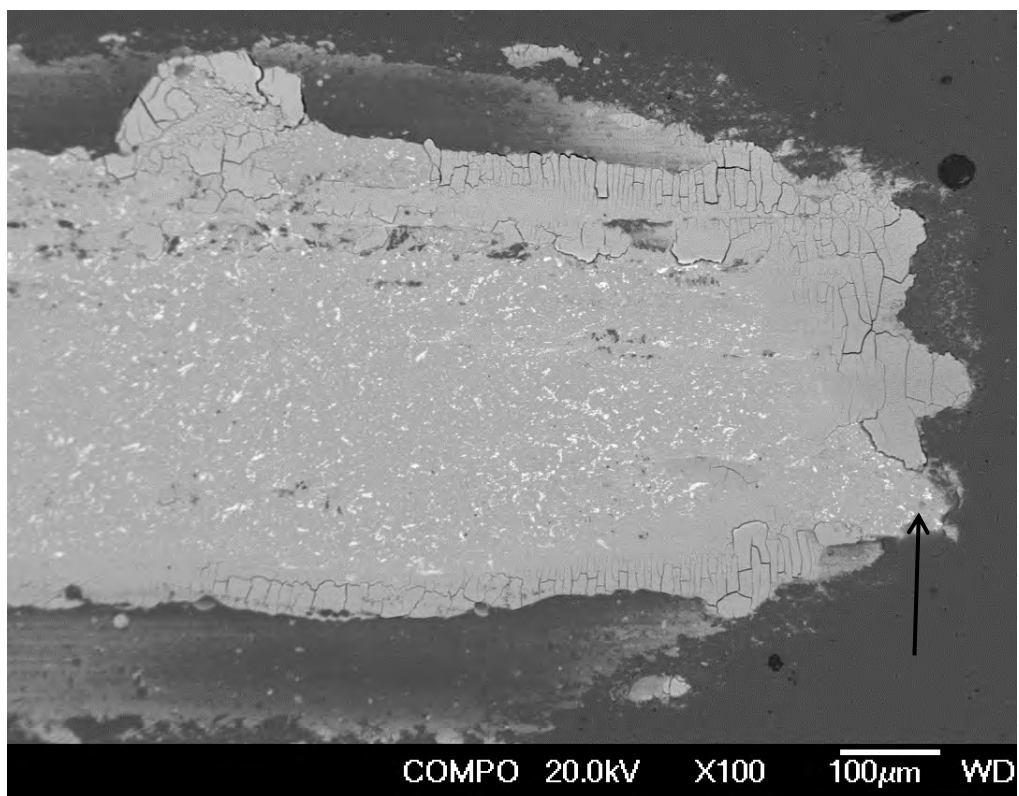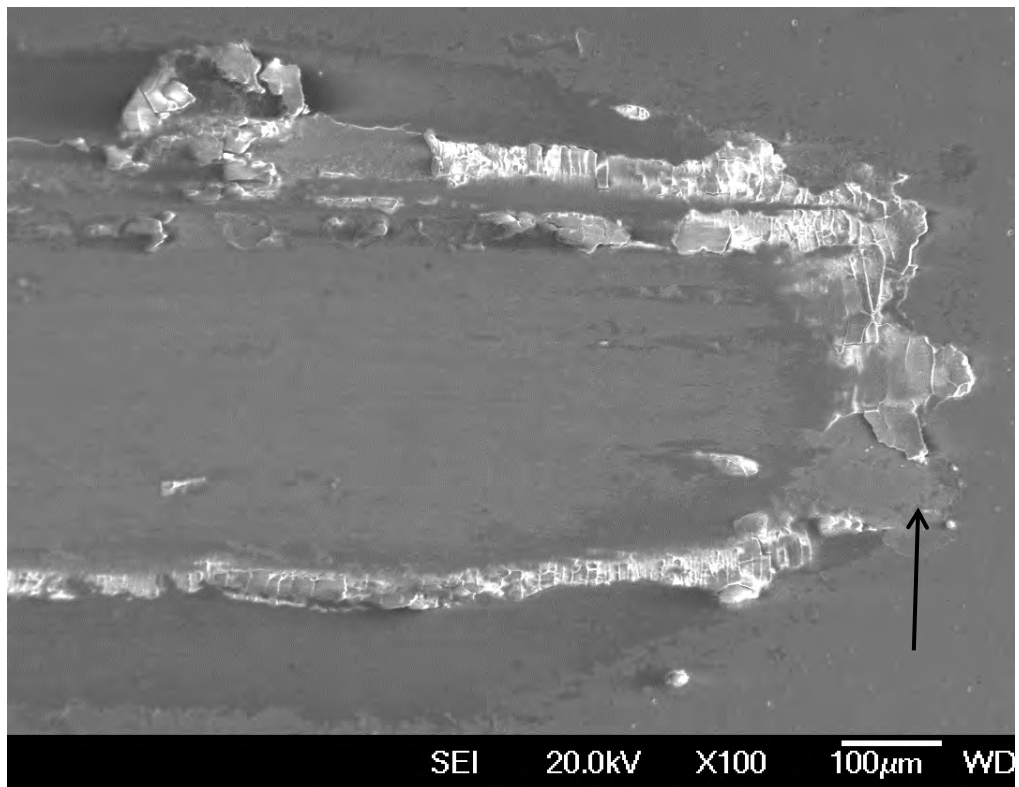
Figure 5.3.1- 1 SEM images of one end the wear track for C-I-8 after reciprocating sliding wear test against WC-Co ball at room temperature, in a) SE and b) BSE mode
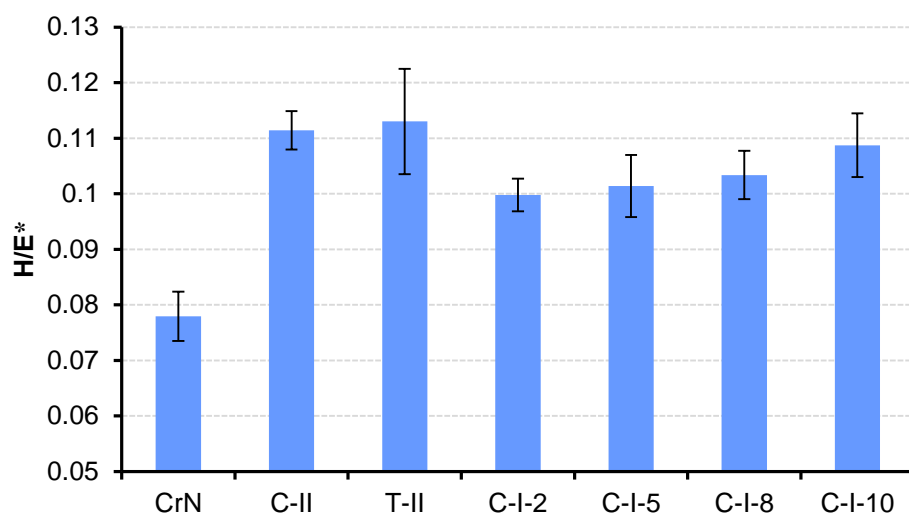
Figure 5.3.1- 2 The H/E* ratio of all coatings at room temperature
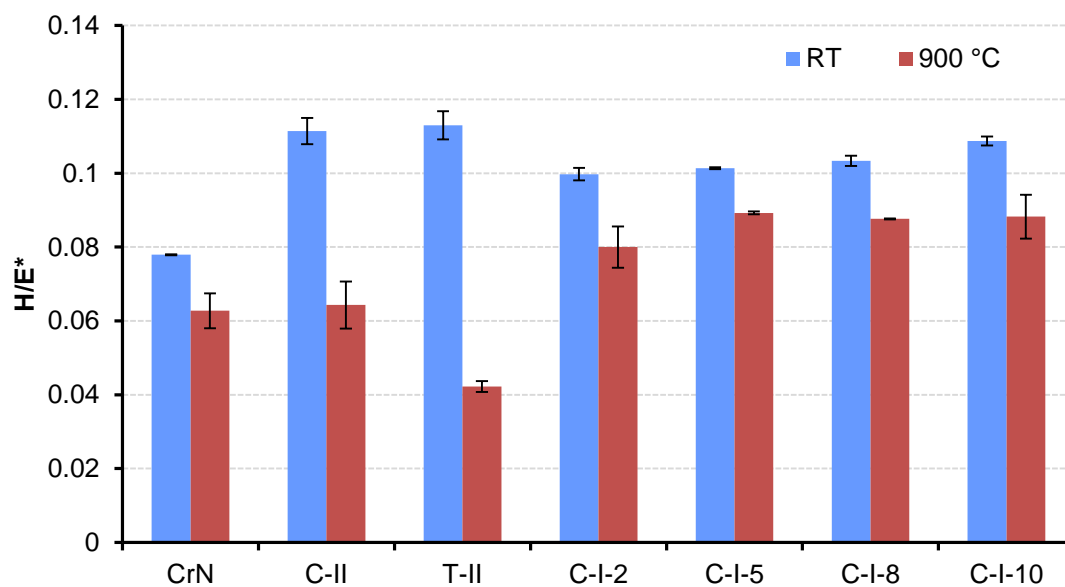
Figure 5.3.2- 1 H/E* ratio of as-deposited coatings and coatings after oxidation at 900 ℃
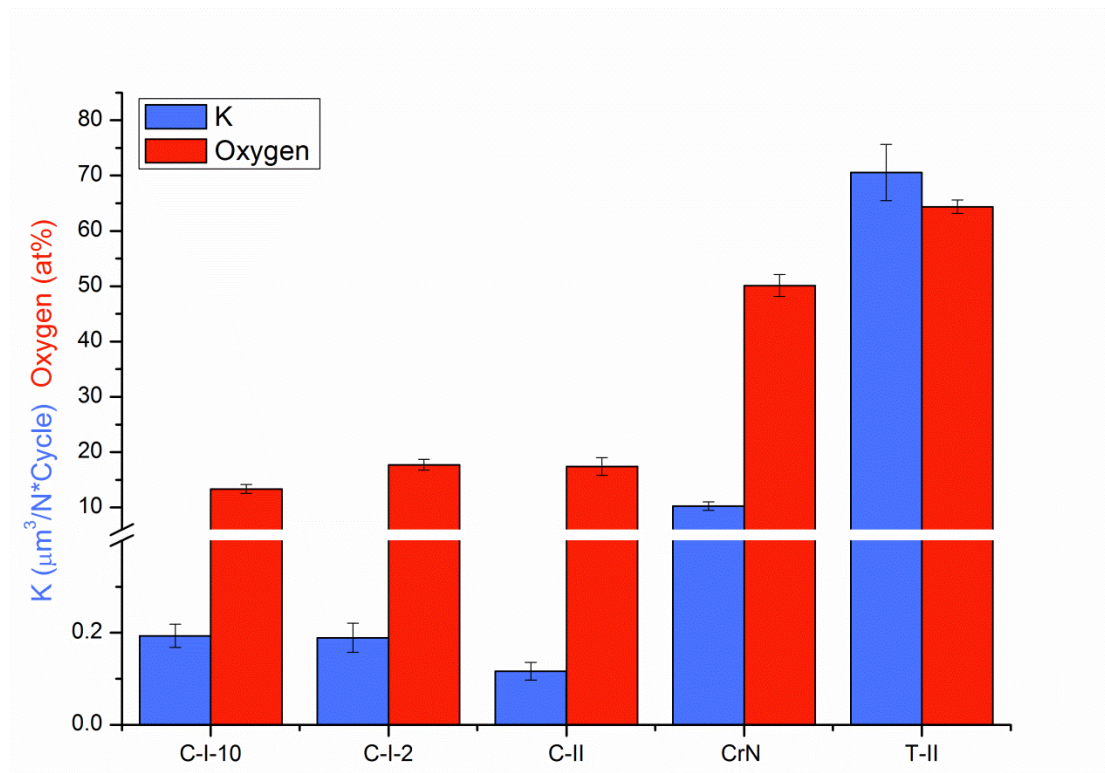
Figure 5.3.2- 2 Wear factor of selected coatings at 400 ℃ and surface oxygen content of corresponding coatings after oxidation at 900 ℃

Chapter 9 References

1.   Navinsek, B., P. Panjan, and A. Cvelbar, *Characterization of low temperature CrN and TiN (PVD) hard coatings.* Surface and Coatings Technology, 1995(74-75): p. 155-161.

2.   Durand-Drouhina, O., et al., *Mechanical properties and failure modes of TiAl(Si)N single and multilayer thin films.* Surface and Coatings Technology, 2003(163-164): p. 260-266.

3.   Nordin, M., M. Herranen, and S. Hogmark, *Influence of lamellae thickness on the corrosion behaviour of multilayered PVD TiN/CrN coatings.* Thin Solid films, 1999(348): p. 202-209.

4.   Kim, S.K., et al., *Deposition of superhard TiAlSiN thin films by cathodic arc plasma deposition.* Surface and Coatings Technology, 2005(200): p. 1391-1394.

5.   Chang, C.-L., J.-W. Lee, and M.-D. Tseng, *Microstructure, corrosion and tribological behaviors of TiAlSiN coatings deposited by cathodic arc plasma deposition.* Thin Solid films, 2009. **517**(17): p. 5231-5236.

6.   Martin, P.M., *Handbook of deposition technologies for films and coatings : science, applications and technology*. 3rd ed. 2010, Amsterdam: Elsevier. xviii, 912 p.

7.   Nakonechna, O., et al., *On the behaviour of indentation fracture in TiAlSiN hard thin films.* Thin Solid films, 2004. **447-448**: p. 406-412.

197

8. Holubar, P., M. Jilek, and M. Sima, *Present and Possible Future Applicaitons of Superhard Nanocomposite Coatings.* Surface and Coatings Technology, 2000(133-134): p. 145-151.

9. Chen, H.-W., et al., *Oxidation resistance of nanocomposite CrAlSiN under long-time heat treatment.* Surface and Coatings Technology, 2011. **206**(7): p. 1571-1576.

10. Chen, H.-W., et al., *Oxidation behavior of Si-doped nanocomposite CrAlSiN coatings.* Surface and Coatings Technology, 2010. **205**(5): p. 1189-1194.

11. Childs, T.H.C., *Metal Machining: Theory and Applications*. Referex Engineering. 2000: Arnold.

12. Edwards, R., *Cutting tools*. 1993: Institute of Materials.

13. Bunshah, R.F., *Handbook of hard coatings*. 2001, Norwich, NY: Noyes Publications. xvii,550 p.

14. Upadhyaya, G.S., *Cemented Tungsten Carbides: Production, Properties, and Testing*. Materials Science and Process Technology Series. Ceramic and Other Materials--Processing and Technology. 1998: Noyes Publ.

15. Grzesik, W., *Chapter Four - Cutting Tool Materials*, in *Advanced Machining Processes of Metallic Materials*. 2008, Elsevier: Amsterdam. p. 27-I.

16. Bhushan, B., *Principles and Applications of Tribology*. 1999: Wiley.

17. Gohar, R. and H. Rahnejat, *Fundamentals Of Tribology*. 2008: Imperial College Press.

18.   Herman, H., *Treatise on materials science and technology*. 1974: Academic Press.

19.   Bhushan, B., *Introduction to Tribology*. 2002: Wiley.

20.   NEALE, M.J., *Tribology Handbook*. 1996: Elsevier Science.

21.   Peterson, M., *Wear Control Handbook*. 1985: Asme Publications.

22.   Buckley, D.H., *Surface Effects in Adhesion, Friction, Wear, and Lubrication*. 1981: Elsevier Scientific Publishing Company.

23.   Suh, N.P., *Tribophysics*. 1986: Prentice-Hall.

24.   Bayer, R.G., *Mechanical wear prediction and prevention*. 1994: M. Dekker.

25.   Dong, H., *Development of novel surface engineering technologies for Ti6A14V alloy*, in *Department of Metallurgy and Materials*. 1997, University of Birmingham: Birmingham, UK.

26.   Bowden, F.P. and D. Tabor, *The Friction and Lubrication of Solids*. Oxford Classic Texts in the Physical Sciences Series. 2001: Oxford University Press, Incorporated.

27.   Sarkar, A.D., *Friction and wear*. 1980: Academic Press.

28.   Holm, R. and A. Heijne, *Electric contacts*. 1946: H. Geber.

29.   Rabinowicz, E., *Friction and Wear of Materials*. 1995: Wiley.

30.   Rabinowicz, E., *The Influence of Compatibility on Different Tribological Phenomena*. A S L E Transactions, 1971. **14**(3): p. 206-212.

31.   Ohmae, N., T. Okuyama, and T. Tsukizoe, *Influence of electronic structure on the friction in vacuum of 3d transition metals in contact with copper.* Tribology International, 1980. **13**(4): p. 177-180.

32.   Bhushan, B., R.E. Davis, and H.R. Kolar, *Metallurgical re-examination of wear modes II: adhesive and abrasive.* Thin Solid films, 1985. **123**(2): p. 113-126.

33.   Evans, A.G. and D.B. Marshall, *Wear Mechanisms in Ceramics.* Fundamentals of friction and wear of materials, ed. D.A. Rigney. 1981, Materials Park, OH: American Society for Metals.

34.   Quinn, T.F.J., *The effect of "hot-spot" temperatures on the unlubricated wear of steel* WearASLE Trans., 1967. **10**: p. 158-168.

35.   Quinn, T.F.J., *Review of oxidational wear: Part I: The origins of oxidational wear.* Tribology International, 1983. **16**(5): p. 257-271.

36.   Bowden, F.P. and K.E.W. Ridler, *Physical Properties of Surfaces. III. The Surface Temperature of Sliding Metals The Temperature of Lubricated Surfaces.* Proceedings of the Royal Society of London. Series A - Mathematical and Physical Sciences, 1936. **154**(883): p. 640-656.

37.   Quinn, T.F.J. and W.O. Winer, *The thermal aspects of oxidational wear.* Wear, 1985. **102**(1–2): p. 67-80.

38.   Gee, A.W.J.d., *Friction and wear as related to the composition, structure, and properties of metals.* International Metals Reviews, 1979. **24**(1): p. 57-67.

39. Uetz, H. and K. Sommer, *Investigations of the effect of surface temperatures in sliding contact.* Wear, 1977. **43**(3): p. 375-388.

40. Quinn, T.F.J., *Role of oxidation in the mild wear of steel.* British Journal of Applied Physics, 1962. **13**(1): p. 33.

41. Faga, M.G., et al., *AlSiTiN nanocomposite coatings developed via Arc Cathodic PVD: Evaluation of wear resistance via tribological analysis and high speed machining operations.* Wear, 2007(263): p. 1306-1314.

42. Kim, J.S., et al., *Cutting performance of Ti–Al–Si–N-coated tool by a hybrid-coating system for high-hardened materials.* Surface and Coatings Technology, 2005(193): p. 249-254.

43. Veprek, S. and M.J.G. Veprek-Heijman, *Industrial applications of superhard nanocomposite coatings.* Surface and Coatings Technology, 2008. **202**(21): p. 5063-5073.

44. Bell, T., *SURFACE ENGINEERING: PAST, PRESENT, AND FUTURE.* Surface Engineering, 1990. **6**(1): p. 31-40.

45. Bell, T., *Surface engineering: its current and future impact on tribology.* Journal of Physics D: Applied Physics, 1992. **25**(1A): p. A297.

46. Grzesik, W., *Advanced Protective Coatings for Manufacturing and Engineering.* 2003: Carl Hanser GmbH.

47. Bhushan, B., *Modern tribology handbook: Principles of tribology.* The Mechanics and Materials Science Series. 2001: CRC PressINC.

48. Rebenne, H.E. and D.G. Bhat, *Review of CVD TiN coatings for wear-resistant applications: deposition processes, properties and performance.* Surface and Coatings Technology, 1994. **63**(1–2): p. 1-13.

49. Zhang, S. and W. Zhu, *TiN coating of tool steels: a review.* Journal of Materials Processing Technology, 1993. **39**(1–2): p. 165-177.

50. Vera, E.E., et al., *A study of the wear performance of TiN, CrN and WC/C coatings on different steel substrates.* Wear, 2011. **271**(9–10): p. 2116-2124.

51. Lin, J., et al., *CrN/AlN superlattice coatings synthesized by pulsed closed field unbalanced magnetron sputtering with different CrN layer thicknesses.* Thin Solid films, 2009. **517**(20): p. 5798-5804.

52. Xu, Y.F., *Fabrication of nanocomposite Ti-Al-Si-N films deposited by reactive unbalanced magnetron sputtering and their proterties-modification by high-energy carbon ion implantation*, in *Department of Manufacturing Engineering and Engineering Management* 2009, City University of Hong Kong: HongKong. p. 96.

53. Knotek, O., T. Leyendecker, and F. Jungblut, *On the properties of physically vapour-deposited Ti-Al-V-N coatings.* Thin Solid films, 1987. **153**(1-3): p. 83-90.

54. Jarms, C., H.R. Stock, and P. Mayr, *Mechanical properties, structure and oxidation behaviour of Ti1-xAlxN-hard coatings deposited by pulsed d.c. plasma-assisted chemical vapour deposition (PACVD).* Surface and Coatings Technology, 1998. **108-109**(1-3): p. 206-210.

55.   Vennemann, A., et al., *Oxidation resistance of titanium-aluminium-silicon nitride coatings.* Surface and Coatings Technology, 2003. **174-175**: p. 408-415.

56.   Navinšek, B. and P. Panjan, *Novel applications of CrN (PVD) coatings deposited at 200 °C.* Surface and Coatings Technology, 1995. **74–75, Part 2**(0): p. 919-926.

57.   Yao, S.H. and Y.L. Su, *The tribological potential of CrN and Cr(C,N) deposited by multi-arc PVD process.* Wear, 1997. **212**(1): p. 85-94.

58.   Su, Y.L., et al., *Comparison of tribological behavior of three films—TiN, TiCN and CrN—grown by physical vapor deposition.* Wear, 1997. **213**(1–2): p. 165-174.

59.   Wilson, A., et al., *A comparison of the wear and fatigue properties of plasma-assisted physical vapour deposition TiN, CrN and duplex coatings on Ti-6Al-4V.* Surface and Coatings Technology, 1993. **62**(1–3): p. 600-607.

60.   Navinšek, B., P. Panjan, and I. Milošev, *Industrial applications of CrN (PVD) coatings, deposited at high and low temperatures.* Surface and Coatings Technology, 1997. **97**(1–3): p. 182-191.

61.   Lamni, R., et al., *Microstructure and nanohardness properties of Zr–Al–N and Zr–Cr–N thin films.* Journal of Vacuum Science & Technology A Vacuum Surfaces and Films, 2005. **23**(4): p. 593.

62.   Wang, Q. and K.H. Kim, *Effect of negative bias voltage on CrN films deposited by arc ion plating. II. Film composition, structure, and properties.*

Journal of Vacuum Science & Technology A Vacuum Surfaces and Films, 2008. **26**(5): p. 1267.

63. Lembke, M.I., et al., *Joint second prize - Significance of Y and Cr in TiAlN hard coatings for dry rich speed cutting.* Surface Engineering, 2001. **17**(2): p. 153-158.

64. Smith, I.J., et al., *Dry cutting performance of HSS twist drills coated with improved TiAlN.* Surface & Coatings Technology, 1997. **90**(1-2): p. 164-171.

65. Luo, Q.H. and Y.H. Lu, *Microstructure and mechanical properties of reactive magnetron sputtered Ti–B–C–N nanocomposite coatings.* Applied Surface Science, 2011. **258**(3): p. 1021-1026.

66. Mitterer, C., et al., *Microstructure and properties of nanocomposite Ti–B–N and Ti–B–C coatings.* Surface and Coatings Technology, 1999. **120–121**(0): p. 405-411.

67. Jehn, H.A., *Multicomponent and multiphase hard coatings for tribological applications.* Surface and Coatings Technology, 2000. **131**(1-3): p. 433-440.

68. Hultman, L., *Thermal stability of nitride thin films.* Vacuum, 2000. **57**(1): p. 1-30.

69. Holleck, H., *METASTABLE COATINGS - PREDICTION OF COMPOSITION AND STRUCTURE.* Surface & Coatings Technology, 1988. **36**(1-2): p. 151-159.

70. Makino, Y. and K. Nogi, *Synthesis of pseudobinary Cr-Al-N films with B1 structure by rf-assisted magnetron sputtering method.* Surface & Coatings Technology, 1998. **98**(1-3): p. 1008-1012.

71. Ulrich, S., et al., *Influence of low energy ion implantation on mechanical properties of magnetron sputtered metastable (Cr,Al)N thin films.* Thin Solid films, 2003. **437**(1–2): p. 164-169.

72. Madan, A., et al., *Stabilization of cubic AlN in epitaxial AlN/TiN superlattices.* Physical Review Letters, 1997. **78**(9): p. 1743-1746.

73. Setoyama, M., et al., *Formation of cubic-AlN in TiN/AlN superlattice.* Surface and Coatings Technology, 1996. **86–87, Part 1**(0): p. 225-230.

74. Hörling, A., et al., *Mechanical properties and machining performance of Ti1−xAlxN-coated cutting tools.* Surface and Coatings Technology, 2005. **191**(2–3): p. 384-392.

75. Weber, F.R., et al., *Cathodic arc evaporation of (Ti,Al)N coatings and (Ti,Al)N/TiN multilayer-coatings--correlation between lifetime of coated cutting tools, structural and mechanical film properties.* Surface and Coatings Technology, 2004. **177-178**: p. 227-232.

76. PalDey, S. and S.C. Deevi, *Single layer and multilayer wear resistant coatings of (Ti,Al)N: a review.* Materials Science and Engineering A, 2003. **342**(1-2): p. 58-79.

77. Durand-Drouhin, O., et al., *Mechanical properties and failure modes of TiAl(Si)N single and multilayer thin films.* Surface and Coatings Technology, 2003(163-164): p. 260-266.

78. Fox-Rabinovich, G.S., et al., *Effect of mechanical properties measured at room and elevated temperatures on the wear resistance of cutting tools with TiAlN and AlCrN coatings.* Surface and Coatings Technology, 2006. **200**(20–21): p. 5738-5742.

79. Hovsepian, P.E., et al., *TiAlN based nanoscale multilayer coatings designed to adapt their tribological properties at elevated temperatures.* Thin Solid films, 2005. **485**(1-2): p. 160-168.

80. Mayrhofer, P.H., et al., *Self-organized nanostructures in the Ti-Al-N system.* Applied Physics Letters, 2003. **83**(10): p. 2049-2051.

81. Bao, M., et al., *Microstructure and wear behaviour of silicon doped Cr–N nanocomposite coatings.* Thin Solid films, 2009. **517**(17): p. 4938-4941.

82. Park, J.H., et al., *Synthesis and mechanical properties of Cr–Si–N coatings deposited by a hybrid system of arc ion plating and sputtering techniques.* Surface and Coatings Technology, 2004. **188–189**(0): p. 425-430.

83. Kim, K.H., S.-r. Choi, and S.-y. Yoon, *Superhard Ti–Si–N coatings by a hybrid system of arc ion plating and sputtering techniques.* Surface and Coatings Technology, 2002. **161**(2–3): p. 243-248.

84.   Vepřek, S., et al., *Novel thermodynamically stable and oxidation resistant superhard coating materials.* Surface and Coatings Technology, 1996. **86–87, Part 1**(0): p. 394-401.

85.   Banakh, O., et al., *High-temperature oxidation resistance of Cr1−xAlxN thin films deposited by reactive magnetron sputtering.* Surface and Coatings Technology, 2003. **163–164**(0): p. 57-61.

86.   Cheng, Y.H., T. Browne, and B. Heckerman, *Nanocomposite TiSiN coatings deposited by large area filtered arc deposition.* Journal of Vacuum Science & Technology A, 2009. **27**(1): p. 82-88.

87.   Hu, X., et al., *Microstructure and properties of Ti-Si-N nanocomposite films.* Journal of Vacuum Science and Technology A: Vacuum, Surfaces and Films, 2002. **20**(6): p. 1921-1926.

88.   Zhang, S., et al., *A superhard CrAlSiN superlattice coating deposited by multi-arc ion plating: I. Microstructure and mechanical properties.* Surface and Coatings Technology, 2012(0).

89.   Vaz, F., et al., *Characterisation of Ti1-xSixNy nanocomposite films.* Surface and Coatings Technology, 2000. **133-134**: p. 307-313.

90.   Briois, P., et al., *Structural and Mechanical Properties of (Al,Cr)N and (Al,Cr)SiN Coatings Reactively Sputter Deposited.* Plasma Processes and Polymers, 2007. **4**(S1): p. S677-S680.

91.   Ding, X.-z., X.T. Zeng, and Y.C. Liu, *Structure and properties of CrAlSiN Nanocomposite coatings deposited by lateral rotating cathod arc.* Thin Solid films, 2011. **519**(6): p. 1894-1900.

92.   Männling, H.D., et al., *Thermal stability of superhard nanocomposite coatings consisting of immiscible nitrides.* Surface and Coatings Technology, 2001. **146–147**(0): p. 263-267.

93.   Cavaleiro, A. and C. Louro, *Nanocrystalline structure and hardness of thin films.* Vacuum, 2002. **64**(3–4): p. 211-218.

94.   Vaz, F., et al., *Physical, structural and mechanical characterization of Ti 1-xSi xN y films.* Surface and Coatings Technology, 1998. **108-109**: p. 236-240.

95.   Martinez, E., et al., *Electrical, optical and mechanical properties of sputtered CrNy and Cr1−xSixN1.02 thin films.* Thin Solid films, 2004. **447–448**(0): p. 332-336.

96.   Benkahoul, M., et al., *Microstructure and mechanical properties of Cr–Si–N coatings prepared by pulsed reactive dual magnetron sputtering.* Surface and Coatings Technology, 2008. **202**(16): p. 3975-3980.

97.   Castaldi, L., et al., *High temperature phase changes and oxidation behavior of Cr–Si–N coatings.* Surface and Coatings Technology, 2007. **202**(4–7): p. 781-785.

98.   Soldán, J., et al., *Structure–property relations of arc-evaporated Al–Cr–Si–N coatings.* Surface and Coatings Technology, 2008. **202**(15): p. 3555-3562.

99.   Choi, J.B., et al., *Effects of Si content and free Si on oxidation behavior of Ti–Si–N coating layers.* Thin Solid films, 2004. **447–448**(0): p. 365-370.

100.   Holubář, P., M. J lek, and M.   ma, *Nanocomposite nc-TiAlSiN and nc-TiN–BN coatings: their applications on substrates made of cemented carbide and results of cutting tests.* Surface and Coatings Technology, 1999. **120–121**(0): p. 184-188.

101.   Parlinska-Wojtan, M., et al., *Conventional and high resolution TEM investigation of the microstructure of compositionally graded TiAlSiN thin films.* Surface and Coatings Technology, 2004. **177–178**(0): p. 376-381.

102.   Martin, P.J. and A. Bendavid, *The filtered arc process and materials deposition.* Surface and Coatings Technology, 2001. **142–144**(0): p. 7-10.

103.   Karimi, A., et al., *Fracture mechanisms in nanoscale layered hard thin films.* Thin Solid films, 2002. **420–421**(0): p. 275-280.

104.   Murakami, R.-i., Y. Matsuda, and D. Yonekura, *Tribological properties of TiAlSiN film coated by AIP equipment onto SKD61 substrate*, in *Tribology Series*, M.P.G.D. D. Dowson and A.A. Lubrecht, Editors. 2003, Elsevier. p. 315-321.

105.   Parlinska-Wojtan, M., et al., *Characterization of thermally treated TiAlSiN coatings by TEM and nanoindentation.* Surface and Coatings Technology, 2004. **188–189**(0): p. 344-350.

106. Kim, S.K., et al., *Effect of cathode arc current and bias voltage on the mechanical properties of CrAlSiN thin films.* Surface and Coatings Technology, 2008. **202**(22–23): p. 5400-5404.

107. Settineri, L., et al., *Evaluation of wear resistance of AlSiTiN and AlSiCrN nanocomposite coatings for cutting tools.* CIRP Annals - Manufacturing Technology, 2008. **57**(1): p. 575-578.

108. Rafaja, D., et al., *Internal structure of clusters of partially coherent nanocrystallites in Cr–Al–N and Cr–Al–Si–N coatings.* Surface and Coatings Technology, 2007. **201**(24): p. 9476-9484.

109. Zhang, S., et al., *A superhard CrAlSiN superlattice coating deposited by a multi-arc ion plating: II. Thermal stability and oxidation resistance.* Surface and Coatings Technology, 2013. **214**(0): p. 153-159.

110. Polcar, T. and A. Cavaleiro, *High-temperature tribological properties of CrAlN, CrAlSiN and AlCrSiN coatings.* Surface and Coatings Technology, 2011. **206**(6): p. 1244-1251.

111. Lee, D.B., T.D. Nguyen, and S.K. Kim, *Air-oxidation of nano-multilayered CrAlSiN thin films between 800 and 1000 °C.* Surface and Coatings Technology, 2009. **203**(9): p. 1199-1204.

112. Chang, Y.-Y., et al., *High temperature oxidation resistance of CrAlSiN coatings synthesized by a cathodic arc deposition process.* Journal of Alloys and Compounds, 2008. **461**(1–2): p. 336-341.

113.   Polcar, T., et al., *Tribological Performance of CrAlSiN Coatings at High Temperatures.* Plasma Processes and Polymers, 2009. **6**(S1): p. S935-S940.

114.   Endrino, J.L., et al., *Determination of the local environment of silicon and the microstructure of quaternary CrAl(Si)N films.* Acta Materialia, 2007. **55**(6): p. 2129-2135.

115.   Hasegawa, H., et al., *Characterization of quaternary (Cr,Al)N-based films synthesized by the cathodic arc method.* Surface and Coatings Technology, 2007. **202**(4–7): p. 786-789.

116.   Rafaja, D., et al., *Microstructure development in Cr–Al–Si–N nanocomposites deposited by cathodic arc evaporation.* Surface and Coatings Technology, 2006. **201**(6): p. 2835-2843.

117.   Park, I.-W., et al., *Deposition and mechanical evaluation of superhard Ti-Al-Si-N nanocomposite films by a hybrid coating system.* Thin Solid films, 2004. **447-448**: p. 443-448.

118.   Tanaka, Y., et al., *Structure and properties of Al-Ti-Si-N coatings prepared by the cathodic arc ion plating method for high speed cutting applications.* Surface and Coatings Technology, 2001. **146-147**: p. 215-221.

119.   Holleck, H. and V. Schier, *Multilayer PVD coatings for wear protection.* Surface and Coatings Technology, 1995. **76–77, Part 1**(0): p. 328-336.

120.   Hall, E.O., *The Deformation and Ageing of Mild Steel: III Discussion of Results.* Proceedings of the Physical Society. Section B, 1951. **64**(9): p. 747.

121. Petch, N.J., *THE CLEAVAGE STRENGTH OF POLYCRYSTALS.* Journal of the Iron and Steel Institute, 1953. **174**(1): p. 25-28.

122. Vepřek, S. and S. Reiprich, *A concept for the design of novel superhard coatings.* Thin Solid films, 1995. **268**(1–2): p. 64-71.

123. Siegel, H.J. *Introduction to the 1996 ICPP Workshop on Challenges for Parallel Processing.* in *Parallel Processing, 1996. Proceedings of the 1996 ICPP Workshop on Challenges for.* 1996.

124. Musil, J., *Hard nanocomposite coatings: Thermal stability, oxidation resistance and toughness.* Surface and Coatings Technology, 2012. **207**(0): p. 50-65.

125. Musil, J., *Hard and superhard nanocomposite coatings.* Surface and Coatings Technology, 2000. **125**(1–3): p. 322-330.

126. Procházka, J., et al., *Conditions required for achieving superhardness of ≥45 GPa in nc-TiN/a-Si3N4 nanocomposites.* Materials Science and Engineering: A, 2004. **384**(1–2): p. 102-116.

127. Veprek, S., *The search for novel, superhard materials.* Journal of Vacuum Science & Technology A: Vacuum, Surfaces, and Films, 1999. **17**(5): p. 2401-2420.

128. Barshilia, H.C., et al., *Deposition and characterization of TiAlSiN nanocomposite coatings prepared by reactive pulsed direct current unbalanced magnetron sputtering.* Applied Surface Science, 2010. **256**(21): p. 6420-6426.

129. Carvalho, S., et al., *In-service behaviour of (Ti,Si,Al)Nx nanocomposite films.* Wear, 2012. **274–275**(0): p. 68-74.

130. Carvalho, S., et al., *Microstructure and mechanical properties of nanocomposite (Ti,Si,Al)N coatings.* Thin Solid films, 2001. **398–399**(0): p. 391-396.

131. Mège-Revil, A., et al., *Oxidation and tribo-oxidation of nanocomposite Cr–Si–N coatings deposited by a hybrid arc/magnetron process.* Surface and Coatings Technology, 2009. **204**(6–7): p. 973-977.

132. Lin, J., et al., *Structure and properties of CrSiN nanocomposite coatings deposited by hybrid modulated pulsed power and pulsed dc magnetron sputtering.* Surface and Coatings Technology, 2013. **216**(0): p. 251-258.

133. Veprek, S., et al., *Composition, nanostructure and origin of the ultrahardness in nc-TiN/a-Si3N4/a- and nc-TiSi2 nanocomposites with HV=80 to ≥105 GPa.* Surface and Coatings Technology, 2000. **133–134**(0): p. 152-159.

134. Veprek, S., S. Reiprich, and L. Shizhi, *Superhard nanocrystalline composite materials: The TiN/Si$_3$N$_4$ system.* Applied Physics Letters, 1995. **66**(20): p. 2640-2642.

135. Zhang, S., et al., *Toughening of hard nanostructural thin films: a critical review.* Surface and Coatings Technology, 2005. **198**(1–3): p. 2-8.

136. Yao, S.H., et al., *Tribology and oxidation behavior of TiN/AlN nano-multilayer films.* Tribology International, 2006. **39**(4): p. 332-341.

137. Koehler, J.S., *Attempt to Design a Strong Solid.* Physical Review B, 1970. **2**(2): p. 547.

138. Carvalho, N.J.M., et al., *Stress analysis and microstructure of PVD monolayer TiN and multilayer TiN/(Ti,Al)N coatings.* Thin Solid films, 2003. **429**(1–2): p. 179-189.

139. Chen, L., et al., *Microstructure and mechanical properties of Ti(C,N) and TiN/Ti(C,N) multilayer PVD coatings.* International Journal of Refractory Metals and Hard Materials, 2008. **26**(5): p. 456-460.

140. Nordin, M. and M. Larsson, *Deposition and characterisation of multilayered PVD TiN/CrN coatings on cemented carbide.* Surface and Coatings Technology, 1999. **116–119**(0): p. 108-115.

141. Leyendecker, T., et al., *TiAlN–Al2O3 PVD-multilayer for metal cutting operation.* Surface and Coatings Technology, 1997. **97**(1–3): p. 790-793.

142. Holleck, H., *Material selection for hard coatings.* Journal of Vacuum Science & Technology A: Vacuum, Surfaces, and Films, 1986. **4**(6): p. 2661-2669.

143. Fukumoto, N., et al., *Effects of bilayer thickness and post-deposition annealing on the mechanical and structural properties of (Ti,Cr,Al)N/(Al,Si)N multilayer coatings.* Surface and Coatings Technology, 2009. **203**(10–11): p. 1343-1348.

144. Cselle, T., et al., *Nanostructured Coatings and Processes on an Industrial Scale*, in *Advanced Coatings and Surface Systems for Cutting Tools & Wear Parts Gorham Conference*. 2002: Atlanta, GA, USA.

145. Ho, W.-Y., et al., *Characteristics of PVD-CrAlSiN films after post-coat heat treatments in nitrogen atmosphere.* Applied Surface Science, 2011. **257**(8): p. 3770-3775.

146. *Physical vapour deposition for tool steel.* Tribology International, 1986. **19**(5): p. 272-272.

147. Mattox, D.M., *Handbook of physical vapor deposition (PVD) processing.* 1998, New Jersey: Noyes Publications. 944.

148. Boxman, R.L., P.J. Martin, and D.M. Sanders, *Handbook of vacuum arc science and technology.* 1996: Noyes Publications.

149. Tien, S.-K., et al., *Effect of nitrogen flow on the properties of quaternary CrAlSiN coatings at elevated temperatures.* Surface and Coatings Technology, 2007. **202**(4–7): p. 735-739.

150. Hamilton, G.M., *EXPLICIT EQUATIONS FOR THE STRESSES BENEATH A SLIDING SPHERICAL CONTACT.* Proceedings of the Institution of Mechanical Engineers, Part C: Mechanical Engineering Science, 1983. **197**: p. 53-59.

151. Teixeira, V., *Residual stress and cracking in thin PVD coatings.* Vacuum, 2002. **64**(3–4): p. 393-399.

152. Arnell, R.D., *THE MECHANICS OF THE TRIBOLOGY OF THIN FILM SYSTEMS*, in *Metallurgical Coatings and Thin Films 1990*, B.D. Sartwell, Editor. 1990, Elsevier. p. 674-687.

153. Drory, M.D., M.D. Thouless, and A.G. Evans, *On the decohesion of residually stressed thin films.* Acta Metallurgica, 1988. **36**(8): p. 2019-2028.

154. Evans, A.G. and J.W. Hutchinson, *On the mechanics of delamination and spalling in compressed films.* International Journal of Solids and Structures, 1984. **20**(5): p. 455-466.

155. Jurci, P., et al., *plasma nitriding of P/M M2 tool steel- structure and properties.* Material in technologije, 2003. **37**: p. 3-4.

156. Kwietniewski, C., et al., *Nitrided layer embrittlement due to edge effect on duplex treated AISI M2 high-speed steel.* Surface and Coatings Technology, 2004. **179**(1): p. 27-32.

157. da Silva Rocha, A., et al., *Microstructure and residual stresses of a plasma-nitrided M2 tool steel.* Surface and Coatings Technology, 1999. **115**(1): p. 24-31.

158. Pessin, M.A., et al., *The effects of plasma nitriding process parameters on the wear characteristics of AISI M2 tool steel.* Tribology Letters, 2000. **8**(4): p. 223-228.

159. Wadhwa, A.S. and E.H.S. Dhaliwal, *A Textbook of Engineering Material and Metallurgy.* 2008: Laxmi Publications Pvt Ltd.

160. Pye, D., *Practical Nitriding and Ferritic Nitrocarburizing.* 2003: Asm International.

161.   Hirsch, T., et al., *Residual stress-affected diffusion during plasma nitriding of tool steels.* Metallurgical and Materials Transactions A, 2004. **35**(11): p. 3523-3530.

162.   Gallo, S.C., *Active screen plasma surface engineering of austenitic stainless steel for enchanced tribological and corrosion properties*, in *School of Metallurgy and Materials*. 2009, University of Birmingham: Birmingham. p. 272.

163.   Keshavarz Hedayati, M., F. Mahboubi, and T. Nickchi, *Comparison of conventional and active screen plasma nitriding of hard chromium electroplated steel.* Vacuum, 2009. **83**(8): p. 1123-1128.

164.   Alves Jr, C., et al., *Use of cathodic cage in plasma nitriding.* Surface and Coatings Technology, 2006. **201**(6): p. 2450-2454.

165.   Ahangarani, S., F. Mahboubi, and A.R. Sabour, *Effects of various nitriding parameters on active screen plasma nitriding behavior of a low-alloy steel.* Vacuum, 2006. **80**(9): p. 1032-1037.

166.   Li, C.X., *Active screen plasma nitriding an overview.* Surface Engineering, 2010. **26**: p. 135-141.

167.   Bell, T. and C.X. Li, *Active screen plasma nitriding of materials.* International Heat Treatment and Surface Engineering, 2007. **1**: p. 34-38.

168.   Corujeira Gallo, S. and H. Dong, *On the fundamental mechanisms of active screen plasma nitriding.* Vacuum, 2009. **84**(2): p. 321-325.

169.   Doyle, E.D. and P. Hubbard, *Innovation in nitriding.* International Heat Treatment and Surface Engineering, 2010. **4**: p. 33-40.

170.   Bell, T., H. Dong, and Y. Sun, *Realising the potential of duplex surface engineering.* Tribology International, 1998. **31**(1–3): p. 127-137.

171.   Boloye, A., *Private conversation*

172.   Li, X.Y., Y. Sun, and A. Bloyce, *XTEM characterisation of low temperature plasma nitrided AISI316 austenitic stainless steel*, in *Institute of Physics Conference Series*. 1997. p. 633-636.

173.   Li, C.X., T. Bell, and H. Dong, *A Study of Active Screen Plasma Nitriding.* Surface Engineering, 2002. **18**: p. 174-181.

174.   Baker, M.A., et al., *A study of the nanostructure and hardness of electron beam evaporated TiAlBN Coatings.* Thin Solid films, 2010. **518**(15): p. 4273-4280.

175.   Petrov, I., et al., *Microstructural evolution during film growth.* Journal of Vacuum Science and Technology A: Vacuum, Surfaces and Films, 2003. **21**(5): p. S117-S128.

176.   Zhao, J.P., et al., *Overall energy model for preferred growth of TiN films during filtered arc deposition.* Journal of Physics D: Applied Physics, 1997. **30**(1): p. 5.

177.   Pelleg, J., et al., *Reactive-sputter-deposited TiN films on glass substrates.* Thin Solid Films, 1991. **197**(1–2): p. 117-128.

178. Je, J.H., et al., *Preferred orientation of TiN films studied by a real time synchrotron x-ray scattering.* Journal of Applied Physics, 1997. **81**(9): p. 6126-6133.

179. Uglov, V.V., et al., *Formation of complex Al–N–C layer in aluminium by successive carbon and nitrogen implantation.* Nuclear Instruments and Methods in Physics Research Section B: Beam Interactions with Materials and Atoms, 1999. **147**(1–4): p. 332-336.

180. Yonenaga, I., T. Shima, and M.H.F. Sluiter, *Nano-Indentation Hardness and Elastic Moduli of Bulk Single-Crystal AIN : Short Note.* Japanese journal of applied physics. Pt. 1, Regular papers & short notes, 2002. **41**: p. 4620-4621.

181. [cited 2013 08/04/2013]; Available from: http://www.edgepolishing.com/aluminum-nitride.htm.

182. Shinn, M., L. Hultman, and S.A. Barnett, *Growth, structure, and microhardness of epitaxial TiN/NbN superlattices.* Journal of Materials Research, 1992. **7**(04): p. 901-911.

183. Nordin, M., M. Larsson, and S. Hogmark, *Mechanical and tribological properties of multilayered PVD TiN/CrN, TiN/MoN, TiN/NbN and TiN/TaN coatings on cemented carbide.* Surface and Coatings Technology, 1998. **106**(2–3): p. 234-241.

184. Zhou, Y., et al., *Hardness anomaly, plastic deformation work and fretting wear properties of polycrystalline TiN/CrN multilayers.* Wear, 1999. **236**(1–2): p. 159-164.

185. Selinder, T.I., et al., *Performance of PVD TiN/TaN and TiN/NbN superlattice coated cemented carbide tools in stainless steel machining.* Surface and Coatings Technology, 1998. **105**(1–2): p. 51-55.

186. Yang, Q., et al., *Preferred orientation and hardness enhancement of TiN/CrN superlattice coatings deposited by reactive magnetron sputtering.* Scripta Materialia, 2002. **46**(4): p. 293-297.

187. Zeng, X.T., *TiN/NbN superlattice hard coatings deposited by unbalanced magnetron sputtering.* Surface and Coatings Technology, 1999. **113**(1-2): p. 75-79.

188. Lehoczky, S.L., *Strength enhancement in thin-layered Al-Cu laminates.* Journal of Applied Physics, 1978. **49**(11): p. 5479-5485.

189. Wei, G., A. Rar, and J.A. Barnard, *Composition, structure, and nanomechanical properties of DC-sputtered CrNx (0≤x≤1) thin films.* Thin Solid films, 2001. **398–399**(0): p. 460-464.

190. Sue, J.A., A.J. Perry, and J. Vetter, *Young's modulus and stress of CrN deposited by cathodic vacuum arc evaporation.* Surface and Coatings Technology, 1994. **68–69**(0): p. 126-130.

191. Evans, A.G. and E.A. Charles, *Fracture Toughness Determinations by Indentation.* Journal of the American Ceramic Society, 1976. **59**(7-8): p. 371-372.

192. Lawn, B.R., A.G. Evans, and D.B. Marshall, *Elastic/Plastic Indentation Damage in Ceramics: The Median/Radial Crack System.* Journal of the American Ceramic Society, 1980. **63**(9-10): p. 574-581.

193. Hainsworth, S.V., M.R. McGurk, and T.F. Page, *The effect of coating cracking on the indentation response of thin hard-coated systems.* Surface and Coatings Technology, 1998. **102**(1–2): p. 97-107.

194. Page, T.F. and J.C. Knight, *Factors affecting the tribological behaviour of thin hard TiN and TiC coatings.* Surface and Coatings Technology, 1989. **39–40, Part 1**(0): p. 339-354.

195. Knight, J.C., T.F. Page, and I.M. Hutchings, *The influence of substrate hardness on the response of TiN-coated steels to surface deformation.* Thin Solid films, 1989. **177**(1–2): p. 117-132.

196. Jayaram, V., et al., *Contact deformation of TiN coatings on metallic substrates.* Materials Science and Engineering: A, 2006. **423**(1–2): p. 8-13.

197. Jacobson, D.M. and G. Humpston, *Principles of Brazing.* 2005: ASM International.

198. Tien, S.-K., J.-G. Duh, and J.-W. Lee, *Oxidation behavior of sputtered CrN/AlN multilayer coatings during heat treatment.* Surface and Coatings Technology, 2007. **201**(9–11): p. 5138-5142.

199. Huber, E. and S. Hofmann, *Oxidation behaviour of chromium-based nitride coatings.* Surface and Coatings Technology, 1994. **68–69**(0): p. 64-69.

200. Kacsich, T., et al., *Oxidation of thin chromium nitride films: Kinetics and morphology.* Journal of Physics Condensed Matter, 1996. **8**(49): p. 10703-10719.

201. Zhu, M., M. Li, and Y. Zhou, *Oxidation resistance of Cr1−xAlxN (0.18 ≤ x ≤ 0.47) coatings on K38G superalloy at 1000–1100 °C in air.* Surface and Coatings Technology, 2006. **201**(6): p. 2878-2886.

202. Leyland, A. and A. Matthews, *On the significance of the H/E ratio in wear control: a nanocomposite coating approach to optimised tribological behaviour.* Wear, 2000. **246**(1–2): p. 1-11.

203. Khruschov, M.M., *Principles of abrasive wear.* Wear, 1974. **28**(1): p. 69-88.

204. Fuentes, G.G., et al., *High temperature tribological characterisation of TiAlSiN coatings produced by cathodic arc evaporation.* Surface & Coatings Technology, 2010. **205**(5): p. 1368-1373.

205. Lassner, E. and W.D. Schubert, *Tungsten: Properties, Chemistry, Technology of the Elements, Alloys, and Chemical Compounds*. 1999: Kluwer Academic/Plenum Publishers.

206. Dong, H. and T. Bell, *Enhanced wear resistance of titanium surfaces by a new thermal oxidation treatment.* Wear, 2000. **238**(2): p. 131-137.

207. Neubrand, J. and H. Weiss, *Dry rolling wear of different materials induced by a non-uniform hertzian pressure distribution.* Surface and Coatings Technology, 1995. **76–77, Part 2**(0): p. 462-468.

208. Akazawa, M. and K. Kato, *Wear properties of Si3N4 in rolling-sliding contact.* Wear, 1988. **124**(2): p. 123-132.

209. Schiotz, J., in *Proceeding of the 22th Riso International Symposium on Material Science* 2001: Roskilde, Denmark. p. 127.

210. Chen, W.L., *Study on high temperature oxidation behaviors of nano-composite TiAlSiN coatings*, in *Department of Materials Science and Engineering*. 2009, MINGDAO University: Changhua. p. 117.

211. Zhang, Q.B., *Study on the microstructure, mechanical properties and high temperature oxidation behavior of cathodic arc evaporation deposited AlTiN/CrN and CrAlSiN thin film*, in *Department of Materials Science and Engineering*. 2008, MINGDAO University: Changhua.

212. Drescher, D., et al., *A model for particle growth in arc deposited armophous carbon films.* Diamond and Related Materials, 1998. **7**(9): p. 1375-1380.